CORA Cork Open Research Archive
Cartlann Taighde Oscailte Chorcaí

Title	Development of biopolymeric patterned thin films
Authors	Banta, Russell A.
Publication date	2020-11-23
Original Citation	Banta, R. A. 2020. Development of biopolymeric patterned thin films. PhD Thesis, University College Cork.
Type of publication	Doctoral thesis
Rights	© 2020, Russell A. Banta. - https://creativecommons.org/licenses/by-nc-nd/4.0/
Download date	2026-11-15 15:25:18
Item downloaded from	https://hdl.handle.net/10468/10894

UCC
University College Cork, Ireland
Coláiste na hOllscoile Corcaigh

Development of biopolymeric patterned thin films

Russell Alan Banta, BSc. (Hons)

School of Chemistry,

University College Cork,

Ireland.



ucc

Coláiste na hOllscoile Corcaigh, Éire
University College Cork, Ireland

Presented for the PhD. Degree to the National University of Ireland

Supervisors: Dr. Eoin Flynn, Dr. Paul Young, Prof. Justin Holmes,

DECLARATION

I, Russell Alan Banta, certify that this thesis is my own research and I have not obtained a degree in University College Cork or elsewhere on the basis of this PhD Thesis.

_____

Russell Alan Banta

ACKNOWLEDGEMENTS

Looking back, it's hard to believe I've spent 8 years in UCC. I've met some of the best friends in UCC, who have enriched my life. Firstly, I would like to thank Prof. Justin Holmes, for taking me in when I got dropped on his lab. This work wouldn't have gotten this far without him, and I'm forever grateful for him taking me in. I would also like to thank Prof. Michael Morris and Dr. Paul Young for taking a chance on me in the third year of my undergrad, and encouraging me to do a PhD on my own work. I wouldn't be here today without them.

There are too many people to name thank in 343, 420, and 115. Thank you to Tandra and Dave for your insight into my work when it wasn't going as well as I hoped. I would also like to thank Tim, for those tireless nights he spent fixing the AFM, scanning samples, and allowing to bounce ideas off of him. Not enough thanks I can give him.

To all the ERI lads, Ricky, Tommy, Aoibhinn, and Joe, I miss tea breaks with you all. Y'all made the lab great to be in, and it's not the same without you. Thanks to John for all his advice and banter throughout the PhD,

To Eoin, I owe the most thanks. In my first year as an undergrad, after a lab, he suggested I follow on with chemistry. He was great in labs, and really encouraged me to do better in them. He helped with my summer project, even though he wasn't working in UCC, and his work and encouragement is why I am here today. I would not have gotten as interested in chemistry had he not spoken about his work after labs to us, and I can't thank him enough for the last eight years.

To my dad, I wouldn't have gotten interested in science without you as an inspiration. When in college, for elec. eng., he would take home the circuits he was working on, explain what he was doing, and how it worked. He always encouraged me to take an interest in science, and ensured I had the chance to go to college. I will always be grateful for that.

Finally, after my accident, to everyone came together and helped with my hospital bills, offered me lifts, help with experiments, and were always checking in on me. I can't thank you all enough for that. It really made the difference and there aren't enough words to thank you all. Thank you to the entire Chemistry Department for that.

PUBLISHED ARTICLES

1] Russell A. Banta, Timothy W. Collins, Rickey A. Curley, Paul W. Young, Justin D. Holmes, Eoin J. Flynn. **Nanopatterned protein-polysaccharide thin films by humidity regulated phase separation.** *Journal of Colloid and Interface Science* **2018,** *532,* 171-181. DOI: 10.1016/j.jcis.2018.07.109.

2] Russell A. Banta, Timothy W. Collins, Rickey A. Curley, John J. O'Connell, Paul W. Young, Justin D. Holmes, Eoin J. Flynn. **Regulated Phase Separation in Nanopatterned Protein-Polysaccharide Thin Films by Spin Coating.** *Colloids and Surfaces B: Biointerfaces* **2020,** *190,* 110967. DOI: 10.1016/j.colsurfb.2020.110967.

SUBMITTED ARTICLES

1] Russell A. Banta, Timothy W. Collins, Rickey A. Curley, Paul W. Young, Justin D. Holmes, Eoin J. Flynn. **Biopolymer Metal Inclusion Lithography (BioMIL): A simple, renewable method to produce metal oxide masks**.

CONFERENCES

1] "**Patterned Protein-Polysaccharide Thin Films Through Humidity Regulated Phase Separation**" 28th Irish Environmental Researchers Colloquium 28th ENVIRON – Cork Institute of Technology, March 27th – 29th, 2018 (Poster)

TABLE OF CONTENTS

Declaration *2*

Acknowledgements *3*

Published Articles *4*

Submitted Articles *4*

Conferences *4*

Table of Contents *5*

Figures & Tables *10*

Terminology *20*

CHAPTER 1 INTRODUCTION *23*

1.1. Introduction and Motivation *24*

1.1.1. Introductory Statement **24**

1.1.2. Current Applications and Environmental Cost **25**

1.1.3. Overview **26**

1.2. Biopolymers vs. Synthetic Polymers *27*

1.3. Patterning Thin-Films: Polymer Blends *28*

1.3.1. Miscibility and Immiscibility in Blends **29**

1.3.1.1. Associative Phase Separation 29

1.3.1.2. Segregative Phase Separation 30

1.4. Other Morphology Determinants *30*

1.4.1. Thickness **31**

1.4.2. Solvent Evaporation Method **32**

1.4.2.1. Solvent Evaporation – Changing air capacity 32

1.4.2.2. Solvent Evaporation – Temperature effects 32

1.4.2.3. Solvent Evaporation – Solvent type 33

1.4.3. Substrate **33**

1.5. Growth mechanisms *34*

1.5.1. Spinodal Decomposition **35**

1.5.2. Nucleation & Growth **35**

1.5.2.1. Ostwald Ripening 35

1.5.2.2. Coalescence 36

1.6. State of the Art: PTFs ***36***

1.6.1. State of the Art: Hydrophobic Surfaces **37**

1.6.1.1. Replicating the Lotus Leaf 37

1.6.1.2 State of the Art: Synthetic Polymer Hydrophobic Surfaces 38

1.6.1.3 State of the Art: Biopolymer Hydrophobic Surfaces 40

1.6.1.4 State of the Art: Semi-synthetic Hydrophobic Surfaces 41

1.6.2. State of The Art: Responsive Surfaces **42**

1.6.2.1 Replicating Leaf Stomata 42

1.6.2.2 State of the Art: Synthetic Responsive Surfaces 43

1.6.2.3 State of the Art: Biopolymer Responsive Surfaces 44

1.6.3. State of The Art: Antireflective Surfaces **44**

1.6.3.1 Replicating Butterfly Wings 44

1.6.3.2 State of the Art: Synthetic Polymers in AR Surface Production 46

1.6.3.3 State of the Art: Semisynthetic Polymers in AR Surface Production 48

1.6.3.4 State of the Art: Biopolymers in AR Surface Production 49

1.6.4. State of The Art: Biomedical Surfaces **50**

1.6.4.1 Replicating Wood and Bone Surfaces 50

1.6.4.2 State of the Art: Synthetic Biomedical PTFs 51

1.6.4.3 State of the Art: Semi-Synthetics Biomedical PTFs 52

1.6.4.4 State of the Art: Biopolymer Biomedical PTFs 54

1.7. Beyond State of the Art: PTFs ***56***

1.8. References ***60***

CHAPTER 2 NANOPATTERNED PROTEIN-POLYSACCHARIDE THIN FILMS BY HUMIDITY REGULATED PHASE SEPARATION ***75***

2.1. Abstract ***76***

2.2 Introduction ***76***

2.3 Experimental *78*

2.3.1 Biopolymers, Casting Solutions and Substrate **78**

2.3.2 Solution Preparation **79**

2.3.3. Coating Preparation **80**

2.3.3.1 Thin-film Casting 80

2.3.3.2 Atomic Force Microscopy (AFM) 80

2.4 Results and Discussion *81*

2.4.1. SINGLE POLYMER SOLUTION THIN-FILMS **81**

2.4.2 Pr-Ps-S Solution Thin-Films **81**

2.4.2.1 Thin-films from Phase Separation of BSA-Ch-FA Solutions 81

2.4.2.2 THIN-FILMS FROM PHASE SEPARATION OF PG-CH-FA SOLUTIONS 86

2.4.2.3 GENERAL TRENDS IN PR-PS-S SOLUTION THIN-FILMS 90

2.4.3 Feature Growth in Pr-Ps-S Thin-Films **92**

2.5 Conclusion *96*

2.6. References *98*

2.7. Appendix *105*

CHAPTER 3 REGULATED PHASE SEPARATION IN NANOPATTERNED PROTEIN-POLYSACCHARIDE THIN FILMS BY SPIN COATING *111*

3.1. Abstract *112*

3.2. Graphical Abstract *112*

3.3. Introduction *113*

3.4. Experimental *114*

3.4.1. BIOPOLYMERS, CASTING SOLUTION AND SUBSTRATE **114**

3.4.2. SOLUTION PREPARATION **115**

3.4.3. COATING PREPARATION AND ANALYSIS **115**

3.4.3.1. Thin-film Casting 115

3.4.3.2. Atomic Force Microscopy 115

3.4.3.3. X-Ray Photoelectron Spectroscopy (XPS) 116

3.4.3.4. Attenuated Total Reflection Fourier Transform Infra-Red (ATR-FTIR) Spectroscopy....116
3.4.3.5. Selective Etching....117
3.4.3.6. Selective Metal Inclusion....117
3.4.3.7. Water Contact Angle (WCA)....117
3.5. Results and Discussion....118
3.5.1. SINGLE POLYMER SOLUTION THIN-FILMS....118
3.5.1.1. Thin-films from Phase Separation of BSA-Ch-FA Solutions....118
3.5.1.2. Chemical Characterisation of BSA-Ch Blend Films....124
3.5.2. PROTUBERANCE GROWTH IN BLEND THIN-FILMS....130
3.6. Conclusion....133
3.7. References....135
3.8. Appendix....145
3.8.1. SOLUTION PREPARATION....145
3.8.2. GENERAL TRENDS IN BLEND THIN-FILMS....158
3.8.3. PORE GROWTH IN BLEND THIN-FILMS....163
3.8.4. WATER CONTACT ANGLE....166
CHAPTER 4 METAL INCLUSION LITHOGRAPHY (BIOMIL): A SIMPLE, RENEWABLE METHOD TOOXIDE MASKS....168
4.1. Abstract....169
4.2. Introduction....169
4.3 Results and Discussion....172
4.3.1. Fabrication of metal oxide hard mask patterns....172
4.3.1.1 $FeCl_3$ Precursor....175
4.3.1.2 $Fe(NO_3)_3.9H_2O$ Precursor....178
4.3.2. Speed and humidity variation....180
4.3.2.1 α-Fe_2O_3 MASK ETCHING AND ANALYSIS....186
4.4. Experimental....190

4.4.1. Biopolymers, Casting Solutions and Substrate 190

4.4.2. Metal Inclusion 190

4.4.3. Characterization 191

4.5. Conclusion 192

4.6. References 195

4.7. Appendix 206

4.7.1. APPENDIX REFERENCES 223

CHAPTER 5 CONCLUSION AND FUTURE WORK 226

5.1 Conclusion 227

5.2 Future Work 228

5.3 References 232

FIGURES & TABLES

CHAPTER 1

Figure 1.1: (A) AFM image showing PTF produced using PS/PMMA blend. Adapted from Johnston.[3] **(B)** SEM image showing PTF produced using PS-b-PMMA BCP. Adapted from Tian et al.[4] 25

Figure 1.2: Publications corresponding to biopolymer (BP) blend applications and synthetic polymer (P) over 20 years. From SCOPUS database for years 1998 - 2018 (Source: https://www.scopus.com).....26

Figure 1.3: (i) shows homogenous solution before phase separation; **(ii)** shows blend phase separation; **(iii-iv)** shows increase in phase size due to Ostwald ripening; **(v)** elongated features which may result from coalescence or response to shear; **(iv)** phase occlusion and adoption of salami structure.....31

Figure 1.4: A) Current and future applications of biopolymer PTFs. **B**) Top-down method of patterning such as lithography. **C**) Bottom-up method of patterning such as phase separation. 34

Figure 1.5: A) Shows the typical SD of a polymer blends features. **B**) Shows the SD of (A) after a given period of time, where features have undergone Ostwald ripening. Greyed out plot is original SD. **C**) Shows the SD of **(A)** after a given period of time where features have undergone coalescence.....36

Figure 1.6: Selective solvent preferentially removes one (bio)polymer component (blue) over another (red) allowing for identification of domains or generation of a structured homopolymer surface.....40

Figure 1.7: (**A-C**) Selective polymer phase removal. The remaining polymer is sometimes referred to as a soft resist, in certain processes, and may be used to transfer patterns. (**D**) Metal deposition on top of remaining polymer phase, forming a metal pattern. (**E**) Lift off of underlying polymer phase leaving metal adhered to substrate. Any metal deposited on the polymer phase is removed, while metal in contact with the substrate remains. The final metal pattern is the inverse of the soft resist in **(C)**. This metal pattern may be used for pattern transfer (lithography). 47

Figure 1.8: Image **A** is a scanning electron microscope image of PCL/PLA blend annealed in CO2 at 150 °C for 60 min, with an average pore size approx. 150 µm. Adapted from Huang et al, 2017.[129] Image **B** shows a confocal laser scanning microscope image of

gelatin/starch film thermally annealed for 30 min. Bright regions are gelatin, dark are starch. Adapted from Firoozmand et al, 2009.[145] 55

CHAPTER 2

Figure 2.1: **(A)** 3D structure of BSA (Protein Data Bank ID: 3v03, www.rcsb.org) using Swiss-Pdb Viewer V.4.1 software. **(B)** Structure of chitosan polysaccharide created using Chemdraw Professional V16.0.1.4. **(C)** Basic structure of gelatin.....79

Figure 2.2: AFM image grid and associated line profiles showing results of casting thin-films at 12µm from specific Pr-Ps-S solutions of BSA-Ch-FA at specific humidities. Each image in column A and column B is 40 µm × 40 µm area. Each image in column C and column D is 10 µm × 10 µm area. Column A = 4 w/v% BSA 1 w/v% Ch (4:1), column B = 2 w/v% BSA 1 w/v% Ch (2:1), column C = 1 w/v% BSA 2 w/v% Ch (1:2), column D = 1 w/v% BSA 4 w/v% Ch (1:4). Row 1 = 10% humidity, row 3 = 30% humidity, row 3 = 60% humidity and row 4 = 90% humidity. 83

Figure 2.3: Statistical analysis of BSA-Ch blends for feature size and density. All but the 4:1 blend refers to protuberance measurements, with the 4:1 blend data displaying pore data. **A)** Refers to feature diameter plotted against humidity while **B)** Details features/µm^2 vs.% humidity for 4:1, 2:1, 1:2 and 1:4 blends respectively. 85

Figure 2.4: AFM image grid and associated line profiles showing results of casting thin-films at 12µm from specific Pr-Ps-S solutions of PG-Ch-FA at specific humidities. Each image in column A and column B is 40 µm × 40 µm area. Each image in column C and column D is 10 µm × 10 µm area. Column A = 4 w/v% PG 1 w/v% Ch (4:1), column B = 2 w/v% PG 1 w/v% Ch (2:1), column C = 1 w/v% PG 2 w/v% Ch (1:2), column D = 1 w/v% PG 4 w/v% Ch (1:4). Row 1 = 10% humidity, row 2 = 30% humidity, row 3 = 60% humidity and row 4 = 90% humidity.....87

Figure 2.5: Shows statistical analysis of PG-Ch blends for feature size and density. **A)** Refers to feature diameter plotted against humidity. **B)** Details features/µm^2 vs.% humidity. 89

Figure 2.6: Plots the RMS vs % humidity for all BSA-Ch blends. **B)** Plots the RMS vs % humidity for all PG-Ch blends.....91

Figure 2.7: Statistical analysis of BSA-Ch blends for feature and frequency of feature sizes. All but the 4:1 blend refers to protuberance measurements, with the 4:1 blend data

displaying pore data. **A - D** displays feature count vs diameter of observed features for 4:1, 2:1, 1:2 and 1:4 blends respectively.....93

Figure 2.8: Statistical analysis of PG-Ch blends for feature size and frequency of feature sizes. **A - D** displays feature count vs diameter of observed features for 4:1, 2:1, 1:2 and 1:4 blends respectively.....94

Figure S2.1: AFM image grid showing results of casting thin-films at 12µm wet deposit from specific P-S or Ps-S solutions. Each image is 10 µm x 10 µm area. Films produced from solutions containing 4%w/v, 2% w/v or 1%w/v biopolymer. 105

Figure S2.2: AFM image grid showing results of casting thin-films at 12µm from specific P-Ps-S solutions of BSA-chitosan-formic acid at specific humidities. Each image in column A and column B is 40 µm × 40 µm area. Each image in column C and column D is 10 µm × 10 µm area. Column A = 4 w/v% BSA 1 w/v% chitosan (4:1), column B = 2% BSA 1% chitosan (2:1), column C = 1% BSA 2% chitosan (1:2), column D = 1% BSA 4% Chitosan (1:4). Row 1 = 10% humidity, row 3 = 30% humidity, row 3 = 60% humidity, row 4 = 90% humidity. 106

Figure S2.3: AFM image grid showing results of casting thin-films at 12µm from specific P-Ps-S solutions of PG-Ch-FA at specific, controlled humidities with the automatic film applicator and 12µm bar. Each image in column A and column B is 40 µm × 40 µm area. Each image in column C and column D is 10 µm × 10 µm area. Column A = 4 w/v% PG 1 w/v% Ch (4:1), column B = 2% PG 1% Ch (2:1), column C = 1% PG 2% Ch (1:2), column D = 1% PG 4% Ch (1:4). Row 1 = 10% humidity, row 2 = 30% humidity, row 3 = 60% humidity and row 4 = 90% humidity. 107

Figure S2.4: Graph depicts the size distribution of 1w/v% PG 2w/v% Ch displaying overlayed Gaussian profile dried under various ambient humidities. 108

Figure S2.5: AFM topography and phase images for each blend system. Phase imaging is a standard technique for mapping the spatial variations in the surface elasticity. The blend structures can be observed due to the difference in elasticity between Ch and BSA or PG..109

Figure S2.6: Topography and map of the elastic modulus of the both the BSA:Ch and PG:Ch blend. Each image is 6.5 × 6.5 µm area. The protein and polysaccharide can be distinguished in the Young's modulus map. The Young's modulus map resembles the phase shift image maps of **Figure S2.5**. 110

CHAPTER 3

Figure 3.1: AFM image grid showing results of casting thin-films at 65% relative humidity from specific Pr-Ps (protein-polysaccharide) solutions of BSA-Ch-FA at various spin speeds. Each image is 40 µm × 40 µm area (scale bar 10 µm, shown in 4:1 blend at 500 rpm). In the image, bright areas are higher and dark areas are lower. Line profile (blue lines) may be found in each image and its corresponding **Figure S3.2 – Figure S3.6**. Column A = 4 w/v% BSA and 1 w/v% Ch (4:1), column B = 2 w/v% BSA and 1 w/v% Ch (2:1), column C = 1 w/v% BSA and 1 w/v% Ch (1:1), column D = 1 w/v% BSA and 2 w/v% Ch (1:2), column E = 1 w/v% BSA and 4 w/v% Ch (1:4). Row 1 = 500 rpm, row 2 = 1000 rpm, row 3 = 2000 rpm, row 4 = 3000 rpm and row 5 = 4000 rpm. 119

Figure 3.2: Statistical analysis of BSA-Ch blends for feature diameter and feature number/area. All but the 4:1 blend refers to protuberance measurements, with the 4:1 and 2:1 blend data displaying both protuberance and pore data separately. The circular legend for the 4:1 blend refers to feature diameter in the discontinuous domain, i.e. salami structure regions. **A)** Refers to feature diameter plotted against spin speed while **B)** details features/µm^2 vs spin speed for 4:1, 2:1, 1:1, 1:2 and 1:4 blends respectively. 120

Figure 3.3: AFM images and surface profiles of 1:1 BSA-Ch blends, 3000 rpm on planar silicon substrates. **A)** Refers to blend before Tris-HCl etch. **B)** Refers to blend post selective etching. **C)** Enhanced view of selectively etched BSA domains demonstrating extruded rim structure in Ch film. **D)** Refers to blend post selective metal incorporation and calcination. 126

Figure 3.4: **A)** FTIR spectra of **i)** bare silicon wafer, **ii)** 1 w/v% BSA film 3000 rpm deposition, **iii)** 1 w/v% Ch film 3000 rpm deposition, **iv)** 1:1 BSA-Ch blend film 3000 rpm deposition, **v)** 1 w/v% BSA film 3000 rpm deposition crosslinked, **vi)** 1 w/v% Ch film 3000 rpm deposition crosslinked, **vii)** 1:1 BSA-Ch blend film 3000 rpm deposition crosslinked, **viii)** 1:1 BSA-Ch blend crosslinked film after Tris-HCl etch and **ix)** porous iron oxide matrix after annealing and calcination treatment. **B)** Shows the XPS Fe 2p spectra of iron porous matrix after annealing and calcination treatment. 128

Figure 3.5: Statistical analysis of BSA-Ch blends for protuberances and frequency of protuberance sizes. Each curve based on approx. 1000 protuberance diameter measurements. All but the 4:1 blend refers to protuberance measurements contained within the matrix, with the 4:1 blend data displaying protuberance data for the continuous and discontinuous (salami

structure) domain. **A – E** displays feature frequency vs diameter of observed features for 4:1, 2:1, 1:1, 1:2 and 1:4 blends respectively.....131

Figure 3.6: Protuberance SD of **A)** 4:1 BSA-Ch blend, 4000 rpm deposition, **B)** 4:1 BSA-Ch blend, 500 rpm deposition, **C)** 1:4 BSA-Ch blend, 4000 rpm deposition and **D)** 1:4 BSA-Ch blend, 500 rpm deposition. The black curve (solid) denotes the best unimodal or polymodal fit with the distribution. The deconvouted peaks, shown in red (dashed), show the separate populations in the SD.....132

Figure S3.1: AFM images showing results of casting neat thin-films at 65% relative humidity at 2000 rpm prepared in the same manner as BSA-Ch blends. Biopolymer AFM images are red, glass substrate AFM image is grey. Shows 1% BSA film (left), 1% chitosan film (right) and glass substrate (bottom)**.** Scale bars top left hand corner of each image. ...145

Figure S3.2: AFM images depicting the effect spin speed in ambient air (65% RH) for the 4:1 BSA-Ch blend. Each image is 40 µm × 40 µm area (scale bar 10 µm, shown in the 500 rpm image). Line profile denoted by blue line. 146

Figure S3.3: AFM images depicting the effect spin speed in ambient air (65% RH) for the 4:1 BSA-Ch blend. Each image is 40 µm × 40 µm area (scale bar 10 µm, shown in the 500 rpm image). Line profile denoted by blue line. 147

Figure S3.4: AFM images depicting the effect spin speed in ambient air (65% RH) for the 1:1 BSA-Ch blend. Each image is 40 µm × 40 µm area (scale bar 10 µm, shown in the 500 rpm image). Line profile denoted by blue line. 148

Figure S3.5: AFM images depicting the effect spin speed in ambient air (65% RH) for the 1:2 BSA-Ch blend. Each image is 40 µm × 40 µm area (scale bar 10 µm, shown in the 500 rpm image). Line profile denoted by blue line. 149

Figure S3.6: AFM images depicting the effect spin speed in ambient air (65% RH) for the 1:2 BSA-Ch blend. Each image is 40 µm × 40 µm area (scale bar 10 µm, shown in the 500 rpm image). Line profile denoted by blue line. 150

Figure S3.7: 20 µm line profiles for all 4:1 BSA-Ch. 151

Figure S3.8: 20 µm line profiles for all 2:1 BSA-Ch. 152

Figure S3.9: 20 µm line profiles for all 1:1 BSA-Ch. 153

Figure S3.10: 20 µm line profiles for all 1:2 BSA-Ch. 154

Figure S3.11: 20 µm line profiles for all 1:4 BSA-Ch. 155

Figure S3.12: Statistical analysis of BSA-Ch blends feature diameter plotted against spin speed. All but the 2:1 blend refers to protuberance measurements, with the 2:1 blend data

displaying both protuberance and pore data separately. The circular legend for the 4:1 blend refers to feature diameter in the discontinuous domain, i.e. salami structure regions. 156

Figure S3.13: A and **B)** 2D and 3D AFM images of 4:1 BSA-Ch blend salami structures, inset scale bar 5 µm. **C)** Mechanism of occlusion of the discontinuous phase. **Figure S3.14 (i)** shows homogenous solution before phase separation, **(ii)** shows blend phase separation, **(iii)** shows elongated structures which may result from coalescence or high shear forces and **(iv)** phase occlusion and adoption of salami structure.....157

Figure S3.15: Plots the average film thickness (nm) vs spin speed (rpm) for all BSA-Ch blends. 158

Figure S3.16: A) Plots the RMS roughness vs spin speed for all BSA-Ch blends. **B)** Plots the surface area ratio (%) vs spin speed for all BSA-Ch blends. 159

Figure S3.17: AFM images and surface profiles of 1:4 BSA-Ch blends, 500 rpm on planar silicon substrates. Sample was etched using buffered solutions contained 200 mM Tris-HCl, pH 8.8 for 20 hrs after crosslinking with 20 wt% glutaraldehyde for 20 hr. 161

Figure S3.18: Survey spectra of porous iron oxide matrix following calcination treatment. 162

Figure S3.19: Statistical analysis of BSA-Ch blends for feature diameter and frequency of feature diameters. **A)** Displays feature frequency vs diameter of observed features for the 4:1 blends and **B)** displays feature frequency vs diameter of observed features for the 2:1 blends respectively. 165

Figure S3.20: Displays plot of average receding contact angle as a function of time for BSA, Ch, BSA-Ch blend, Tris-HCl etched blend and porous iron oxide matrix. 166

CHAPTER 4

Figure 4.1: AFM images and surface profiles (blue lines) of biopolymer template and resulting metal structures. Scale bar bottom right of image. **A)** Refers to the biopolymer template 1:1 BSA-Ch blend, 3000 rpm, 60% RH on planar silicon substrates. Nanoporous metal templates were prepared with alternative precursors (1 w/w%-EtOH). **B)** 1 w/w% $FeCl_3$ anhydrous precursor, **C)** 1 w/w% $Al(NO3)_3.9H_2O$ precursor, and **D** and **E)** 1 w/w% $AgNO_3$ respectively. 172

Figure 4.2: AFM images displaying surface morphology and line profiles (blue), showing the growth nanoporous iron oxide matrix prepared with different biopolymer template–metal solution contact times. All images 20 x 20 µm, scale bar provided in image **A**.

FeCl3-EtOH solution stirred for 30 min. **A – C)** display iron patterns generated with using 5 s, 15 s and 60 s respectively. 176

Figure 4.3: Surface morphology and line profiles (blue) showing the growth nanoporous iron oxide matrix prepared with different concentrations of $FeCl_3$–EtOH solution stirred for 30 min. All images 20 x 20 µm, scale bar provided in image **A**. **A – E)** display iron patterns generated with 0.1 w/w%, 0.2 w/w%, w/w%, 0.6 w/w% and 0.8 w/w% respectively.....177

Figure 4.4: AFM images and z scales of iron oxide matrix prepared with different biopolymer template–metal solution contact times. 1 w/w% Fe(NO3)3.9H2O – EtOH solution stirred for 30 min. All images 20 x 20 µm, scale bar provided in image A. **A – H)** display iron patterns generated with using 2.5 s, 5 s, 7.5 s, 10 s, 15 s, 30 s, 45 s and 60 s biopolymer template–metal solution contact time respectively. Annealing and calcination was performed with a preheated furnace (700 °C) for 1hr. 178

Figure 4.5: AFM images and line profiles (blue) of iron oxide matrix prepared with different metal solution concentrations, stirred for 30 min. All images 20 x 20 µm, scale bar provided in image **A**. **A – E)** display iron patterns generated with using 0.6 w/w%, 0.8 w/w%, 1 w/w%, 1.2 w/w% and 2 w/w% $Fe(NO_3)_3.9H_2O$–EtOH solution respectively. Annealing and calcination was performed with a preheated furnace (700 °C) for 1 hr.....180

Figure 4.6: AFM images and 2 µm surface profiles (blue lines) of nanoporous metal structures. Metal templates produces with biopolymer template (1:1 BSA-Ch, 4000 RPM, 20% RH) on planar silicon substrates, annealed and calcined at 700ºC. Nanoporous metal templates were prepared with alternative precursors (1 w/w%-EtOH). **(A, F)** Fe_2O_3, **(B, G)** Ce_2O_3, **(C, H)** Al_2O_3, **(D, I)** NiO, and **(E, J)** CuO respectively.....181

Figure 4.7: Shows AFM images of metal masks generated using biopolymer templates cast at reduced humidity (20% RH). Masks were produced using metal incorporation of $Fe(NO_3)_3.9H_2O$, subsequent annealing at 160 °C for 2 hr to remove any water, and calcination at 700 °C for 1 hour to remove biopolymer template. **(A, B)** AFM images of Fe_2O_3 metal masks generated from 1:1 BSA-Ch biopolymer template, cast at 4000 RPM. **(B)** Provides an enhanced view of the tessellated morphology, and variance found within. **(C-E)** AFM images of Fe_2O_3 metal masks generated from 1:1 BSA-Ch biopolymer template, cast at 3000 RPM. **(F)** Scheme for "border coalescence", driving the formation of metastable quad-junctions observed in **(B)** and **(E)**, a metastable structure resulting from structure observed in **(D)**....184

Figure 4.8: Each image is 10 x 10 µm, 2 µm scale bar provided in image **A** and **E,** and line profiles denoted by a blue line. **(A, E)** AFM images of 1:1 BSA-Ch biopolymer template, 20% RH, cast at 3000 RPM and 4000 RPM respectively. **(B, F)** AFM images of Fe_2O_3 metal

masks generated from biopolymer templates **(A)** and **(E)**, following metal incorporation of $Fe(NO_3)_3.9H_2O$, and subsequent annealing at 160 °C for 2 hr and calcination at 700 °C for 1 hour. **(C, G)** AFM images of substrates post-etching samples **(B)** and **(F)** with $NH_4F/HNO_3/H_2O$ solutions for 5 min. **(D, G)** line profiles of samples **(A, B, C)** and **(E, F, G)** respectively. 186

Figure 4.9: Statistical analysis of 1:1 BSA-Ch blends. Each curve is based on approximately 1000 diameter measurements performed with Gwyddion, and interdomain distance performed with ImageJ. PSD's were fitted with log-normal curves, while interdomain distances were fitted Gaussian curves. The black curve (solid) denotes the best polymodal fit with the distribution, while the deconvouted peaks, shown in red (dashed), show the separate populations in the PSD. **A** and **D)** display the normalized PSD and interdomain distance of biopolymer blends cast at 4000 rpm and 20% RH. **(B, E)** corresponds to the PSD and interdomain distance biopolymer blends cast at 3000 rpm, 20% RH. **C, F)** corresponds to the PSD and interdomain distance of biopolymer blends cast at 3000 rpm, 60% RH. 188

Figure S4.1: AFM and optical microscopy images of the metal surfaces after metal incorporation and calcination after various different biopolymer template–metal solution contact times. **(A)** and **(B)** 5 s; **(C)** and **(D)** 15 s; and **(E)** and **(F)** 60 s contact times.....206

Figure S4.2: XPS survey spectra of the metal surfaces after metal incorporation and calcination at 700 ºC, at a ramp rate of 20 ºC/min. Survey spectra for **(A)** Fe; **(B)** Ce; **(C)** Al; **(D)** Ni; and **(E)** Cu surfaces. 207

Figure S4.3: Shows the XPS **(A)** Fe 2p; **(B)** Ce 3d; **(C)** Al 2p; **(D)** Cu 2p; **(E)** Ni 2p and **(F)** Ni 3p spectra of the metal matrix after annealing and calcination treatment. 208

Figure S4.4: Plot of humidity of the spin-coating chamber as solvent is lost from the sample. The average % RH (black line) plotted as a function of time, with the standard deviation of 4 runs plotted as blue region. Humidity of the chamber never exceeded 22% RH. The majority of solvent loss was achieved after approx. 50 s. Relative Humidity (RH) readings from HOBO MX Temp/RH Logger sensor for 1:1 BSA-Ch blend film cast at 3000 RPM, 20% RH. 209

Figure S4.5: Geometry of Fe2O3 masks. Distribution of angles at the vertices of polygonal pores. Masks generated with biopolymer template 1:1 BSA-Ch blends cast at 20% RH, at **(A)** 4000 rpm and **(B)** 3000 rpm. Higher casting speed corresponds to earlier drying. 210

Figure S4.6: (A) FTIR spectra of Si substrate, biopolymer template and Fe_2O_3 porous matrix after annealing and calcination. **(B)** Raman spectra of Si substrate and Fe_2O_3 porous matrix after annealing and calcination. 211

Figure S4.7: Each image is 2 x 2 µm, scale bar provided in image **A**. AFM images of Fe_2O_3 metal masks, produced with 1:1 BSA-Ch blend at 20% RH. Metal precursor used was 1 wt% $Fe(NO)_3.9H_2O$-EtOH solution. A-C) Shows Fe_2O_3 mask created using BSA-Ch blend cast at 3000 RPM. D-F) Shows Fe_2O_3 mask created using BSA-Ch blend cast at 4000 RPM. ...212

Figure S4.8: Statistical analysis of Fe_2O_3 masks generated using various biopolymer blends templates. Metal masks were produced as in **Figure 4.6**, using 1 wt% $Fe(NO_3)_3.9H_2O$. **A**, **D)** display the normalized PSD and interdomain distance of pores generated with biopolymer blend cast at 4000 rpm and 20% RH. **(B, E)** corresponds to the PSD and interdomain distance of pores generated with biopolymer blends cast at 3000 rpm, 20% RH. **C, F)** corresponds to the PSD and interdomain distance pores generated with biopolymer blends cast at 3000 rpm, 60% RH.....213

Figure S4.9: Statistical analysis substrate after 5 min etch with NH_4F/HNO_3H_2O solution. **A, C)** Correspond to diameter and interpore distance of images in **Figure 4.8g** (3000 rpm, 20% RH). **B, D)** Correspond to diameter and interpore distance of images in **Figure 4.8c** (4000 rpm, 20% RH).....215

Figure S4.10: AFM images of the metal surfaces after metal incorporation and calcination biopolymer template–metal solution contact times. Each image is 20 x 20 µm, scale bar provided in image **A**. Metal templates were produced with biopolymer template (1:1 BSA-Ch, 3000 RPM, 60% RH) on planar silicon substrates. 1 wt% $Fe(NO_3)_3.9H_2O$-solvent was incorporated for 5 s. Samples were heated to 160 °C for 1 hr, with a ramp rate of 20 °C/min to remove water before calcination. Samples were then placed into a cold furnace, heated to 700 °C and left for 1 hr before removal. Solvents used for incorporation were **(A)** isopropyl alcohol (IPA); **(B)** acetone and **(C)** dH_2O. 217

Figure S4.11: AFM images of metal oxide structures using **(A)** $CuCl_2$; **(B)** $Cu(CO_2CH_3).H_2O$; **(C)** $CuSO_4.H_2O$ and **(D)** $NiCl_2.6H_2O$ precursors for metal incorporation. Image **A** is 10 x 10 µm, while image **B – D** are image 20 x 20 µm in size. Metal templates were produced with biopolymer template (1:1 BSA-Ch, 3000 RPM, 60% RH) on planar silicon substrates. Metal templates were prepared with 1 wt% metal precursor-EtOH. Samples were annealed and calcined as with **Figure S4.2**. 219

Figure S4.12: AFM images of iron oxide structures using (A) iron (II) acetylacetonate; (B) iron (II) acetate; and (C) iron (III) acetylacetonate. Metal templates produces with biopolymer template (1:1 BSA-Ch, 3000 RPM, 60% RH) on planar silicon substrates. Image A and B are 20 x 20 µm, while image C is 10 x 10 µm in size. Metal templates were prepared with 1 wt% metal precursor-EtOH. Samples were heated to 160 °C for 1 hr, with a ramp rate of 20 °C/min to remove water before calcination. Samples were then placed into a cold furnace, heated to 700 °C and left for 1 hr before removal. 220

Scheme S4.1: (A) 3D structure of BSA (Protein Data Bank ID: 3v03, www.rcsb.org) using Swiss-Pdb Viewer V.4.1 software, where the metal binding sites are indicated by colour. Cysteine (Cys, 35 residues, sulfhydryl groups, blue) and histidine (His, 16 residues, imidazole groups, green). **(B)** Proposed structure for His-M complex. **(C)** Proposed structure for Cys-M complex. Metal-AA structures drawn using Chemdraw Professional V16.0.1.4.[19-23].....221

Scheme S4.2: (A) Structure of chitosan polysaccharide created using Chemdraw Professional V16.0.1.4(77). **(B,C)** Proposed structure for Ch-M complex. 222

Scheme S4.3: Arrows depict strong Coulomb interactions between ion species and film surface. **A)** Depicts hard cations binding to polysaccharide via amine groups. Anion (i.e. Cl^-) does not direct cation to protein domain. **B)** Depicts late stage cation binding to protein domain. Ions approach surface in a pairwise fashion. Anions (i.e. NO_3^-) chaperone cation to protein domain. Any repulsion of the cation to the protein domain is offset by the anion. Cation binding to polysaccharide domain is omitted for clarity in **(B).** 222

TERMINOLOGY

AA: Amino Acid

AR: Anti-reflective

AFM: Atomic Force Microscope

BCP: Block copolymer

Blend: Throughout the scientific literature on materials produced by separating polymers there is a consistent ambiguity in the use of the word "blend", which can refer to the final solid materials produced or to the solutions containing the polymers from which materials are produced. In this thesis the word "blend" will refer solely to the solutions from which patterned thin-films and surfaces are produced.

2EHA: 2-ethylhexyl acrylate

BSA: Bovine serum albumin

Ch: Chitosan

CA: Cellulose acetate

CC: Cellulose carbamate

CP: Cellulose propionate

CTA: Cellulose triacetate

dH_2O: Distilled water

DIB: 1,4-diiodobutane

EGMA: ethyleneglycol dimethacrylate

EtOH: Ethanol

FA: Formic Acid

Features/area: Features per area

FMA: Perfluorooctylethyl methacrylate

FTIR: Fourier Transform Infrared Spectroscopy

His-tag: Polyhistidine-tag, 6 histidine amino acids in succession

HSAB: Hard Soft Acid Base

LAc: Acetylated Lignin

MIL: Metal inclusion lithography

Metal-PBL: Metal polymer blend lithography

M_w: Molecular weight

NaAlg: Sodium alginate

NP: Nano-particle

OECD: Organisation for Economic Co-operation and Development

P2VP*:* Poly(2-vinylpyridine)

P3HT: Poly-3-hexylthiophene

P(3HB): Poly(3-hydroxybutyrate)

P(4HB): Poly(4-hydroxybutyrate)

P4VP*:* Poly(4-vinylpyridine)

PAN: Polyacrylonitrile

PBL: Polymer blend lithography

PCL: Polycaprylactone

PDMS*:* Poly(dimethylsiloxane)

PDI: Polydispersity index

PEG: Polyethylene glycol

PEO: Poly(ethylene oxide)

PFDA: *1H, 1H, 2H, 2H-perfluorodecyl acrylate*

PG*:* Pigskin gelatin

PHB: Poly(3-hydroxybutyrate)

PHFMA: *2,2,3,4,4,4-hexafluorobutyl methacrylate*

pI*:* Isoelectric point

PHEMA*:* Poly(hydroxyethyl methacrylate)

PLA: Poly(lactic acid)

PMMA*:* Poly(methyl methacrylate)

Pores/area: Pores per area

Pr*:* Protein

Ps*:* Polysaccharide

PS: Poly(styrene)

PS-co-P5FS: poly(2,3,4,5,6-pentafluorostyrene)-co-polystyrene

PSD: Particle size distribution

p(TAN-co-MMA)**:** p(perfluoroacrylate-co-methyl methacrylate

PTF: Patterned thin-film

r: *(*Bio)polymer ratio

RH: Relative humidity

RIE: Reactive ion etching

RMS: Root mean squared

SD: Size distribution

SFE: Surface free-energy

Si*:* Silicon

Std. Dev.*:* Standard deviation

TBMA: tert-butyl methacrylate

THF*:* Tetrahydrofuran

TMSC: Trimethylsilyl cellulose

WCA: Water contact angle

XPS: X-ray Photoelectron Spectroscopy

Chapter 1

Introduction

1.1. INTRODUCTION AND MOTIVATION

1.1.1. INTRODUCTORY STATEMENT

Patterned surfaces are a crucial technology in material science. According to the OECD (Organisation for Economic Co-operation and Development), over 20% of emerging technologies (in renewable energy, biomedical devices, smart devices and anti-reflective surfaces) utilize patterned surfaces.[1] The widespread use of these materials is because nano- and microscale patterns on a surface impart specific physicochemical properties to that surface. Thus, being able to control the nano and micro- surface patterns allows for modification of a material's surface properties, which in turn allows for tailorable materials for technological needs.[2] However, currently the fabrication methods of almost all the necessary technologies of everyday life are unsustainable, including the current generation of patterned surfaces, which rely on inefficient manufacturing methods (in certain instances), and unsustainable feedstocks (petrochemically derived polymers) that require expensive extraction. We are living through an unprecedented sustainability crisis. Almost every functional system humans rely on – energy, transport, food, technology, communications – is dependent on fundamentally unsustainable materials and practices. To alleviate this, we must produce as much of the critical components of our technologies as sustainably as possible. Patterned surfaces are just such a critical component. To ensure that things like future renewable energy technologies are truly renewable, we must ensure that their fundamental components are sustainable. Patterned surfaces are produced by phase separating synthetic polymer blends or block copolymers (BCPs), **Figure 1.1**. Little work has been done in producing patterned surfaces using sustainably sourced materials. This thesis describes the production of patterned surfaces using waste biopolymers. Biopolymers, unlike synthetic polymers, are renewable, biocompatible, biodegradable and are some of the most abundant materials on the planet. Utilizing waste biopolymers, agricultural waste can be minimized using a circular economy system, while simultaneously reducing our reliance on petrochemicals. Not only are biopolymers more sustainable but their innate physico-chemical characteristics will permit larger scale pattern features and superior, application-specific functionalities.

The aim of this project was to produce patterned thin-films (PTFs), using biopolymer blends. To produce these biopolymer blend thin films, a technique called segregative phase separation was used to promote pattern development using a protein and polysaccharide biopolymer, in an acidic solvent. These patterned films have similar size profiles and

chemistries to synthetic polymer blends, and demonstrate that we need not rely on petrochemically derived polymers when producing patterned surfaces.

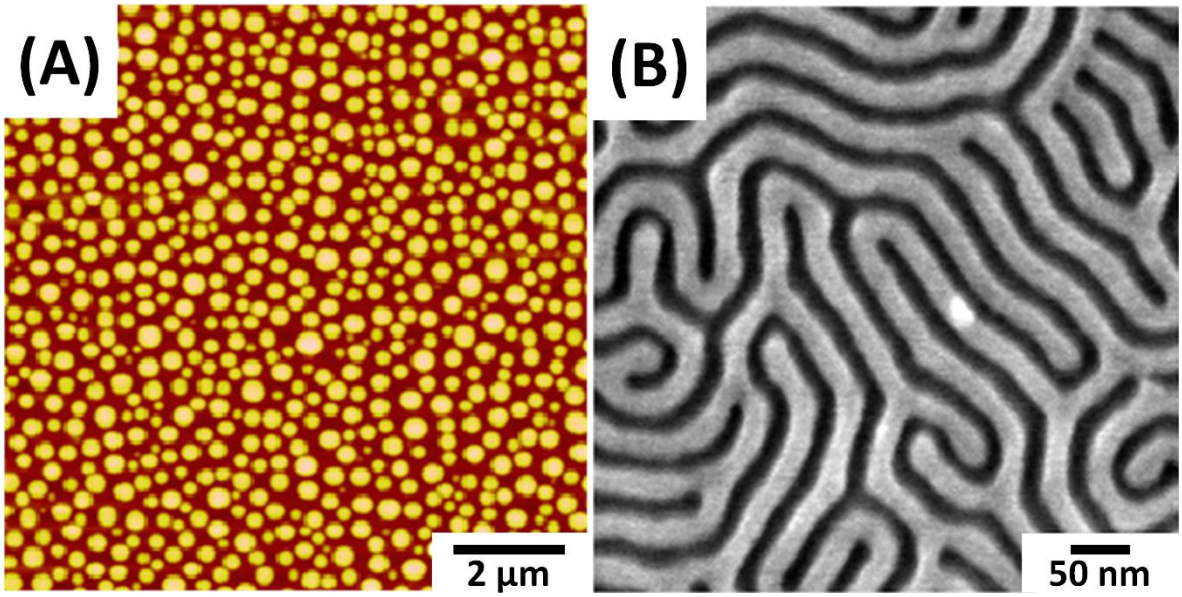


Figure 1.1: (A) *AFM image showing PTF produced using PS/PMMA blend. Adapted from Johnston.*[3] ***(B)*** *SEM image showing PTF produced using PS-b-PMMA BCP. Adapted from Tian et al.*[4]

1.1.2. CURRENT APPLICATIONS AND ENVIRONMENTAL COST

Currently, most patterned thin-films used industrially are made from synthetic polymers primarily derived from petrochemicals Due to their chemical inertness, these plastics survive in the environment for decades. Many of these plastics can be recycled in theory, but in reality, when used in applications such as food packaging, contamination prevents cost effective recycling for companies. Added to this are more basic issues such as; consumers not recycling; the unpleasant appearance of some recycled plastics; certain plastics are simply not recyclable; and plastics being destroyed during normal use. These issues result in a lot of petrochemical plastic ending up in landfills, in the environment, or incinerated.[6] These are not sustainable ends-of-life-cycle for plastics. Ideally, environmentally friendly biopolymers and biopolymer blends could be used to replace unsustainable petrochemical polymers where possible. By doing this in an advanced material that is fundamental to many current and future critical technologies, we can prove that it is possible. We can then apply the lessons learned to less advanced, more readily adaptable technologies. Biopolymers have many of the same

functionalities as traditional polymers; in fact, for many applications they have superior functionalities. Crucially, using them would not rely on petrochemically-derived feedstocks.

Since 2004, the study of biopolymer composites has seen a substantial increase. Meanwhile, the use of neat and blended biopolymers has undergone a modest increase in the last 10 years. However, in 2018 the number of publications/year of synthetic polymer blends (approx. 22,000 publications) vastly outnumbered that of biopolymer blends (2,000 publications), with specific applications of biopolymer blends below this number. While the need for biopolymers is obvious, the lack of research into biopolymer blends has limited their application in a number of fields, **Figure 1.2**. Out of the technologies and sectors listed, the questions are, "Do biopolymer blends meet the requirements for scalable, affordable, environmentally friendly production of green products?" and, "Why have biopolymers not been adapted in sectors other than the food and medical industries?" The answers to these questions lies in willingness of manufacturers to change production methods, and in the innate properties of these biopolymers.

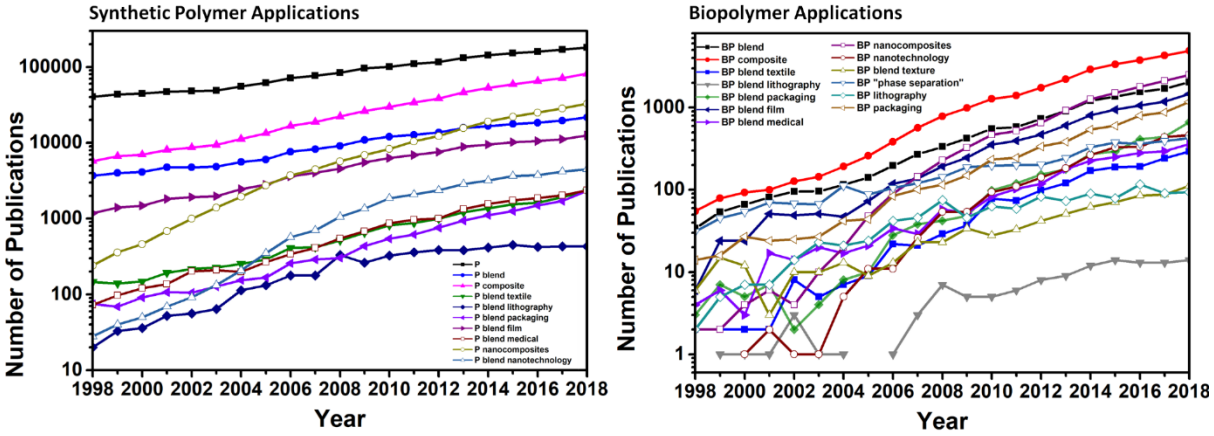


Figure 1.2: *Publications corresponding to biopolymer (BP) blend applications and synthetic polymer (P) over 20 years. From SCOPUS database for years 1998 - 2018 (Source: https://www.scopus.com).*

1.1.3. OVERVIEW

Chapter 1 will introduce key concepts needed to understand the science behind the work detailed in subsequent chapters. **Chapter 2** will focus on the thin film pattern of pigskin gelatin (PG), bovine serum albumin (BSA) and chitosan (Ch) blends when cast in a controlled environment in an attempt to achieve feature sizes akin to synthetic polymer blends. Parameters including (bio)polymer ratio (r) between the two polymers and ambient relative humidity (RH) are used to vary the evaporation rate of the solvent and growth of the biopolymer

domains. **Chapter 3** focuses on BSA (non-gelling biopolymer) using spin-coating (an industrially established technique) of controlling feature size and resulting film properties. BSA was identified by selective removal using a buffer solution, while Ch was identified using metal incorporation. Successful identification of the growth mechanism was achieved using deconvolution. **Chapter 4** focuses on achieving selective metal incorporation of metal into the polysaccharide domain, with parameters such as time of adsorption, metal precursor concentration, cation, type and solvent type and rate of annealing, while combining the environmental control of **Chapter 2** with the deposition technique of **Chapter 3**.

We generate metal patterns from the micro- and nano-patterned biopolymers films by a method known as *metal inclusion lithography* (MIL), which produces sub-micron patterns rapidly. The technique is similar to selective metal ion inclusion achieved in *block co-copolymers* (BCPs) and metal pattern production in *metal polymer blend lithography* (metal-PBL). BCPs use the variant chemistries of differing blocks of monomer units within their polymeric molecular structures to promote metal ion inclusion exclusively in one domain.[7] However, BCPs, are restricted by price, complex syntheses, upper feature size limitations, and annealing time.[8] Biopolymers, by contrast, are not, as this thesis will show. In metal-PBL, a blend of two synthetic polymers are phase separated, one phase is then selectively removed with solvents, a metal is thermally deposited on top of the remaining phase, which is subsequently removed to produce a porous or dot matrix. Unlike BCPs, this does not suffer from domain size limitations or require long annealing times. However, the production is lengthy, complex, requires multiple steps and expensive equipment.[9–11] Our technique (BioMIL) proposes a middle ground, where metal ions can be included into one domain by chelation, similar to BCPs, and adopt a larger range of feature sizes, like metal PBL. The scope of this technique is not limited to just metal patterning as will be seen in the review below.

1.2. BIOPOLYMERS VS. SYNTHETIC POLYMERS

Synthetic polymers are primarily sourced from petroleum (though they can be produced by other means) and are non-renewable.[12] They consist of simple monomer units - molecules of a specific chemistry - combined together in repeating chains. They do not have consistent tertiary or quaternary structures. They can be readily engineered to have a wide variety of physicochemical properties. Their production methods are not sustainable.[13]

Biopolymers are naturally occurring polymers, such as proteins, polysaccharides, and DNA, and they are renewable.[14] Protein chains are comprised of amino acids (AAs) while

polysaccharide chains are sugar based. Proteins may be sourced from plants (e.g. zein, soy, wheat, corn, etc.), animals (e.g. keratin, casein, collagen, silk, etc.) or bacteria (e.g. chymotrypsin and fumarase).[15] Polysaccharides may be sourced from plants (e.g. cellulose, alginate, pectin or starch), animals (e.g. chitin, chitosan and heparin), and bacteria (e.g. dextran).[16] Extraction and refinement of the raw materials necessary to produce synthetic plastics and BCPs destroys ecosystems and is unsustainable method of future production of plastic technologies. The cost of these synthetic polymers will also rise as oil reserves dwindle, and usage becomes heavily regulated.

The lack of industrial adoption of biopolymers is due to historical shortcomings in their physiochemical properties. Biopolymers are often brittle, water soluble, and susceptible to heat resulting from their hydrophilic nature.[17] Synthetic polymers, though environmentally damaging, are quite robust and have seen their mechanical properties improve since the 1950s.[18] The resulting increase in usage of synthetic polymers has already contaminated our ecosystems, as microplastics build up in upper trophic levels. Biopolymers do have some advantages over synthetic polymers: They are highly functionalized, and contain polar and non-polar groups that allow them to adopt complex structures and perform specific tasks. By contrast, the chemistry of a synthetic polymer is limited in some ways by the simplicity of its monomer. Many biopolymers exist as ultrahigh molecular weight, water soluble chains, and thus could be used to develop technologies similar to BCPs without the same environmental cost. Biopolymers are common in the waste streams of food and agricultural industries. This is an underutilised resource requiring no additional arable land to produce. Lastly, the historical shortcomings of the physicochemical properties of biopolymers that have limited their industrial use can be overcome with the right scientific approaches – like those in this thesis.

1.3. PATTERNING THIN-FILMS: POLYMER BLENDS

Patterned films are produced from thin castings of polymer blends that are subsequently phase separated. Polymer blends are mixtures of two or more polymers, not chemically bound to one another, in a single solvent. Phase separation in polymer blend systems is the formation of two distinct regions of polymers from an initially homogenous solution. Phase separation can occur associatively (i.e. by polymer domains attracted to one another), resulting in a separation of polymer phase from solvent phase, or segregatively, (i.e. by polymer domains repulsed by one another), resulting in separation of one polymer in solvent from another in the

same solvent. This can be done with biopolymers as well as synthetic polymers. Only segregative phase separation produces patterned films. This review focuses on the most relevant biopolymers, blended morphologies, mechanisms of phase separation, and current and future applications for these methods.

1.3.1. MISCIBILITY AND IMMISCIBILITY IN BLENDS

In general, polymer blends produce a homogenous phase (unpatterned film) if the blended polymer molecular structures and polarity are similar, resulting in less repulsion between polymer chains.[19,20] Interactions between polymer chains such as hydrogen bonding improve blend miscibility.[21] This does not yield patterned surfaces. For patterns one needs some degree of immiscibility. Molecular weight plays a large role in polymer-polymer immiscibility. While entropy drives mixing of small molecules, its contribution to polymer blend miscibility is minimal, increasing the contribution of all other factors. Polymers are heavily influenced by chain connectivity, unlike solvent or small molecules. This imposes contiguity limits on the number of states a solvated polymer system can hold. Therefore, mixing must be exothermic, as the entropy gain is negligible to achieve negative free energy of mixing.[22] External processing parameters and processing conditions also play a role in blend miscibility and so also influence final film morphology. Extrinsic factors include (bio)polymer ratio (r), concentration, pH, ionic strength and charge density. Intrinsic factors are predominantly molecular conformation, charge distribution and molecular weight. Finally processing parameters such as shear, pressure, temperature and the method of acidification can affect film morphology.[23,24] If the two polymers in a polymer blend are immiscible, two phases can be observed. This is the key to producing pattern films. The first phase is a discontinuous domain which is formed by the polymer of lower concentration. The second phase is the continuous (matrix) domain, formed by the polymer of higher concentration. In biopolymer systems, pH is an important factor in determining the mechanism of phase separation, while in synthetic polymers temperature controls phase separation.[25]

1.3.1.1. ASSOCIATIVE PHASE SEPARATION

Biopolymers are characterised by their isoelectric point (pI); the pH at which the biopolymer's negative and positive charges result in a net-charge of zero.[26,27] Associative phase separation occurs when oppositely charged groups of each biopolymer associate with one another. This is typified by a biopolymer enriched phase suspended in solvent. Unlike the phase separation

of synthetic immiscible polymer blends, this is entropically driven. Association of charged biopolymer groups generate a neutral structure releasing counterions, increasing overall system entropy.[28] Accordingly, solution pH is an important parameter in determining the resultant blend morphology, as it controls the route of phase separation.[26,29] In low ionic strength solutions, associative phase separation occurs when bulk concentration exceed a critical concentration (approximately 3 – 4 wt%).[24] Different distribution of groups along the biopolymer can affect phase separation.[30] Associative phase separation has typically been employed by the food industry for encapsulation[31], emulsions[32] and altering food texture.[26] As previously mentioned, depositing layers of polymer blends that associative phase separate does not yield patterned surfaces. For patterns, one needs segregative phase separation.

1.3.1.2. SEGREGATIVE PHASE SEPARATION

In segregative phase separation, biopolymers separate into two phases. This can be used to produce patterned thin-film (PTF) surfaces. This occurs in biopolymers with similar charges. Segregative phase separation is observed with two non-ionic biopolymers, two likely charged polyelectrolytes, or a non-ionic biopolymer mixed with a polyelectrolyte.[27] Unlike associative phase separation, segregative phase separation occurs at high biopolymer concentration, with biopolymers of similar charge, in solutions of high ionic strength.[27,33] Polysaccharide-polysaccharide blends are incompatible if they are structurally dissimilar.[33,34] Polysaccharide incompatibility is determined by their functional groups *i.e.* incompatibility in order of carboxyl-containing polysaccharides > neutral polysaccharides > sulfated polysaccharides.[35] Proteins are incompatible if they belong to different Osborne' classifications such as globulins, prolamines, or albumins. Proteins of the same class are incompatible if they differ in their conformations (natured vs denatured conformations). Even with the same protein, aggregated and non-aggregated forms of the protein can cause incompatibility. Most importantly, a large difference in hydrophilicity between the proteins results in higher incompatibility.[33,36] This type of phase separation is most like that observed in BCPs and synthetic polymer blends, and is what promotes pattern formation. In short, there are plenty of ways one can take advantage of segregative phase separation of biopolymers to effectively produce patterned thin-films.

1.4. OTHER MORPHOLOGY DETERMINANTS

Apart from the biopolymers themselves and how they interact with one another, there are some more prosaic variables that affect the ultimate morphology, i.e. the pattern of a patterned thin-

film. There is a virtually endless list of such variables, many of them not practically controllable. But chief among those that can be controlled are film thickness, means of controlling solvent evaporation, and film's substrate type.

1.4.1. THICKNESS

Film thickness is a prominent factor among many that determine phase-separated, patterned film morphology. Sufficiently thin films can result in blends miscible in the bulk becoming immiscible, producing morphologies ranging from 1 – 3 μm spheres in a continuous matrix, to a bicontinuous morphology. This is due to close interactions with the substrate.[37] Furthermore, elaborate "salami structures" occur when the size/length of the morphology approach sample thickness, resulting in late stage wetting.[38] This can result in secondary phase separations, **Figure 1.3**.[38,39]

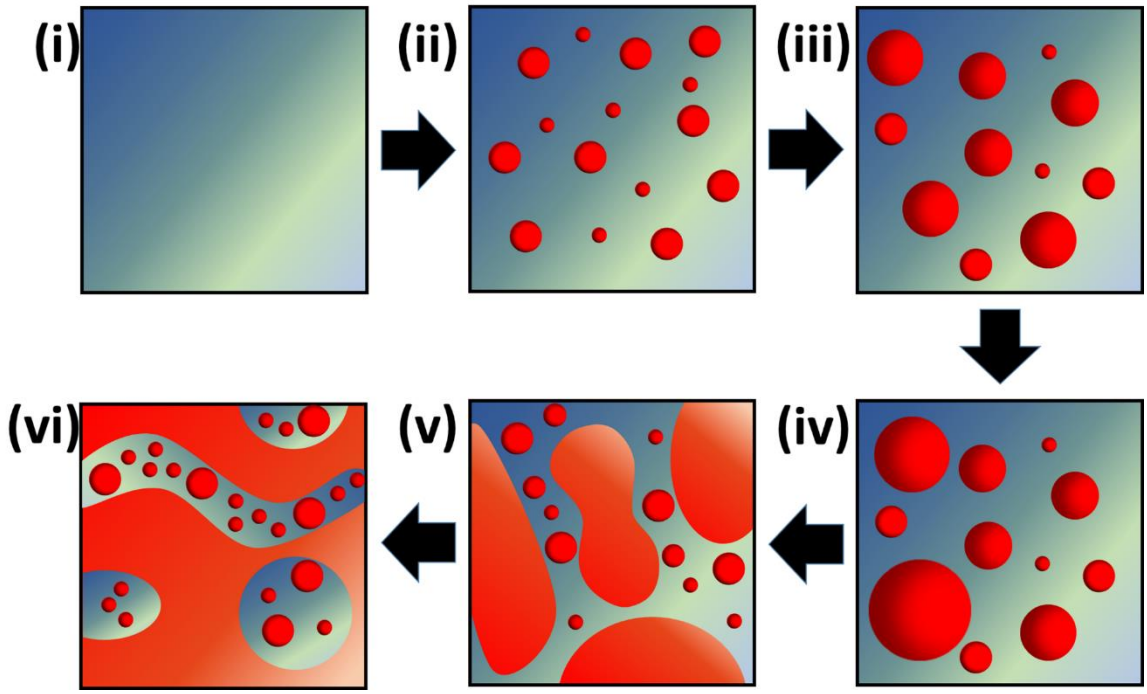


Figure 1.3: ***(i)*** *shows homogenous solution before phase separation;* ***(ii)*** *shows blend phase separation;* ***(iii-iv)*** *shows increase in phase size due to Ostwald ripening;* ***(v)*** *elongated features which may result from coalescence or response to shear;* ***(iv)*** *phase occlusion and adoption of salami structure.*

1.4.2. SOLVENT EVAPORATION METHOD

Drying times have a complex relationship with polymer film formation. If one wished to increase domain sizes in the final pattern of a PTF, one could increase the thickness of the deposited layer of polymer blend used to make that film. The thicker deposition would take longer to dry, thus extending drying times. This would increase the period of time in which domain growth can occur, thereby increasing domain size. However, this is also likely to result in "salami structures" in the final PTF.[38,9] If smaller structures are desired, the solvent could be evaporated quicker by depositing the blend at high spin speeds while spin coating. However, at high spin speeds, the increase in shear could force mixing between the biopolymers at low concentrations.[40] Additionally, increased spin speed increase shear forces, deforming spherical particles, creating longer, irregularly shaped particles. The extent of this would depend on the viscosity ratio between both phases.[41]

1.4.2.1. SOLVENT EVAPORATION – CHANGING AIR CAPACITY

Environmental factors like % relative humidity (% RH) can control solution evaporation rates. Reducing % RH increases the air capacity for solvent vapour, increasing the rate of evaporation rate.[42] This produces smaller features without changing film composition. Hygroscopic polymers can absorb ambient moisture. If absorbed, the polarity and interaction parameter of the hygroscopic polymer's domain increases, allowing for external control of the morphology.[43] As biopolymers are typically hygroscopic this would have to be considered.[44] At high % RH, water vapour can condense on the surface creating breath figures. Polymer blends can stabilize and reassemble these water droplets if a hydrophilic polymer is present, creating honeycomb arrays.[45] Finally, wetting must be considered. During phase separation, one polymer usually enriches the substrate while the other enriches at the air interface. This lowers surface free energy (SFE) at the air-polymer interface, lowering surface tension.[46,47] Changes in % RH alter a polymer's affinity for the air interface which results in lateral, vertical, or mixed internal structures.[9,10,48,49] Humidity is rarely discussed in relation to polymer blends in the literature.[48]

1.4.2.2. SOLVENT EVAPORATION – TEMPERATURE EFFECTS

Higher temperatures increase the drying rate of blend films. Elevating temperatures changes multiple parameters in polymer blend systems. Two simple examples are viscosity and solvent evaporation rate. Increased temperature increases rate of solvent loss, vitrifying the polymer

blend earlier in its growth process and producing smaller features. However, increasing temperature past a critical point increases polymer mobility, reducing blend viscosity and producing larger features. Thus, temperature control has limitations.[50] Temperature control is usually employed in synthetic polymer systems, not biopolymer blends.[25]

1.4.2.3. SOLVENT EVAPORATION – SOLVENT TYPE

Solvent "quality" affects blend morphology.[11,51] Simply put, one polymer may dry quicker than another, leaving one phase without solvent and the other still solvated. During demixing, the less soluble polymer precipitates earlier. The precipitated phase typically adopts the discontinuous phase or enriches the substrate, while the solvated phase forms around the minor phase or enriches at the air interface.[52] Thus, the evaporation rates of the solvent from an individual polymer may be controlled by suitable solvent, which better solubilizes one component over another.[53,54] The vapour pressure of the solvent also plays a role in determining feature size. This is further discussed in **Chapters 2** and **3**.

1.4.3. SUBSTRATE

Substrates can determine the patterns of BCPs and polymer blends films. Solvated blends deal with two interfaces; the air-polymer and the substrate-polymer interface. Preferential adsorption of one polymer onto the substrate can occur when using a suitable solvent.[53,54,55] Phase separation is "surface-orientated" if one polymer has an affinity for the substrate. *Walheim et al* showed that PMMA (polar) in PS/PMMA films selectively adsorbed onto the polar SiO_x surface. Coating SiO_x with octadecylmercaptan (an alkane) produced a low energy surface which selectively adsorbed PS, while PMMA adsorbed at the air interface, *i.e.* phase inversion.[54] More recently, selective adsorption has complimented dip-pen nanolithography, directing polymers to control pattern growth. Coffey & Ginger patterned a gold surface with 16-mercaptohexadecanoic acid using an atomic force microscope (AFM), passivating the gold with benzenethiol. This directed the growth of a PS/poly-3-hexylthiophene (PS/P3HT) blend film. PS selectively adsorbed onto the benzenethiol faster than onto 16-mercaptohexadecanoic acid dots as both are chemical similar.[56] This requires expensive, specialized equipment, while requiring multiple steps. Ambient air conditions and film thickness also play a role in substrate-polymer interactions, described earlier.[9,10,48,49] Finally, lateral phase separation in films can occur in blends with polymers of similar surface tension.[53]

1.5. GROWTH MECHANISMS

Everything, whether it be a natural or man-made, exists on a spectrum of production methods, ranging from entirely top-down to entirely bottom-up. Top-down manufacturing removes material from the bulk to produce the desired morphology; a subtractive process.[57] An example of a top-down fabrication would be resist-based nanolithography.[58] While top-down has worked well for the microelectronics industry[57], scalability[8], slow processing, substrate requirements, and high capital cost limit application in general products.[59]

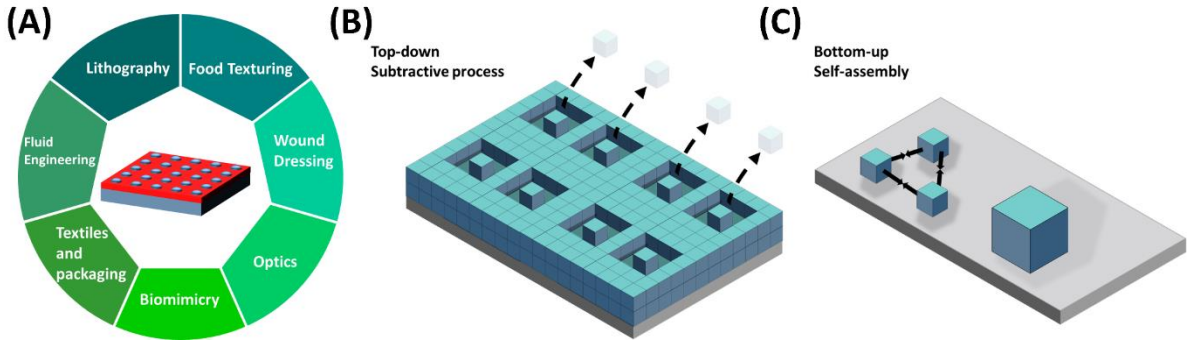


Figure 1.4: ***A****) Current and future applications of biopolymer PTFs.* ***B****) Top-down method of patterning such as lithography.* ***C****) Bottom-up method of patterning such as phase separation.*

Bottom-up manufacturing uses physical forces between molecules to direct self-assembly into larger structures. Biopolymers have recently gained attention for the self-assembly of many materials and devices **(Figure 1.4)**. Self-assembled manufacturing is attractive as it produces little-to-no waste and can achieve complex hierarchal structures. Nature produces structures using this type of bottom-up approach. It is more efficient than top-down production. There are 3 main routes governing morphology growth: spinodal decomposition, Ostwald ripening, and coalescence. Examination of size distributions (SDs) of the non-continuous phases that form via growth mechanisms can provide a means of determining the exact mechanism occurring in a given phase separation and coalescence. This is useful when examining the patterns formed in thin-films by phase separating polymer blends depositions.

1.5.1. SPINODAL DECOMPOSITION

Phase separation occurs either through nucleation and growth **or** spinodal decomposition. Spinodal decomposition occurs in the unstable region of a phase diagram. When a solution is thermodynamically unstable, it is sensitive to spontaneous fluctuations in concentration.[25] Material diffuses from regions of low concentration (regions of high chemical potential) to regions of high concentration (low chemical potential), coined "uphill diffusion".[60] Spinodal decomposition typically results in bicontinuous morphology[25], though, upon annealing, larger, spheroidal structures may develop as the system attempts to minimize interfacial energy[61,62] This primarily distinguishes spinodal decomposition from nucleation & growth. Spinodal decomposition usually results in formation of continuous phases, there are no discreet particulate structures that can be used to obtain an SD. So this is an instance where an SD cannot provide insight into formation mechanisms.

1.5.2. NUCLEATION & GROWTH

Nucleation & growth occurs in the metastable region of the phase diagram.[61] Nucleation & growth mechanisms are examples of cooperative self-assembly that results in features with typically biomodal SDs, rather than monomodal, monodisperse SDs. This reflects the mechanism of formation. Bimodal SDs indicate a nucleation (early growth features) & growth (late growth aggregates) mechanism.[63] In nucleation and growth mechanisms diffusion is downhill, as the concentration of dissolved polymers in closest proximity to stable nuclei is reduced. The system's free energy is minimized by polymer chains migrating from regions of high concentration to regions of low concentration. Growth typically results in a drop-in-matrix or spheroidal morphology.[62] Typically, lognormal curves are observed in the SDs of growth mechanisms.[64] Usually monomodal and monodisperse SDs are desired, as large particles in a bimodal distribution have a low surface area to volume ratio reducing the efficiency of materials (e.g. catalysts and bioimaging particles).[65] The growth of the discontinuous domain occurs by Ostwald ripening or coalescence, discussed below.

1.5.2.1. OSTWALD RIPENING

Ostwald ripening is a downhill diffusion process. Consider the SD of a thin film blend, vitrified early in its growth, as in **Figure 1.5A**. **Figure 1.5A** has both small and large features (Mode I and II respectively). Material transfers from smaller, more soluble particles (Mode I) by

resolvating into the matrix and feeding into the larger features (Mode II).[66] This increases the size of larger features, while decreasing the size of smaller features (**Figure 1.5B**).[67]

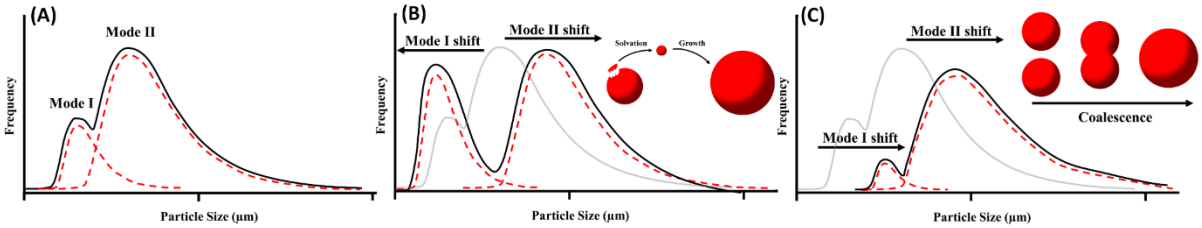


Figure 1.5: A) *Shows the typical SD of a polymer blends features.* ***B)*** *Shows the SD of (A) after a given period of time, where features have undergone Ostwald ripening. Greyed out plot is original SD.* ***C)*** *Shows the SD of* ***(A)*** *after a given period of time where features have undergone coalescence.*

As a result, mode II shifts to the right (a larger diameter) while Mode I shifts to the left (smaller diameter), increasing the difference in mode I and mode II. This is the characteristic trait of Ostwald ripening. Discontinuous droplet phases of approximate diameter 200 – 1,000 nm usually undergo Ostwald ripening.[68]

1.5.2.2. COALESCENCE

Coalescence is an attempt by a system to reduce interfacial energy between separated phases by fusing separate domains into larger, more circular domains. A characteristic morphological attribute of coalescence is "*8-shaped particles*", where two contacting particles merge.[69] Coalescence occurs in 4 steps: (i) approach, (ii) drainage, (iii) breakup, and (iv) relaxation.[69,70] Coalescence can be inferred from examination of PSDs. Coalescing particles result in an increase in average particle size. As merging occurs, the average particle diameter increases. Particles of small diameter (mode I) reduce in frequency and increase in size as they are consumed, and as time advances they have less partners to combine with decreasing coalescence probability. The frequency of particles in the mode II increase as the full width at half maximum (FWHM) broadens. In late stage coalescence, unimodality is achieved, though the sample distribution is polydisperse.

1.6. STATE OF THE ART: PTFS

The shared morphologies of synthetic polymer and biopolymer blend films ensures that there is much overlap in their potential applications **Figure 1.4A**).[71] The same is true for their

production methods. Some processes used to create micro- and nano-patterned features in surfaces, particularly in the most advanced applications, are top-down (**Figure 1.4B**) but the majority are bottom-up manufactured, using self-assembly guided by intermolecular forces (**Figure 1.4C**). Bottom-up processes are a highly sustainable means of manufacturing and are akin to natural growth. Taking cues from nature has become commonplace in the field of micro- and nano-patterned surfaces. For almost every application - from the most advanced anti-reflective surfaces in electronic and smart devices, to "smart" responsive surfaces, to structural materials, to hydrophobic "self-cleaning" materials - nature has already provided examples that engineers and scientists aspire to and are inspired by. Here we will take a look at the major applications of micro- and nano-patterned surfaces with direct relevance to the work of this thesis; antireflective surfaces, biomedical materials, hydrophobic coatings, and responsive surface. In each case we will examine the state of the art, comparing current synthetic standards to new biopolymer and semi-synthetic based materials. All will be explored through the lens of the natural materials that have spurred their development.

1.6.1. STATE OF THE ART: HYDROPHOBIC SURFACES

1.6.1.1. REPLICATING THE LOTUS LEAF

Textile industries have long adored hydrophobic surfaces for their water repellent, self-cleaning, anti-corrosive, antifouling, and stain-resistant properties.[72,73] Hydrophobicity is rooted in surface morphology and chemistry.[74] Immiscible blends produce an array of roughened morphologies that mimic natural hydrophobic surfaces, like kale leaves, springtail carapaces, and rose petals. Chief among nature's hydrophobic surfaces are lotus leaves.

The lotus leaf surface is a hierarchal structure, comprised of spheroidal papillae, with a protruding apex coated in wax tubules. Hydrophobicity stems from a combination of surface roughness (papillae) and chemical composition (wax tubules). This reduces the contact area between leaf. The higher the angle, the more hydrophobic the surface. Generally, a water contact angle below 90° is hydrophilic, above 90° is hydrophobic, and above 120° is superhydrophobic.[75] On a lotus leaf, water droplets make a contact angle of 163°.[76] The "lotus effect" can be replicated using artificially roughened surfaces, wherein the structures that render a surface rough also make it hydrophobic through mechanical and electrostatic effects. Nature achieved superhydrophobicity long before humanity, and without the need for fluorinated polymers and petrochemicals. Most attempts to emulate the lotus leaf have been

conducted using synthetic polymer surfaces as they are typically hydrophobic. However, biopolymers can, and have, been used with the same goal, though there are few examples that use biopolymers exclusively. Often biopolymers have been combined with synthetic polymers are have been artificially modified, rendering the final hydrophobic surfaces "semi-synthetic". We shall explore synthetic, semi-synthetic, and biopolymeric examples below.

1.6.1.2 STATE OF THE ART: SYNTHETIC POLYMER HYDROPHOBIC SURFACES

The lotus leaf's superhydrophobic surface is composed of natural compounds that are in balance with the ecosystems in which it prevails. By contrast, synthetic polymer PTFs are produced from blends that use environmentally unsustainable fluorinated components, organic solvents, and petrochemically sourced polymers. These are by far the most common type of hydrophobic surface that exist today. Though the materials and some of the methods of producing synthetic, hydrophobic surface are often unsustainable, much can be learned from such systems and applied to biopolymer films to enhance their hydrophobicity. Many surface structures that enhance hydrophobicity in synthetic films can be readily replicated in biopolymeric films. Blends which produce PTFs with protruding discontinuous domains are desired, though pores can yield similar result. Optimum feature size and number of features/area vary for each PTF, with hydrophobicity dependent upon the chemistries of the polymers used. Features can range from 200 nm – 20 μm.[77,78] Rougher films generally produce more hydrophobic surfaces, but numerical values for roughness are misleading: both the microscale roughness of the film, and nanoscale roughness of features, must be considered together.[52] Films with identical roughness, but different feature shapes or polymers, can have different hydrophobic properties.

Gengec *et al* phase separated a fluorinated (hydrophobic) copolymer p(perfluoroacrylate-co-methyl methacrylate) (p(TAN-co-MMA)) from PS, using tetrahydrofuran (THF) as a solvent. Obtention and refinement of such synthetic polymers comes with a large carbon footprint, and the solvent (THF) used is highly toxic. Blends demixed through drying or vitrification using a non-solvent (EtOH) creating a patterned film. Vitrification using EtOH produced a superhydrophobic surface, with WCAs approx. 170°. Nano-granules (0.5 – 2 μm diameter) around the pore rims provided micro- and nano-roughness. This type of hierarchal morphology gives the lotus leaf its superhydrophobicity. Blend films, with equivalent PS and copolymer, formed particles between 1 – 4 μm.[52]

Similarly, López *et al* created patterned films from a copolymer of 1H, 1H, 2H, 2H-perfluorodecyl acrylate and 2-ethylhexyl acrylate (PFDA-2EHA)[77] which was blended with

PFDA to yield PFDA/PFDA-2EHA blends that were used to create patterned surfaces similar to the lotus leaf. PFDA formed the fluorinated, hydrophobic, discontinuous phase. Patterned blend films with 75% PFDA had WCAs of approx. 130°. These films required a highly toxic fluorinated synthetic polymer component, and were not as effective as the films created by Gengec *et al*. López claims that no phase-separating blend films reviewed are environmentally friendly, and in another publication, López *et al* noted that no coating technique produces resilient hydrophobic structures while being environmentally friendly and scalable.[79]

Wei *et al* phase separated a styrene and 2,2,3,4,4,4-hexafluorobutyl methacrylate copolymer (PS-co-PHFMA) using THF and EtOH. Large spheres (> 20 μm) were surrounded by sub-micron spheres when using 50% EtOH. High non-solvent concentration increased the strength of phase separation, increasing surface roughness. Here, a Cassie state (a heterogeneous wetting state, where water contacts both the substrate, and air pockets formed by substrate features) with a maximum WCA of 154° was achieve, as air occupied 89.5% of the interfacial area between the water and the coating.[78] Again, this used THF and fluorinated, synthetic polymers - both environmentally damaging.

Vargas-Alfredo and Rodríguez Hernández spray deposited PTFs of PS with 3 different copolymers in chloroform. Neat PS produced a fibrous morphology, while PS and poly(2,3,4,5,6-pentafluorostyrene)-co-polystyrene (PS/PS-co-P5FS) blend, or neat PS-co-P5FS, produced droplet-in-matrix films. Neat, phase separated PS-co-PSFS had WCA of 159°. Blending PS-co-PSFS with PS reduced WCA (113°). This is explained by the reduced film surface area, due to the reduced features/area, despite the fluorinated copolymer.[80] There are typical sustainability concerns with these films (chlorinated solvents, fluorinated components, synthetic polymers, etc.).

Kato & Sato used polymerization-induced phase separation, creating a textured, hydrophobic surface from a mixture of ethyleneglycol dimethacrylate (EGDMA), tert-butyl methacrylate (TBMA), and perfluorooctylethyl methacrylate (FMA). Monomers and porogen were coated on a surface, phase separated by UV exposure. Unusually, porogens were either a solvent or, an EtOH soluble polymer phase removed to produce a microtexture (**Figure 1.6**). The fluorinated additive (FMA) was not needed to achieve superhydrophobicity (160°). WCA increased with RMS roughness (max approx. 400 nm). Roughness increased with film thickness; thicker films (max 5 μm) yielded larger features. Like lotus leaves, patterns with micro- and nano-scale roughness were the most hydrophobic.[81] Though this work used no biopolymers, the use of EtOH and avoidance of fluorinated compounds increased sustainability. Such methods are readily applicable to biopolymer systems.

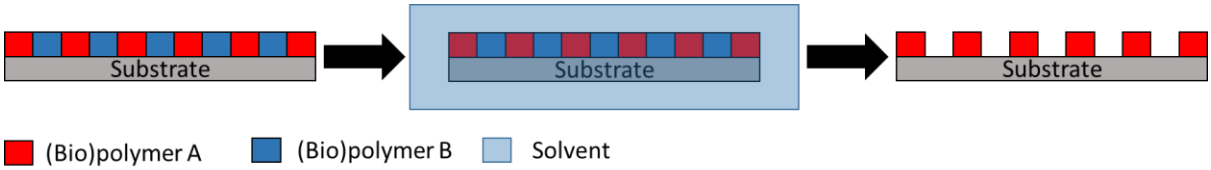


Figure 1.6: *Selective solvent preferentially removes one (bio)polymer component (blue) over another (red) allowing for identification of domains or generation of a structured homopolymer surface.*

1.6.1.3 State of the Art: Biopolymer Hydrophobic Surfaces

There is an obvious issue when using biopolymers to make hydrophobic surface – the majority of them are water soluble. This is a particular problem for polysaccharides. Some few polysaccharides are not water soluble, such as cellulose, but are still hygroscopic. Cellulose is the most widely used because it is abundant, renewable, and insoluble in water. However, its insolubility proposes a problem when considering how to process it. Among proteins there are more options for water insoluble and even hydrophobic materials. However, they are more difficult to source, and processing difficulties arise from their inherently complex molecular structures. These problems explain the lack of exclusively biopolymer based surfaces and the general lack of sustainable materials in this field of application. Cellulose derivatives dominate, but these are not true biopolymers, requiring processing with unsustainable materials and methods to render them suitable for common hydrophobic surface applications. Below is a breakdown of the most prominent biopolymeric, hydrophobic materials in the literature into pure polysaccharide, protein-polysaccharide, pure protein, and semi-synthetic materials.

Though not for hydrophobic applications, Czibula *et al* created microstructured, phase separated, cellulose derivative/cellulose film. The WCA for blend films was not reported. Derivatives were more hydrophobic than cellulose. Blend film SFE decreased as cellulose derivative contribution increased, indicating lower wettability. Though not stated, lower roughness appears to favour lower SFE, likely due to lessened exposure of hydrophilic cellulose.[82] This is counter to the above discussed synthetic blend films with a fluorinated component, as biopolymers are innately hydrophilic.

Hydrophobic surfaces made from patterned protein/polysaccharide blend films are the scarcest bio-based hydrophobic surfaces. Partially phase separated fish gelatin/curdlan blend films had higher WCAs than neat films (fish gelatin, 88.6°; fish gelatin/curdlan, 95.4°; and curdlan, 92.0°). This was attributed to increased surface roughness. Increasing curdlan content reduced wettability, similar to synthetic blend films incorporating a fluorinated component.[83]

Crosslinking protein/polysaccharide blend films can increase film hydrophobicity by reducing the number of free polar groups. However, these films were subject to swelling, and did not exceed a WCA of 80 °, making these films unsuitable for textiles. [84] Whey protein/pullalan films incorporated with bees wax increases blend film hydrophobicity (max WCA - 92°), with the bees wax behaving in a similar manner to fluorinated additives. [85]

Though not from a blend, Luís *et al* created hydrophobic zein-based films. Zein, unlike most proteins, is insoluble in water. It is also rich in hydrophobic amino acids, making it the ideal candidate to form hydrophobic PTFs. Initially, poly(dimethylsiloxane) (PDMS) was used to create a negative template of a lotus leaf. PTFs of zein (with lotus leaf patterns) were produced by pouring zein solution into the PDMS template. Liquorice essential oil was incorporated into the zein films to improve antibacterial and hydrophobic character. These films achieved a WCA of 112.5° - the highest to date for any zein film. The authors note that the top-down method used is not feasible for large scale production. However, this work indicates that zein may be a suitable material to produce hydrophobic, biopolymer blend films.[86]

Similarly, neat hydrophobic soy-protein isolate films were produced via molding. Upon acrylation, hydrophobic regions of the soy-protein phase separated from the hydrophilic regions. Phase separation formed hydrophobic microspheres, achieving a WCA > 65°. Unfortunately, the plasticizers used are toxic, and unsustainable. However, phase separation would offer a method of producing hydrophobic protein-based PTFs in a scalable fashion.

1.6.1.4 State of the Art: Semi-synthetic Hydrophobic Surfaces

The most hydrophobic biopolymer based films incorporate semi-synthetic cellulose derivatives, usually trimetylsilyl cellulose (TMSC). Acetylated lignin/TMSC (LAc/TMSC) films show no change in WCA regardless of blend ratio (91°), the same as a neat TMSC film. After deacetylation and hydrolysis, films with higher lignin content had a higher WCA. The 1:1 blend film (highest roughness of measured blends, 4.4 nm) had the highest WCA (55°).[87] Cellulose triacetate (CTA)/TMSC blends WCAs are approx. 90 – 100°. Converting TMSC to cellulose, and removing CTA, results in WCAs higher than neat cellulose films due to the films' high roughness. Cellulose/CTA patterned blend films had higher WCAs at lower cellulose fractions, likely due to increasing CTA contribution and increased roughness (approx. 10 – 30 nm).[88] PCL(polycaprylactone)/TMSC blend films behave identically after hydrolysis to the above TMSC blends.[89] PHB (poly(3-hydroxybutyrate), bacterial biopolymer)/cellulose and PHB/TMSC blend films are an interesting aside. Cellulose or PHB can be removed with

enzymes, similar to **Figure 1.6**. Features ranged from 50 – 1,400 nm. Cellulose films with PHB removed had WCAs of approx. 40°. Films with cellulose removed had WCAs between 50 – 60°. 3:1 PHB/TMSC blend films achieved the highest WCA (approx. 100°, likely due to TMSC at the surface).[90] The above films which use TMSC require chlorinated solvents to prepare and develop the films. Additionally, the cellulose must be derived to create TMSC, and hydrolysed to convert it back to cellulose, which is environmentally unfriendly. Finally, after converting the TMSC back to cellulose, most of the hydrophobicity of the film is lost.

Most of the above films are hydrophilic, and few technically classify as hydrophobic. No biopolymer blend films approach superhydrophobicity. K. Trommer[50] showed how cellulose derivatives and polyacrylonitrile (PAN) blends could produce similar structures to Gengec *et al* and the PS/p(TAN-co-MMA) blends.[52] Trommer chose three cellulose derivatives; cellulose carbamate (CC), cellulose propionate (CP), and cellulose acetate (CA). Similar to Gengec *et al*, Trommer varied blend *r* and used a non-solvent combined with thermal evaporation. Solvent evaporation resulted in a porous morphology, while precipitation in DMA/water before drying produced a droplet-in-matrix morphology (similar to López *et al*[77] and Gegnec *et al*[52]), approx. 0.2 μm in diameter. Unlike previous biopolymer blends with large domain sizes, early precipitation and the use of a volatile solvent produced features of sub-micron size. Increasing temperature reduced solvated blend viscosity, increasing feature size. Past a critical threshold, higher temperatures rapidly evaporated solvent, increasing solvated blend viscosity and reducing feature size. However, to achieve hydrophobicity, fluorinated agents were used. A WCA of 111° was achieved using fluorocarbons, and a WCA of 131° degrees was achieved using a fluoralkyl silane. This is the closest true analogue of a lotus leaf to date in the literature.

1.6.2. STATE OF THE ART: RESPONSIVE SURFACES

1.6.2.1 REPLICATING LEAF STOMATA

Materials which respond to environmental cues are called stimuli responsive surfaces. Guard cells in leaves, which open and close stomata (pores) in response to stimuli, to control gas exchange and water loss, are a natural example. They allow for a plant to respond to stimuli automatically. Such surfaces can be used as containers for drugs, cells, or particles. They can also act as sensors, permitting selective filtration and fluid flow regulation. Synthetic stimuli-responsive surfaces work on the same principle as stomata guard cells; volumetric swelling to

control the state of the pore (open or closed). The field of semi-synthetic, stomata-like surfaces is relatively new. There are no examples of such surfaces to be found in the literature. Thus, no semi-synthetic section is included here. But, biopolymer and synthetic examples abound.

1.6.2.2 State of the Art: Synthetic Responsive Surfaces

Stomatal aperture depends on environmental cues. Stomata are typically open during the day for CO_2 diffusion. This makes sense, as it is when light is available for photosynthesis. For state-of-the-art smart devices, the ability of a material to self-regulate under different environmental conditions is of paramount importance. While some of the examples below use synthetic polymers, many of the methods of production, and applications, are applicable to biopolymer PTFs.

Schacher *et al* produced a double stimuli-responsive surface from synthetic polymer blends; PS-b-PDMAEMA (PDMAEMA being temperature and pH sensitive). Pores were 20 – 80 nm, 1 µm deep. Varying pH and temperature opened pores, increasing permeability/flux of water seven-fold. Silica particles were used to test the film's micro- and ultrafiltration properties. At pH 5, no particles passed through; *i.e.* closed pores (swelling). Increasing pH to 10 filtered particles 36 – 104 nm diameter, resulting in passage of 63% of particles. This material is a strong candidate for ultrafiltration device, to remove bacteria, viruses and particles.[91]

Tokarev created stimuli responsive films by crosslinking P2VP with 1,4-diioodobutane (DIB). In excess, DIB also acted as the pore forming agent, phase separating from P2VP. Pore diameter was controlled by DIB concentration (0.3 – 1.5 µm diameter, tessellated). Pores were open at pH 3, closed at pH 2 due to pyridine rings on the P2VP being protonated, resulting in swelling.[92] Another study showed high humidity was the reason DIB phase separated from P2VP, due to the limited solubility of DIB in water. In this study, larger pores were attributed to early phase separation.[93] However, this work did not consider the reduced evaporation rate of the solvent at higher humidities, leading to larger feature sizes. Additionally, the effect Voronoi tessellation (a mechanism in which features rearrange to form mechanically stable, polygonal features) had on pore morphology was not discussed. Pores were responsive to pH, of value for biomedical applications such as drug release. Similar applications to Schacher are envisioned for these PTFs.

The above methods were used to create a porous P2VP film. Ag and Au nanoparticles (NPs) were synthesized inside the pores. After synthesis, stimuli controlled film swelling governed interparticle distance between NPs. Interparticle distance determines the plasmon

coupling strength of the NPs, allowing the film to behave as a nanosensor[94] with potential use monitoring glucose levels.[95] Such films could also mimic skin, or be imbued with sensing, antibacterial, and biocatalytic properties, increasing their applicability. Another application of particle infused films is non-invasive examination of biomaterials, such as implants, where degradation or local changes occur in the material.[96,97] Porous P2VP films also respond to cholesterol, making it a suitable material for electrochemical gates, used in biosensors. These films are extremely sensitive to cholesterol, reducing porosity by a factor of 3 (51.7% to 18.3%). The rate of change was much higher than other approaches, including monolayers, or other thin films.[98]

1.6.2.3 State of the Art: Biopolymer Responsive Surfaces

Switching to biopolymers, Gopishetty *et al* also created biological responsive film by blending sodium alginate (NaAlg) and gelatin in a heated H_2O/NaCl solution.[96] The NaAlg was crosslinked with $CaCl_2$, while simultaneously removing the gelatin producing a porous film, similar to Nady & Kandil.[84] Pores (380 ± 116 nm in diameter) were open at pH < 4, and closed at a pH > 5 due to volumetric swelling. This altered film permeability, demonstrated with switchable diffusion of a water soluble dye (rhodamine B) across the membrane. Similarly, membrane adhesion could be "switched", from low adhesion in the swollen state to high adhesion in the non-swollen state. Finally, loading the membrane with nanoparticles and enzymes imparted bactericidal and metabolic utility.[96] Alginate membranes are notably antifouling and biocompatible, an advantage over the P2VP membranes mentioned above.[97]

Similar results were achieved by Tokarev *et al*, using alginate and diamine-PEG. The pores achieved by Tokarev were more monodisperse and smaller (< 100 nm) than Gopishetty *et al*, depending on the total polymer concentration and polymer ratio. Pores were pH responsive, with similar applications to Gopishetty in mind.[99] These types of membranes may also be used to separate protein mixtures or allow for controlled release of drugs.[97]

1.6.3. State of The Art: Antireflective Surfaces

1.6.3.1 Replicating Butterfly Wings

Everything we see is due to reflection of photons of light off surfaces and into our eyes. However, certain artificial materials, like phone screens, tv panels, lenses, etc. - by virtue of

their relatively featureless, smooth surfaces - sometimes reflect too much light.[100] This results in glare, temporarily blindness, and renders certain technologies, like solar panels, less effective. To remedy this issue, *anti-reflective* (AR) materials became a focus of research. AR materials have micro- and nano-patterned surface structures that essentially trap photons of light, preventing their reflection. Hence, "anti-reflective". Nature, again, leads the way. Butterfly wings and moth eyes are the classic examples of AR surfaces, typifying the two structural archetypes in AR materials; those with micro- and nano-scale pillars on their surface (moth eyes), and those with porous structures at similar scales (butterfly wings).[101,102] The AR properties of butterfly wings is a consequence of porous quasi-honeycomb-arrays with the parallel-lamellae structure on their surfaces. These confer "super light trapping" properties.[102] Porous structures are more desirable than the nanopillars of moth eyes. Pillars are easily contaminated, impossible to clean, have lower damage tolerance, and require complex fabrication techniques, unlike porous materials. Pillars distort and break to different heights during cleaning, whereas pores do not.[103] Porous surfaces have better mechanical properties than pillars. Butterfly wing pores have a hexagonal morphology, random in size, spacing, and pores/area. Currently, complex, toxic methods are used to create synthetic analogues of moth eye and butterfly wing structures.[100] Butterfly wing pores are hexagonal (tessellated), 490 nm long 380 nm wide, and separated by ribs (max 170 nm wide).[104] Across species, pores can range from 300 – 800 nm, with the same core features.[105–108] Current pores created using lithography are circular, have narrow SD, are equally spaced, and are smaller than natural butterfly wing pores. Large pores have applications outside of AR surfaces such as photocatalysis[108], and increasing the dye sorption in solar cells.[105]

AR surfaces can be produced directly, or indirectly, from polymers; whether they are synthetic or natural. In direct methods, bottom-up or top-down manufacturing produces patterned structures in a polymer surface, which provides the AR effects. In indirect methods a patterned polymer layer is deposited on an underlying substrate material, typically a metal surface. The pattern in the polymer layer can be transferred to the metal substrate. This is done by selectively removing one polymer domain of the patterned polymer layer (what remains is, in certain processes, called a "resist"). On the remaining domain, a metal, different to the substrate metal, is selectively deposited. The polymer below this newly deposited metal is then removed, leaving the deposited metal on top of the substrate in the pattern of one domain of the original patterned polymer layer. This method, often called metal polymer blend lithography (metal-PBL) forms what is called a "mask" (masks are more permanent than

resists, which can be thought of as temporary masks) which can used for pattern transfer in AR surface production. In some instances, the resist alone is enough for pattern transfer.

The methods outlined above are top-down and intensive. The use of biopolymers will make them a little more sustainable but the absolute amounts of polymer used are relatively small. The potential advantage of using biopolymers is that they permit production of AR structures at scales not feasible with BCPs, making broadband AR materials a possibility.

1.6.3.2 State of the Art: Synthetic Polymers in AR Surface Production

Synthetic AR surfaces are typically made with BCPs, usually with pillared, rather than porous, surfaces. Recent work by Mokarian-Tabari *et al* shows that such surfaces can achieve 1.75% reflectivity from 400 – 900 nm, using up to a 75° incidence angle.[8] Patterning was achieved by phase separating PS-*b*-P2VP, incorporating metal into the P2VP domain, and transferring the pattern with a plasma etch. This produced 870 nm diameter nanopillars, with Gaussian SD (80 – 160 nm), hexagonal arrangement (not to be confused with tessellated), and wide spacing (180 nm). Smaller diameter pillars did not suppress reflectivity as well as larger ones. As always with BCPs, pattern generation required solvent annealing (THF, chloroform), and the patterning agent was a petrochemical polymer, both environmentally damaging and time consuming. Etches > 870 nm caused the capillary forces of the pillars to exceed the supportive force of the pillars, resulting in pillar aggregation at the surface, increasing reflectivity.[8]

Unlike BCPs, using polymer blends can achieve broad pore SDs (like butterfly wings), in a rapid and economical manner. Huang *et al* achieved lateral phase separation of PS discontinuous domains in a PMMA matrix, by controlling % RH during spin casting. Lateral phase separation is achieved through self-stratification, driven by lower surface tension, lower solubility of one component, and polymer-substrate interactions.[109] Feature diameter was controlled by varying the PS m_w, and *r*. Increased PS m_w resulted in larger, less monodisperse PS domains while increasing interdomain spacing. SDs could be tuned from 50 – 150 nm to 200 – 800 nm ranges - comparable to butterfly wings.[104–108] To create a mask, one polymer was selectively dissolved, a functional silane was deposited by vapour-phase deposition, and the remaining polymer phase removed to yield a patterned silane surface. That surface could be used for lithography, cell-adhesion, and the growth of various oxide nanostructures.[9]

Guo *et al* produced similar micro and nanoporous films, metal masks, and substrates by phase separating PS/PEG blends.[11] The discontinuous domain (PEG) was removed through dissolution with a selective solvent (water) producing a nanoporous PS matrix. Using e-beam

evaporation, nickel was deposited on the surface. The remaining polymer was removed with solvent, leaving a nanodot array (**Figure 1.7**). The silicon was reactive ion etched, producing tapered pillars under the nickel dots. Alternatively, Ag was deposited via e-beam evaporation and solvent removal of the porous PS matrix. PS nanopores (and resulting Ni dots) typically ranged from 200 – 400 nm. Again, these were within the range of butterfly wing pores.[104–108] Between 4.57 x 10^8 and 8.48 x 10^9 features/inch^2 were formed in PS/PEG blend films. Pillars produced with Ni template were 870 nm tall, < 500 nm in diameter, and had reflectance for silicon below 3% in the 450 – 950 nm range. [11] Guo may not have tried to etch beyond 870 nm due to the capillary forces that would exceed supportive forces of the nanopillars.[8] The Ag nanodot arrays had a surface enhanced Raman scattering of 1.64 x 10^8, making it suitable for chemical and biological sensing applications such as environmental and food monitoring.[11,110]

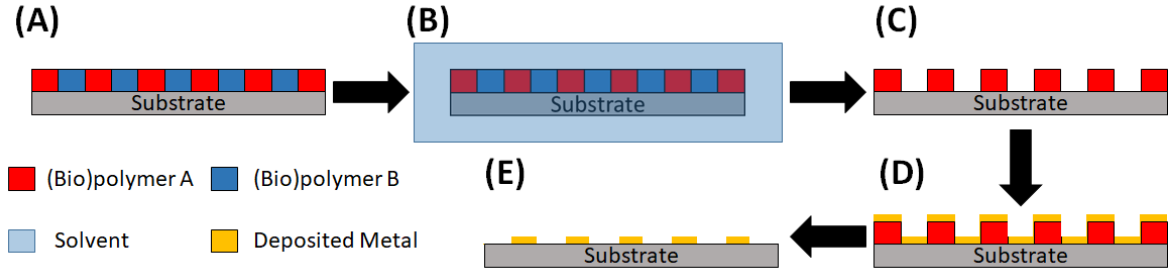


Figure 1.7: *(**A-C**) Selective polymer phase removal. The remaining polymer is sometimes referred to as a soft resist, in certain processes, and may be used to transfer patterns. (**D**) Metal deposition on top of remaining polymer phase, forming a metal pattern. (**E**) Lift off of underlying polymer phase leaving metal adhered to substrate. Any metal deposited on the polymer phase is removed, while metal in contact with the substrate remains. The final metal pattern is the inverse of the soft resist in **(C)**. This metal pattern may be used for pattern transfer (lithography).*

Huang, in another study using a PS/PMMA PTF, could selectively remove either the PS or PMMA domain using cyclohexane or acetic acid respectively (Guo only removed the PEG phase). This produced either a porous PMMA matrix, or a PS island array - a more robust blend. Again, metal was thermally evaporated to produce a mask (**Figure 1.7**) using Fe, Au, Cu, Pd and Cr, demonstrating the feasibility of the technique to produce different metal films. Features were typically 200 – 800 nm in diameter with a minimum diameter of 50 nm, achieving a maximum feature/area of 220 million/cm^2.[8] Again, this is similar to butterfly

wings[104–108], and exceeds the size limitations of BCPs. It was suggested these metal films would act as good etch resists (as with Guo *et al*'s publication), and as selective optical filters.[10]

Metal-PBL has been used recently to create nanopillars on solar cells to increase light retention. Pillars (0.5 μm spacing, 140 – 560 nm in diameter) were created using a PS/PMMA blend. PMMA was removed using acetic acid, and PS pillar heights optimized by O_2 plasma etch. Unlike previous work, metal was deposited directly onto the polymer, now behaving as a patterned back-reflector. Removal of PS, and subsequent etching of the substrate, was not required. Compared to an Asahi cell, PS nanopillars increased power conversion by 65%, due to a decrease in reflection loss, with improved light trapping above 600 nm. Asahi cells also have local thickness variations, which can result in electrical shorts. The PS layer assisted the growth of high quality Si layers upon it, minimizing the possibility of an electrical short. [111]

1.6.3.3 State of the Art: Semisynthetic Polymers in AR Surface Production

There is no reason that PBL and metal-PBL techniques could not be applied to biopolymer PTFs. It is useful to contemplate the possible pros and cons. Using biopolymers would make use of water or dilute acid as a common solvent for blends, possible. As with Nady & Kandil, EtOH/H_2O or buffered solutions could be used to selectively remove components resulting in dots or tessellated porous matrices, akin to butterfly wings[84], or pillars[111] as discussed above.

Niegelhell *et al* created a PTF using PHB/TMSC blends.[90] Similar to Taajamaa *et al*[88] and Czibula *et al*[82], TMSC was converted to cellulose using HCl vapour. Buffered enzyme solutions (either PHB-depolymerase or cellulose) then selectively removed either the PHB domain or cellulose domain (similar to **Figure 1.6**). This results in either a porous or dot-matrix of either cellulose or PHB. Features ranged from 50 nm – 1.4 μm, with varying size polydispersity. The resulting biopolymer pattern is described as a biopolymer resist, with the aim of using it as a replacement for petrochemically derived polymer blend resists, biosensors or, antifouling surfaces.[90] The morphology is remarkably similar to the synthetic materials of Huang *et al*[9,10] and Guo *et al*.[11] Similar cellulose blends have been made by Taajamaa *et al* for use as diagnostic membranes, catalysts, templates and sensors.[88] Pores (2 μm diameter) with elevated rims formed through dewetting. Pore formation was controlled by humidity. Removal of the cellulose triacetate phase left a sub-micrometre dot matrix - perfect candidates for metal-PBL.[10] Czibula *et al* worked with cellulose derivative blends to create structures inhibiting bacterial adhesion and biofilm formation.[82] The TMSC phase in Taajamaa *et al*[88] and Czibula *et al's* [82] work was converted to cellulose in the same manner as Niegelhell *et al*

technique[90], though both removed remaining derivative with chloroform in place of enzymes. Though these are ideal candidates for PBL in terms of feature size, the "green appeal" is lost when using cellulose derivatives and chlorinated solvents. Taajamaa continued work on cellulose blends, using a PS/TMSC blend to immobilize gold nanoparticles (AuNPs) on the surface in an organized manner. This was achieved by; **1)** phase separating PS from TMSC; **2)** adsorbing BSA onto PS; and **3)** attaching AuNPs onto the adsorbed BSA. The described goal was to create a 2D architecture decorated with AuNPs for diagnostic, electronic and biomedical applications such as drug release. In 1:5 cellulose/PS blends, spherical PS domains were approx. 200 nm in diameter. With the differing solubility of cellulose and PS, this blend would be suitable for metal PBL. But PS and toluene precludes this as a true green alternative.[112]

Finally, many of the blends in the stimuli responsive membrane section (detailed above) meet the morphological requirements for metal-PBL. As an example, Na-Alg/PVA blends with 50% PVA fraction produce porous structures (pores 130 nm in diameter).[113]. The size and disordered nature of these features (incorporated with metal-PBL) would allow for greater suppression of reflectivity than the typically produced sub-100 nm BCP features.[8,111] Orlov *et al*'s showed that tessellated pores (84 – 1,500 nm diameter) were achievable with up to 16.2 pores/μm^2.[93] In metal-PBL, Huang *et al* produced porous metal matrices, with pores between 200 – 800 nm. The maximum number of pores/area was 2.2 holes/μm^2.[10] Guo *et al* produced pore ranging from 200 – 400 nm, 100 nm apart, with pores/area ranging from 0.7 pores/μm^2 to 13.1 pores/μm^2.[11] Given that butterfly wing pores are highly tessellated, Orlov *et al's* method of producing films may be a better method of achieving AR films. Finally, Nady & Kandil pores morphologically are identical to that which gives butterfly wings their AR properties (highly tessellated, dense packing), though are approx. 24 times larger than the required dimensions for AR applications. Further refinement of this blend could provide the best AR properties due to the enhanced packing ability of this blend.[84]

1.6.3.4 State of the Art: Biopolymers in AR Surface Production

The only conceivable issues which may arise from using biopolymers in PBL would be obtaining laterally phase separated structures. Though not an issue for metal PBL, as biopolymers are generally hydrophilic[17], using humidity to organize the internal structure would be a complex process.[9] Niegelhell *et al*[90], and Czibula *et al*[82] showed that enzymes can be used to create a mask from semi-synthetic polymers. This is possible with biopolymers too, as is the use of water as a solvent.

Caillau *et al* showed that nanopatterned polysaccharides could be used as resists for silicon etching, without the need for metal masks. Using e-beam, regions of the chitosan film were degraded, increasing their solubility, allowing removal with deionised water, leaving 50 nm wide chitosan lines on the silicon wafer. The SiO_2 was etched by reactive ion etching (RIE) using CHF_3 gas, which removed the 90 nm oxide layer exposing the silicon. The chitosan was able to tolerate the CHF_3 etch, successfully transferring the pattern into the silica layer.[114]

Jiang *et al*[115] used egg-white protein as a resist material, aiming for a simpler, more environmentally friendly, and cheaper process. This was much cheaper than derived polymers such as PMMA, dramatically reducing the cost of fabrication. The egg-white was either mixed with glycerol to inhibit aggregation and promote chain scission upon UV or e-beam exposure (positive resist), or used without glycerol to promote protein aggregation upon UV or e-beam exposure (water insoluble regions, negative resist). Patterned films could then be produced with just water. These patterns could then be transferred with few defects to Si, SiO_2, Au and Cu substrates using HF, HF vapour, aqueous N-bromosuccinimide and pyridine, or RIE. The protein could then be removed in 15 hr using the enzyme trypsin at 37 °C. Though lengthy, this is a process with improved sustainability.[114] It is the first study to report deep etching using a biomaterial. Features 60 nm in size could be transferred to a typical depth of 5 μm.[115]

This showcases the capacity of biopolymers in substrate etching, without the need of metal incorporates. Considering all of the above biopolymer blends, the potential to produce lithographic masks and resists is there. Similar techniques have been used to create fibroin features approx. 100 nm features, using UV crosslinking and e-beam treatment. Though these used DMSO[116], it could be replaced by using only water as a solvent, if the fibroin conformation is carefully controlled.[117] Unlike for hydrophobic surfaces, there is no innate property needed to be overcome for protein pattern development.

1.6.4. STATE OF THE ART: BIOMEDICAL SURFACES

1.6.4.1 REPLICATING WOOD AND BONE SURFACES

For cell adherence, few structures compare to the natural morphologies of wood and bone. Bone is porous, with hierarchal, microscale, sub-microscale, and nanoscale morphologies, that are key to vascularisation, and the ability of cells to attach, proliferate, differentiate, and grow.[118] Woods have a range of structures that imitate bone, such as, bamboo (honeycomb structure)[119], pine (honeycomb)[120], rattan (hierarchal pore structure mimicking the Haversian

and Volkmann system pores)[120], and sipo (micropores similar to cortical bone).[121] Much of biomedical materials research focuses on mimicking wood and bone structures in surfaces and thin-films on medical devices.

Unlike the other fields we have explored, in biomedical industries, biopolymers are already extensively used because they are innately antimicrobial and biocompatible. They have the added advantage of being renewable, less toxic, cheap, abundant, biodegradable, and more effective than industry standard materials like polymeric quaternary ammonium salts.[122] Another advantage of biopolymers in is that most are hydrophilic, so they do not produce inflammatory responses, unlike synthetic polymers which cause inflammation and inhibit cell adherence.[123] But even synthetic polymers, despite this disadvantage, can be made into effective biomedical surfaces with the right surface structures, such as those of wood and bone.[124] The most commonly used polymers in this field are polyesters, which are hydrophobic, inhibiting cell adherence, and their degradation promotes inflammatory responses.[123] Biopolymer PTFs with wood and bone like pore structures in their surfaces provide enhanced biofactor delivery[125], vascularization, cell profileration, and migration.[126] Pores are typically 10 – 1,000 μm in diameter[125]. Specific applications of various pore sizes are summarized by Guarino & Ambrosio[127], and Sarazin *et al*.[128]

1.6.4.2 STATE OF THE ART: SYNTHETIC BIOMEDICAL PTFS

Huang *et al* produced bi-continuous porous networks in a PTF by phase separating immiscible polymers; PLA (poly(lactic acid)) and PCL. The phases were coarsened with supercritical CO_2 (environmentally friendly). The PCL phase was removed using acetic acid to yield a porous structure (**Figure 1.8A)**.[129] Pores size was controlled at 50 – 150 μm - suitable for biological scaffolds. Fibroblasts were grown on the material, showing the potential for biomedical applications. No further cell growth data was provided, though it is the focus of future work[129] in which the PTF is expected to be a good scaffold, as pores from bottom-up methods have better mechanical and fluid exchange properties than those from salt leeching.[123]

Similarly, de Moura *et al* created a porous PTF using a PLA/PCL blend for bone regeneration. Hydroxyapatite particles (80 – 90 nm in size) were incorporated to improve the PTFs bioactivity. PTF roughness ranged from 1.24 – 3.92 μm. Median pore size ranged from 3.05 – 4.79 μm. Hydroxyapatite had no effect on cell viability, though increasing hydroxyapatite content increased PTF roughness, improved PTF degradation temperature, and prevented microfracture formation (improving PTF mechanical properties).[130]

Guarino & Ambrosio explored the use of co-continuous PCL/PEO blends through melt blending and extrusion. PEO was selectively removed with water, leaving a porous matrix behind. Pores were 30 μm, and shear stress prevented developing domain growth, limiting max pore size to 50 μm, thereby limiting possible applications.[127] Sarazin *et al* also achieved a porous scaffold through melt blending of PLLA and PCL, and also selectively removed PEO with water. Pore size was controlled through *r* and annealing, achieving average sizes from 1.5 – 88 μm, claiming they were suitable for both tissue regeneration and drug release.[128] Both studies use melt blending which removes the need for organic solvents, but cannot be used with biopolymers which decompose under melt blending conditions. Though each uses petroleum based polymer, the use of water eliminates the need for toxic organic solvents.

Bui *et al* fabricated a honeycomb PTF using PLA in a chloroform/methanol (solvent/nonsolvent) solution. Methanol has a high affinity for water, allowing for the water adsorption, and so formation of the honeycomb array. The gel-like layer formed by the chloroform/methanol solution also stabilized water droplets, preventing them from coalescing, forming tessellated pores. Pores were highly ordered. PTFs contained pores approx. 2.8 – 6.1 μm in diameter, 1 μm in depth, with 0.03 – 0.11 pores/μm^2. Pores were either circular or tessellated. When compared to unpatterned PLA, PLA PTFs enhanced cell adhesion. Cell filopodia attached to honeycomb pore walls. Films containing 6 μm pores provided the best cell proliferation within a 24-hour period, approx. 25% more effective than films with 2.8 μm pores. It must be noted, while this method does produce PTFs in a timely manner, the requirement of chloroform and methanol is unsustainable for large scale production.[131]

1.6.4.3 State of the Art: Semi-Synthetics Biomedical PTFs

PCL has been blended with TMSC (subsequently converted to cellulose) to create nano- and micropatterned surfaces. This is a formulation of a biodegradable hydrophobic polyester and hydrophilic polysaccharide. Hydrophobic polyesters adsorb proteins, which result in clot formation after implantation of a medical device. The blend produced spheres and salami structures, with features approximately 0.5 – 1 μm in diameter. The hydrophilic cellulose domains repelled blood clotting protein. The blend surface acts as an anti-coagulative, and promoted better cell viability than neat, unpatterned cellulose. These are key attributes in devices such as vascular grafts or other regenerative medicine devices.[89]

Pulieri *et al* created a gelatin/chitosan PTF using a PDMS micromold, creating microstructured thin films with different morphologies.[132] Cell adhesion and proliferation was tested using NIH-3T3 fibroblasts (indicative of tissue regeneration) and S5Y5 neuroblastoma

(indicative of nerve regeneration cells). Cell growth was better on blends containing 2D architectures. After 24 hrs, adhesion of fibroblast cells was higher on PTF blends than unpatterned films. Similarly, PTFs with higher chitosan content promoted more fibroblast adhesion, due to the higher surface charge. In contrast, PTF blends with 80 wt% gelatin was the best for neuroblastoma cell adhesion and proliferation. Similarly, neuroblastoma achieved 90% of the cell proliferation of the control (poly-l-lysine, a superb material for tissue regeneration[133]). It was not stated which microstructured film was used for cell adhesion. However, the chitosan/gelatin blends PTFs demonstrated themselves suitable candidates for nerve and tissue regeneration.[132]

Peschel *et al* blended poly(3-hydroxybutyrate), P(3HB), and poly(4-hydroxybutyrate), (P(4HB), with the polysaccharides alginic acid, chitosan, hyaluronic acid, and pectin, to produce porous PTFs. Pore diameter depended on blend composition; P(4HB)/hyaluronic acid (30 – 150 µm); P(4HB)/chitosan (25 - 65 µm); P(3HB)/hyaluronic acid (30 – 150 µm); P(3HB)/chitosan (20 – 110 µm); P(3HB)/pectin (100 – 300 µm); P(3HB)/alginic acid (30 – 70 µm). Similarly, porous PTF WCAs varied from 75 – 93°. Porosity increased PTF hydrophobicity (which normally would impede cell proliferation). However, the macroporous pores counteracted this. HaCaT (keratinocytes) proliferated 25% better with the P(4HB)/hyaluronic acid blend, when compared to the control. This was attributed to the pore size range pore. P(3HB) PTFs were more hydrophobic than P(4HB) PTFs, resulting in poorer cell attachment on the P(3HB) PTFs. HaCaT cells had fewer filaments on P(3HB) PTFs, resulting in poor cell attachment and adherence.[134]

Mahato *et al* created a hydrogel PTF, blending chitosan lactate and PVA to produce a porous matrix, which could be loaded with a drug (ciprofloxacin). The cytotoxic effect of the PTF was evaluated with and without ciprofloxacin. Increased chitosan lactate content resulted in smaller pores, though no numerical value was given. Smaller pores showed reduced drug loading. Antimicrobial efficiency was tested using *E. coli*. PTFs with the largest pores showed zones of inhibition approx. 2.3 times the diameter of PTFs with the smallest pores. Both neat and blend films effectively inhibited *E. coli* growth. All PTFs showed a similar ability for cell proliferation, though the PTF with the smallest pores showed a small reduction in fibroblast cell viability. Cell viability over the PTF surface was > 80%. The PTFs described are good candidates for wound dressing, due to their biocompatibility and drug-loading capability.[135]

1.6.4.4 STATE OF THE ART: BIOPOLYMER BIOMEDICAL PTFS

One of the more elegant applications of biopolymer immiscibility is by Hu *et al*,[136] who blended recombinant tropoelastin (an unstructured protein which assembles to form elastin)[137] and silk fibroin (a fibrous protein with excellent mechanical properties).[138] The proteins were slowly mixed together to prevent aggregation, not an issue with synthetic blend films. This system used water as the common solvent, making the process more environmentally friendly. 10:90 *r* tropoelastin/fibroin films contained small diameter pores (pores approx. 20 – 50 nm). At 75:25 tropoelastin:fibroin *r*, pore depth (2 nm) and size (50 – 90 nm) increased. In 90:10 blends, 0.1 – 0.4 μm pores appear in the film, surrounded by smaller sub-20 nm pores. Hu suggests a morphology formation mechanism described by Reguera *et al*[139]. However, disparity between results obtained using DSC and AFM suggest segregative phase separation occurs. The statement "silk forms hydrogen bonds and becomes miscible with tropoelastin at different blend ratios without macrophase separation." contradicts the statement "the tropoelastin proteins tend to microphase-separate and formed [sic] only monomers or discontinuous small aggregates in the silk "solvent". The lack of information on casting solution pH, and unreliability of phase imaging in rough biological samples[140], would suggests the phase separation was incorrectly assigned or miscommunicated.[84] Regardless, by addition of a small amount of tropoelastin, cells adhered faster and easier, growing twice as fast with only 10% tropoelastin content. On unpatterned surfaces, cells could not easily attach and proliferate.[136]

Hu *et al* followed this paper up in 2011, testing the mechanical, topographical and biological activity of the tropoelastin/fibroin blends.[141] Increasing the ratio of tropoelastin increased surface roughness (max. roughness 90.9 nm) and decreased in stiffness (elastic modulus). Lowering the tropoelastin ratio to get low film roughness and high stiffness favoured C2C12 myoblasts. Specifically, 10% tropoelastin blend films exhibited 3 times the myogenic markers after 2 weeks, indicative of improved differentiation. Human mesenchymal stem cell proliferation and differentiation was enhanced by high surface roughness films with phase separated patterns. Osteogenic-differentiation markers were up to 8 times higher in 50% tropoelastin blends than pure fibroin films.[141] Similarly, Skopinska-Wisniewska *et al* found that blended elastin/collagen films exposed to UV-radiation induced better cell adhesion and growth attributed to the morphological and chemical properties of the blend.[142]

Lee *et al* phase separated fibroin and alginate, creating macrophase separated sponges. Incorporating alginate made the sponges suitable for wound dressing by improving physical properties and biocompatibility.[143] De Moraes evaluated fibroin/alginate blends as versatile

wound dressings. Fibrils (resulting from macroscopic phase separation) occurred at fibroin contents > 25 wt%. In 25/75 fibroin/alginate blends morphology was droplet-in-matrix. Feature SD was typical of a nucleation and growth mechanism, though the exact mechanism was not specified. The blend film was non-cytotoxic, had good permeability, and had better elongation at break and tensile strength than pure fibroin films. It is speculated that compounds could be incorporated into the fibroin domain, allowing for controlled release over a time.[144]

A possible replacement material for the synthetic biomedical PTF made by Huang *et al*[129] (**Figure 1.8**) would be non-gelling oxidized starch/gelatin blends, used to alter the texture of food.[145] Using Nady & Kandil's method[84], the gelatin could be leeched to produce a continuous porous starch matrix, while avoiding the use of a polyester. Starch scaffolds have been shown to be a suitable "mineralized bone-like extracellular matrix" due to their porous and hydrophilic nature, and have doubled the number of osteoblast cells grown, when compared to a control.[146]

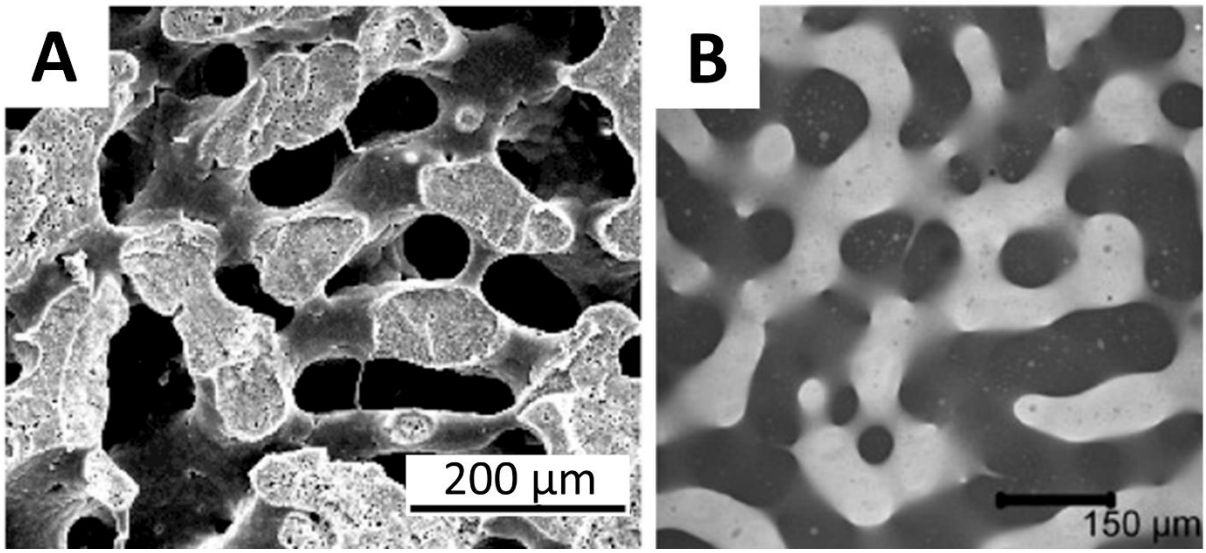


Figure 1.8: *Image **A** is a scanning electron microscope image of PCL/PLA blend annealed in CO2 at 150 °C for 60 min, with an average pore size approx. 150 µm. Adapted from Huang et al, 2017.*[129] *Image **B** shows a confocal laser scanning microscope image of gelatin/starch film thermally annealed for 30 min. Bright regions are gelatin, dark are starch. Adapted from Firoozmand et al, 2009.*[145]

Nady & Kandil produced biopolymeric PTFs for biomedical applications (cell growth and cytotoxicity assays). Chitosan and gelatin were dissolved in acetic or formic acid and mixed in the presence of a crosslinker (ferulic acid). Upon phase separation, the gelatin may be removed with 80% EtOH, acting as a porogen. The assigned phase separation mechanism

was coacervation, though this is incorrect. Both biopolymers have a net positive charge below pH 6.5.[147,148] Blend solutions pH was 2.57 for formic acid blends, and 3.95 for acetic acid blends.[84] Coacervation occurs when biopolymers of opposite charge, suspended in a supernatant, associate.[149] Both would behave as polycations in the acidic solvent, thus segregatively phase separate.[148] Rather than forming an associative complex in a supernatant, a discontinuous gelatin phase formed in a continuous chitosan matrix, indicating segregation. Though the mechanism attributed is incorrect, forming a porous matrix with this method is interesting. The tesselated array with large and small pores demonstrates the capacity to form organised hierarchal structures.[118,119] Hexagonal pores produced using hydrophilic synthetic polymers are used as cell scaffolds, greatly increasing their efficacy.[124,150] The benefits of using biopolymers outweigh the benefits of using synthetic polymers. EtOH/water is a benign solvent mixture, improving the environmental aspects of using this process. Ferulic acid use in the synthesis is also a nice inclusion, as it is antioxidizing, antimicrobial, and a by-product of wheat, sugar beet, and rice production. No effort was made to deduce the mechanism of gelatin domain growth. No cytotoxic or cell growth studies were done on these surfaces, though pore SD range seems ideal for fibroblast growth[127], and possibly hepatocytes.[128] Unlike Bui *et al*, this did not require a chlorinated solvent, or methanol, to create a honeycomb array, a much more environmentally conscious method of producing tessellated arrays.[131]

1.7. BEYOND STATE OF THE ART: PTFS

Taking PTFs beyond state of the art in all of the aforementioned industries seems, at first glance, like a daunting task. Acute research focus on biopolymeric PTF developments in each specific sector is underway. However, because of the common structural motifs of all PTFs across biomedical device, hydrophobic, smart, and antireflective surfaces, it is possible to develop research methodologies that make fundamental progress on biopolymeric PTFs which benefits all these sectors at once. This is the aim of the work detailed in this thesis.

The demands made of biopolymeric PTFs for their successful application in AR materials are the most onerous. The degrees of control required for feature scale, density, and morphology exceed those required for biomedical devices, hydrophobic surfaces, or smart materials. As such, if one can successfully meet the demands of AR materials with biopolymeric PTFs, the lesser demands of these other sectors are automatically met. This is the optimal research approach for future developments.

Ideally, future PTFs will achieve a smaller carbon footprint than those currently in use. Appropriate choice of biopolymer, solvent, environmental conditions, and film developer are how this will be achieved. Biopolymers already exist which outperform synthetic polymers in terms of price and performance.[115] Through wider adoption of biopolymers in existing technologies, economies of scale in manufacturing will reduce bulk prices of biopolymers. Alternatively, waste products from agriculture offer themselves as a cheap, renewable method of obtaining polymers. Such sources of biopolymers are easily accessible, when compared to finding (and exploiting) ever dwindling oil reserves.

As most biopolymers are water soluble, their adoption will reduce the need for organic, or chlorinated solvents. Similarly, biopolymer PTFs may be developed using enzymes, further removing the need for organic solvents. Phase separation is the greenest method for PTF production. Bottom-up processes mimic nature; nature wastes no energy, as energy is the means to survival. For manufacturing, it would mean less wasted material, while achieving ever-more complex architectures. Phase separation already provides a plethora of available morphologies. However, there is little understanding on how environmental conditions (such as humidity) play in feature formation. Furthermore, biopolymers, particularly proteins, are innately more complex than industrially produced synthetic polymers. More work needs to be conducted using solely biopolymeric blends if we are to exploit these materials for future PTFs.

Few PTFs attempt to achieve micro- and nanoscale roughness, relying mainly on a droplet-in-matrix morphology.[52,81] Deposition of a wax tubule 50 – 100 nm long may be sufficient to achieve superhydrophobicity on a bottom-up, phase separated cellulose film. Alternatively, approaches such as functionalizing the surface with natural, environmentally friendly, hydrophobic chemicals such as liquorice essential oil, cinnamic acid, or bees wax could lower SFE reducing wettability.[85,86,151]

For responsive surfaces with biological applications, materials must work within the narrow range of biological temperature and pH. Similarly, for medical applications, biocompatible biopolymers are favoured over almost universally incompatible synthetic polymers. Current research is attempting to control pore size, morphology, and develop sensing techniques for biological markers. (There is an interesting secondary application to these blends – their use as nanopatterned templates. This can be achieved using metal-PBL methods.) This technology has the potential not just for selective filtration, but release of biological payloads such as enzymes and drugs. A benefit of this technique is the protection of payloads, by sequestering it in a material that releases it with the target stimuli. Biopolymer PTFs are promising way of producing stimuli controlled devices in non-invasive, easily monitored

materials.[97] Finally, the ability to produce tessellated PTF structures could be exploited to enhance cell growth. [124]

Many biopolymer derived blends achieve the feature size demands that must be met for AR applications. Thus far, this has been mostly ignored in favour of BCP based methods that are more limited in the feature sizes that can be obtained but are a far more familiar technology to the industries involved. But the surface features needed for effective AR materials, particularly broadband AR materials, can be produced most effectively through a synthesis of nature-inspired bottom-up and artificial top-down methods: Producing biopolymer PTFs and transferring their patterns to substrates using etching techniques of synthetic polymer PTF pattern transfers. Rather than metal-PBL, this new synthesis of methods should be called "metal-bioPBL". The volumes of polymeric materials used in production of AR surfaces, even at scale, are relatively small. So the use of biopolymers, while undoubtedly making processes a little more sustainable, would not make for vast improvements in sustainability. Far greater gains will instead come from the far cleaner production methods that biopolymers permit, wherein water can used as a PTF solvent, while either pure water, buffered water, or enzymes could be used as film developers.

While the future of biopolymers in production of hydrophobic, AR, and biomedical surfaces is obvious, the route for biomedical surfaces is not as apparent. This is due to the numerous types of cells one may wish to adhere to a PTF, or repel. Each type of cell can show different preferences for PTF morphology, or blend chemistry.[133,141] However, unlike other fields, the applications of various pore sizes have been thoroughly investigated and identified for biomedical surfaces. Production of biopolymer PTFs with pores at these requisite scales has been repeatedly demonstrated, particularly in the food industry. Food texturing produces pores within the range for cell adherence, while using biocompatible materials. Phase separated biopolymers for food are well documented, with information on feature size, resistance to water, and mechanical properties. What remains is to bring together these two disparate fields of materials knowledge to produce biopolymeric materials tailored to the demands of the biomedical industry, thereby improving the future of biomedical devices.

The work presented in this thesis aims to add to the knowledge of biopolymer blends, so that they might be more easily adopted into industrial processes, and replace synthetic polymer materials. **Chapter 2** aims to determine the effect of ambient humidity and blend ratio, on the phase separation of 2 biopolymer blends, when casting with a Meyer bar. From this, a deeper understanding of biopolymeric blend systems will be gained, so that an optimum blend for surface patterning (either BSA-Ch or PG-Ch) could be used for further surface

patterning. **Chapter 3** focuses on the BSA-Ch blend. **Chapter 3** aims to form patterned BSA-Ch thin films, using spin-coating as a rapid and facile deposition technique. Here, we aimed to determine; **1)** the effect of increased spin speeds and; **2)** the effect of blend viscosity on pattern formation. Additionally, both the BSA and Ch phases are identified through selective etching and selective metal inclusion. Finally, the growth mechanism of high protein content films was evaluated, and contrasted, with high polysaccharide content films, through an analysis of feature SD's, and deconvolution of the distribution peaks. Finally, **Chapter 4** focuses on two primary areas. Firstly, the metal incorporation of **Chapter 3** is refined**,** so that biopolymer blends may be used as a template to produce hard metal masks. Secondly, the growth mechanisms of the biopolymer blend are identified, and modified, by changing casting conditions to inhibit coalescence. Through this, tessellated structures can be formed, mimicking the natural, AR morphology of butterfly wings. **Chapter 5** summarizes the findings of the previous chapters, and suggests areas which could be the primary focus of future work.

1.8. REFERENCES

(1) *OECD Science, Technology and Innovation Outlook*; 2016. https://doi.org/10.1787/sti_in_outlook-2016-en.

(2) Paul, D. R. Control of Phase Structure in Polymer Blends. In Functional Polymers; Bergbreiter, D. E., Martin, C. R., Eds.; *Springer US*: Boston, MA, 1989; pp 1–18. https://doi.org/10.1007/978-1-4613-0815-7_1.

(3) Tian, C.; Liu, Z.; Jin, J.; Lebedkin, S.; Huang, C.; You, H.; Liu, R.; Wang, L.; Song, X.; Ding, B.; Barczewski, M.; Schimmel, T.; Fang, J. Gold Mesoflower Arrays with Sub-10nm Intraparticle Gaps for Highly Sensitive and Repeatable Surface Enhanced Raman Spectroscopy. *Nanotechnology* 2012, **23** (16), Article No. 165604. https://doi.org/10.1088/0957-4484/23/16/165604.

(4) Johnston, D. E. Plasma Etch Transfer of Self-Assembled Polymer Patterns. *J. Micro/Nanolithography, MEMS, MOEMS* 2012, **11** (3), Article No. 031306. https://doi.org/10.1117/1.jmm.11.3.031306.

(5) Hopewell, J.; Dvorak, R.; Kosior, E. Plastics Recycling: Challenges and Opportunities. *Philos. Trans. R. Soc. B Biol. Sci.* 2009, **364** (1526), 2115–2126. https://doi.org/10.1098/rstb.2008.0311.

(6) Song, J. H.; Murphy, R. J.; Narayan, R.; Davies, G. B. H. Biodegradable and Compostable Alternatives to Conventional Plastics. *Philos. Trans. R. Soc. B Biol. Sci*. 2009, **364** (1526), 2127–2139. https://doi.org/10.1098/rstb.2008.0289.

(7) Ghoshal, T.; Maity, T.; Senthamaraikannan, R.; Shaw, M. T.; Carolan, P.; Holmes, J. D.; Roy, S.; Morris, M. A. Size and Space Controlled Hexagonal Arrays of Superparamagnetic Iron Oxide Nanodots: *Magnetic Studies and Application. Sci. Rep*. 2013, **3** (1), Article No. 2772. https://doi.org/10.1038/srep02772.

(8) Mokarian-Tabari, P.; Senthamaraikannan, R.; Glynn, C.; Collins, T. W.; Cummins, C.; Nugent, D.; O'Dwyer, C.; Morris, M. A. Large Block Copolymer Self-Assembly for Fabrication of Subwavelength Nanostructures for Applications in Optics. *Nano Lett.* 2017, **17** (5), 2973–2978. https://doi.org/10.1021/acs.nanolett.7b00226.

(9) Huang, C.; Moosmann, M.; Jin, J.; Heiler, T.; Walheim, S.; Schimmel, T. Polymer Blend Lithography: A Versatile Method to Fabricate Nanopatterned Self-Assembled Monolayers. Beilstein J. Nanotechnol. 2012, **3**, 620–628. https://doi.org/10.3762/bjnano.3.71.

(10) Huang, C.; Förste, A.; Walheim, S.; Schimmel, T. Polymer Blend Lithography for Metal Films: Large-Area Patterning with over 1 Billion Holes/Inch^2. *Beilstein J. Nanotechnol*. 2015, **6**, 1205–1211. https://doi.org/10.3762/bjnano.6.123.

(11) Guo, X.; Liu, L.; Zhuang, Z.; Chen, X.; Ni, M.; Li, Y.; Cui, Y.; Zhan, P.; Yuan, C.; Ge, H.; Wang, Z.; Chen, Y. A New Strategy of Lithography Based on Phase Separation of Polymer Blends. *Sci. Rep.* 2015, **5** (Article 15947). https://doi.org/10.1038/srep15947.

(12) Tokiwa, Y.; Calabia, B.; Ugwu, C.; Aiba, S.; Tokiwa, Y.; Calabia, B. P.; Ugwu, C. U.; Aiba, S. Biodegradability of Plastics. Int. *J. Mol. Sci.* 2009, **10** (9), 3722–3742. https://doi.org/10.3390/ijms10093722.

(13) Hong, M.; Chen, E. Y. X. Chemically Recyclable Polymers: A Circular Economy Approach to Sustainability. Green Chemistry. *Royal Society of Chemistry* 2017, pp 3692–3706. https://doi.org/10.1039/c7gc01496a.

(14) Muthuraj, R.; Misra, M.; Mohanty, A. K. Biodegradable Compatibilized Polymer Blends for Packaging Applications: A Literature Review. *J. Appl. Polym. Sci.* 2018, **135** (24), Article 45726. https://doi.org/10.1002/app.45726.

(15) Silva, N. H. C. S.; Vilela, C.; Marrucho, I. M.; Freire, C. S. R.; Pascoal Neto, C.; Silvestre, A. J. D. Protein-Based Materials: From Sources to Innovative Sustainable Materials for Biomedical Applications. *J. Mater. Chem.* B 2014, **2** (24), 3715–3740. https://doi.org/10.1039/c4tb00168k.

(16) Li, Q.; Niu, Y.; Xing, P.; Wang, C. Bioactive Polysaccharides from Natural Resources Including Chinese Medicinal Herbs on Tissue Repair. *Chin. Med*. 2018, **13** (7), 1–11. https://doi.org/10.1186/s13020-018-0166-0.

(17) Goettler, L. A.; Scobbo, J. J. Applications of Polymer Blends. In Polymer Blends Handbook; Utracki, L. A., Wilkie, C. A., Eds.; *Springer Netherlands: Dordrecht*, 2014; pp 1433–1458. https://doi.org/10.1007/978-94-007-6064-6_17.

(18) Laville, S.; Taylor, M. A Million Bottles a Minute: World's Plastic Binge "as Dangerous as Climate Change." *The Guardian*. 2017, June 28th.

(19) Gaylord, N. G. Compatibilizing Agents: Structure and Function in Polyblends. *J. Macromol. Sci. Part A - Chem.* 1989, **26** (8), 1211–1229. https://doi.org/10.1080/00222338908052043.

(20) Choudhary, P.; Mohanty, S.; Nayak, S. K.; Unnikrishnan, L. Poly(L-Lactide)/Polypropylene Blends: Evaluation of Mechanical, Thermal, and Morphological Characteristics. *J. Appl. Polym. Sci.* 2011, **121** (6), 3223–3237. https://doi.org/10.1002/app.33866.

(21) Yang, Z.; Dae Han, C. Rheology of Miscible Polymer Blends with Hydrogen Bonding. *Macromolecules* 2008, **41** (6), 2104–2118. https://doi.org/10.1021/ma7025385.

(22) Senichev, V. Y.; Tereshatov, V. V. Simple Solvent Characteristics. In Handbook of Solvents; Wypych, G., Ed.*; ChemTec Publishing*: Toronto, 2014; Vol. **1**, pp 117–149. https://doi.org/10.1016/B978-1-895198-64-5.50006-4.

(23) Nayak, N.; Singh, H. Milk Protein–Polysaccharide Interactions in Food Systems. *In Encyclopedia of Food Chemistry*; Melton, L., Shahidi, F., Varelis, P., Eds. 1st; *Elsevier*: Amsterdam, 2019; pp 431-438 https://doi.org/10.1016/B978-0-08-100596-5.21472-8.

(24) Tolstoguzov, V. Structure—Property Relationships in Foods. In Macromolecular Interactions in Food Technology; Parris, N., Kato, A., Creamer, L. K., Pearce, J., Eds.; *American Chemical Society*: Washington, DC, 1996; pp 2–14. https://doi.org/10.1021/bk-1996-0650.ch001.

(25) Xavier, P.; Rao, P.; Bose, S. Nanoparticle Induced Miscibility in LCST Polymer Blends: Critically Assessing the Enthalpic and Entropic Effects. *Phys. Chem. Chem. Phys.* 2016, **18** (1), 47–64. https://doi.org/10.1039/C5CP05852J.

(26) van de Velde, F.; de Hoog, E. H. A.; Oosterveld, A.; Tromp, R. H. Protein-Polysaccharide Interactions to Alter Texture. *Annu. Rev. Food Sci.* Technol. 2015, **6** (1), 371–388. https://doi.org/10.1146/annurev-food-022814-015558.

(27) Yapeng, F; Li, Liangbin; Inoue, C; Lundin, L; & Appelqvist, I. Associative and Segregative Phase Separations of Gelatin/κ-Carrageenan Aqueous Mixtures. *Languir* 2006, **22** (23). https://doi.org/10.1021/LA061865E.

(28) Kayitmazer, A. B.; Seeman, D.; Minsky, B. B.; Dubin, P. L.; Xu, Y. Protein–Polyelectrolyte Interactions. *Soft Matter* 2013, **9** (9), 2553. https://doi.org/10.1039/c2sm27002a.

(29) Turgeon, S. L.; Laneuville, S. I. Protein + Polysaccharide Coacervates and Complexes: From Scientific Background to Their Application as Functional Ingredients in Food Products. In *Modern Biopolymer Science*, Eds. 1st ; Academic Press: Cambridge, Massachusetts, 2009; pp 327–363. https://doi.org/10.1016/B978-0-12-374195-0.00011-2.

(30) Takahashi, D.; Kubota, Y.; Kokai, K.; Izumi, T.; Hirata, M.; Kokufuta, E. Effects of Surface Charge Distribution of Proteins in Their Complexation with Polyelectrolytes in an Aqueous Salt-Free System. *Langmuir* 2000, **16** (7), 3133–3140. https://doi.org/10.1021/la991108z.

(31) de Kruif, C. G.; Weinbreck, F.; de Vries, R. Complex Coacervation of Proteins and Anionic Polysaccharides. *Curr. Opin. Colloid Interface Sci*. 2004, **9** (5), 340–349. https://doi.org/10.1016/J.COCIS.2004.09.006.

(32) Li, X.; Fang, Y.; Al-Assaf, S.; Phillips, G. O.; Jiang, F. Complexation of Bovine Serum Albumin and Sugar Beet Pectin: Stabilising Oil-in-Water Emulsions. *J. Colloid Interface Sci.* 2012, **388** (1), 103–111. https://doi.org/10.1016/j.jcis.2012.08.018.

(33) Stokes, J. R. Food Biopolymer Gels, Microgel and Nanogel Structures, Formation and Rheology. In *Food Materials Science and Engineering*; Bhandari, B., Roos, Y. H., Eds.; Wiley-Blackwell: Oxford, UK, 2012; pp 151–176. https://doi.org/10.1002/9781118373903.ch6.

(34) Antonov, Y. A.; Pletenko, M. G.; Tolstoguzov, V. B. Phase State of the Systems Water-Polysaccharide-I-Polysaccharide-II. *Polym. Sci. U.S.S.R.* 1987, **29** (12), 2724–2729. https://doi.org/10.1016/0032-3950(87)90185-7.

(35) Tolstoguzov, V. Compositions and Phase Diagrams for Aqueous Systems Based on Proteins and Polysaccharides. *Int. Rev. Cytol.* 2000, **192**, 3–31.

(36) Polyakov, V. I.; Grinberg, V. Y.; Tolstoguzov, V. B. Thermodynamic Incompatibility of Proteins. *Food Hydrocoll*. 1997, **11** (2), 171–180. https://doi.org/10.1016/S0268-005X(97)80024-0.

(37) Keiji Tanaka; Atsushi Takahara, A.; Kajiyama, T. Film Thickness Dependence of the Surface Structure of Immiscible Polystyrene/Poly(Methyl Methacrylate) Blends. *Macromolecules* 1996, **29** (9), 3232–3239. https://doi.org/10.1021/MA951140+.

(38) Hirose, A.; Shimada, K.; Hayashi, C.; Nakanishi, H.; Norisuye, T.; Tran-Cong-Miyata, Q. Polymer Networks with Bicontinuous Gradient Morphologies Resulting from the Competition between Phase Separation and Photopolymerization. *Soft Matter* 2016, **12** (6), 1820–1829. https://doi.org/10.1039/c5sm02399h.

(39) Vonka, M.; Kosek, J. Modelling the Morphology Evolution of Polymer Materials Undergoing Phase Separation. *Chem. Eng. J.* 2012, **207**, 895–905. https://doi.org/10.1016/j.cej.2012.06.091.

(40) Onwulata, C. I.; Thomas-Gahring, A. E.; Phillips, J. G. Physical Properties of Mixed Dairy Food Proteins. Int. *J. Food Prop*. 2014, **17** (10), 2241–2262. https://doi.org/10.1080/10942912.2013.791836.

(41) Wolf, B.; Scirocco, R.; Frith, W. J.; Norton, I. T. Shear-Induced Anisotropic Microstructure in Phase-Separated Biopolymer Mixtures. *Food Hydrocoll*. 2000, **14** (3), 217–225. https://doi.org/10.1016/S0268-005X(99)00062-4.

(42) Tripatanasuwan, S.; Zhong, Z.; Reneker, D. H. Effect of Evaporation and Solidification of the Charged Jet in Electrospinning of Poly(Ethylene Oxide) Aqueous Solution. *Polymer (Guildf).* 2007, **48** (19), 5742–5746. https://doi.org/10.1016/J.POLYMER.2007.07.045.

(43) Sprenger, M.; Walheim, S.; Budkowski, A.; Steiner, U. Hierarchic Structure Formation in Binary and Ternary Polymer Blends. *Interface Sci.* 2003, **11** (2), 225–235. https://doi.org/10.1023/A:1022182930454.

(44) Mazeau, K. The Hygroscopic Power of Amorphous Cellulose: A Modelling Study. *Carbohydr. Polym*. 2015, **117**, 585–591. https://doi.org/10.1016/J.CARBPOL.2014.09.095.

(45) Cui, L.; Peng, J.; Ding, Y.; Li, X.; Han, Y. Ordered Porous Polymer Films via Phase Separation in Humidity Environment. Polymer (Guildf). 2005, 46 (14), 5334–5340. https://doi.org/10.1016/J.POLYMER.2005.04.018.

(46) Lhoest, J.-B.; Bertrand, P.; Weng, L. T.; Dewez, J.-L. Combined Time-of-Flight Secondary Ion Mass Spectrometry and X-Ray Photoelectron Spectroscopy Study of the Surface Segregation of Poly(Methyl Methacrylate) (PMMA) in Bisphenol A Polycarbonate/PMMA Blends. *Macromolecules* 1995, **28** (13), 4631–4637. https://doi.org/10.1021/ma00117a038.

(47) Wang, P.; Koberstein, J. T. Morphology of Immiscible Polymer Blend Thin Films Prepared by Spin-Coating. *Macromolecules* 2004, **37** (15), 5671–5681. https://doi.org/10.1021/ma049664.

(48) Huang, C. Phase Separation in Thin Polymer Films: From Self Stratification to Polymer Blend Lithography, *Darmstadt University of Technology*, 2015.

(49) Meier, T. Magnetoresistive and Thermoresistive Scanning Probe Microscopy with Applicati Ons in Micro- and Nanotechnology, *KIT Scientific Publishing*, 2014. https://doi.org/10.5445/ksp/1000042497.

(50) Trommer, K.; Morgenstern, B.; Gähr, F.; Hermanutz, F. Sub-Micrometer Structured Textile Coatings Generated From Cellulose Based Polymer Blends. *Lenzinger Berichte* 2009, **87**, 151–161.

(51) Jara, F.; Pérez, O. E.; Pilosof, A. M. R. Impact of Phase Separation of Whey Proteins/Hydroxypropylmethylcellulose Mixtures on Gelation Dynamics and Gels Properties. *Food Hydrocoll.* 2010, **24** (6–7), 641–651. https://doi.org/10.1016/J.FOODHYD.2010.03.005.

(52) Gengec, N. A.; Cengiz, U.; Erbil, H. Y. Superhydrophobic Perfluoropolymer/Polystyrene Blend Films Induced by Nonsolvent. *Appl. Surf. Sci.* 2016, **383**, 33–41. https://doi.org/10.1016/J.APSUSC.2016.04.160.

(53) Xue, L.; Zhang, J.; Han, Y. Phase Separation Induced Ordered Patterns in Thin Polymer Blend Films. *Prog. Polym. Sci.* 2012, **37** (4), 564–594. https://doi.org/10.1016/J.PROGPOLYMSCI.2011.09.001.

(54) Walheim, S.; Böltau, M.; Mlynek, J.; Georg, K.; Steiner, U. Structure Formation via Polymer Demixing in Spin-Cast Films. *Macromolecules* 1997, **30** (17), 4995–5003. https://doi.org/10.1021/MA9619288.

(55) Jones, R. A. L.; Norton, L. J.; Kramer, E. J.; Bates, F. S.; Wiltzius, P. Surface-Directed Spinodal Decomposition. *Phys. Rev. Lett.* 1991, **66** (10), 1326–1329. https://doi.org/10.1103/PhysRevLett.66.1326.

(56) Coffey, D. C.; Ginger, D. S. Patterning Phase Separation in Polymer Films with Dip-Pen Nanolithography. *J. Am. Chem. Soc.* 2005, **127** (13), 4564–4565. https://doi.org/10.1021/ja0428917.

(57) Gates, B. D.; Xu, Q.; Stewart, M.; Ryan, D.; Willson, C. G.; Whitesides, G. M. New Approaches to Nanofabrication: Molding, Printing, and Other Techniques. *Chem. Rev*. 2005, **105** (4), 1171–1196. https://doi.org/10.1021/cr030076o.

(58) Brunner, T. A. Why Optical Lithography Will Live Forever. *J. Vac. Sci. Technol. B Microelectron. Nanom. Struct.* 2003, **21** (6), 2632–2637. https://doi.org/10.1116/1.1619954.

(59) Kitayaporn, S.; Hoo, J. H.; Böhringer, K. F.; Baneyx, F.; Schwartz, D. T. Orchestrated Structure Evolution: Accelerating Direct-Write Nanomanufacturing by Combining Top-down Patterning with Bottom-up Growth. *Nanotechnology* 2010, **21** (19), 195306 (7pp). https://doi.org/10.1088/0957-4484/21/19/195306.

(60) Favvas, E. P.; Mitropoulos, A. C. What Is Spinodal Decomposition? *J. Eng. Sci. Technol. Rev*. 2008, **1** (1), 25–27. https://doi.org/10.25103/jestr.011.05.

(61) Van De Witte, P.; Dijkstra, P. J.; Van Den Berg, J. W. A.; Feijen, J. Phase Separation Processes in Polymer Solutions in Relation to Membrane Formation. Elsevier *J. Membr. Sci.* 1996, 117, 1–31.

(62) Sperling, L. H. Concentrated Solutions, Phase Separation Behavior, and Diffusion. In Introduction to Physical Polymer Science; *John Wiley & Sons, Inc.*: Hoboken, NJ, USA, 2005; pp 145–195. https://doi.org/10.1002/0471757128.ch4.

(63) Kelley, E. G.; Murphy, R. P.; Seppala, J. E.; Smart, T. P.; Hann, S. D.; Sullivan, M. O.; Epps, T. H. Size Evolution of Highly Amphiphilic Macromolecular Solution Assemblies via a Distinct Bimodal Pathway. *Nat. Commun.* 2014, **5** (1), 3599. https://doi.org/10.1038/ncomms4599.

(64) Wallecan, J.; McCrae, C.; Debon, S. J. J.; Dong, J.; Mazoyer, J. Emulsifying and Stabilizing Properties of Functionalized Orange Pulp Fibers. *Food Hydrocoll*. 2015, **47**, 115–123. https://doi.org/10.1016/J.FOODHYD.2015.01.009.

(65) Shih, C.-Y.; Streubel, R.; Heberle, J.; Letzel, A.; Shugaev, M. V.; Wu, C.; Schmidt, M.; Gökce, B.; Barcikowski, S.; Zhigilei, L. V. Two Mechanisms of Nanoparticle Generation in Picosecond Laser Ablation in Liquids: The Origin of the Bimodal Size Distribution. *Nanoscale* 2018, **10** (15), 6900–6910. https://doi.org/10.1039/C7NR08614H.

(66) Madras, G.; McCoy, B. J. Distribution Kinetics of Ostwald Ripening at Large Volume Fraction and with Coalescence. *J. Colloid Interface Sci.* 2003, **261** (2), 423–433. https://doi.org/10.1016/S0021-9797(03)00129-2.

(67) Dimitrova, L. M.; Boneva, M. P.; Danov, K. D.; Kralchevsky, P. A.; Basheva, E. S.; Marinova, K. G.; Petkov, J. T.; Stoyanov, S. D. Limited Coalescence and Ostwald Ripening in Emulsions Stabilized by Hydrophobin HFBII and Milk Proteins. *Colloids Surfaces A Physicochem. Eng. Asp.* 2016, **509**, 521–538. https://doi.org/10.1016/J.COLSURFA.2016.09.066.

(68) Zeeb, B.; Mi-Yeon, L.; Gibis, M.; Weiss, J. Growth Phenomena in Biopolymer Complexes Composed of Heated WPI and Pectin. *Food Hydrocoll.* 2018, **74**, 53–61. https://doi.org/10.1016/J.FOODHYD.2017.07.026.

(69) Filippone, G.; Netti, P. A.; Acierno, D. Microstructural Evolutions of LDPE/PA6 Blends by Rheological and Rheo-Optical Analyses: Influence of Flow and Compatibilizer on Break-up and Coalescence Processes. *Polymer (Guildf).* 2007, **48** (2), 564–573. https://doi.org/10.1016/j.polymer.2006.11.050.

(70) Jůza, J.; Fortelný, I. Flow-Induced Coalescence: Evaluation of Some Approximations. *Macromol. Symp.* 2017, **373** (1), 1–10. https://doi.org/10.1002/masy.201600097.

(71) Hu, X.; Cebe, P.; Weiss, A. S.; Omenetto, F.; Kaplan, D. L. Protein-Based Composite Materials. *Mater. Today* 2012, **15** (5), 208–215. https://doi.org/10.1016/S1369-7021(12)70091-3.

(72) Li, X.-M.; Reinhoudt, D.; Crego-Calama, M. What Do We Need for a Superhydrophobic Surface? A Review on the Recent Progress in the Preparation of Superhydrophobic Surfaces. *Chem. Soc. Rev.* 2007, **36** (8), 1350–1368. https://doi.org/10.1039/b602486f.

(73) Il'darkhanova, F. I.; Mironova, G. A.; Bogoslovsky, K. G.; Men'shikov, V. V.; Bykov, E. D. Development of Paint Coatings with Superhydrophobic Properties. *Prot. Met. Phys. Chem. Surfaces* 2012, **48** (7), 796–802. https://doi.org/10.1134/S2070205112070076.

(74) Ramaratnam, K.; Iyer, S. K.; Kinnan, M. K.; Chumanov, G.; Brown, P. J.; Luzinov, I. Ultrahydrophobic Textiles Using Nanoparticles: Lotus Approach. *J. Eng. Fiber. Fabr*. 2008, **3** (4), 1–14. https://doi.org/10.1177/155892500800300402.

(75) Contact Angle Goniometry. In Surface Design: Applications in Bioscience and Nanotechnology; Forch, R., Shonherr, H., Jenkins, A. T. A., Eds.; *Wiley-VCH Verlag GmbH & Co. KGaA*: Weinheim, 2009; pp 471–473.

(76) Ensikat, H. J.; Ditsche-Kuru, P.; Neinhuis, C.; Barthlott, W. Superhydrophobicity in Perfection: The Outstanding Properties of the Lotus Leaf. *Beilstein J. Nanotechnol*. 2011, **2** (1), 152–161. https://doi.org/10.3762/bjnano.2.19.

(77) López, A. B.; De La Cal, J. C.; Asua, J. M. Highly Hydrophobic Coatings from Waterborne Latexes. *Langmuir* 2016, **32** (30), 7459–7466. https://doi.org/10.1021/acs.langmuir.6b01072.

(78) Wei, Z. J.; Liu, W. L.; Tian, D.; Xiao, C. L.; Wang, X. Q. Preparation of Lotus-like Superhydrophobic Fluoropolymer Films. *Appl. Surf. Sci.* 2010, **256** (12), 3972–3976. https://doi.org/10.1016/J.APSUSC.2010.01.059.

(79) López, A. B.; de la Cal, J. C.; Asua, J. M. Controlling Film Topography to Form Highly Hydrophobic Waterborne Coatings. *Soft Matter* 2016, **12** (33), 7005–7011. https://doi.org/10.1039/C6SM01081D.

(80) Vargas-Alfredo, N.; Rodríguez Hernández, J. Microstructured Polymer Blend Surfaces Produced by Spraying Functional Copolymers and Their Blends. *Mater*. 2016, **9** (6), Article 431. https://doi.org/10.3390/ma9060431.

(81) Kato, S.; Sato, A. Micro/Nanotextured Polymer Coatings Fabricated by UV Curing-Induced Phase Separation: Creation of Superhydrophobic Surfaces. *J. Mater. Chem*. 2012, **22** (17), 8613–8621. https://doi.org/10.1039/c2jm16675e.

(82) Czibula, C.; Teichert, G.; Nau, M.; Hobisch, M.; Palasingh, C.; Biesalski, M.; Spirk, S.; Teichert, C.; Nypelö, T. Design of Friction, Morphology, Wetting, and Protein Affinity by Cellulose Blend Thin Film Composition. *Front. Chem.* 2019, **7** (Article 239), 1–10. https://doi.org/10.3389/fchem.2019.00239.

(83) Ahmad, M.; Nirmal, N. P.; Chuprom, J. Blend Film Based on Fish Gelatine/Curdlan for Packaging Applications: Spectral, Microstructural and Thermal Characteristics. *RSC Adv.* 2015, **5** (120), 99044–99057. https://doi.org/10.1039/C5RA20925K.

(84) Nady, N.; Kandil, S. H. Novel Blend for Producing Porous Chitosan-Based Films Suitable for Biomedical Applications. *Membranes (Basel).* 2018, **8** (1), 1–18. https://doi.org/10.3390/membranes8010002.

(85) Jafari, S. M.; Khanzadi, M.; Mirzaei, H.; Dehnad, D.; Chegini, F. K.; Maghsoudlou, Y. Hydrophobicity, Thermal and Micro-Structural Properties of Whey Protein Concentrate-Pullulan-Beeswax Films. *Int. J. Biol. Macromol.* 2015, **80**, 506–511. https://doi.org/10.1016/j.ijbiomac.2015.07.017.

(86) Luís, Â.; Domingues, F.; Ramos, A. Production of Hydrophobic Zein-Based Films Bioinspired by The Lotus Leaf Surface: Characterization and Bioactive Properties. *Microorganisms* 2019, **7** (8), Article No. 267. https://doi.org/10.3390/microorganisms7080267.

(87) Hoeger, I. C.; Filpponen, I.; Martin-Sampedro, R.; Johansson, L.-S.; Österberg, M.; Laine, J.; Kelley, S.; Rojas, O. J. Bicomponent Lignocellulose Thin Films to Study the Role of Surface Lignin in Cellulolytic Reactions. *Biomacromolecules* 2012, **13** (10), 3228–3240. https://doi.org/10.1021/bm301001q.

(88) Taajamaa, L.; Rojas, O. J.; Laine, J.; Kontturi, E. Phase-Specific Pore Growth in Ultrathin Bicomponent Films from Cellulose-Based Polysaccharides. *Soft Matter* 2011, **7** (21), 10386. https://doi.org/10.1039/c1sm06020a.

(89) Mohan, T.; Nagaraj, C.; Nagy, B. M.; Bračič, M.; Maver, U.; Olschewski, A.; Stana Kleinschek, K.; Kargl, R. Nano- and Micropatterned Polycaprolactone Cellulose Composite Surfaces with Tunable Protein Adsorption, Fibrin Clot Formation, and Endothelial Cellular Response. *Biomacromolecules* 2019, **20** (6), 2327–2337. https://doi.org/10.1021/acs.biomac.9b00304.

(90) Niegelhell, K.; Su, M.; Jammernegg, K.; Ganner, T.; Schwendenwein, D.; Schwab, H.; Stelzer, F.; Plank, H.; Spirk, S. Enzymes as Biodevelopers for Nano- And Micropatterned Bicomponent Biopolymer Thin Films. *Biomacromolecules* 2016, **17** (11), 3743–3749. https://doi.org/10.1021/acs.biomac.6b01263.

(91) Schacher, F.; Ulbricht, M.; Müller, A. H. E. Self-Supporting, Double Stimuli-Responsive Porous Membranes From Polystyrene- Block -Poly(N , N -Dimethylaminoethyl Methacrylate) Diblock Copolymers. *Adv. Funct. Mater*. 2009, **19** (7), 1040–1045. https://doi.org/10.1002/adfm.200801457.

(92) Tokarev, I.; Orlov, M.; Minko, S. Responsive Polyelectrolyte Gel Membranes. *Adv. Mater*. 2006, **18** (18), 2458–2460. https://doi.org/10.1002/adma.200601288.

(93) Orlov, M.; Tokarev, I.; Scholl, A.; Doran, A.; Minko, S. PH-Responsive Thin Film Membranes from Poly(2-Vinylpyridine): Water Vapor-Induced Formation of a Microporous Structure. *Macromolecules* 2007, **40** (6), 2086–2091. https://doi.org/10.1021/MA062821F.

(94) Tokarev, I.; Tokareva, I.; Minko, S. Gold-Nanoparticle-Enhanced Plasmonic Effects in a Responsive Polymer Gel. *Adv. Mater.* 2008, **20** (14), 2730–2734. https://doi.org/10.1002/adma.200702885.

(95) Tokarev, I.; Tokareva, I.; Gopishetty, V.; Katz, E.; Minko, S. Specific Biochemical-to-Optical Signal Transduction by Responsive Thin Hydrogel Films Loaded with Noble Metal Nanoparticles. *Adv. Mater.* 2010, **22** (12), 1412–1416. https://doi.org/10.1002/adma.200903456.

(96) Gopishetty, V.; Roiter, Y.; Tokarev, I.; Minko, S. Multiresponsive Biopolyelectrolyte Membrane. *Adv. Mater*. 2008, **20** (23), 4588–4593. https://doi.org/10.1002/adma.200801610.

(97) Kuroki, H.; Tokarev, I.; Minko, S. Responsive Surfaces for Life Science Applications. *Annu. Rev. Mater. Res.* 2012, **42** (1), 343–372. https://doi.org/10.1146/annurev-matsci-070511-155044.

(98) Tokarev, I.; Orlov, M.; Katz, E.; Minko, S. An Electrochemical Gate Based on a Stimuli-Responsive Membrane Associated with an Electrode Surface. *J. Phys. Chem. B* 2007, **111** (42), 12141–12145. https://doi.org/10.1021/JP0757208.

(99) Tokarev, I.; Gopishetty, V.; Minko, S. Highly Porous 3D Fibrous Nanostructured Bioplolymer Films with Stimuli-Responsive Porosity via Phase Separation in Polymer Blend. *ACS Appl. Mater. Interfaces* 2015, **7** (23), 12463–12469. https://doi.org/10.1021/am5076327.

(100) Han, Z. W.; Wang, Z.; Feng, X. M.; Li, B.; Mu, Z. Z.; Zhang, J. Q.; Niu, S. C.; Ren, L. Q. Antireflective Surface Inspired from Biology: A Review. *Biosurface and Biotribology* 2016, **2** (4), 137–150. https://doi.org/10.1016/J.BSBT.2016.11.002.

(101) Stavenga, D. G.; Foletti, S.; Palasantzas, G.; Arikawa, K. Light on the Moth-Eye Corneal Nipple Array of Butterflies. *Proc. R. Soc. B Biol. Sci*. 2006, **273** (1587), 661–667. https://doi.org/10.1098/rspb.2005.3369.

(102) Han, Z.; Li, B.; Mu, Z.; Yang, M.; Niu, S.; Zhang, J.; Ren, L. An Ingenious Super Light Trapping Surface Templated from Butterfly Wing Scales. *Nanoscale Res. Lett*. 2015, **10** (1), Article Number: 344. https://doi.org/10.1186/s11671-015-1052-7.

(103) Diao, Z.; Hirte, J.; Chen, W.; Spatz, J. P. Inverse Moth Eye Nanostructures with Enhanced Antireflection and Contamination Resistance. *ACS Omega* 2017, **2** (8), 5012–5018. https://doi.org/10.1021/acsomega.7b01001.

(104) Zhao, Q.; Guo, X.; Fan, T.; Ding, J.; Zhang, D.; Guo, Q. Art of Blackness in Butterfly Wings as Natural Solar Collector. *Soft Matter* 2011, **7** (24), 11433–11439. https://doi.org/10.1039/c1sm06167d.

(105) Zhang, W.; Zhang, D.; Fan, T.; Gu, J.; Ding, J.; Wang, H.; Guo, Q.; Ogawa, H. Novel Photoanode Structure Templated from Butterfly Wing Scales. *Chem. Mater*. 2009, **21** (1), 33–40. https://doi.org/10.1021/cm702458p.

(106) Zhang, Z.; Yu, K.; Lou, L.; Yin, H.; Li, B.; Zhu, Z. Morphology-Controlled Synthesis of ZnO Replicas with Photonic Structures from Butterfly (Papilio Paris) Wing Scales for Tunable Optical Properties. Nanoscale 2012, **4** (8), 2606. https://doi.org/10.1039/c2nr30284e.

(107) Siddique, R. H.; Donie, Y. J.; Gomard, G.; Yalamanchili, S.; Merdzhanova, T.; Lemmer, U.; Hölscher, H. Bioinspired Phase-Separated Disordered Nanostructures for Thin Photovoltaic Absorbers. *Sci. Adv.* 2017, **3** (10), e1700232. https://doi.org/10.1126/sciadv.1700232.

(108) Liu, H.; QibinZhao; Zhou, H.; Ding, J.; Zhang, D.; Zhu, H.; Fan, T. Hydrogen Evolution via Sunlight Water Splitting on an Artificial Butterfly Wing Architecture. Phys. Chem. Chem. Phys. 2011, **13** (23), 10872. https://doi.org/10.1039/c1cp20787c.

(109) Jaczewska, J.; Budkowski, A.; Bernasik, A.; Raptis, I.; Moons, E.; Goustouridis, D.; Haberko, J.; Rysz, J. Ordering Domains of Spin Cast Blends of Conjugated and Dielectric Polymers on Surfaces Patterned by Soft- and Photo-Lithography. *Soft Matter* 2009, **5** (1), 234–241. https://doi.org/10.1039/B811429C.

(110) Creedon, N. C.; Lovera, P.; Furey, A.; O'Riordan, A. Transparent Polymer-Based SERS Substrates Templated by a Soda Can. *Sensors Actuators B Chem*. 2018, **259**, 64–74. https://doi.org/10.1016/j.snb.2017.12.039.

(111) Donie, Y. J.; Smeets, M.; Egel, A.; Lentz, F.; Preinfalk, J. B.; Mertens, A.; Smirnov, V.; Lemmer, U.; Bittkau, K.; Gomard, G. Light Trapping in Thin Film Silicon Solar Cells via Phase Separated Disordered Nanopillars. *Nanoscale* 2018, **10** (14), 6651–6659. https://doi.org/10.1039/C8NR00455B.

(112) Taajamaa, L.; Rojas, O. J.; Laine, J.; Yliniemi, K.; Kontturi, E. Protein-Assisted 2D Assembly of Gold Nanoparticles on a Polysaccharide Surface. *Chem. Commun*. 2013, **49** (13), 1318–1320. https://doi.org/10.1039/c2cc37288f.

(113) Gopishetty, V.; Tokarev, I.; Minko, S. Biocompatible Stimuli-Responsive Hydrogel Porous Membranes via Phase Separation of a Polyvinyl Alcohol and Na-Alginate Intermolecular Complex. *J. Mater. Chem*. 2012, **22** (37), 19482–19487. https://doi.org/10.1039/c2jm31778h.

(114) Caillau, M.; Crémillieu, P.; Laurenceau, E.; Chevolot, Y.; Leclercq, J.-L.; Alekseev, S.; Chevalier, C.; Delair, T. Fifty Nanometer Lines Patterned into Silica Using Water Developable Chitosan Bioresist and Electron Beam Lithography. *J. Vac. Sci. Technol. B Nanotechnol.*

Microelectron. Mater. Process. Meas. Phenom. 2017, **35** (60GE01). https://doi.org/10.1116/1.4996870.

(115) Jiang, B.; Yang, J.; Li, C.; Zhang, L.; Zhang, X.; Yang, P. Water-Based Photo- and Electron-Beam Lithography Using Egg White as a Resist. *Adv. Mater. Interfaces* 2017, **4** (7), Article No. 1601223. https://doi.org/10.1002/admi.201601223.

(116) Pal, R. K.; Yadavalli, V. K. Silk Protein Nanowires Patterned Using Electron Beam Lithography. *Nanotechnology* 2018, **29** (33), 335301. https://doi.org/10.1088/1361-6528/aac855.

(117) Kim, S.; Marelli, B.; Brenckle, M. A.; Mitropoulos, A. N.; Gil, E.-S.; Tsioris, K.; Tao, H.; Kaplan, D. L.; Omenetto, F. G. All-Water-Based Electron-Beam Lithography Using Silk as a Resist. *Nat. Nanotechnol*. 2014, **9** (4), 306–310. https://doi.org/10.1038/nnano.2014.47.

(118) Wang, X.; Xu, S.; Zhou, S.; Xu, W.; Leary, M.; Choong, P.; Qian, M.; Brandt, M.; Xie, Y. M. Topological Design and Additive Manufacturing of Porous Metals for Bone Scaffolds and Orthopaedic Implants: A Review. *Biomaterials* 2016, **83**, 127–141. https://doi.org/10.1016/j.biomaterials.2016.01.012.

(119) Wegst, U. G. K.; Bai, H.; Saiz, E.; Tomsia, A. P.; Ritchie, R. O. Bioinspired Structural Materials. *Nat. Mater*. 2015, **14** (1), 23–36. https://doi.org/10.1038/nmat4089.

(120) Tampieri, A.; Sprio, S.; Ruffini, A.; Celotti, G.; Lesci, I. G.; Roveri, N. From Wood to Bone: Multi-Step Process to Convert Wood Hierarchical Structures into Biomimetic Hydroxyapatite Scaffolds for Bone Tissue Engineering. *J. Mater. Chem*. 2009, **19** (28), 4973. https://doi.org/10.1039/b900333a.

(121) Filardo, G.; Kon, E.; Tampieri, A.; Cabezas-Rodríguez, R.; Di Martino, A.; Fini, M.; Giavaresi, G.; Lelli, M.; Martínez-Fernández, J.; Martini, L.; Ramírez-Rico, J.; Salamanna, F.; Sandri, M.; Sprio, S.; Marcacci, M. New Bio-Ceramization Processes Applied to Vegetable Hierarchical Structures for Bone Regeneration: An Experimental Model in Sheep. *Tissue Eng. - Part A* 2014, **20** (3–4), 763–773. https://doi.org/10.1089/ten.tea.2013.0108.

(122) Kumar, L.; Brice, J.; Toberer, L.; Klein-Seetharaman, J.; Knauss, D.; Sarkar, S. K. Antimicrobial Biopolymer Formation from Sodium Alginate and Algae Extract Using Aminoglycosides. *PLOS One* 2019, **14** (3), e0214411. https://doi.org/10.1371/journal.pone.0214411.

(123) Janik, H.; Marzec, M. A Review: Fabrication of Porous Polyurethane Scaffolds. Mater. *Sci. Eng. C* 2015, **48** (1), 586–591. https://doi.org/10.1016/J.MSEC.2014.12.037.

(124) Fukuhira, Y.; Kitazono, E.; Hayashi, T.; Kaneko, H.; Tanaka, M.; Shimomura, M.; Sumi, Y. Biodegradable Honeycomb-Patterned Film Composed of Poly(Lactic Acid) and

Dioleoylphosphatidylethanolamine. *Biomaterials* 2006, **27** (9), 1797–1802. https://doi.org/10.1016/j.biomaterials.2005.10.019.

(125) Hollister, S. J. Porous Scaffold Design for Tissue Engineering. *Nat. Mater*. 2005, **4** (7), 518–524. https://doi.org/10.1038/nmat1421.

(126) Khoda, A. K. M. B.; Koc, B. Functionally Heterogeneous Porous Scaffold Design for Tissue Engineering. *Comput. Des*. 2013, **45** (11), 1276–1293. https://doi.org/10.1016/j.cad.2013.05.005.

(127) Guarino, V.; Ambrosio, L. Temperature-Driven Processing Techniques for Manufacturing Fully Interconnected Porous Scaffolds in Bone Tissue Engineering. Proc. Inst. Mech. *Eng. Part H J. Eng. Med*. 2010, **224** (12), 1389–1400. https://doi.org/10.1243/09544119JEIM744.

(128) Sarazin, P.; Roy, X.; Favis, B. D. Controlled Preparation and Properties of Porous Poly(l-Lactide) Obtained from a Co-Continuous Blend of Two Biodegradable Polymers. *Biomaterials* 2004, **25** (28), 5965–5978. https://doi.org/10.1016/j.biomaterials.2004.01.065.

(129) Huang, E.; Liao, X.; He, Y.; He, B.; Yang, Q.; Li, G. A Novel Route to the Generation of Porous Scaffold Based on the Phase Morphology Control of Co-Continuous Poly(ε-Caprolactone)/Polylactide Blend in Supercritical CO_2. *Polymer (Guildf)*. 2017, **118**, 163–172. https://doi.org/10.1016/J.POLYMER.2017.04.065.

(130) Moura, N. K. de; Siqueira, I. A. W. B.; Machado, J. P. de B.; Kido, H. W.; Avanzi, I. R.; Rennó, A. C. M.; Trichês, E. de S.; Passador, F. R. Production and Characterization of Porous Polymeric Membranes of PLA/PCL Blends with the Addition of Hydroxyapatite. *J. Compos. Sci*. 2019, **3** (2), Article No. 45. https://doi.org/10.3390/jcs3020045.

(131) Bui, V.-T.; Thuy, L. T.; Tran, Q. C.; Nguyen, V.-T.; Dao, V. D.; Choi, J. S.; Choi, H.-S. Ordered Honeycomb Biocompatible Polymer Films via a One-Step Solution-Immersion Phase Separation Used as a Scaffold for Cell Cultures. *Chem. Eng. J*. 2017, **320**, 561–569. https://doi.org/10.1016/j.cej.2017.03.086.

(132) Pulieri, E.; Chiono, V.; Ciardelli, G.; Vozzi, G.; Ahluwalia, A.; Domenici, C.; Vozzi, F.; Giusti, P. Chitosan/Gelatin Blends for Biomedical Applications. *J. Biomed. Mater. Res. - Part A* 2008, **86** (2), 311–322. https://doi.org/10.1002/jbm.a.31492.

(133) Zhang, H.; Jiao, J.; Jin, H. Degradable Poly-L-Lysine-Modified PLGA Cell Microcarriers with Excellent Antibacterial and Osteogenic Activity. *Artif. Cells, Nanomedicine, Biotechnol*. 2019, **47** (1), 2391–2404. https://doi.org/10.1080/21691401.2019.1623230.

(134) Peschel, G.; Dahse, H.-M.; Konrad, A.; Wieland, G. D.; Mueller, P.-J.; Martin, D. P.; Roth, M. Growth of Keratinocytes on Porous Films of Poly(3-Hydroxybutyrate) and Poly(4-Hydroxybutyrate) Blended with Hyaluronic Acid and Chitosan. *J. Biomed. Mater. Res. Part A* 2008, 85A (4), 1072–1081. https://doi.org/10.1002/jbm.a.31666.

(135) Mahato, K. K.; Yadav, I.; Singh, R.; Monika; Singh, B. N.; Singh, S. K.; Ray, B.; Kumar, M.; Misra, N. Polyvinyl Alcohol/Chitosan Lactate Composite Hydrogel for Controlled Drug Delivery. *Mater. Res. Express* 2019, **6** (11), Article No. 115408. https://doi.org/10.1088/2053-1591/AB4FBD.

(136) Hu, X.; Wang, X.; Rnjak, J.; Weiss, A. S.; Kaplan, D. L. Biomaterials Derived from Silk–Tropoelastin Protein Systems. *Biomaterials* 2010, **31** (32), 8121–8131. https://doi.org/10.1016/j.biomaterials.2010.07.044.

(137) Baldock, C.; Oberhauser, A. F.; Ma, L.; Lammie, D.; Siegler, V.; Mithieux, S. M.; Tu, Y.; Chow, J. Y. H.; Suleman, F.; Malfois, M.; Rogers, S.; Guo, L.; Irving, T. C.; Wess, T. J.; Weiss, A. S. Shape of Tropoelastin, the Highly Extensible Protein That Controls Human Tissue Elasticity. *Proc. Natl. Acad. Sci. U. S. A.* 2011, **108** (11), 4322–43277. https://doi.org/10.1073/pnas.1014280108.

(138) Koh, L.-D.; Cheng, Y.; Teng, C.-P.; Khin, Y.-W.; Loh, X.-J.; Tee, S.-Y.; Low, M.; Ye, E.; Yu, H.-D.; Zhang, Y.-W.; Han, M.-Y. Structures, Mechanical Properties and Applications of Silk Fibroin Materials. *Prog. Polym. Sci.* 2015, **46**, 86–110. https://doi.org/10.1016/J.PROGPOLYMSCI.2015.02.001.

(139) Reguera, J.; Fahmi, A.; Moriarty, P.; Girotti, A.; Carlos Rodríguez-Cabello, J. Nanopore Formation by Self-Assembly of the Model Genetically Engineered Elastin-like Polymer [(VPGVG)2(VPGEG)(VPGVG)2]15. *J. AM. CHEM. SOC* 2004, **126** (41), 13212–13213. https://doi.org/10.1021/ja047417f.

(140) YE, Z.; ZHAO, X. Phase Imaging Atomic Force Microscopy in the Characterization of Biomaterials. *J. Microsc.* 2010, **238** (1), 27–35. https://doi.org/10.1111/j.1365-2818.2009.03282.x.

(141) Hu, X.; Park, S.-H.; Gil, E. S.; Xia, X.-X.; Weiss, A. S.; Kaplan, D. L. The Influence of Elasticity and Surface Roughness on Myogenic and Osteogenic-Differentiation of Cells on Silk-Elastin Biomaterials. *Biomaterials* 2011, **32** (34), 8979–8989. https://doi.org/10.1016/J.BIOMATERIALS.2011.08.037.

(142) Skopinska-Wisniewska, J.; Sionkowska, A.; Kaminska, A.; Kaznica, A.; Jachimiak, R.; Drewa, T. Surface Characterization of Collagen/Elastin Based Biomaterials for Tissue

Regeneration. *Appl. Surf. Sci*. 2009, **255** (19), 8286–8292. https://doi.org/10.1016/J.APSUSC.2009.05.127.

(143) Lee, K.-G.; Kweon, H.; Yeo, J.-H.; Woo, S.-O.; Lee, J.-H.; Hwan Park, Y. Structural and Physical Properties of Silk Fibroin/Alginate Blend Sponges. *J. Appl. Polym. Sci*. 2004, **93** (5), 2174–2179. https://doi.org/10.1002/app.20714.

(144) de Moraes, M. A.; Silva, M. F.; Weska, R. F.; Beppu, M. M. Silk Fibroin and Sodium Alginate Blend: Miscibility and Physical Characteristics. *Mater. Sci. Eng. C* 2014, **40**, 85–91. https://doi.org/10.1016/J.MSEC.2014.03.047.

(145) Firoozmand, H.; Murray, B. S.; Dickinson, E. Microstructure and Rheology of Phase-Separated Gels of Gelatin+oxidized Starch. *Food Hydrocoll*. 2009, **23** (4), 1081–1088. https://doi.org/10.1016/j.foodhyd.2008.07.013.

(146) Aidun, A.; Zamanian, A.; Ghorbani, F. Novel Bioactive Porous Starch-Siloxane Matrix for Bone Regeneration: Physicochemical, Mechanical, and in Vitro Properties. *Biotechnol. Appl. Biochem*. 2019, 66 (1), 43–52. https://doi.org/10.1002/bab.1694.

(147) Van Vlierberghe, S.; Graulus, G.-J.; Keshari Samal, S.; Van Nieuwenhove, I.; Dubruel, P. Porous Hydrogel Biomedical Foam Scaffolds for Tissue Repair. In Biomedical Foams for Tissue Engineering Applications; Netti, P. A., Ed.; *Woodhead Publishing*, 2014; pp 335–390. https://doi.org/10.1533/9780857097033.2.335.

(148) Popat, A.; Liu, J.; Lu, G. Q.; Qiao, S. Z. A. PH-Responsive Drug Delivery System Based on Chitosan Coated Mesoporous Silica Nanoparticles. *J. Mater. Chem*. 2012, **22** (22), 11173–11178. https://doi.org/10.1039/c2jm30501a.

(149) Pathak, J.; Priyadarshini, E.; Rawat, K.; Bohidar, H. B. Complex Coacervation in Charge Complementary Biopolymers: Electrostatic versus Surface Patch Binding. *Adv. Colloid Interface Sci*. 2017, **250**, 40–53. https://doi.org/10.1016/j.cis.2017.10.006.

(150) Li, L.; Chen, C.; Li, J.; Zhang, A.; Liu, X.; Xu, B.; Gao, S.; Jin, G.; Ma, Z. Robust and Hydrophilic Polymeric Films with Honeycomb Pattern and Their Cell Scaffold Applications. *J. Mater. Chem*. 2009, **19** (18), 2789–2796. https://doi.org/10.1039/b820279f.

(151) Razavi, S. M. R.; Oh, J.; Sett, S.; Feng, L.; Yan, X.; Hoque, M. J.; Liu, A.; Haasch, R. T.; Masoomi, M.; Bagheri, R.; Miljkovic, N. Superhydrophobic Surfaces Made from Naturally Derived Hydrophobic Materials. *ACS Sustain. Chem. Eng*. 2017, **5** (12), 11362–11370. https://doi.org/10.1021/acssuschemeng.7b02424.

Chapter 2

Nanopatterned Protein-Polysaccharide Thin Films by Humidity Regulated Phase Separation

Published in:

Journal of Colloid and Interface Science 532 (2018) 171–181

2.1. ABSTRACT

Greater sustainability in mass manufacturing is essential to alleviating anthropogenic climate change. High surface-area, micro- and nano-patterned films have become a fundamental tool in materials science, however, these technologies are subject to a dwindling petrochemical supply, increasing costs and disposability concerns. This paper describes the production of patterned biopolymer films utilizing controlled phase separation of biopolymeric thin films into nanopatterns using easily transferable variables and methods. Similar morphologies to those commonly observed with synthetic block-copolymers (BCPs) were achieved across a large range of feature sizes, from 160 nm to > 5 μm: bicontinuous, porous, droplet-matrix, particulated and dimpled. Protein and polysaccharide type, protein to polysaccharide ratio, casting method and ambient humidity were primary conditions found to influence the pore morphology of the films. High protein concentrations (4:1 and 2:1 blends) generally resulted in porous structures whereas high polysaccharide concentrations (1:2 and 1:4 blends) resulted in spherical structures. High humidity conditions (60% + relative humidity) resulted in the growth of large protuberances up to 10 μm in diameter while lower humidity (10% - 30%) resulted in discrete features smaller than 200 nm.

2.2 INTRODUCTION

Sustainable materials is a term that encompasses a sustainable, materials science based approach to technological development and product lifecycles. It focusses on bottom-up production methods; biodegradable, renewably sourced materials; and environmentally benign usage. The development of technologies from sustainable sources is essential to minimising negative anthropogenic effects on environment and climate. Resource finitude; waste management; and production and usage emissions need to be addressed. Our most crucial technologies must be prioritised for the initial developments of these new, sustainable materials.

Electronic and smart devices, and advanced medical materials; these are among our most vital modern technologies. High surface-area, micro- and nano-patterned films are fundamental to the manufacture and function of the aforementioned technologies, as well as finding widespread use in a variety of other applications. Apart from semiconductor[1] and medical technology[2], they are critical to superhydrophobic[3], anti-reflective[4,5] and self-cleaning materials[5]; anti-fouling coatings; and food texture technologies[6] (which will be of increasing importance as more and more synthetic food equivalents are required to replace

environmentally unsustainable foodstuffs).[7] The patterns are produced through phase separation of highly refined, synthetic, block-copolymer thin-films.[8] These polymers are a perfect example of a long term, unsustainable material. Sourced from petrochemicals, they will become prohibitively expensive with time, they are non-renewable, non-biodegradable, and the refinement processes of their production are environmentally damaging. Our research shows the development of a sustainable materials alternative; bottom-up production of patterned films from renewable, biodegradable biopolymers.

Biopolymers (proteins and polysaccharides primarily) are an ideal sustainable material, and an obvious alternative to conventional, petrochemical polymers in all but the most specialised applications.[9] They are abundant, readily accessible, renewable, compostable and; produced and extracted with minimal to no environmental impact.[10] Biopolymers also have a suite of attractive features for manufacturers; high structural specificity; well-defined and varied functionalities; structure dependant solubility[11]; predictable viscosity[12]; bactericidal properties[13]; and biocompatibility.[14] Molecular weight distributions of polysaccharides can vary[15] but are readily refined[16] and in the case of proteins, monodisperse molecular weight distribution is an innate property. For all the above reasons, naturally occurring biopolymers have interested scientists and engineers for decades. They are used in food texturing[17], personal care products[18], cell binding[19], textiles[20] and membranes.[21,22,23] Many of these applications involve patterning of biopolymer surfaces; though the structures obtained have so far been much larger than those required for use in applications such as substrate patterning.[24,25,26,27,28,29] There are only a few notable examples of biopolymer blends being used to create surfaces with structures on a scale akin to those in this work.[30,31,32] However, these typically involve secondary etch steps, with harsh solvents and functionalised biopolymers to achieve desired morphologies, making them environmentally damaging.

Microphase separation phenomena in biopolymer-biopolymer-solvent systems falls into two categories; associative and segregative.[33,34] Categorisation is dependent on the affinity between the biopolymers and the solvent. Associative phase separation occurs when the biopolymers carry opposite charges, and segregative when they carry the same charge. Complexities arise in the form of; kinetic competition between gelation processes and phase separation process[35]; the influence of shear forces on formation mechanisms[36,37]; the influence of humidity on solution behaviours[38]; and the vagaries of biopolymer structure in solution, to name only a few. This paper reports phase separations of a specific type of biopolymer-biopolymer-solvent system; protein-polysaccharide-solvent solutions (hereafter referred to as the Pr-Ps-S solutions). These solutions are used to produce surface patterned, composite thin-

films of polysaccharide and protein. Associative and segregative phase separations have been studied extensively over the past four decades, primarily in food science. However, the latter focussed on limited applications in packaging and biomedical devices.[39,17,40,41]

Most scientific literature details phase separation of a variety of proteins and polysaccharides, generally in one type of solvent; water.[33,42–45] The exception is when the polysaccharide of choice is chitosan, when the solvent of choice is typically dilute acetic acid.[46–48] The research reported here builds upon state-of-the-art in the field of biopolymer phase separation in four ways: firstly, unique Pr-Ps-S solutions are studied; proteins are bovine serum albumin (BSA) and pigskin gelatin (PG), polysaccharide is chitosan (Ch) (, and solvent is formic acid (FA). Secondly, the production of thin-films from these Pr-Ps-S systems is examined with a view to their use in materials applications beyond the food, packaging and biomed industries. Specifically, utilising micro- and nanopatterns in templating, and smart textiles applications. Thirdly, the control of formation conditions under which these phase separations occur is different. Control of conditions such as humidity and ambient temperature is usually more associated with the formation processes of synthetic polymer solutions for medical device and advanced membrane applications.[49–52] Control of biopolymer phase separation of the Pr-Ps-S solutions confers a degree of control over the morphology final thin-films, affecting utility. Fourthly, the analytical data concerning the growth of surface features of the biopolymer thin-films is compared to that of Ostwald ripened structures. The findings described in this paper shows that controlled phase separation of biopolymer blends is an effective method of producing micro- and nano-patterned surfaces.

2.3 EXPERIMENTAL

2.3.1 BIOPOLYMERS, CASTING SOLUTIONS AND SUBSTRATE

Low molecular weight chitosan (50-190 kDa) > 75% deacetylation, high bloom gelatin from porcine skin (~300 bloom, Type A premium grade) and Bovine Serum Albumin (lyophilised powder, ≥ 96%, molecular weight ~66 kDa) were purchased from Sigma Aldrich (**Figure 2.1**). Substrates used in all cases were Fisherbrand™ Microscopic Slides with Ground Edges (plain). The solvent used was Formic acid, 98+ %, pure, ACROS Organics™ and was diluted to 90% w/v before use using distilled water. Casting solutions were prepared using 90% formic acid as solvent to ensure that the biopolymers above were below their isoelectric point in solution

and so, positively charged. This was to ensure that any phase separation processes occurring in the Pr-Ps-S solutions were segregative.

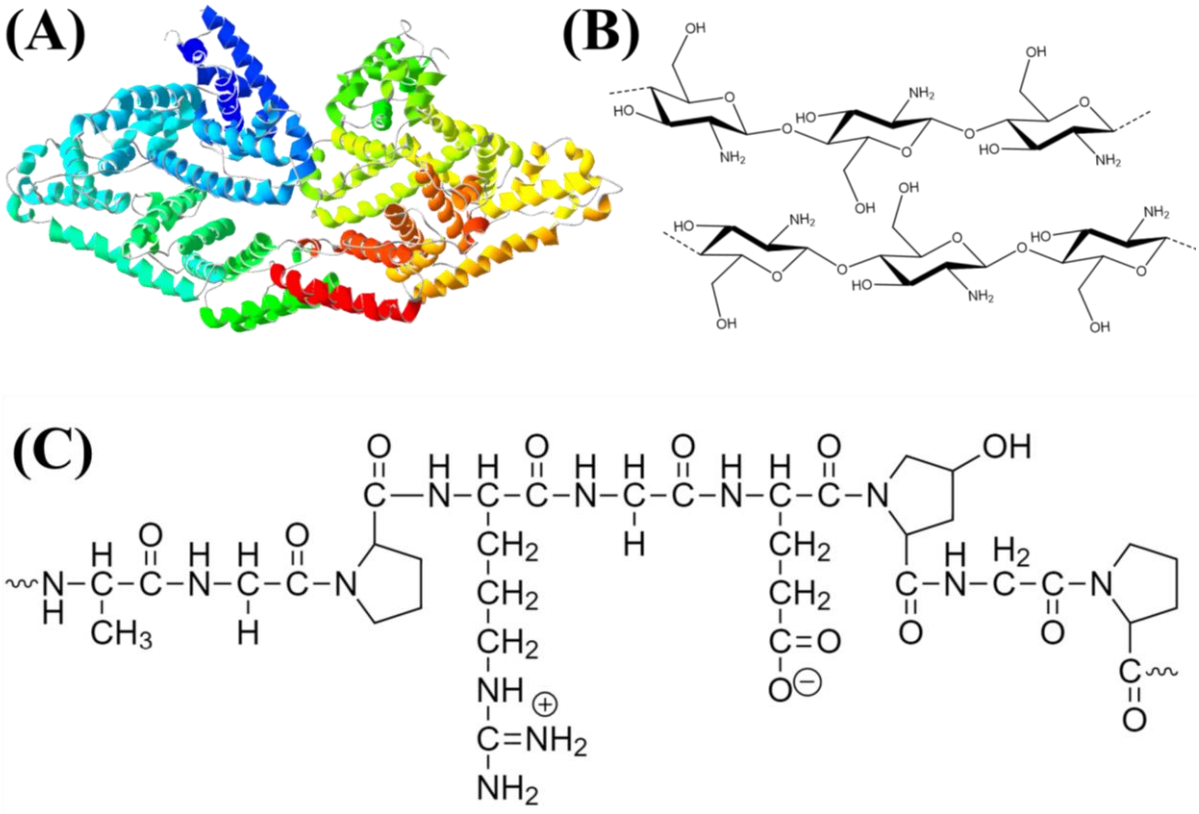


***Figure 2.1**: **(A)** 3D structure of BSA (Protein Data Bank ID: 3v03, www.rcsb.org) using Swiss-Pdb Viewer V.4.1 software. **(B)** Structure of chitosan polysaccharide created using Chemdraw Professional V16.0.1.4. **(C)** Basic structure of gelatin created using Chemdraw Professional V16.0.1.4.*

2.3.2 SOLUTION PREPARATION

Prior to dissolution, proteins and polysaccharides were dried overnight at room temperature under vacuum. Polymer stock solutions were made by solubilising chitosan (Ch), bovine serum albumin (BSA) and pigskin Gelatin (PG) in 90% formic acid (FA) acid at 5 w/v% and 10 w/v%. These solutions were stirred in a closed vessel for 3 hr in a closed container at room temperature. The solutions were then centrifuged at 13,000 rpm in a Beckman Coulter Avanti J-26XPI centrifuge at 18 ºC for 15 min and decanted. Following this, stock solutions were stored at -20 ºC for further use or used immediately. Stock solutions were diluted with fresh formic acid and/or mixed with each other to produce coating solutions.

2.3.3. COATING PREPARATION

2.3.3.1 THIN-FILM CASTING

Thin-films were prepared in triplicate using an automatic film applicator, (K202 Control Coater, RK Printcoat Instruments Ltd, UK) to produce biopolymer solution coatings of uniform thickness. Standard conditions: applicator electrical drive speed 3, 12 μm casting bar calibrated to height of thin film substrate (note that initial solution casting thickness does not match final thin-film thickness). Substrates were glass slides onto which single biopolymer solutions and Pr-Ps-S solutions were cast. Humidity controlled experiments were conducted in a purpose built chamber, also described by Idris *et al.*[53] Air passed through a humidification system. Ambient air was mixed with dry, synthetic air to influence humidity. Humidity control was achieved by passing the air through a Dreschel bottle containing distilled water and air, respectively. Monitoring of humidity was achieved through use of a humidity meter (*HOBO MX Temp/RH Logger*), which also functioned as an ambient temperature meter. Temperature was stabilised by laboratory air conditioning, at approx. 18 ºC. Air pressure was normal atmospheric pressure at sea level in our geographical region (approx.10.1 N/cm^2).

2.3.3.2 ATOMIC FORCE MICROSCOPY (AFM)

The surface topography and phase of the prepared samples was analysed by atomic force microscopy (AFM) using a Park Systems, XE-100 instrument under ambient conditions. Scans were performed in non-contact mode with high resolution, silicon micro-cantilever tips. Topographic images were recorded at a resonance frequency of 270-300 kHz. Images were analysed using "Gwyddion" and "Park XEI" image analysis software. Features were measured using "Gwyddion" and descriptive statistics calculated using "Origin". Surface roughness was measured using "XEI" software. RMS (*root means square arithmetical mean roughness* or *root means square average roughness*) is the average between the height deviations and the mean line/surface, taken over the evaluation length/area. All figures were calculated from AFM data with equations defined by the Japanese Standards Association.[54,55] Surface feature diameters were measured using the Gwyddion watershed algorithm for scanning probe microscopy. Force-distance mapping was performed using a Park XE-100 AFM using silicon probes (NCSTR, resonance frequency ≈160 kHz, spring constant 7.4 N m^{-1}, tip radius 8 nm).

Data was processed using XEI and SPIP software, where young's modulus was calculated using a Hertzian model. A minimum of 64 data points were recorded for each sample.

2.4 RESULTS AND DISCUSSION

2.4.1. SINGLE POLYMER SOLUTION THIN-FILMS

Biopolymer thin-films were cast from the three single biopolymers; Ch, BSA and PG. Solutions of 4 w/v%, 2 w/v% and 1 w/v% were used for each, to confirm that no patterned structures were forming from the pure polymers. If present in pure biopolymer films, such features in the composite films would be difficult to distinguish from those due solely to the composite formation mechanisms. Furthermore, their formation may influence the formation of the composite film features. AFM images (see **Figure S2.1**, in section 2.7 **Appendix**) showed that films were indistinguishable from one another. No structures likely to align at the interface of the biopolymer domains, thereby increasing mutual solubility of the biopolymers and retarding the phase separation processes of the Pr-Ps-S solutions, were noted.

2.4.2 PR-PS-S SOLUTION THIN-FILMS

2.4.2.1 THIN-FILMS FROM PHASE SEPARATION OF BSA-CH-FA SOLUTIONS

Growth mechanisms typically describe the increase in size of features in phase separated films. This is most typically shown in graphs of feature size per unit time, where, for example, feature diameter is seen to increase with time. **Figure 2.2** (and **Figure S2.2**, in section 2.7 **Appendix**) shows AFM images of BSA-Ch composite thin-films cast from BSA-Ch-FA Pr-Ps-S solutions. At biopolymer ratio of 4 w/v% BSA to 1 w/v% Ch, across all humidities (**Figure 2.2**, Column A), predominantly pores were formed. AFM data showed that as the humidity increased, the number of pores increased (**Figure 2.3a**), and the mean pore radius decreased (**Figure 2.3b**); highlighting an inverse correlation between pore growth and humidity. Thus, pore formation at this biopolymer ratio does not occur via a growth mechanism, *i.e.* with an increase of pore mean diameter with time. This is reflected in the negative slope of the trend line for feature size at the 4:1 biopolymer ratio in **Figure 2.3a** in contrast to a positive slope for the other biopolymer ratios (all of which exhibited protuberances as the analysed features). Similarly, in **Figure 2.3b**, the pores show a positive trend to their frequency, *i.e.* increasing frequency, in

contrast to the negative trend-line slopes of the protuberances observed at all other biopolymer ratios.[52]

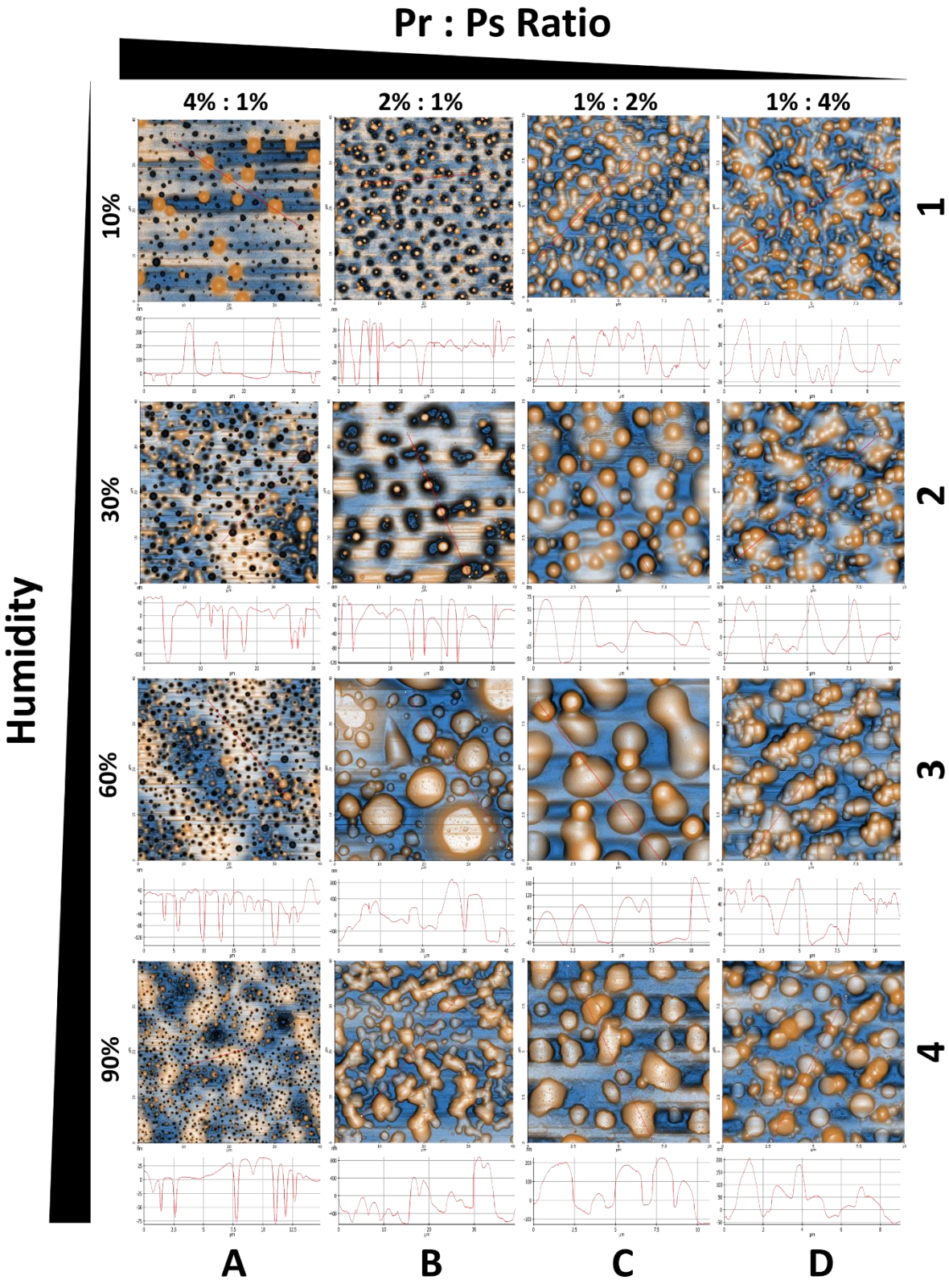


Figure 2.2: *AFM image grid and associated line profiles showing results of casting thin-films at 12µm from specific Pr-Ps-S solutions of BSA-Ch-FA at specific humidities. Each image in column A and column B is 40 µm × 40 µm area. Each image in column C and column*

D is 10 µm × 10 µm area. Column A = 4 w/v% BSA 1 w/v% Ch (4:1), column B = 2 w/v% BSA 1 w/v% Ch (2:1), column C = 1 w/v% BSA 2 w/v% Ch (1:2), column D = 1 w/v% BSA 4 w/v% Ch (1:4). Row 1 = 10% humidity, row 3 = 30% humidity, row 3 = 60% humidity and row 4 = 90% humidity.

At a biopolymer ratio of 2 w/v% BSA to 1 w/v% Ch, (**Figure 2.2**, column B) at 10% and 30% humidity, discontinuous porous domains and protuberances were observed. At 60% and 90% humidity however, (B3 and B4 respectively) no pores were visible and protuberances were solely present, but more globular and larger than those in the images of columns C and D of **Figure 2.2**. The ovoid shape of these protuberances is most likely an attempt at the adoption of a spherical shape, resulting from coalescence. As the only parameter varying in column B is humidity, the large globules observed must result from high humidity conditions. High humidity, *i.e.* 60% +, generates thermodynamic instability in the system which drives phase separation. Excessively high humidity during film formation may excessively increase the water content of the cast solution to be phase separated. This decreases the solubility of any hydrophobic biopolymers in solution; in this instance, Ch.[56,57] This difficult to control reduction in the solubility of Ch within the overall biopolymer solution results in an instability that causes the Ch to crash out. BSA, by contrast is more soluble in formic acid than Ch.[58–60] However, one would expect this effect to be more exaggerated at higher Ch ratios and this does not appear to be the case in the images of **Figure 2.2**, columns C and D.

Across all humidity values, the protuberances follow the general trend outlined above; increasing mean diameter with increasing humidity (**Figure 2.3a**). The aforementioned large jump in the scale of the protuberances results in the slope of the trend line for the data at 2:1 biopolymer ratio in **Figure 2.3a** being the steepest of the four ratios tested. At biopolymer ratio of 1 w/v% BSA to 2 w/v% Ch, across all humidity values (**Figure 2.2**, Column C), only protuberances were formed. Increased humidity resulted in the subsumption of smaller protuberances and interconnects to form much larger well-defined protuberances. This typifies the behaviour of the phase separation of colloidal systems; a growth process proceeding by the nucleation and growth of the dispersed phase from the dispersion medium.[61,62] AFM data in shown in **Figure 2.3a** and **b** corroborate that the mean density of features decreases and mean feature diameter increases as a function of humidity at this biopolymer ratio. There is one deviation from the trend. In proceeding from 60% to 90% humidity, the feature density

decreased while the mean feature diameter increased, also apparent from the AFM images. This is likely due to the increased height of protuberances formed in the 90% blend.

Similar structures to those in shown in image C1 of **Figure 2.2** (and again in image C1 of **Figure 2.4** at the same ratio for PG:Ch) were observed by de Jong and van de Velde by AFM (their images were of 160 µm × 160 µm area, compared to 10 µm × 10 µm areas here).[35] In a later publication, the same authors attributed the formation of these structures to nucleation and growth processes in phase separations.[63] They did not specify any particular growth processes. The diameters of the protuberances in the de Jong and van de Velde images are approx. 7 - 15 µm, while those in image C1 and C3 of **Figure 2.2** are smaller. At a biopolymer ratio of 1 w/v% BSA to 4 w/v% Ch, across all humidity values (**Figure 2.2**, column D), again only protuberances were formed. Here the same general trends outlined in column C were observed without deviations and attributed to a growth process, corroborated by AFM data analysis in **Figure 2.3a** and **2b**.

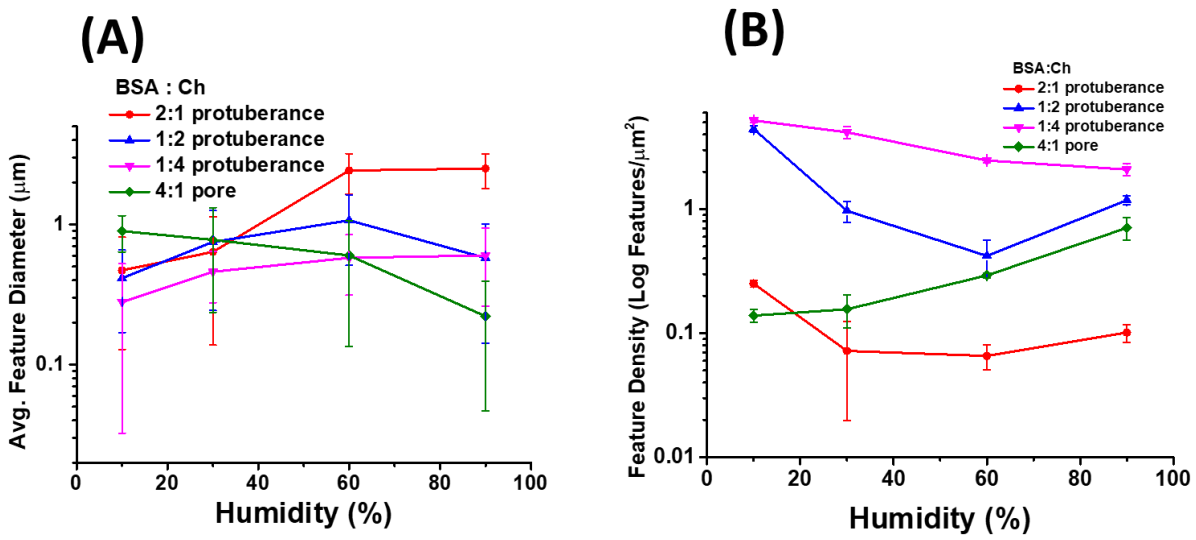


Figure 2.3: *Statistical analysis of BSA-Ch blends for feature size and density. All but the 4:1 blend refers to protuberance measurements, with the 4:1 blend data displaying pore data.* ***A)*** *Refers to feature diameter plotted against humidity while* ***B)*** *Details features/µm^2 vs.% humidity for 4:1, 2:1, 1:2 and 1:4 blends respectively.*

2.4.2.2 THIN-FILMS FROM PHASE SEPARATION OF PG-CH-FA SOLUTIONS

Figure 2.4 (and **Figure S2.3**, in section 2.7 **Appendix**) shows a grid of AFM images of PG-Ch composite thin-films cast from PG-Ch-FA solutions. For these films, the features analysed by software were the protuberances as these were the features we were interested in controlling both the size and morphology of.

In thin films cast from a ratio of 4 w/v% PG to 1 w/v% Ch a wider variety of structures was seen than in the BSA-Ch films (**Figure 2.4**, Column A). In films cast at 10% humidity protuberances were approx. 230 nm wide. Increasing humidity to 30% resulted in larger, but less defined protuberances (**Figure 2.4**, panel A2).

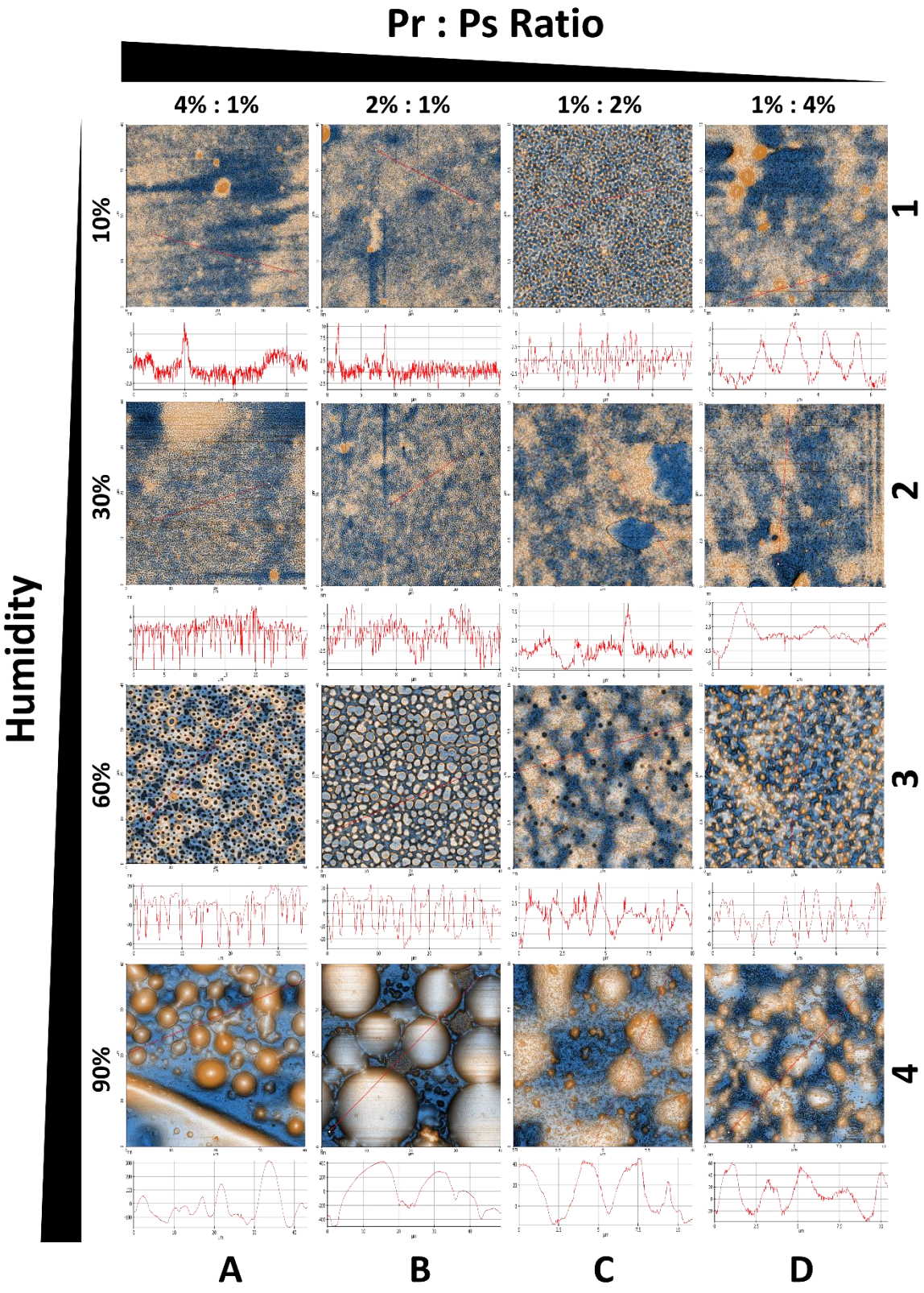


Figure 2.4: *AFM image grid and associated line profiles showing results of casting thin-films at 12µm from specific Pr-Ps-S solutions of PG-Ch-FA at specific humidities. Each image in column A and column B is 40 µm × 40 µm area. Each image in column C and column D is 10 µm × 10 µm area. Column A = 4 w/v% PG 1 w/v% Ch (4:1), column B = 2 w/v% PG 1*

w/v% Ch (2:1), column C = 1 w/v% PG 2 w/v% Ch (1:2), column D = 1 w/v% PG 4 w/v% Ch (1:4). Row 1 = 10% humidity, row 2 = 30% humidity, row 3 = 60% humidity and row 4 = 90% humidity.

Image A3 in **Figure 2.4** shows that 60% humidity yields poorly defined protuberances accompanied by pores. At 90% humidity, shown in image A4, ill-defined protuberances are observed on a much larger scale compared to the well-defined protuberances of image C1 and D3.

Figure 2.5a and **b** show AFM data from PG-Ch blends highlighting a trend of increasing protuberance size and decrease in number with humidity. As with the BSA-Ch films previously discussed, this is indicative of a growth process. The precise nature of the growth process is discussed below.

Films cast from 2 w/v% PG 1 w/v% Ch (**Figure 2.4**, column B) show a similar trend to those cast from 4 w/v% PG to 1 w/v% Ch but with fewer interconnects between protuberances, defining the protuberances more sharply.

Films cast from 1 w/v% PG 2 w/v% Ch (**Figure 2.4**, column C), show a visual deviation from the trends observed in columns A and B of **Figure 2.4**. Image C1 exhibits the best defined and smallest structures of any of the samples produced in this study, with protuberances of approximately 180 nm in diameter.

Image C2 presents a deviation from the trends observed up to now, with a particulated structure. The mean protuberance diameter and features per area of **Figure 2.5** presents no deviation. Software analysis of image C2 identified protuberance structures of a mean diameter larger than those in image C1 and smaller than those in image C3. However, inspection of these images with the naked eye clearly shows that a particulate morphology is formed. According to Doublier *et al*, thin-film microstructures formed from protein/polysaccharide blends can result from two simultaneously occurring processes: phase separation and gelation.[34] De Jong *et al* expanded on this, showing that the final kinetically arrested structure in such instances originates from a competition between these two processes.[63] During the late stages of phase separation for many protein/polysaccharide systems, viscoelasticity in either one or both of the phases builds up, leading to a final gelled state of at least one of the phases. The morphology of this final stage is determined by the ratio of the rates of gelation and phase separation.[33] This creates difficulties when describing the structures arising from such phase-separated systems.[64] When the gelation of both phases is fast, a macroscopic gel is obtained

with a bicontinuous structure. When the gelation is slow, phase separation can proceed until the phase highest in viscosity breaks up into droplets.[33] However, under certain conditions if the gelation of just one phase is rapid, phase separation can be hindered, as is the case with a PG-Ch system. As soon as the gelled protein network is formed, the separation of the phases is minimised or prevented and the system is "frozen" in a state determined by the gelation of the PG phase.[34] This frozen state offers an explanation for the structures observed in images C2, (and D1 and D2) of **Figure 2.4**. What specifically caused the relatively rapid gelation of the PG under these conditions remains unclear. Given the inherent complexity and sensitivity of such systems it could be any number of the system parameters or, uncontrollable interactions between them.

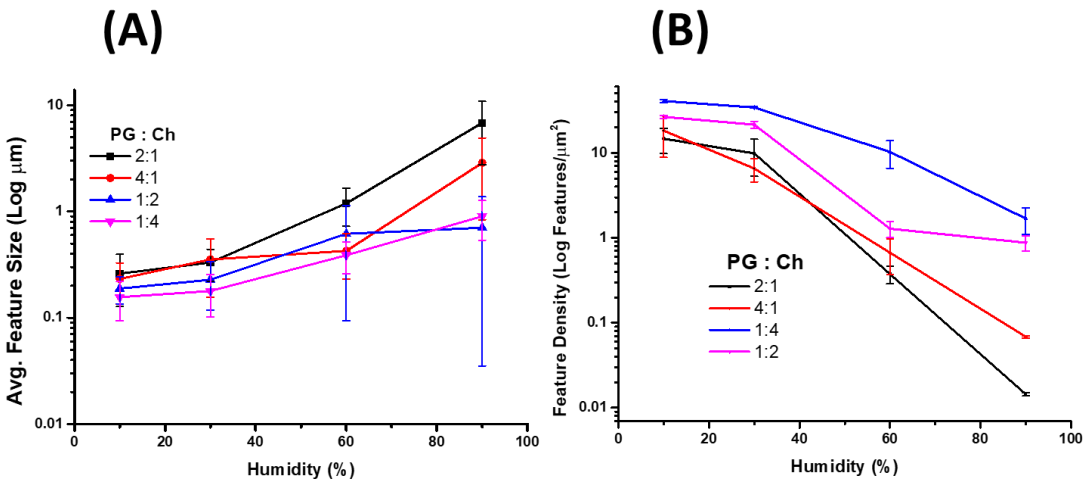


Figure 2.5: *Shows statistical analysis of PG-Ch blends for feature size and density.* ***A)*** *Refers to feature diameter plotted against humidity.* ***B)*** *Details features/µm^2 vs.% humidity.*

Images D1 and D2 shown in **Figure 2.4**, column D, are notably different from their equivalents in the previous columns, with spherical protuberances. However, according to the data shown in **Figure 2.5a** and **2.4b**, the same trends in feature size and number are also observed. This is a result of the particulated structure as described for image C2. Image D3 in **Figure 2.4** shows the most sharply defined protuberances of all PG-Ch films. These were the second smallest features with clear definition (approx. 389 nm) observed in our study and are in stark contrast to the features seen for the other PG-Ch films of different biopolymer ratio at the same humidity values. The protuberances are sharper, smaller and greater in number, the culmination of a trend in this direction with increasing Ch content at this humidity. These same

observations can be made of the protuberances/globules seen in image D4 in comparison to their equivalents in images A4, B4, and C4.

2.4.2.3 General Trends in Pr-Ps-S Solution Thin-Films

The AFM images shown in **Figure 2.2** highlight a trend in pore formation at high protein (BSA) concentration to protuberance formation at high polysaccharide (Ch) content. Moving down the columns, changing humidity and maintaining the BSA:Ch ratio, there is a trend from smaller protuberance size at low humidity to larger protuberance size at high humidity; indicative of a protuberance growth process as humidity increases. Opposite trends are observed for the pores formed at the 4 w/v% BSA to 1 w/v% Ch ratio, suggesting they do not form by a growth process or, that pore growth is correlated with decreasing humidity. However, this is not the case for any other biopolymer ratios investigated.

Focusing on protuberances as the features conforming to a growth process behaviour, the images of PG-Ch blends from **Figure 2.4**, as with BSA-Ch blends, show that increasing Ch concentration results in smaller protuberances. In addition, as with BSA-Ch, an increase in humidity leads to larger protuberances. Larger BSA-Ch protuberances appeared better defined than larger PG-Ch protuberances.

The root-mean-squared (RMS) roughness vs % humidity graphs in **Figure 2.6** showed similar trends increased protuberance diameter with increased humidity. All blends displayed increased roughness with increased humidity, similar to that of feature size. Slopes of 4:1 compared to 2:1, while 1:2 and 1:4 were similar with one another, except for the 2:1 BSA:Ch blend, which formed the tallest features at 60% humidity. RMS roughness is an indicator for applicability of materials to hydrophobic applications. In recent years, there has been much interest in developing rough high aspect ratio micro- and nanostructured surfaces to emulate the properties of self-cleaning and hydrophobic leaves.[28,65,66]

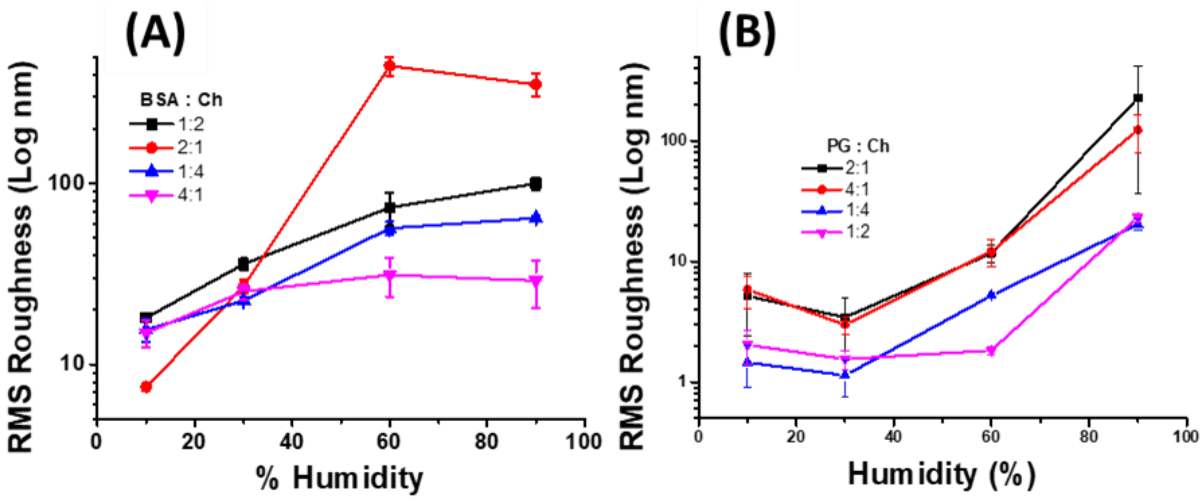


Figure 2.6: *Plots the RMS vs % humidity for all BSA-Ch blends.* ***B)*** *Plots the RMS vs % humidity for all PG-Ch blends.*

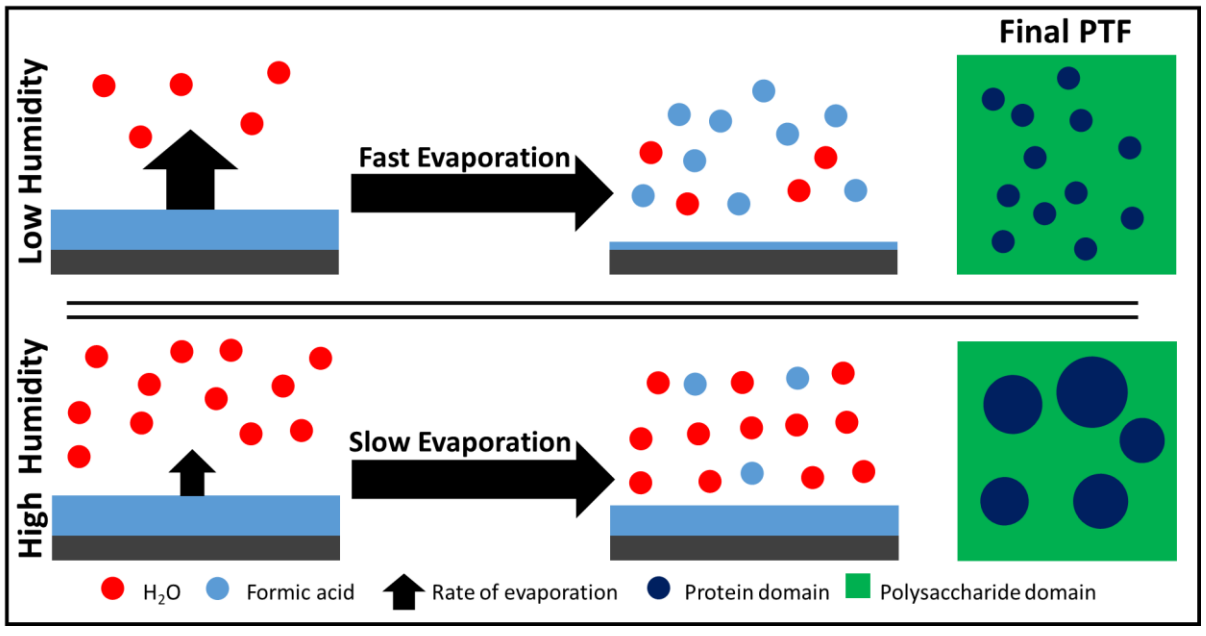
Trommer *et al*[28] have shown how certain mechanisms during demixing of incompatible polymer blends leads to the growth of large spherical structures in thin-films. These structures are similar to those seen throughout the images of **Figure 2.2** and **Figure 2.4**. Size of spherical protuberances was controlled through polymer ratio and solution temperature.[28] Increased temperatures led to more extensive nucleation, due to the reduced viscosity of the solutions and higher polymer mobility, which resulted ultimately in larger structures. However, higher temperatures also resulted in faster rates of solvent evaporation. This loss of solvent increased solution viscosity, reducing polymer mobility, and so reducing the size of the spherical structures.

Although temperature was not varied for the Pr-Ps blends investigated in this study, similar structural growth trends were observed. AFM data shown in **Figure 2.3** and **2.4** revealed that humidity was the predominant factor for protuberance diameter. Drying time was proportional to relative humidity within the chamber. Low humidity permitted faster drying times while higher humidity provided longer drying times. As in the Trommer study[28] the greater rate of solvent loss increased solution viscosity, reducing polymer mobility, and so reducing the final size of the spherical structures. Such a growth process would explain the trends observed in the images of **Figure 2.2** and **Figure 2.4**. Overall the AFM images of **Figure 2.2** and **Figure 2.4** seem to show the subsumption of smaller protuberances into larger ones with increased humidity. This is corroborated by the statistical data shown in **Figure 2.3**

and **Figure 2.5**, which highlights the increase in the mean protuberance size (approx. 7 µm) subsequent decrease in protuberance frequency for each blend with humidity; conforming to known growth processes, specifically, Ostwald ripening.

2.4.3 Feature Growth in Pr-Ps-S Thin-Films

Ostwald ripening is a phase transition resulting from the coalescence of material. Ostwald ripening has been extensively studied in the formation of emulsions[67–69], controlling the size of crystals[70–72] and growing selective nanostructures.[73–75] The driving force of the process is a decrease in the total surface energy.[76–78] Characteristic trends in the evolution of cluster size distributions over time indicate Oswald ripening growth processes. In this instance, those characteristic trends were observed in the distribution and growth of spherical structures in the thin film surfaces. Unlike in materials where Oswald ripening is more commonly studied, annealing time was not a factor in the formation of the Pr-Ps thin films. Instead, relative humidity was controlled to limit the evaporation rate of formic acid .[79] As such, film drying rate and the length of time that the system has sufficient molecular mobility for growth to occur is controlled. Once the formic acid leaves the system, the biopolymer chains become locked in place. Thus, humidity in these experiments is proportional to time when observing Ostwald ripening (**Scheme 2.1**).



Scheme 2.1: *Shows the effect of humidity on blend drying rate. At low humidity, the solvent (formic acid) rapidly evaporates into the atmosphere, quickly vitrifying the blend pattern early in development. At high humidity, the solvent evaporates slowly, allowing more*

time for blend features to grow, before vitrification. This results in high humidity environments producing PTFs with larger feature sizes.

The following observation was expected of a system undergoing Ostwald ripening; the counts per unit area (#) of protuberances would increase at lower humidities while particle dimensions would decrease at low humidity due to high evaporation rate/insufficient time for growth phase. Furthermore, the opposite was expected to be observed at higher humidity values. This is precisely what was observed, with inset histograms required in **Figure 2.7b**, **Figure 2.8a** and **b** to show the expanded range at high humidity. Increased frequency of protuberances of smaller diameter are seen at low humidities. Conversely, fewer protuberances of greater diameter are observed at higher humidities.

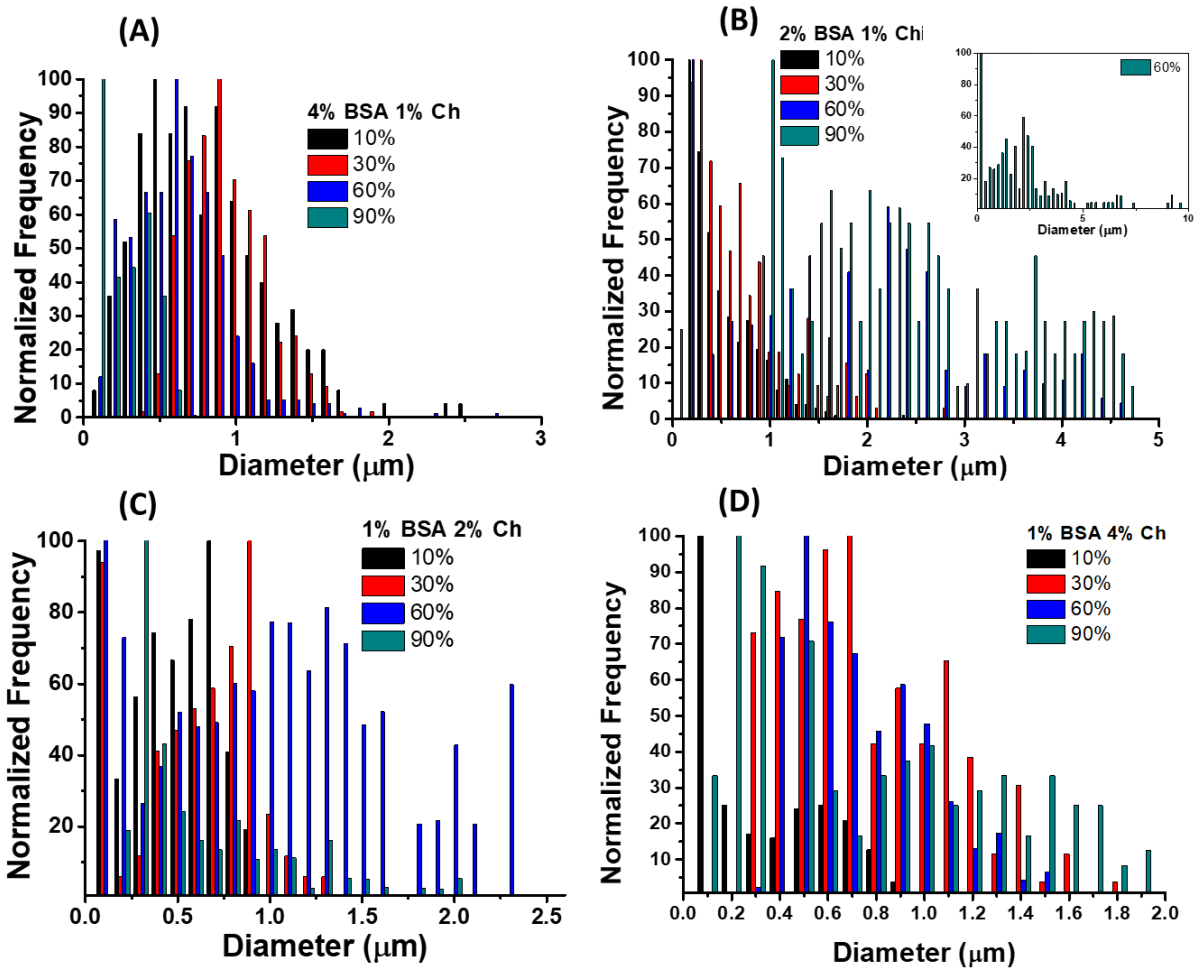


Figure 2.7: *Statistical analysis of BSA-Ch blends for feature and frequency of feature sizes. All but the 4:1 blend refers to protuberance measurements, with the 4:1 blend data displaying pore data.* ***A - D*** *displays feature count vs diameter of observed features for 4:1, 2:1, 1:2 and 1:4 blends respectively.*

Figure 2.7 shows histogram data of feature diameter gathered for BSA-Ch blends. **Figure 2.7a** displays the size distribution of the pores (predominant feature) in a 4:1 blend. As shown in the mean feature diameter size and humidity graphs, there is a shift towards smaller sizes with increased humidity. **Figure 2.7b - d** display the size distributions of protuberances in the films. There is an increased frequency of protuberances of smaller diameter at low humidities, parallel to increased feature density. This effect is attributed to viscous Ch solutions reducing BSA polymer mobility, retarding the growth process. The frequency of larger protuberances increases with increased humidity and may be attributed to the formation of larger structures with longer drying times; suggesting that the growth mechanism occurs similarly to that of Ostwald ripening, as discussed earlier, with the consumption of smaller particles to form fewer larger particles.

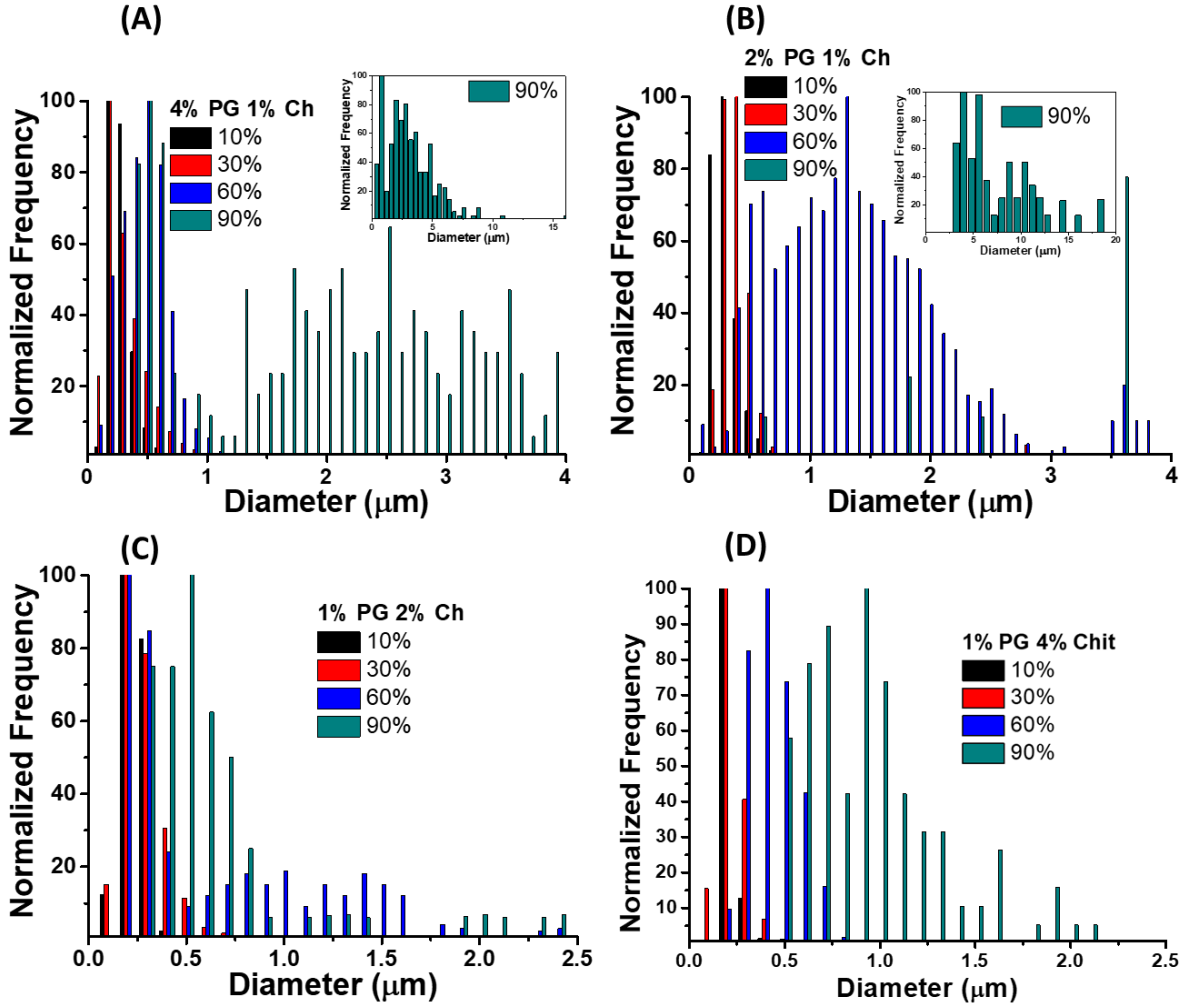


Figure 2.8: *Statistical analysis of PG-Ch blends for feature size and frequency of feature sizes.* ***A - D*** *displays feature count vs diameter of observed features for 4:1, 2:1, 1:2 and 1:4 blends respectively.*

Ostwald ripening in thin films follows a sinusoidal curve, so 2:1 may be closer to the midpoint. The 4:1 closely mirrors 1:2, again due to increasing number of holes preceding to the development of hills, and perhaps indicating that hole formation follows an inverse Ostwald ripening process.

Figure 2.8 shows histogram data gathered for PG-Ch blends. A to D display the size distribution of protuberances in the film. Going from A to D results in an increased frequency of smaller protuberances at lower humidities, parallel to the increase in feature density. Again, this effect is attributed to viscous Ch solutions reducing PG polymer mobility, retarding the growth process. Frequency of protuberance numbers also reduced with increased humidity.

Histograms were normalised on the y axis for clarity. Data shows that for protuberance forming blends, a Gaussian population of protuberances was observed. For the 1:2 PG:Ch blend, it was possible to overlay Gaussian plots for 10%, 30%, 60% and 90%, showing the formation of larger features at higher humidities (see **Figure S2.4,** in section 2.7 **Appendix**). Phase imaging and the Young's modulus of both blends show protuberances (discontinuous domains) are composed of different a material to the underlying matrix (see **Figure S2.5** and **Figure S2.6,** 2.7 **Appendix**). The 4:1 BSA:Ch plot shows the opposite, as in previous graphs, shifting towards smaller, more numerous holes consistent with other observations. They show the shift from a small number of large features to a large number of small features.

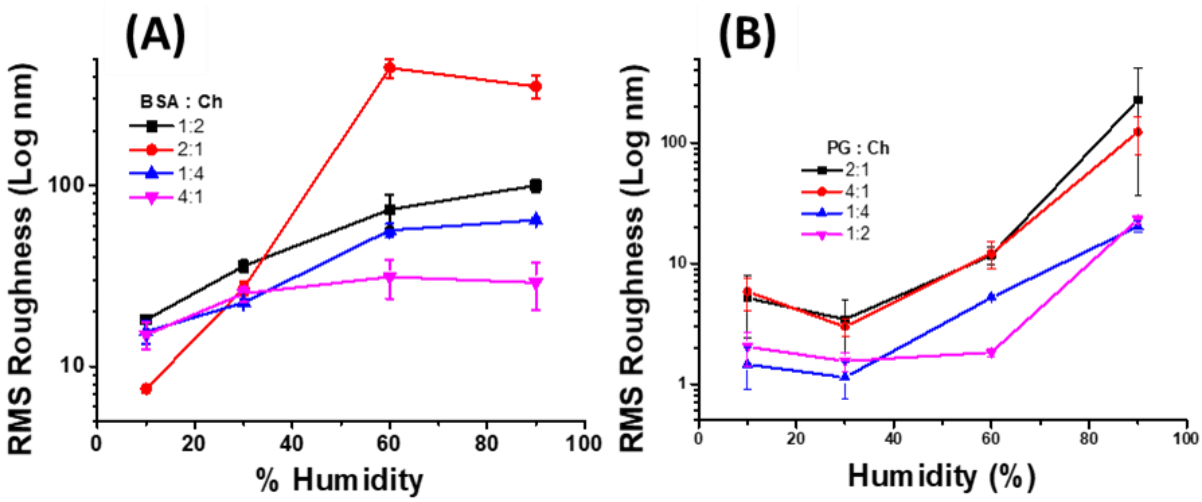


Figure 2.6: *Plots the RMS vs % humidity for all BSA-Ch blends. B) Plots the RMS vs % humidity for all PG-Ch blends.*

Figure 2.6 displays RMS roughness of biopolymer blend films. There is an increase in the RMS roughness, parallel to the increase in feature size with increased humidity.

These results show it is possible to achieve sub-micron features utilizing only biologically sourced polymers. A particularly attractive property of biopolymer blends includes their self-assembly upon deposition and solvent evaporation, facilitating rapid pattern realisation and feature size tunability by easy control of the evaporation rate upon casting. This technique avoids the use of solvent annealing, functionalisation and pH control, while achieving the smallest domain size of such films to date. The combination of a viscous polysaccharide, volatile solvent and low humidity resulted in the first sub-micron structures obtained with a biopolymer blend seen in the literature. This could be further enhanced by choosing a higher molecular weight (M_w) chitosan. The increased viscosity due to the higher M_w would impede Ostwald ripening, resulting in smaller features of uniform spacing due to inhibited polymer mobility. A similar effect would be observed with a more viscous protein. Furthermore, other casting methods such as spin coating would achieve smaller feature sizes due to the faster rate of solvent removal, and would be further enhanced by humidity control. Reducing the overall concentration of the phase system could optimize domain spacing, size and definition. This would result in smaller features by reducing the amount of material available to feed into the discontinuous domain, and reduce the number of aggregated features on the surface, resulting in uniform monodispersed features. However, this method would likely result in conflicting mechanisms due to a reduction in overall viscosity of the system, promoting discontinuous domain growth. Finally, as with Trommer *et al's* work[28], temperature control could be employed in conjunction with this humidity regulated approach to achieve highly tuneable structures which would allow greater control over the materials properties and avoid functionalisation of components to improve domain definition. Such improvements would be required for applications in patterning and textiles.

2.5 CONCLUSION

This work has demonstrated that humidity is the defining factor in determining feature morphology and size in biopolymer blends, exceeding previously attained feature sizes in a facile and benign manner. [28,30,31,32,39,63] Segregative phase separation is successfully employed to achieve sub-micron structures. The use of a viscous polysaccharide, thin, wet deposit and low humidity in the casting process achieved a feature size of approx. 200 nm. Formic acid serves as a proficient solvent for most biopolymers, ensuring segregative phase separation and

fast evaporation rates. The smallest feature sizes of both blends were achieved at 10% humidity with a high proportion of Ch in the casting blend. Protuberances observed in our films generally displayed higher monodispersity at lower humidites and at higher Ch contribution, indicating this is caused by an impeded growth process. BSA blends produced well-defined large structures while PG blends produced well-defined small structures. The increased viscosity of PG solutions explains the smaller feature sizes in PG blends. Blend films display a similar growth mechanism regardless of category (high protein or high polysaccharide concentration); Ostwald ripening. The growth processes could be controlled more effectively with this insight. Our results show the smallest and most monodisperse features yet seen in such biopolymer films. However, the insights we have gained into the growth processes permit even smaller and more monodisperse feature size than those shown here, subject to effective controls. Due to the chemical properties of these blends, it is hoped that they will be employed as a cheaper and greener templating alternative. Such shifts in materials design are paramount in the progression towards a more sustainable future.

2.6. REFERENCES

(1) Ferrarese Lupi, F.; Giammaria, T. J.; Volpe, F. G.; Lotto, F.; Seguini, G.; Pivac, B.; Laus, M.; Perego, M. High Aspect Ratio PS-b-PMMA Block Copolymer Masks for Lithographic Applications. *ACS Appl. Mater. Interfaces* 2014, **6** (23), 21389–21396. https://doi.org/10.1021/am506391n.

(2) Sardella, E.; Favia, P.; Gristina, R.; Nardulli, M.; d'Agostino, R. Plasma-Aided Micro- and Nanopatterning Processes for Biomedical Applications. *Plasma Process. Polym.* 2006, **3** (6–7), 456–469. https://doi.org/10.1002/ppap.200600041.

(3) Ouhib, F.; Dirani, A.; Aqil, A.; Glinel, K.; Nysten, B.; Jonas, A. M.; Jerôme, C.; Detrembleur, C. Transparent Superhydrophobic Coatings from Amphiphilic-Fluorinated Block Copolymers Synthesized by Aqueous Polymerization-Induced Self-Assembly. *Polym. Chem.* 2016, **7** (24), 3998–4003. https://doi.org/10.1039/C6PY00661B.

(4) Gao, J.; Li, X.; Li, B.; Han, Y. Fabrication of Polymer Antireflective Coatings by Self-Assembly of Supramolecular Block Copolymer. *Polymer (Guildf).* 2010, **51**, 2683–2689. https://doi.org/10.1016/j.polymer.2010.03.035.

(5) Guldin, S. Block Copolymer Assembled Antireflective Coatings with Self-Cleaning Properties in *Inorganic Nanoarchitectures by Organic Self-Assembly*; Springer International Publishing; eds 1st **2013**; pp 141–154. https://doi.org/10.1007/978-3-319-00312-2_10.

(6) Vliet, T. van. Mechanical Properties of Concentrated Food Gels in *Food Macromolecules and Colloids*; eds 1st; **1995**; pp 447–455. https://doi.org/10.1039/9781847550873-00447.

(7) Wilde, P.; Mackie, A.; Husband, F.; Gunning, P.; Morris, V. Proteins and Emulsifiers at Liquid Interfaces. *Adv. Colloid Interface Sci.* 2004, **108–109**, 63–71. https://doi.org/10.1016/J.CIS.2003.10.011.

(8) Matsushita, Y. Microphase Separation (of Block Copolymers) in *Encyclopedia of Polymeric Nanomaterials*; Springer Berlin Heidelberg, **2015**; pp 1255–1260.

(9) Chassenieux, C.; Durand, D.; Jyotishkumar, P.; Thomas, S. Biopolymers: State of the Art, New Challenges, and Opportunities in *Handbook of Biopolymer-Based Materials*; Wiley-VCH Verlag GmbH & Co. KGaA: Weinheim, Germany, **2013**; pp 1–6. https://doi.org/10.1002/9783527652457.ch1.

(10) Tang, X. Z.; Kumar, P.; Alavi, S.; Sandeep, K. P. Recent Advances in Biopolymers and Biopolymer-Based Nanocomposites for Food Packaging Materials. *Crit. Rev. Food Sci. Nutr.* 2012, **52** (5), 426–442. https://doi.org/10.1080/10408398.2010.500508.

(11) Whistler, R. L. Solubility of Polysaccharides and Their Behavior in Solution in *Carbohydrates in Solution*; eds 1st; **1973**; pp 242–255. https://doi.org/10.1021/ba-1971-0117.ch014.

(12) Striegel, A. M.; Timpa, J. D. Molecular Characterization of Polysaccharides Dissolved in Me_2NAc-LiC1 by Gel-Permeation Chromatography. *Carbohydr. Res.* 1995, **267** (267), 271–290.

(13) Jovanović, G. D.; Klaus, A. S.; Nikšić, M. P. Antimicrobial Activity of Chitosan Coatings and Films against Listeria Monocytogenes on Black Radish. *Rev. Argent. Microbiol.* 2016, **48** (2), 128–136. https://doi.org/10.1016/j.ram.2016.02.003.

(14) Sun, J.; Tan, H. Alginate-Based Biomaterials for Regenerative Medicine Applications. *Materials (Basel).* 2013, **6** (4), 1285–1309. https://doi.org/10.3390/ma6041285.

(15) Saavedra-Leos, Z.; Leyva-Porras, C.; Araujo-Díaz, S.; Toxqui-Terán, A.; Borrás-Enríquez, A. Technological Application of Maltodextrins According to the Degree of Polymerization. *Molecules* 2015, **20** (12), 21067–21081. https://doi.org/10.3390/molecules201219746.

(16) Cheng, H.; Feng, S.; Jia, X.; Li, Q.; Zhou, Y.; Ding, C. Structural Characterization and Antioxidant Activities of Polysaccharides Extracted from Epimedium Acuminatum. *Carbohydr. Polym*. 2013, **92** (1), 63–68. https://doi.org/10.1016/j.carbpol.2012.09.051.

(17) Tolstoguzov, V. Texturising by Phase Separation. *Biotechnol. Adv.* 2006, **24** (6), 626–628. https://doi.org/10.1016/j.biotechadv.2006.07.001.

(18) Sakamoto, K.; Lochhead, R. Y.; Maibach, H. I.; Yamashita, Y. The Use of Polymers in Cosmetic Products in *Cosmetic Science and Technology: Theoretical Principles and Applications*; eds 1st; **2017**; pp 171-221.

(19) Zhao, J.-H.; Wang, J.; Tu, M.; Luo, B.-H.; Zhou, C.-R. Improving the Cell Affinity of a Poly(D,L-Lactide) Film Modified by Grafting Collagen via a Plasma Technique. *Biomed. Mater*. 2006, **1** (4), 247–252. https://doi.org/10.1088/1748-6041/1/4/011.

(20) Petrulyte, S. Advanced Textile Materials and Biopolymers in Wound Management. *Dan. Med. Bull.* 2008, **55** (1), 72–77.

(21) Jami'an, W. N. R.; Hasbullah, H.; Mohamed, F.; Yusof, N.; Ibrahim, N.; Ali, R. R. Effect of Evaporation Time on Cellulose Acetate Membrane for Gas Separation. *IOP Conf. Ser. Earth Environ. Sci.* 2016, **36** (1), 012008. https://doi.org/10.1088/1755-1315/36/1/012008.

(22) Moghadassi, A. R.; Rajabi, Z.; Hosseini, S. M.; Mohammadi, M. Fabrication and Modification of Cellulose Acetate Based Mixed Matrix Membrane: Gas Separation and Physical Properties. *J. Ind. Eng. Chem.* 2014, **20** (3), 1050–1060. https://doi.org/10.1016/j.jiec.2013.06.042.

(23) Rahman, S. A.; Ismail, A. F.; Rahman, W. A. W. Formation of Cellulose Acetate Membrane for Gas Separation from Binary Dope System: Effect of Shear Rate in *Proceedings of Regional Symposium on Membrane Science and Technology*, 21–25 **April 2004**, Puteri Pan Pacific Hotel, Johor Bharu, Malaysia.

(24) Robeson, L. M. Polymer Blends in Membrane Transport Processes. *Ind. Eng. Chem. Res.* 2010, **49** (23), 11859–11865. https://doi.org/10.1021/ie100153q.

(25) Tallawi, M.; Rosellini, E.; Barbani, N.; Cascone, M. G.; Rai, R.; Saint-Pierre, G.; Boccaccini, A. R. Strategies for the Chemical and Biological Functionalization of Scaffolds for Cardiac Tissue Engineering: A Review. *J. R. Soc. Interface* 2015, **12** (108), 20150254. https://doi.org/10.1098/rsif.2015.0254.

(26) Hu, X.; Park, S. H.; Gil, E. S.; Xia, X. X.; Weiss, A. S.; Kaplan, D. L. The Influence of Elasticity and Surface Roughness on Myogenic and Osteogenic-Differentiation of Cells on Silk-Elastin Biomaterials. Biomaterials 2011, **32** (34), 8979–8989. https://doi.org/10.1016/j.biomaterials.2011.08.037.

(27) Dörr, S.; Hofacker, S.; Viala, S. 'Hair setting composition' U.S. Patent Application 2010/0215608. **2010**.

(28) Trommer, K.; Morgenstern, B.; Gähr, F.; Hermanutz, F. Sub-Micrometer Structure Textile Coatings Generated from Cellulose Based Polymer Blend. *Lenzinger Berichte* 2009, **87**, 151–161.

(29) Yao, M.; Wu, J.; Li, B.; Xiao, H.; McClements, D. J.; Li, L. Microencapsulation of Lactobacillus Salivarious Li01 for Enhanced Storage Viability and Targeted Delivery to Gut Microbiota. Food Hydrocoll. 2017, **72**, 228–236. https://doi.org/10.1016/j.foodhyd.2017.05.033.

(30) Hoeger, I. C.; Filpponen, I.; Martin-Sampedro, R.; Johansson, L.-S.; Österberg, M.; Laine, J.; Kelley, S.; Rojas, O. J. Bicomponent Lignocellulose Thin Films to Study the Role of Surface Lignin in Cellulolytic Reactions. *Biomacromolecules* 2012, **13** (10), 3228–3240. https://doi.org/10.1021/bm301001q.

(31) Strasser, S.; Niegelhell, K.; Kaschowitz, M.; Markus, S.; Kargl, R.; Stana-Kleinschek, K.; Slugovc, C.; Mohan, T.; Spirk, S. Exploring Nonspecific Protein Adsorption on

Lignocellulosic Amphiphilic Bicomponent Films. *Biomacromolecules* 2016, **17** (3), 1083–1092. https://doi.org/10.1021/acs.biomac.5b01700.

(32) Peer, A.; Dhakal, R.; Biswas, R.; Kim, J. Nanoscale Patterning of Biopolymers for Functional Biosurfaces and Controlled Drug Release. *Nanoscale* 2016, **8** (44), 18654–18664. https://doi.org/10.1039/C6NR05197A.

(33) van de Velde, F.; de Hoog, E. H. A.; Oosterveld, A.; Tromp, R. H. Protein-Polysaccharide Interactions to Alter Texture. *Annu. Rev. Food Sci. Technol*. 2015, **6** (1), 371–388. https://doi.org/10.1146/annurev-food-022814-015558.

(34) Doublier, J.; Garnier, C.; Renard, D.; Sanchez, C. Protein-Polysaccharide Interactions. *Curr. Opin. Colloid Interface Sci.* 2000, **5**, 202–214.

(35) de Jong, S.; van de Velde, F. Charge Density of Polysaccharide Controls Microstructure and Large Deformation Properties of Mixed Gels. Food Hydrocoll. 2007, 21 (7), 1172–1187. https://doi.org/10.1016/j.foodhyd.2006.09.004.

(36) Tromp, R. H.; De Hoog, E. H. A. Band Formation on Shearing in Phase-Separated Polymer Solutions. Phys. Rev. E - Stat. Nonlinear, *Soft Matter Phys*. 2008, **77** (3), 1–7. https://doi.org/10.1103/PhysRevE.77.031503.

(37) Vermant, J.; Solomon, M. J. Flow-Induced Structure in Colloidal Suspensions. *J. Phys. Condens. Matter* 2005, **17**, R187–R216. https://doi.org/10.1088/0953-8984/17/4/R02.

(38) Yip, Y.; Mchugh, A. J. Modeling and Simulation of Nonsolvent Vapor-Induced Phase Separation. *J. Memb. Sci*. 2006, **271** (May 2005), 163–176. https://doi.org/10.1016/j.memsci.2005.06.063.

(39) Sun, J.; Tan, H. Alginate-Based Biomaterials for Regenerative Medicine Applications. *Materials (Basel).* 2013, **6** (4), 1285–1309. https://doi.org/10.3390/ma6041285.

(40) Tripathi, S.; Mehrotra, G. K.; Dutta, P. K. Chitosan Based Antimicrobial Films for Food Packaging Applications. *e-Polymers* 2008, **8** (1). https://doi.org/10.1515/epoly.2008.8.1.1082.

(41) Compatibilization in Bio-Based and Biodegradable Polymer Blends. *Eur. Polym. J.* 2013, **49** (6), 1215–1233. https://doi.org/10.1016/J.EURPOLYMJ.2013.01.019.

(42) Nesmeyanov, A. N.; Kikxadze, E. V. Concentration of Proteins as a Result of the Phase Separation of Water-Protein-Polysaccharide Systems Part 1. Phase Equilibria in Water-Milk Proteins-Plysaccharide Systems. *Nahrung* 1986, **30** (6), 591–599.

(43) Nesmeyanov, A. N.; Zhuravskaya, N. A.; Kiknadze, E. V; Tolstoguzov, V. B. Concentration of Proteins as a Result of the Phase Separation of Water-Protein-Polysaccharide Systems Part 2. Concentration of Milk Proteins. *Nahrung* 1986, **30** (6), 601–613.

(44) Fang, Y.; Li, L.; Inoue, C.; Lundin, L.; Appelqvist, I. Associative and Segregative Phase Separations of Gelatin/κ- Carrageenan Aqueous Mixtures. *Langmuir* 2006, **22** (23), 9532–9537. https://doi.org/10.1021/la061865e.

(45) Chun, J. Y.; Hong, G. P.; Surassmo, S.; Weiss, J.; Min, S. G.; Choi, M. J. Study of the Phase Separation Behaviour of Native or Preheated WPI with Polysaccharides. *Polymer (Guildf)*. 2014, **55** (16), 4379–4384. https://doi.org/10.1016/j.polymer.2014.06.082.

(46) Huang, G. Q.; Sun, Y. T.; Xiao, J. X.; Yang, J. Complex Coacervation of Soybean Protein Isolate and Chitosan. *Food Chem*. 2012, **135** (2), 534–539. https://doi.org/10.1016/j.foodchem.2012.04.140.

(47) Yuan, Y.; Wan, Z. L.; Yang, X. Q.; Yin, S. W. Associative Interactions between Chitosan and Soy Protein Fractions: Effects of PH, Mixing Ratio, Heat Treatment and Ionic Strength. *Food Res. Int*. 2014, **55**, 207–214. https://doi.org/10.1016/j.foodres.2013.11.016.

(48) Elmer, C.; Karaca, A. C.; Low, N. H.; Nickerson, M. T. Complex Coacervation in Pea Protein Isolate-Chitosan Mixtures. *Food Res. Int*. 2011, **44** (5), 1441–1446. https://doi.org/10.1016/j.foodres.2011.03.011.

(49) Lee, H. J.; Jung, B.; Kang, Y. S.; Lee, H. Phase Separation of Polymer Casting Solution by Nonsolvent Vapor. *J. Memb. Sci*. 2004, **245** (1–2), 103–112. https://doi.org/10.1016/j.memsci.2004.08.006.

(50) Sun, H.; Liu, S.; Ge, B.; Xing, L.; Chen, H. Cellulose Nitrate Membrane Formation via Phase Separation Induced by Penetration of Nonsolvent from Vapor Phase. *J. Memb. Sci.* 2007, **295**, 2–10. https://doi.org/10.1016/j.memsci.2007.02.019.

(51) Van De Witte, P.; Dijkstra, P. J.; Van Den Berg, J. W. A.; Feijen, J. Phase Separation Processes in Polymer Solutions in Relation to Membrane Formation. *Elsevier J. Membr. Sci.* 1996, **117**, 1–31.

(52) Flynn, E. J.; Arndt, J.; Brothier, L.; Morris, M. A. Control of Pore Structure Formation in Cellulose Nitrate Polymer Membranes. *Adv. Chem. Sci*. 2013, **2** (2), 9–18.

(53) Idris, S. A.; Robertson, C.; Morris, M. A.; Gibson, L. T. A Comparative Study of Selected Sorbents for Sampling of Aromatic VOCs from Indoor Air. *Anal. Methods* 2010, **2** (11), 1803. https://doi.org/10.1039/c0ay00418a.

(54) Japanese-Standards-Association. Geometrical Product Specifications (GPS) -- Surface Texture: Profile Method -- Terms, Definitions and Surface Texture Parameters. *Japanese Ind. Stand. B* 2013, 0601.

(55) Japanese Standards Association. Geometrical Product Specifications (GPS) - Indication of Surface Texture in Technical Product Documentation. *Japanese Ind. Stand. B* 2003, 0031, 1–55.

(56) Kang, Y.-S.; Kim, H.-J.; Kim, Y.-H.; Jo, W.-H. The Mechanism of Assymetric Membrane Formation via Phase Inversion. *Polym. Soc. Korea* 1988, **12** (3), 279–287.

(57) Chae Park, H.; Po Kim, Y.; Yong Kim, H.; Soo Kang, Y. Membrane Formation by Water Vapor Induced Phase Inversion. *J. Memb. Sci*. 1999, **156** (2), 169–178. https://doi.org/10.1016/S0376-7388(98)00359-7.

(58) Ravi Kumar, M. N.. A Review of Chitin and Chitosan Applications. *React. Funct. Polym*. 2000, **46** (1), 1–27. https://doi.org/10.1016/S1381-5148(00)00038-9.

(59) Pillai, C. K. S.; Paul, W.; Sharma, C. P. Chitin and Chitosan Polymers: Chemistry, Solubility and Fiber Formation. *Prog. Polym. Sci.* 2009, **34** (7), 641–678. https://doi.org/10.1016/j.progpolymsci.2009.04.001.

(60) Houen, G. The Solubility of Proteins in Organic Solvents. *Acta Chem. Scand*. 1996, **50**, 68–70. https://doi.org/10.3891/acta.chem.scand.50-0068.

(61) Shaw, D. J. The Colloid State in *Introduction to Colloid and Surface Chemistry*; Butterworth - Heinemann: Oxford, 1992; pp 1–10.

(62) Laidler, K. J.; Meiser, J. H.; Sanctuary, B. C. Surface Chemistry and Colloids in *Physical Chemistry*; Houghton Mifflin Company: Boston, 2003; pp 929–965.

(63) de Jong, S.; Klok, H. J.; van de Velde, F. The Mechanism behind Microstructure Formation in Mixed Whey Protein-Polysaccharide Cold-Set Gels. *Food Hydrocoll.* 2009, **23** (3), 755–764. https://doi.org/10.1016/j.foodhyd.2008.03.017.

(64) Zasypkin, D. V.; Braudo, E. E.; Tolstoguzov, V. B. Multicomponent Biopolymer Gels. *Food Hydrocoll*. 1997, **11** (2), 159–170. https://doi.org/10.1016/S0268-005X(97)80023-9.

(65) Yang, C.; Tartaglino, U.; Persson, B. N. J. Influence of Surface Roughness on Superhydrophobicity. *Physical Chemistry Rev.* 2006, **96** (11); 116103.

(66) Ensikat, H. J.; Ditsche-Kuru, P.; Neinhuis, C.; Barthlott, W. Superhydrophobicity in Perfection: The Outstanding Properties of the Lotus Leaf. *Beilstein J. Nanotechnol*. 2011, **2** (1), 152–161. https://doi.org/10.3762/bjnano.2.19.

(67) Mirabella, F. M. J.; Barley, J. S. Ostwald Ripening in Lmmiscible Polyolefin Blends. *J Polym Sci Pol Phys* 1995, **33**, 2281–2287.

(68) Wooster, T. J.; Golding, M.; Sanguansri, P. Impact of Oil Type on Nanoemulsion Formation and Ostwald Ripening Stability. *Langmuir* 2008, **24** (22), 12758–12765. https://doi.org/10.1021/la801685v.

(69) Gupta, A.; Eral, H. B.; Hatton, T. A.; Doyle, P. S. Nanoemulsions: Formation, Properties and Applications. *Soft Matter* 2016, **12** (11), 2826–2841. https://doi.org/10.1039/C5SM02958A.

(70) Baldan, a. Progress in Ostwald Ripening Theories and Their Applications in Nickel-Base Super Alloys. *J. Mater. Sci.* 2002, **37**, 2379–2405. https://doi.org/10.1023/A:1015408116016.

(71) Zhu, W.; Bao, C.; Wang, Y.; Li, F.; Zhou, X.; Yang, J.; Lv, B.; Wang, X.; Yu, T.; Zou, Z. Coarsening of One-Step Deposited Organolead Triiodide Perovskite Films via Ostwald Ripening for High Efficiency Planar-Heterojunction Solar Cells. *Dalt. Trans*. 2016, **45** (18), 7856–7865. https://doi.org/10.1039/C6DT00900J.

(72) Yang, M.; Zhang, T.; Schulz, P.; Li, Z.; Li, G.; Kim, D. H.; Guo, N.; Berry, J. J.; Zhu, K.; Zhao, Y. Facile Fabrication of Large-Grain $CH_3NH_3PbI_3$-XBr_x Films for High-Efficiency Solar Cells via CH_3NH_3Br-Selective Ostwald Ripening. *Nat. Commun*. 2016, **7** (May), 2–10. https://doi.org/10.1038/ncomms12305.

(73) Oliva-Ramirez, M.; Macías-Montero, M.; Borras, A.; González-Elipe, A. R. Ripening and Recrystallization of NaCl Nanocrystals in Humid Conditions. *RSC Adv*. 2016, **6** (5), 3778–3782. https://doi.org/10.1039/C5RA22425J.

(74) Lotty, O.; Hobbs, R.; O'Regan, C.; Hlina, J.; Marschner, C.; O'Dwyer, C.; Petkov, N.; Holmes, J. D. Self-Seeded Growth of Germanium Nanowires: Coalescence and Ostwald Ripening. *Chem. Mater*. 2013, **25** (2), 215–222. https://doi.org/10.1021/cm3032863.

(75) Imre, Á.; Gontier-Moya, E.; Beke, D. L.; Szabó, I. A.; Erdélyi, G. Ostwald Ripening of Pd Particles on the $(10\bar{1}2)$ Surface of Sapphire. *Surf. Sci*. 1999, **441** (1), 133–139.

(76) Glasner, K. B. Ostwald Ripening in Thin Film Equations. *SIAM J. Appl. Math*. 2008, **69** (2), 473–493. https://doi.org/10.1137/080713732.

(77) Dai, S. On the Ostwald Ripening of Thin Liquid Films. *Commun. Math. Sci*. 2011, **9** (1), 143–160.

(78) Madras, G.; McCoy, B. J. Ostwald Ripening in Two Dimensions: Time Dependence of Size Distributions for Thin-Film Islands. *Phys. Chem. Chem. Phys*. 2003, **5** (24), 5459. https://doi.org/10.1039/b312257c.

(79) Mackay, D.; Van Wesenbeeck, I. Correlation of Chemical Evaporation Rate with Vapor Pressure. *Environ. Sci. Technol*. 2014, **48** (17), 10259–10263. https://doi.org/10.1021/es5029074.

2.7. APPENDIX

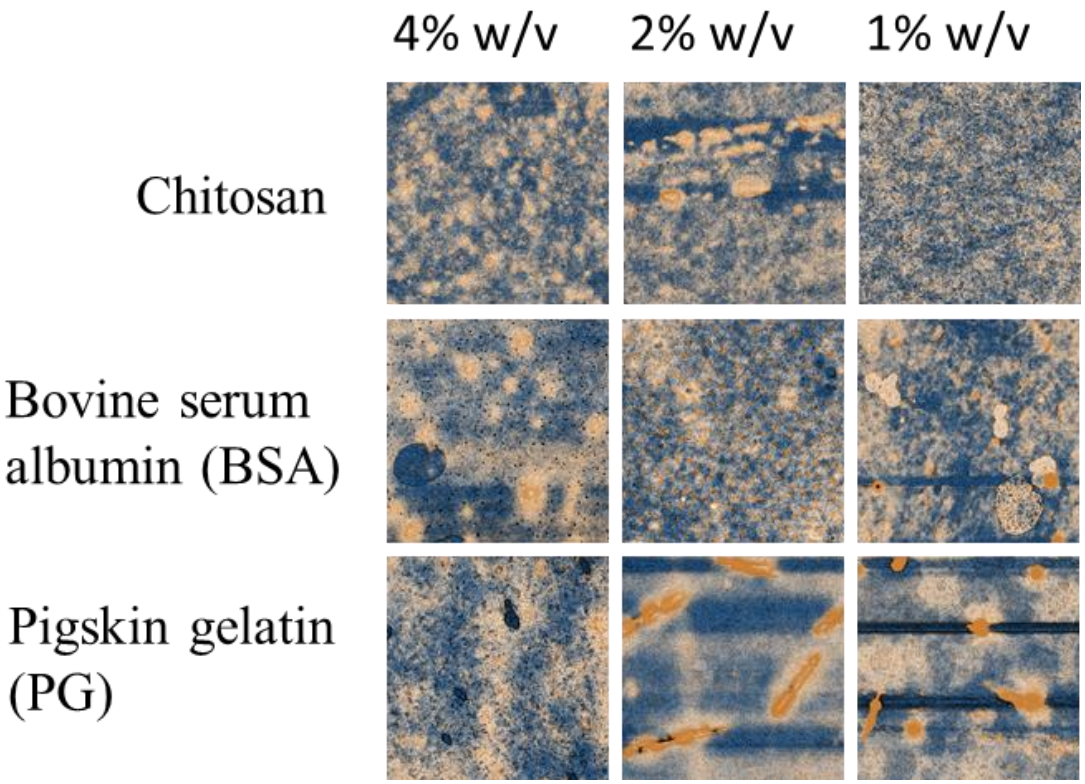


Figure S2.1: *AFM image grid showing results of casting thin-films at 12µm wet deposit from specific P-S or Ps-S solutions. Each image is 10 µm x 10 µm area. Films produced from solutions containing 4%w/v, 2% w/v or 1%w/v biopolymer.*

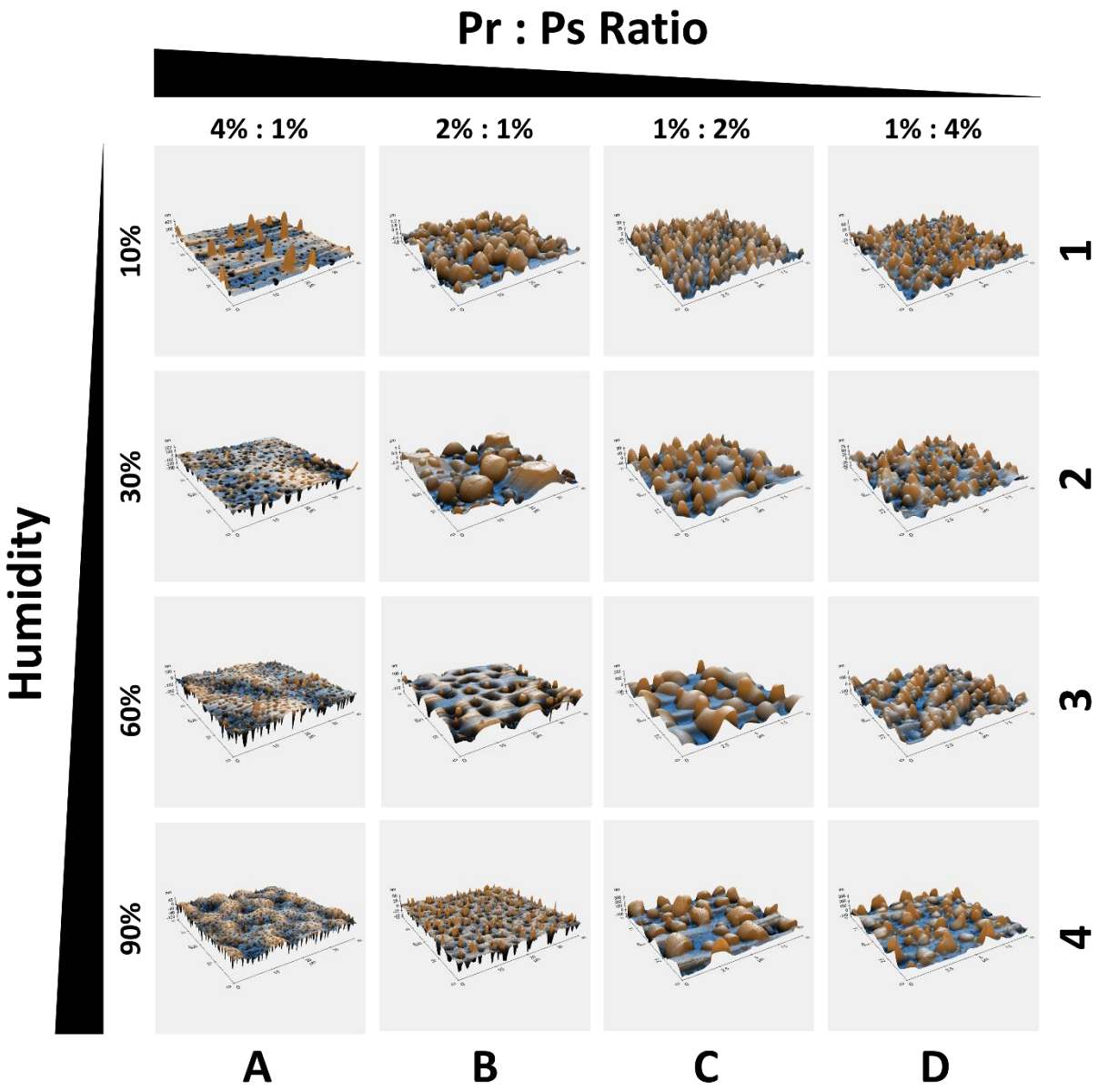


Figure S2.2: *AFM image grid showing results of casting thin-films at 12µm from specific P-Ps-S solutions of BSA-chitosan-formic acid at specific humidities. Each image in column A and column B is 40 µm × 40 µm area. Each image in column C and column D is 10 µm × 10 µm area. Column A = 4 w/v% BSA 1 w/v% chitosan (4:1), column B = 2% BSA 1% chitosan (2:1), column C = 1% BSA 2% chitosan (1:2), column D = 1% BSA 4% Chitosan (1:4). Row 1 = 10% humidity, row 3 = 30% humidity, row 3 = 60% humidity, row 4 = 90% humidity.*

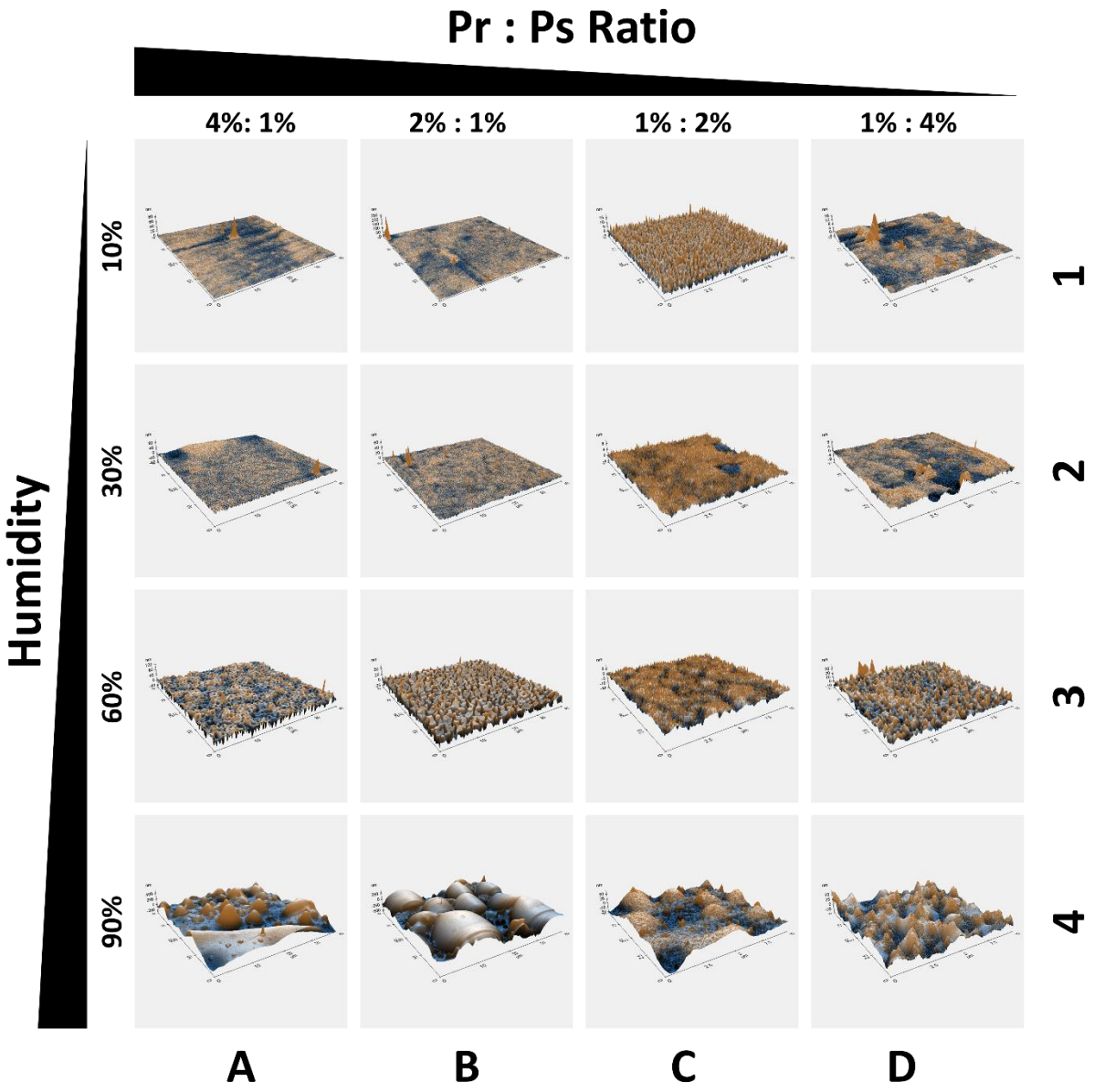


Figure S2.3: *AFM image grid showing results of casting thin-films at 12µm from specific P-Ps-S solutions of PG-Ch-FA at specific, controlled humidities with the automatic film applicator and 12µm bar. Each image in column A and column B is 40 µm × 40 µm area. Each image in column C and column D is 10 µm × 10 µm area. Column A = 4 w/v% PG 1 w/v% Ch (4:1), column B = 2% PG 1% Ch (2:1), column C = 1% PG 2% Ch (1:2), column D = 1% PG 4% Ch (1:4). Row 1 = 10% humidity, row 2 = 30% humidity, row 3 = 60% humidity and row 4 = 90% humidity.*

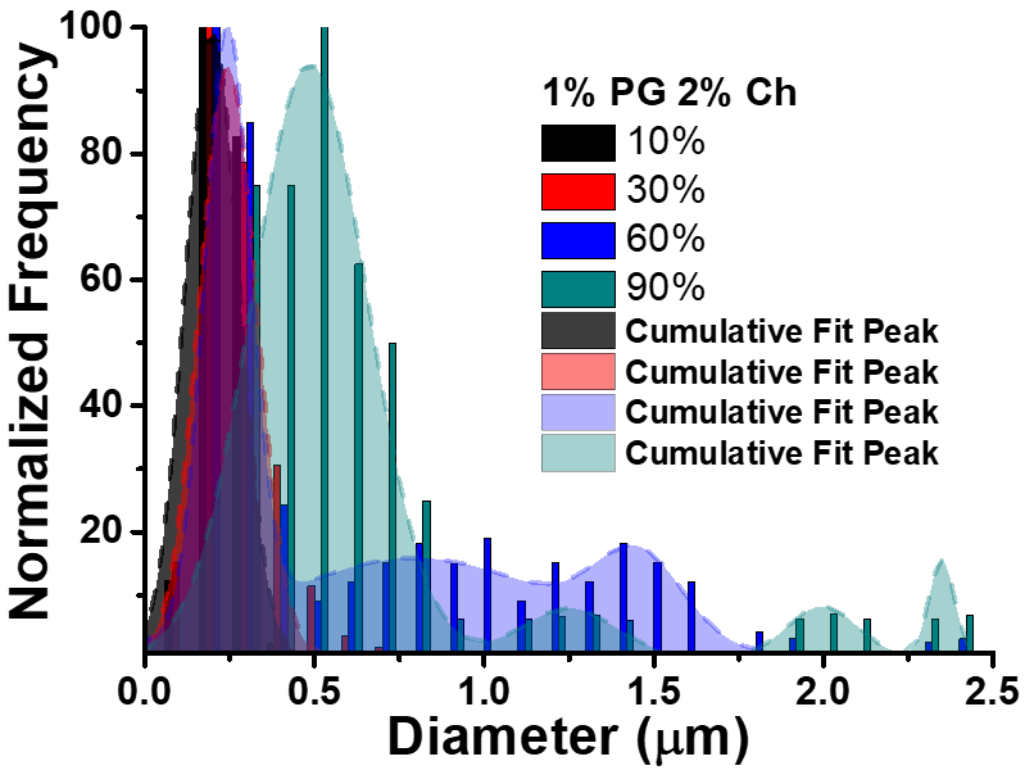


Figure S2.4: *Graph depicts the size distribution of 1w/v% PG 2w/v% Ch displaying overlayed Gaussian p rofile dried under various ambient humidities.*

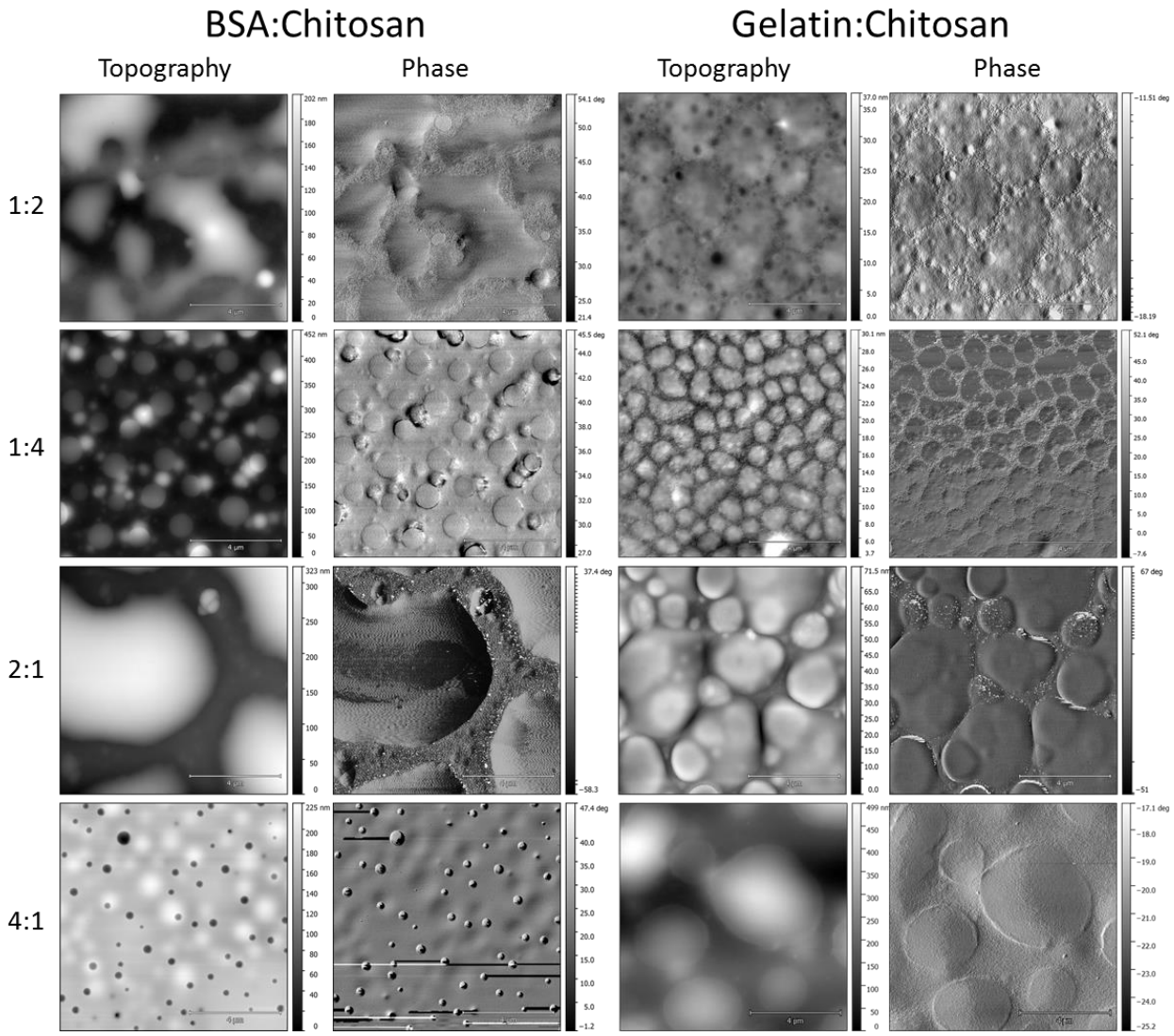


Figure S2.5: *AFM topography and phase images for each blend system. Phase imaging is a standard technique for mapping the spatial variations in the surface elasticity. The blend structures can be observed due to the difference in elasticity between Ch and BSA or PG.*

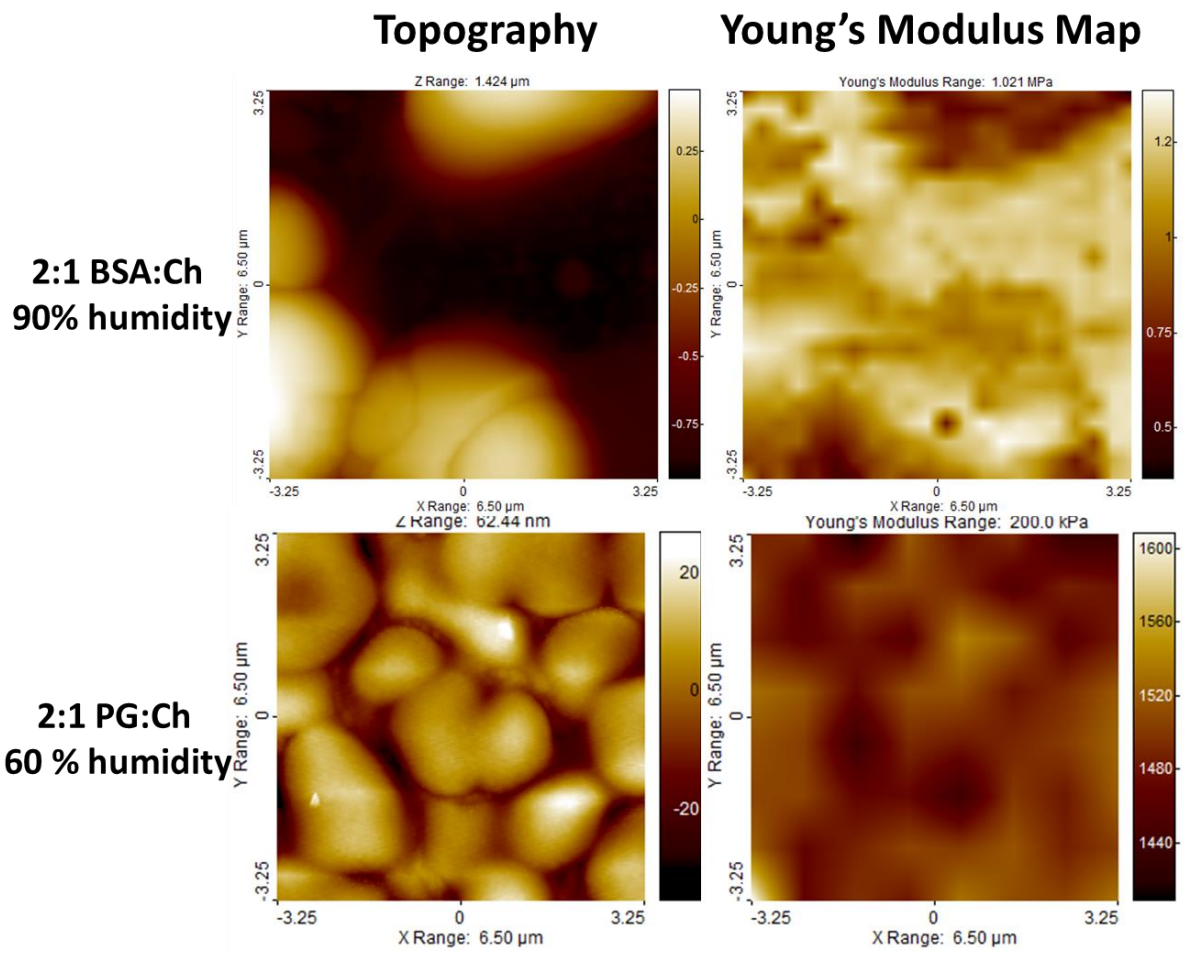


Figure S2.6: *Topography and map of the elastic modulus of the both the BSA:Ch and PG:Ch blend. Each image is 6.5 × 6.5 µm area. The protein and polysaccharide can be distinguished in the Young's modulus map. The Young's modulus map resembles the phase shift image maps of* ***Figure S2.5****.*

Chapter 3

Regulated Phase Separation in Nanopatterned Protein-Polysaccharide Thin Films by Spin Coating

Accepted for publication in:

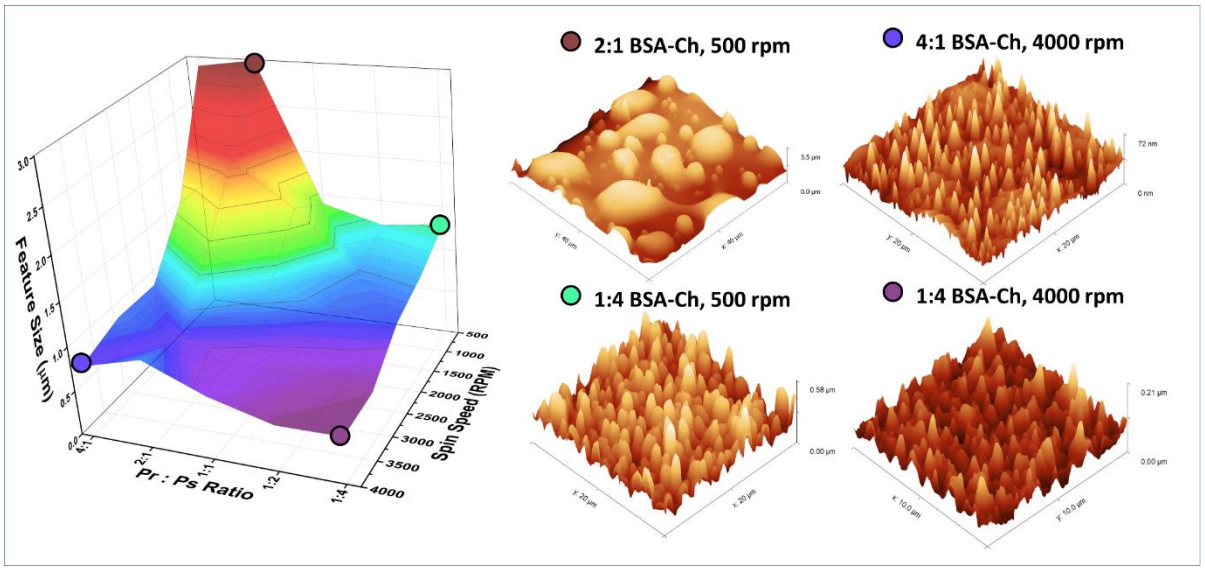
Colloids and Surfaces B: Biointerfaces

March 2020

3.1. ABSTRACT

Greater patterned films are essential to the commonplace technologies of modern life. However, they come at high cost to the planet, being produced from non-renewable, petrochemical-derived polymers and utilising substrates that require harsh, top-down etching techniques. Biopolymers offer a cheap, sustainable and viable alternative easily integrated into existing production techniques. We describe a simple method for the production of patterned biopolymer surfaces and the assignment of each biopolymer domain, which allows for selective metal incorporation used in many patterning applications. Protein and polysaccharide domains were identified by selective etching and metal incorporation; a first for biopolymer blends. Morphologies akin to those observed with synthetic polymer blends and block-copolymers were realised across a large range of feature diameter (200 nm to - 20 μm) and types (salami structure, continuous, porous and droplet-matrix). The morphologies of the films were tuneable with simple recipe changes, highlighting that these biopolymer blends are a feasible alternative to traditional polymers when patterning surfaces. The protein to polysaccharide ratio, viscosity, casting method and spin speed were found to influence the final film morphology. High protein concentrations generally resulted in porous structures whereas higher polysaccharide concentrations resulted in spherical discontinuous domains. Low spin speed conditions resulted in growth of protuberances ranging from 200 nm to 22 μm in diameter, while higher spin speeds resulted in more monodisperse features, with smaller maximal diameter structures ranging from 300 nm to 12.5 μm.

3.2. GRAPHICAL ABSTRACT



3.3. INTRODUCTION

There is an urgent and growing need for micro- and nano-structured surfaces that can be produced at low environmental and economic cost. Micro- and nano-structured surfaces are essential to an array of advanced and emerging technologies. In 2016 the OECD identified 40 key emerging technologies for the future, including the "internet of things" smart devices, light technologies, regenerative medicine and tissue engineering, nanomaterials, nanodevices, carbon nanotubes, functional materials, synthetic biology, and marine and tidal power technologies. One fifth of these require patterned thin-films as integral components or as essential aspects of their production processes.[1]

Micro- and nano-structured surfaces occur throughout the natural world and exhibit a range of useful properties; self-cleaning and hydrophobicity (lotus leaf)[2]; anti-reflectivity (moth eyes)[3]; iridescence (butterfly wings)[3]; anti-ice formation (kale) [4]; and anti-fouling (shark skin)[5], to name only a few. Current human manufacturing of equivalent surfaces uses top-down and bottom-up approaches: top-down is expensive, wasteful, not readily scalable, and generally restricted to planar surfaces.[3] Bottom-up requires the use of block co-polymers (BCPs) which can be expensive, are synthetically derived, require environmentally damaging organic solvents and require intricate control of the polymer-surface interface via brush layers.[6] Feature diameter and spacing is limited to sub-100 nm due to the kinetic penalties imposed on high molecular weight BCPs requiring long annealing times, limiting their applications in the optics industry. Additionally, refining BCPs of a high molecular weight to obtain a polydispersity index (PDI) close to 1 is difficult and costly.[3]

In contrast to BCPs and other synthetic polymers, proteins innately have a PDI of 1, are cheap, abundant, renewable, do not require the use of toxic solvents and are easy to manufacture.[7] More generally, biopolymers (proteins and polysaccharides) are well-defined with varied functionality[8], hydrophilic, photostable, nontoxic, biocompatible[9,10] and have predictable viscosities.[11] The domain sizes of features in polymer blends (synthetic and biopolymer) have been shown to exceed to 10 μm, although feature size showed considerable variance.[12–19] For decades biopolymer blends have been utilised in food texturing[15,16,19,20], with few notable examples using biopolymer blends beyond this.[21,22,31,32,23–30] These, however, incorporated synthetic polymer additives, biopolymer derivatives, and/or specialist enzymes for etching or functionalisation of patterned surfaces. This renders these techniques either unsuitable for large scale manufacturing or environmentally damaging. Protein blends are expected to become prevalent in electronic, optical, chemical, mechanical, biomedical and

nanotech applications in the coming years.[33] However, the use of biopolymer blend thin films in materials science for surface patterning is further limited by the relative infancy of the field.[31]

The aim of this study was the further development of bovine serum albumin (BSA) and chitosan (Ch) blend thin films, using a protic solvent (formic acid, FA) to promote segregative phase separation in a rapid and facile manner. Current efforts to replace BCPs involve the use of synthetic polymer blends to generate patterns. However, as with BCPs, these are not renewable. To offer an alternative, renewable solution to both BCPs and synthetic polymer blends, biopolymer blend thin films must show that they can achieve similar patterns, using established methods. To this end, BSA and Ch were chosen as our biopolymers. BSA and Ch may be blended without fear of gelation when subjected to shear forces.[34] Ch is also antimicrobial[35], biocompatible and biodegradable, increasing the number of possible applications.[36] Finally, both BSA[37] and Ch[38,39] can selectively bind metals, similar to BCPs. Synthetic polymer blends utilize selective removal of one polymer domain, followed by deposition of a metal to generate a patterned hard mask. In our work, we successfully removed the protein domain using a buffer solution, and selectively incorporated metal into the polysaccharide domain. BSA-Ch blends achieve feature diameters comparable with synthetic polymer blends.[3,40,41] This method could be easily employed in other studies of biopolymer blends. Furthermore, this is the first time a hard mask has been produced with bottom-up biopolymer blends. Lastly, we have successfully differentiated the growth mechanisms occurring with dissimilar blend compositions.

3.4. EXPERIMENTAL

3.4.1. BIOPOLYMERS, CASTING SOLUTION AND SUBSTRATE

Low molecular weight chitosan (Ch, 50-190 kDa, > 75% deacetylation) and bovine serum albumin (BSA, lyophilised powder, ≥ 96%, molecular weight ~66 kDa) were purchased from Sigma Aldrich. While the Ch we sourced was the deacetylated form of chitin (i.e. a chitin derivative, which may be considered a semisynthetic), Ch may also be sourced from fungal biomass without the need for derivatization.[42] Ch is renewable, and it is much more easily solubilized than chitin. Hence it was chosen for this work. Low molecular weight chitosan was chosen as it was shown previously shown to be easily solubilized in the FA, while not being excessively viscous.[34] Substrates used in all cases were Fisherbrand™ Microscopic Slides with Ground Edges (plain) or planar substrates. Highly polished single-crystal silicon

<100> wafers (p-type, boron) with a native oxide layer of ~2 nm were also used. For FTIR, XPS, water contact angle, and selective metal inclusion, samples were deposited on a Si substrate. This was done to prevent any deformation of a glass substrate during annealing. The solvent used was formic acid (FA), 98+ %, pure (ACROS Organics™) and was diluted to 90% w/v with distilled water before use. Casting solutions were prepared using 90% formic acid as the solvent to ensure that the biopolymers were below their isoelectric point in solution and so, positively charged.

3.4.2. SOLUTION PREPARATION

Biopolymers blend preparation may be found in our previous work, or in section **2.3.2 Solution Preparation**. In short, stock solutions were made by dissolving biopolymers in 90% FA, and stored at -20 ºC. Before coating, stock solutions mixed with one another and diluted with fresh FA.[34] 5 solutions were prepared. 4 w/v% BSA 1 w/v% Ch (4:1 blend ratio), 2 w/v% BSA 1 w/v% Ch (2:1 blend ratio), 1 w/v% BSA 1 w/v% Ch (1:1 blend ratio), 1 w/v% BSA 2 w/v% Ch (1:2 blend ratio) and 1 w/v% BSA 4 w/v% Ch (1:4 blend ratio).

3.4.3. COATING PREPARATION AND ANALYSIS

3.4.3.1. THIN-FILM CASTING

Thin-films were prepared using a spin coater (Speciality Coating Systems, 6800 Spin Coater Series) to produce biopolymer solution coatings of uniform thickness. Standard conditions: 30 s spin time (ramp time 5 s, dwell 25 s). Substrates were glass slides onto which single biopolymer solutions were cast. Temperature and humidity was maintained at approx. 18 ºC and 65% relative humidity. Monitoring of humidity and ambient temperature was done by *HOBO MX Temp/RH Logger* sensor.

3.4.3.2. ATOMIC FORCE MICROSCOPY

Sample morphology was analysed by atomic force microscopy (AFM) using a Park Systems, XE-100 instrument under ambient conditions in non-contact mode, and this methodology was used in our previous work.[34] Scans were performed in non-contact mode with high resolution, silicon micro-cantilever tips. Topographic images were recorded at a resonance frequency of 270-300 kHz. Images were analysed using *Park XEI* and *Gwyddion*, and resulting data

analysed using *Origin.* Images were flattened by removal of the background plane (using a first or second regression order). Features were then identified using the Gwyddion watershed algorithm for analysis, and descriptive statistics calculated using "Microcal Origin" software. Surface roughness (nm) and surface area ratios (%) were measured using "XEI" software. RMS (*root means square arithmetical mean roughness* or *root means square average roughness*) is the average between the height deviations and the mean line/surface, taken over the evaluation length/area. Surface area ratios (%) were calculated by the following formula: Surface Area Ratio (%) = 100 (%) × (Geometric Area – Surface Area) / (Geometric Area). Surface feature diameters were measured using the Gwyddion watershed algorithm for scanning probe microscopy (approx. 1000 features). Film thickness was determined by AFM. AFM height scans were performed on areas which had been scratched to expose the underlying substrate.[26]

3.4.3.3. X-RAY PHOTOELECTRON SPECTROSCOPY (XPS)

XPS spectra were acquired on an Oxford Applied Research Escabase XPS system equipped with a CLASS VM 100 mm mean radius hemispherical electron energy analyser with a five-channel detector arrangement in an analysis chamber with a base pressure of 10×10^{-10} mbar. Survey scans were acquired between 0-1000 eV with a step size of 0.7 eV, a dwell time of 0.5 s and pass energy of 50 eV. Core level scans were acquired at the applicable binding energy range for each core level, with a step size of 0.1 eV, dwell time of 0.1 s and pass energy of 20 eV averaged over 20 scans. A non-monochromated Al Kα x-ray source at 200 W power was used for all scans. Multiplier voltage was maintained at 2.0 kV for all acquisitions. All spectra were acquired at a take-off angle of 90º with respect to the analyser axis and were charge corrected with respect to the C 1s photoelectric line by rigidly shifting the binding energy scale to 285 eV. Data were processed using CasaXPS software where a Shirley background correction was applied and peaks were fitted to Voigt profiles.

3.4.3.4. ATTENUATED TOTAL REFLECTION FOURIER TRANSFORM INFRA-RED (ATR-FTIR) SPECTROSCOPY

Infrared spectra were recorded on a PerkinElmer Spectrum 2 FT-IR Spectrometer. Perkin-Elmer Spectrum v5.0.1 software was used to perform baseline corrections and evaluate spectra. Each spectrum was scanned between 400 and 4000 cm^{-1} with a resolution of 4 cm^{-1} and a minimum of 64 scans were collected and averaged in order to gain good quality spectra.

3.4.3.5. SELECTIVE ETCHING

A wet etch was used in order to selectively remove BSA over Ch due to its limited solubility.[43] Biopolymer blend films were crosslinked with a 20 wt% glutaraldehyde solution for 20 hr. Coated substrates were immersed in a buffered solution stirring for 20 hr at 300 rpm. Buffered solutions contained 200 mM Tris-HCl, pH 8.8. The substrate was then washed thoroughly with deionised water to remove residual salt. Finally, the substrate was washed with isopropanol alcohol and dried under nitrogen for analysis.

3.4.3.6. SELECTIVE METAL INCLUSION

To confirm the results of the selective etching of BSA using a basic buffer solution, and identify the Ch domain, selective inclusion of the metal into the Ch domain used. As a 1:1 BSA-Ch blend was used to identify the BSA domain using a selective etch, the 1:1 BSA-Ch blend was also used for selective metal inclusion. 1:1 blend films were prepared as described in the Thin-film Casting section, producing a film with discontinuous spheres in a matrix. After casting, films were crosslinked with a 20 wt% glutaraldehyde solution for 20 hr to prevent oversaturation of metals in the Ch domain. 1 wt% $FeCl_3$ solutions were produced with anhydrous ethanol. Biopolymer blend films were covered with 1 mL of metal solution for 15 s before spin coating. The films were then immediately spin coated for 30 s (3000 rpm, ramp time 5 s, dwell 25 s). The samples were then oxidised in a furnace at 550 ºC for 2 hr. Calcination at 800 ºC for 20 hr was used to remove the biopolymer template and any residual organic residue. No other processing steps were needed.

3.4.3.7. WATER CONTACT ANGLE (WCA)

Water contact angle measurements were obtained using the Ossila Contact Angle Goniometer (error ± 1º) and accompanying software Ossila Contact Angle v1.0. A deionised water droplet (5 μL) was delivered to the coated surface by a calibrated variable pipettor. Contact angles were measured in triplicate as a function of time. Measurements were taken at 10 s intervals over 160 s including measurements at 0 and 160 s.

3.5. RESULTS AND DISCUSSION

3.5.1. SINGLE POLYMER SOLUTION THIN-FILMS

AFM images (see **Figure S3.1**) showed that thin-films cast from the two individual biopolymers (Ch and BSA) did not produce any phase separated patterns. Neat BSA films were totally featureless (**Figure S3.1**), while Ch showed partially aggregated structures, likely due to its limited solubility. Glass slides were smooth and featureless. This shows that features present in subsequent composite biopolymer films are due solely to the composite formation mechanisms and not due to structures from an individual biopolymer. This is consistent with our previous findings.[34]

3.5.1.1. THIN-FILMS FROM PHASE SEPARATION OF BSA-CH-FA SOLUTIONS

Phase separation in polymer blend systems is the development of two distinct regions (phases) of polymers from an initially homogenous solution. Similar to oil and water, polymers which are incompatible separate from one another. Dissolving biopolymers in an acid protonates the polymer chains, promoting segregative phase separation.[15] Upon separation, topographical features develop as the film dries as the system attempts to minimize surface energy. Typically, spheres or pores are formed as they have the lowest surface area to volume ratio. These features grow as the system continues to minimize total surface energy. [44,45]

Figure 3.1 shows AFM images of BSA-Ch blend films. High resolution images each blend are provided in **Figure S3.2** – **S3.6,** with accompanying line profiles provided in **Figure S3.7 – S3.11**). Pores formation in the 4:1 and 2:1 BSA-Ch blend formed through different mechanisms. Pores are discussed in the in the Appendix, section 3.8.3**.**

In the 4:1 BSA-Ch blend, increased spin speed inhibited protuberance (spherical bumps) growth, resulting in smaller, more homogeneously dispersed spheres. Feature diameter and density data (represented as mean±standard deviation, **Figure 3.2** and **Figure S3.12**) shows increased spin speed decreased protuberance diameter, and increased protuberance number per area (protuberances/μm^2). This follows the general trend observed for all films. Mean protuberance diameter decreased from 2.91 μm (500 rpm) to 0.81 μm (4000 rpm) (**Figure 3.1**, A1 – A5). The 4:1 BSA-Ch blend was the only blend to contain salami structures ≥ 50 μm (**Figure S3.13**). Deposition at 500 rpm of the 4:1 blend resulted in dewetting, attributed to the feature length approaching film thickness.[17] This is known to occur during the latter stages of, and interfere with, phase separation. Low spin speeds when casting films allows more time for

phase separation to occur, causing feature diameter to exceed film thickness (**Figure S3.12, Figure S3.15**), leading to the salami structure. The discontinuous salami domain is composed entirely of protuberances. Pores are localised outside perimeter of the salami domains. The formation of the salami morphology at this blend ratio may explain the variation in growth mechanism compared to a high polysaccharide content blend (see below). This indicates that pores within the BSA domain (and protuberances contained within the discontinuous Ch domain) are controlled by a secondary phase separation process, which is consistent with our observations of film thickness [17,46]. Lastly, in the 4:1 blend, higher spin coating speeds resulted in thinner samples, as did blend solutions with lower viscosity (lower w/v% solutions, **Figure S3.15**).

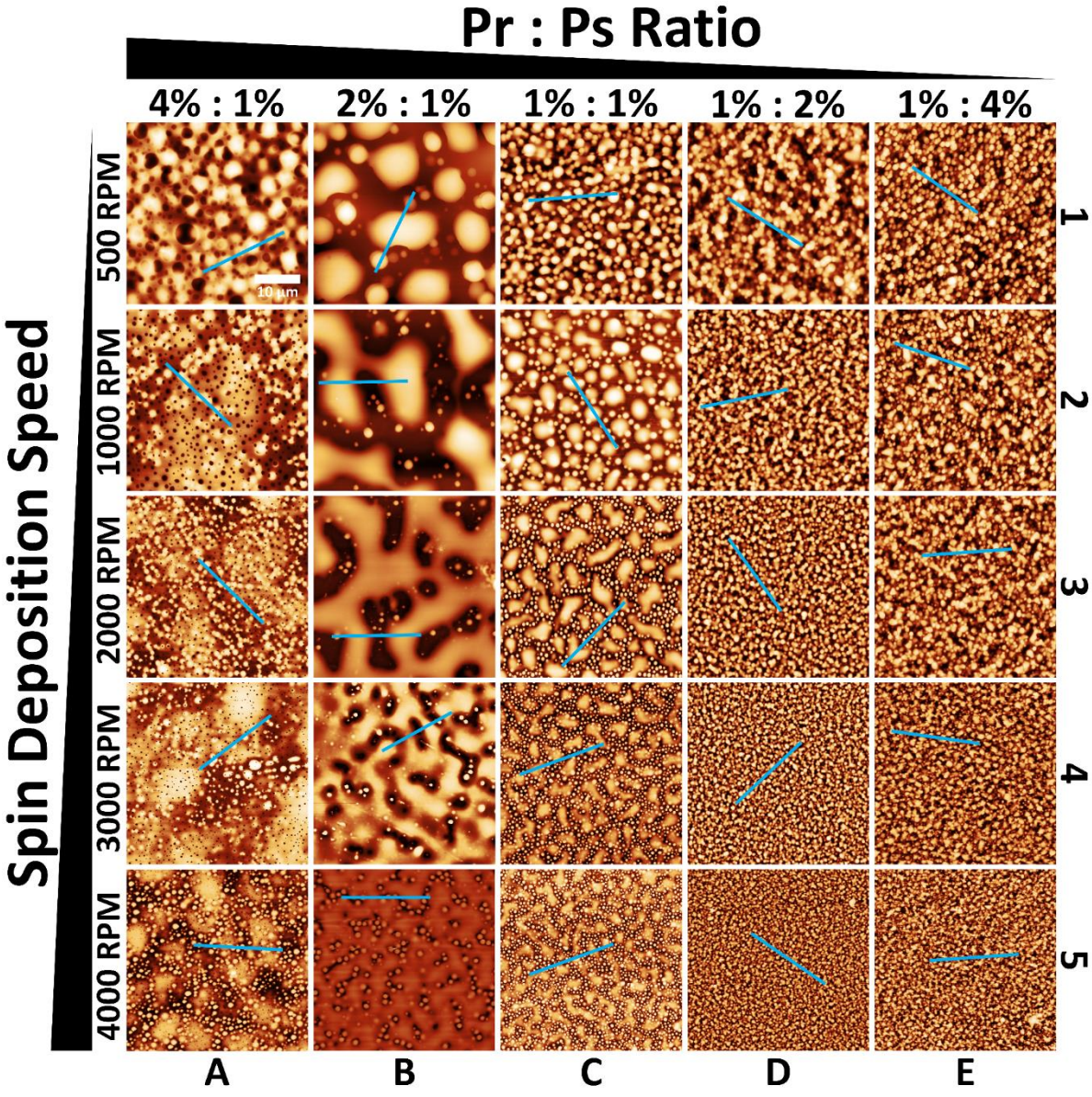


Figure 3.1: *AFM image grid showing results of casting thin-films at 65% relative humidity from specific Pr-Ps (protein-polysaccharide) solutions of BSA-Ch-FA at various spin*

speeds. Each image is 40 µm × 40 µm area (scale bar 10 µm, shown in 4:1 blend at 500 rpm). In the image, bright areas are higher and dark areas are lower. Line profile (blue lines) may be found in each image and its corresponding **Figure S3.2 – Figure S3.6**. *Column A = 4 w/v% BSA and 1 w/v% Ch (4:1), column B = 2 w/v% BSA and 1 w/v% Ch (2:1), column C = 1 w/v% BSA and 1 w/v% Ch (1:1), column D = 1 w/v% BSA and 2 w/v% Ch (1:2), column E = 1 w/v% BSA and 4 w/v% Ch (1:4). Row 1 = 500 rpm, row 2 = 1000 rpm, row 3 = 2000 rpm, row 4 = 3000 rpm and row 5 = 4000 rpm.*

At all spin speeds, protuberances follow a general trend of decreasing mean diameter with increasing spin speed (**Figure 3.2a**). As a result, BSA-Ch blend film root-mean-squared (RMS) roughness of the films and surface area ratio (%) decreases with increasing spin speed, discussed in more detail in section **3.8 Appendix** (**Figure S3.16**). As protuberances are the desired morphology, a simple, predictable and efficient method of controlling feature diameter like this is highly advantageous.

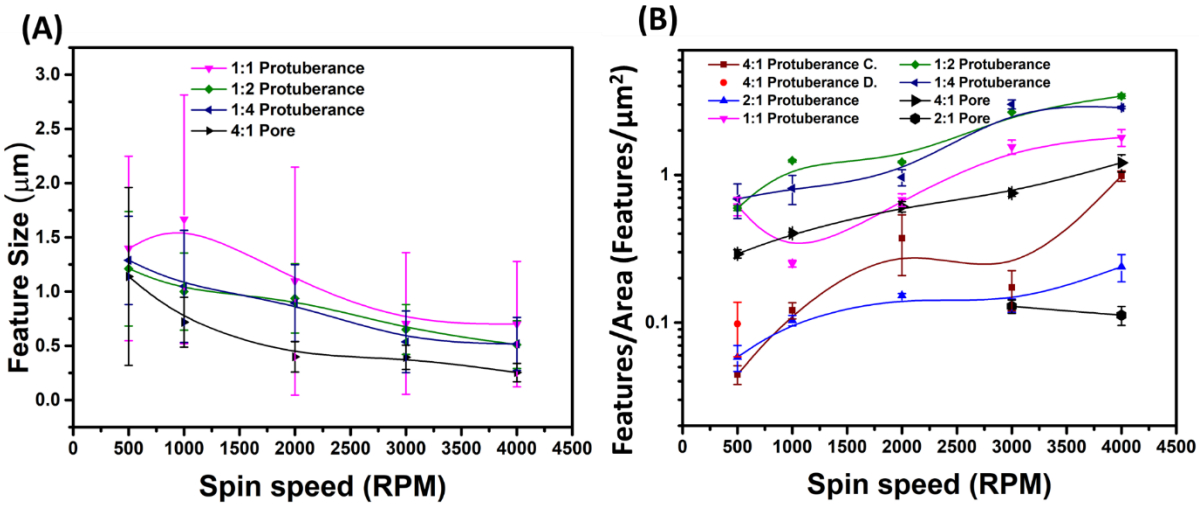
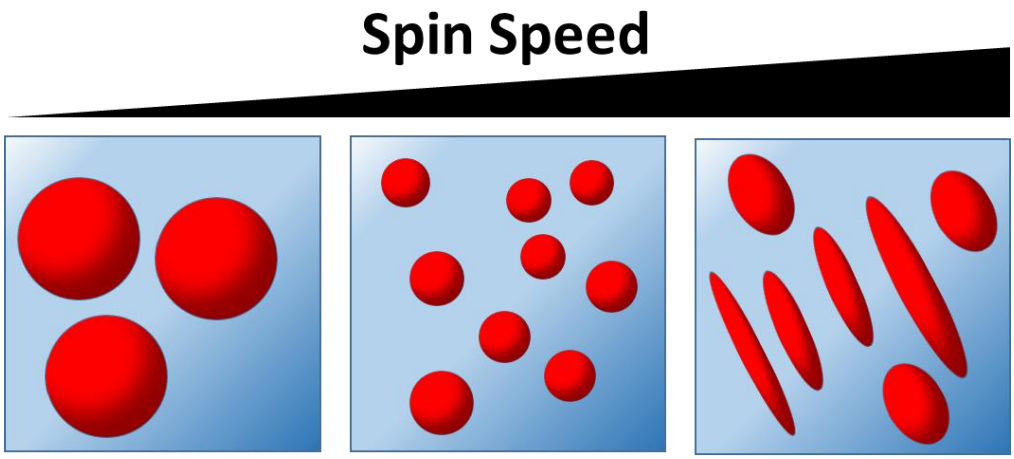


Figure 3.2*: Statistical analysis of BSA-Ch blends for feature diameter and feature number/area. All but the 4:1 blend refers to protuberance measurements, with the 4:1 and 2:1 blend data displaying both protuberance and pore data separately. The circular legend for the 4:1 blend refers to feature diameter in the discontinuous domain, i.e. salami structure regions.* ***A)*** *Refers to feature diameter plotted against spin speed while* ***B)*** *details features/µm^2 vs spin speed for 4:1, 2:1, 1:1, 1:2 and 1:4 blends respectively.*

Figure 3.1 Column B contains the most visually distinct film structures, with the largest protuberances of any blend formed. **Figure 3.1**, B1 and B2, show that increasing the film casting spin speed of 2:1 BSA-Ch blends reduced mean protuberance diameters from 2.91 µm

(500 rpm) to 1.60 µm (1000 rpm). The same increase in rpm also narrowed protuberance size distribution (SD), from 1.5 µm – 6.1 µm to 0.7 µm – 3.2 µm. Spin speeds above 2000 rpm produced a mixed porous/protuberant (**Figure 3.1**, B3 – B5). Protuberance diameter decreases from 1000 rpm to 3000 rpm (1.6 µm to 0.81 µm). This reduction in protuberance diameter is less than the initial reduction from 500 to 1000 rpm (**Figure 3.1**, B2 – B4). Protuberance mean diameter increases at 4000 rpm (**Figure 3.1**, B5) to 0.99 µm. The increase in mean diameter is likely due to shear at high speeds, as increased speeds should remove solvent quicker, inhibiting growth. Spin speed thereby reduces the diameter of protuberances through faster solvent evaporation and create larger ovoid protuberances (non-spherical protuberances elongated on one axis) through shear forces, similar to the pore effect described in the 2:1 blend (**Scheme 3.1**)..[18] The number of protuberances per area increased linearly from 500 rpm to 4000 rpm with increased spin speed (**Figure 3.2b**). The submicron features in **Figure 3.1** are smaller than most biopolymer blends in the literature (typically 10 µm in diameter and above). We attribute our smaller features to the chosen biopolymers, spin speed, and chosen solvent.[12]



Scheme 3.1*: Increasing deposition speed results in an initial reduction of the diameter of discontinuous features, followed by an elongation of these features at excessive spin speeds, due to the shear forces exerted on the blend.*

Solvents likely play a large role in forming the large features typically associated with biopolymer thin-films morphologies and other structures produced from biopolymer blends. Slowly evaporating blends produce large scale features.[23,47] Low vapour pressure (non-volatile) solvents evaporate slowly, while high vapour pressure (volatile) solvents evaporate quickly producing smaller feature sizes.[47,48] This may explain why biopolymer blends produce large features, as water is the typical solvent. [12,49–51] De Jong & van de Velde segregatively

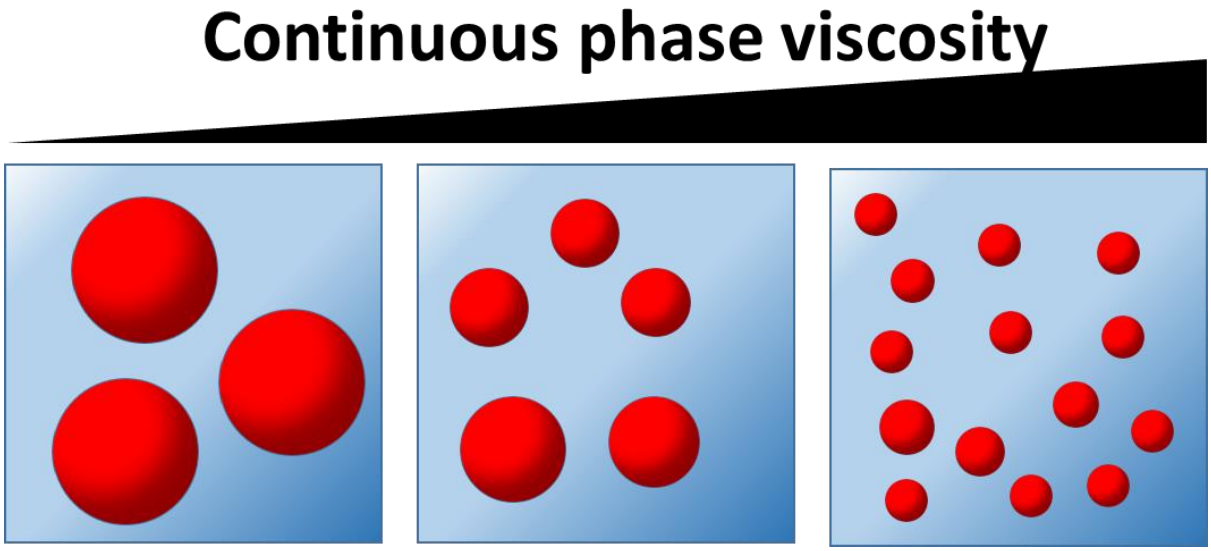
phase separated whey protein/polysaccharide blends using water. Features were 5 – 10 μm in size.[12] PS/PEG blends use toluene, which is much more volatile than water, producing features 200 – 400 nm in diameter.[40] Furthermore, using toluene as a solvent (less volatile) produces larger features than chloroform (more volatile).[47]

When the quantities of protein and polysaccharide are approximately equal (1 w/v% BSA to 1 w/v% Ch (**Figure 3.1**, Column C)) an intermediate state is seen, where larger, coalesced features are observed, but a continuous phase is not sufficiently formed. Protuberance diameter initially increases from approx. 1.40 μm to 1.67 μm with spin speed increase from 500 to 1000 rpm (**Figure 3.2a)**. This is in conjunction with a sharp decrease in protuberances per area (**Figure 3.1b**) suggesting a growth process. From 1000 rpm to 4000 rpm (**Figure 3.1**, C2 – C5), protuberance diameter decreases from 1.67 μm to 0.71 μm, while the number per area increases (**Figure 3.2b**). This data shows that reducing the time for solvent loss produces smaller protuberances and that there is a large degree of control over pattern formation. However, above 1000 rpm protuberances are more irregular and less circular in shape. While the 1:1 BSA-Ch blend produces smaller protuberances than previously discussed blends, higher speeds introduce an undesired pattern inhomogeneity. Increasing spin-coating speed from 2000 rpm to 4000 rpm results in increased average diameter of these irregular protuberances (2.6 – 6.0 μm). These features appear similar to high spin speed 2:1 blends (**Figure 3.1**, B2 – B5). The 1:1 blend at 2000 rpm (**Figure 3.1**, C3) adopts a morphology similar to 2:1 blend at 1000 rpm (**Figure 3.1**, B2) with larger protuberances interconnecting to form irregularly shaped ovoids. 3000 rpm (**Figure 3.1**, C4) produces flatter, larger, more branched features, similar to 2:1 BSA-Ch blends at 2000 rpm (**Figure 3.1**, B3). This effect is further exaggerated at 4000 rpm (**Figure 3.1**, C5). We attribute this to higher shear stresses on larger structures at higher spin speeds.

Reduction of the BSA ratio from 2:1 to 1:1 (**Figure 3.1** Column C, **Figure S3.4**) results in insufficient protein quantity to form a continuous phase as in **Figure 3.1** B3, *i.e.* phase inversion does not occur preventing the pseudo pores seen in the 2:1 blend. This indicates that high protein concentration is required for pore formation. The reduction of protein content to 1 w/v% produced a more monodisperse sample, and provided smaller feature diameters than 2:1 and 4:1 BSA-Ch blends, both desirable traits for patterning surfaces. Equally, the reduced BSA content produced smaller protuberances, as did higher spin speeds. Complicating things further, spin speeds above a certain maximum elongate the larger structures on the surface; that maximum is blend dependant. The reduction of BSA w/v% (in contrast to the 2:1 and 4:1 blends) produces smaller BSA domains as less material is present to form these domains.

While mean diameter reduces with increased spin speed, larger domains increase in diameters under shear with increased spin speed. Nevertheless, the 1:1 BSA-Ch blend results demonstrate the ability to easily control feature diameters and features/area. This is vital for maximising applicability. Use of patterned biopolymer films in a broad range of applications necessitates the ability to produce an equally broad range of features' diameters and frequencies.[33]

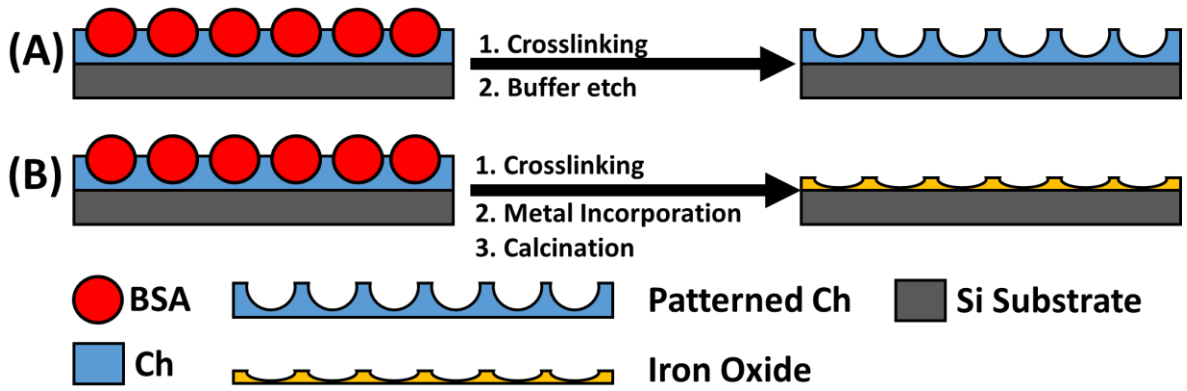
1:2 (**Figure 3.1**, Column D and **Figure S3.5**) and 1:4 blends (**Figure 3.1**, Column E and **Figure S3.6**) follow the simplest, and near identical, trends. Protuberance diameter decreases linearly while increasing spin speed for both blends, with diameters generally smaller for the 1:2 BSA-Ch blend. Mean protuberance diameter ranges from 1.21 - 0.51 μm for 1:2 blends compared to 1.29 - 0.52 μm for 1:4 blends, with spin speeds increased from 500 to 4000 rpm. Both the 1:2 and 1:4 blends show feature diameters smaller than 1:1, 2:1 and 4:1 blends. The increased concentration of the continuous phase (Ch) increases viscosity, limiting coalescence thereby reducing feature diameter (**Scheme 3.2**) .[33] The primary differences lie in the histograms for both blends, with the 1:4 blends showing better defined peaks at higher spin speeds, indicating inhibited growth.[52] Both blends exhibit little growth in protuberances per area until a large increase is observed from 2000 - 3000 rpm (**Figure 3.2b**). This demonstrates that biopolymer blends may be treated the same way as traditional polymer blends, meaning biopolymer blends can be processed with pre-established techniques. Further, this method of producing a patterned surface with biopolymer blends is much quicker than previously discussed techniques, and produces features of approximately 1 μm.[34] This is much smaller than other bottom-up biopolymer techniques, and is similar to blends produced with synthetic polymers.[40,53–57]



Scheme 3.2: *Increasing the viscosity of the continuous phase, the wt% of Ch (blue) reduces the diameter of discontinuous features, BSA (red), by impeding polymer mobility.*

3.5.1.2. Chemical Characterisation of BSA-Ch Blend Films

Immersing coated substrates in a basic aqueous solution selectively dissolves the readily water-soluble BSA. This allows for selective removal of the protein (**Scheme 3.3a**). **Figure 3.3a** shows the 1:1 BSA-Ch blend, while **Figure 3.3b** shows both the large and small BSA domains removed from the Ch matrix. Line profile analysis shows that larger domains do not penetrate directly to the substrate, but are suspended in the Ch matrix. Smaller spherical domains protrude much deeper into the Ch domain confirming late stage dewetting. Many of the pores in **Figure 3.3b** contain extruded rims extending from the surface, producing a crater shape. This provides insight into the protuberances formation mechanism. Coalescence of droplets is generally broken into four steps: (i) droplet approach, (ii) matrix drainage between droplets, (iii) breakup of the matrix film and (iv) relaxation of coalesced droplet into spherical shape.[58–60] Drainage of the Ch matrix is observed in smaller BSA protuberances in contact with larger BSA domains. However, many pores retain this crater morphology (**Figure 3.3c**). Other work on polymer blends has shown these sharp, elevated rims occur when the continuous phase climbs around the discontinuous droplets, *i.e.* pinning of the triple-phase protein-polysaccharide-air boundary, droplet breakup, and resultant inhibited growth.[61,62] Note that the features in our etched BSA-Ch blend are over thirty times smaller than those of polystyrene/poly(methyl methacrylate) blends, and are equivalent to polyfluorene blends. This was seen in other blends (**Figure S3.17** in section) with rim height approx. 40 nm.



Scheme 3.3: ***(A)*** *Details the removal of BSA (the discontinuous phase) via a buffered etch, to leave a porous array of Ch.* ***(B)*** *Shows the infusion of metal into the Ch phase, with calcination of the biopolymer template resulting in a porous metal array, mimicking the Ch phase.*

When using BCPs to pattern metals, metal is incorporated in to a single domain due to the different chemistries of each BCP block.[63] Ch is well known for its metal binding capacity, due to the free electron pair on the amino group.[64–67] $FeCl_3$ was chosen as the metal incorproate, as the amino group of Ch will chelate hard cations such as Fe^{3+} (**Scheme 3.3b**).[68] Unlike Ch, BSA binds to soft metal cations.[37] $FeCl_3$ was chosen as the metal incorporate for a second reason. Metal anions can promote, or inhibit, the binding of metal cations to proteins. In particular, the Cl^- anion has a low affinity for BSA, as it is weakly hydrated. This effect is described by the Hofmeister series.[69,70] By choosing $FeCl_3$ as the metal precursor, both the hard nature of the metal cation, and weakly hydrated nature of the metal counter-anion, ensure that metal is incorporated only into the Ch domain. This allows for identification of the Ch phase. Water was not chosen as a solvent for $FeCl_3$, as BSA is soluble in water. Using water as a solvent for metal incorporation would result in the solubilization (and removal) of BSA during the metal incoporation step, interfering with the identification of the Ch phase. The use of anhydrous EtOH ensures the BSA domain is not solubilized. Though the number of factors considered may seem excessive, trying to incoproate metal into a singular biopolymer domain is no small feat. **Figure 3.3d** confirms that the continuous phase is Ch due to the Fe_3O_4 uptake mirroring the BSA-Ch blend. Large BSA ovoid protuberances are reflected as large irregularly shaped voids (large areas absent of metal uptake) in **Figure 3.3d**. Smaller BSA protuberances are reflected as circular pores in the metallic film. Both the BSA etch and metal incorporation do not reveal the bottom silicon substrate, indicating a thin layer of Ch separates the BSA droplets from the substrate, blocking the Si surface, a feature observed in almost all polymer

blends.[53] Any application this may have as a hard mask would require perforation of the BSA domain to the Si substrate, as the Si must be accessible to the etchant. To the best of our knowledge, purely lateral phase separation of a polymer blend has only been achieved once.[53]

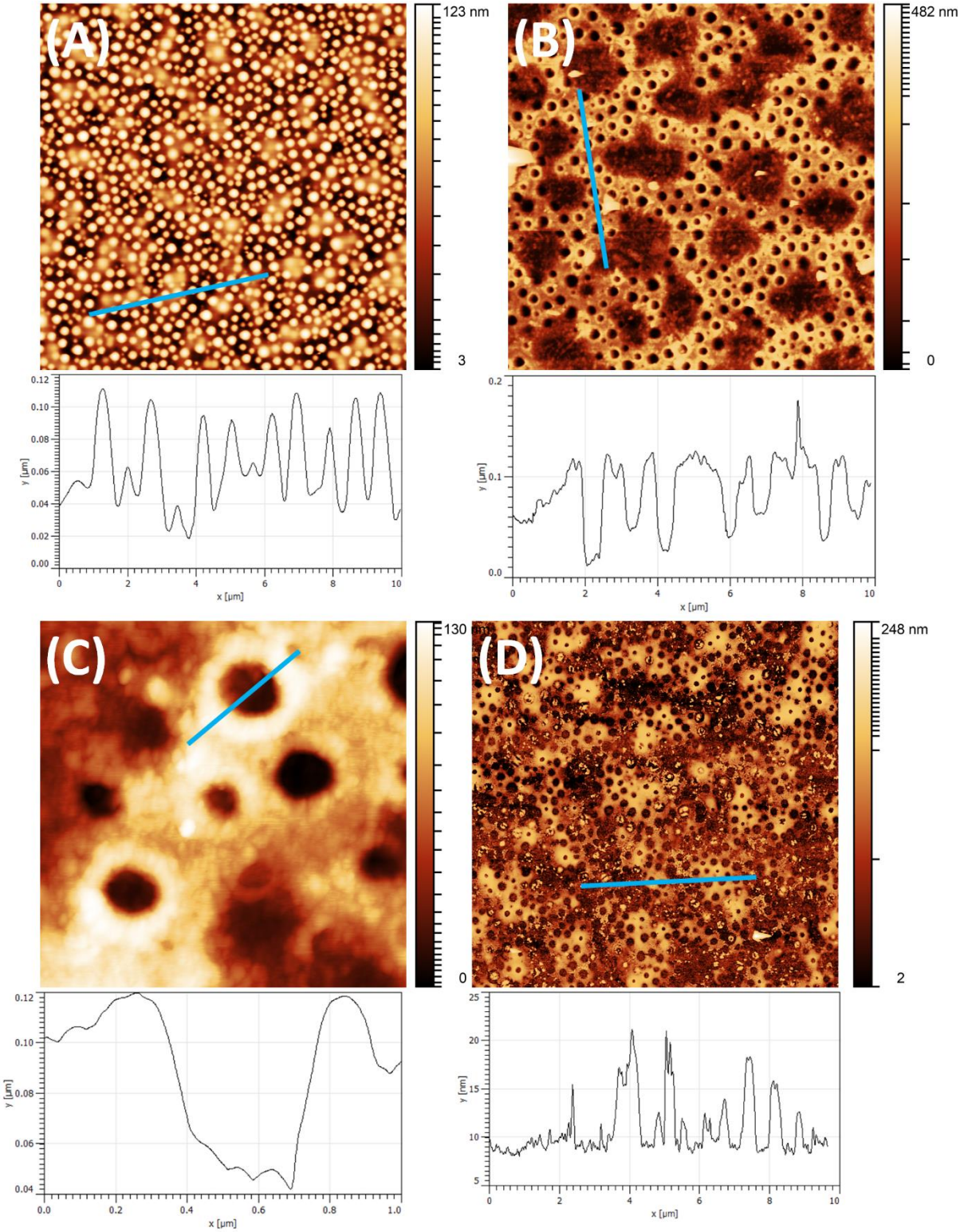


Figure 3.3: *AFM images and surface profiles of 1:1 BSA-Ch blends, 3000 rpm on planar silicon substrates.* ***A)*** *Refers to blend before Tris-HCl etch.* ***B)*** *Refers to blend post*

selective etching. ***C)*** *Enhanced view of selectively etched BSA domains demonstrating extruded rim structure in Ch film.* ***D)*** *Refers to blend post selective metal incorporation and calcination.*

Figure 3.4A shows FTIR transmission spectra of the biopolymer blend after various processes. This was done to confirm chemical changes in the sample after BSA removal, crosslinking, and calcination. For clarity of comparison, a bare Si wafer, plain BSA, and plain Ch were analysed so that their identifying peaks could be differentiated from any unique to the blend films. The bare Si wafer (**Figure 3.4A**, spectra i) has standard identifying peaks at 514 (Si–O deformation)[71], 611 (Si–Si bond vibrations in the bulk)[72], 739 (O–H out of plane bending)[71], 891 (Si–O–H mode due to oxidation of upper silicon layer)[72] and 1108 cm^{-1} (Si–O–Si asymmetric stretching).[73] The shape and intensity of these peaks are similar for all samples**.** The neat BSA film spectrum (**Figure 3.4A**, spectra ii) contained a weak band at 1376 cm^{-1} due to CH_3 symmetric bending.[74] The amide I, and amide II modes of BSA were observed at 1656 cm^{-1} and 1544 cm^{-1} respectively.[74] The amide II' transmission band is seen at 1448 cm^{-1}.[75] The peak at 3208 cm^{-1} can be assigned to asymmetric and symmetric H–O–H stretching, resulting from residual water in the film after casting.[74] Peaks in the Ch spectra (**Figure 3.4A**, spectra iii) are observed at 1718 cm^{-1}, 1573 cm^{-1} and 1374 cm^{-1} corresponding to the amide I, amide II, and amide III bands, respectively.[74,76,77] The peak at 1445 cm^{-1} can be assigned to an N-H bending of Ch. [78,79]

The 1:1 blend (**Figure 3.4A**, spectra iv) exhibited no new peaks indicating no new bonds occur. The Amide II peak for the non-crosslinked BSA film and the non-crosslinked Ch film becomes less prominent after crosslinking (**Figure 3.4A**, spectra v and vi). This indicates a reduction in free amines after crosslinking and the formation of a Schiff base.[80] After crosslinking, the 1:1 BSA-Ch blend (**Figure 3.4A**, spectra vii) has a peak at 3264 cm^{-1}: this is due to water retained in the film after nitrogen drying. The crosslinked 1:1 film's amide II peaks are less prominent post crosslinking, confirming crosslinking occurred. As the peaks appear similar to those in the neat biopolymer films after crosslinking, we can infer only intramolecular crosslinking has occurred which would suggest no BSA remains on the film after etching. This is expected as BSA is segregated from the Ch domain. However, some small degree of intermolecular crosslinking may occur at the BSA-Ch interface, though this may be below the detection limit of the machine.[10]

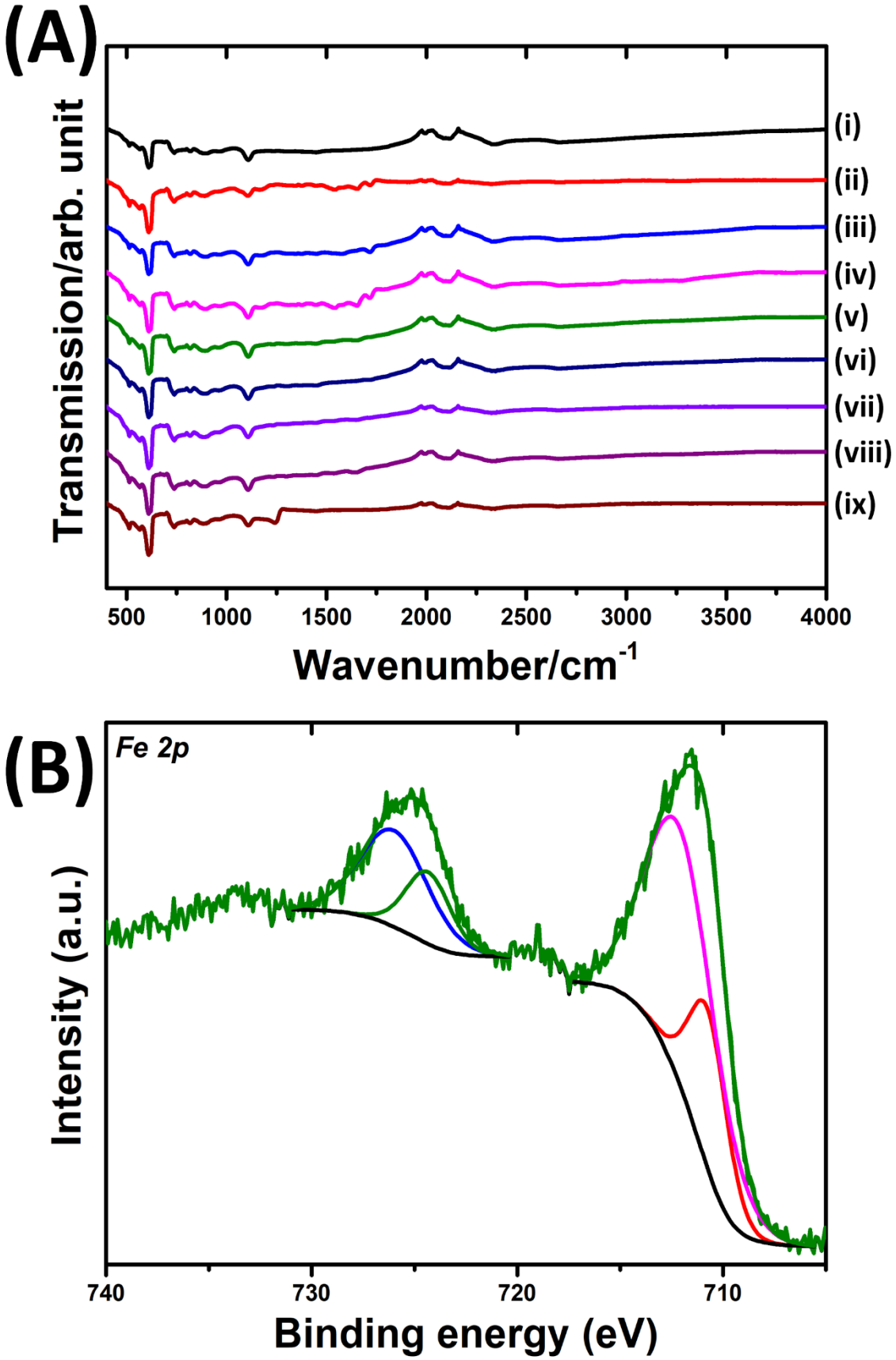


***Figure 3.4**: A) FTIR spectra of **i)** bare silicon wafer, **ii)** 1 w/v% BSA film 3000 rpm deposition, **iii)** 1 w/v% Ch film 3000 rpm deposition, **iv)** 1:1 BSA-Ch blend film 3000 rpm*

deposition, ***v)*** *1 w/v% BSA film 3000 rpm deposition crosslinked,* ***vi)*** *1 w/v% Ch film 3000 rpm deposition crosslinked,* ***vii)*** *1:1 BSA-Ch blend film 3000 rpm deposition crosslinked,* ***viii)*** *1:1 BSA-Ch blend crosslinked film after Tris-HCl etch and* ***ix)*** *porous iron oxide matrix after annealing and calcination treatment.* ***B)*** *Shows the XPS Fe 2p spectra of iron porous matrix after annealing and calcination treatment.*

The spectra of the etched film (**Figure 3.4A**, spectra viii) after crosslinking retains the BSA peaks. This suggests residual BSA on the surface due to intermolecular crosslinking, or after washing. Calcination of the BSA-Ch blend after metal incorporation results in a spectra with no characteristic peaks of BSA or Ch, indicating their removal (**Figure 3.4A**, spectra ix). The more prominent Si–O–Si band at 1108 cm^{-1} after calcination indicates a thicker oxide layer than the native oxide of the original Si wafer. This is further confirmed by the peak in the bare Si wafer (1237 cm^{-1}) shifting to 1245 cm^{-1}, which occurs when oxide thickness increases, a consequence of the long calcination time and high temperature required to ensure complete biopolymer removal.[81] This peak corresponds to the longitudinal optical phonon of SiO_2 (LO) around 1250 cm^{-1}, which occurs in thermal oxides.[82] Fe peaks were not observed at 630 cm^{-1} or 540 cm^{-1}, characteristic of magnetite and hematite respectively. FTIR confirmed successful crosslinking of the biopolymer film before etching and successful removal of the biopolymers after calcination.[83]

XPS was used to determine whether the iron present was predominantly hematite or magnetite to confirm metal incorporation and oxidation (**Figure 3.4B**). The chemical composition of the iron oxide matrix before/after annealing and calcination was confirmed by Fe 2p XPS studies. Following calcination, the Fe 2p core level spectrum (see **Figure 3.4B**) consists of two sharp peaks at 711.6 eV (Fe $2p_{3/2}$) and at 725.7 eV (Fe $2p_{1/2}$) which are broadened due to the presence of Fe^{2+} and Fe^{3+} ions. Curve-fitting using Gaussian–Lorentzian line shapes provides individual binding energies of 710.7/724.3 eV (assigned to Fe^{2+}) and 712.0/726.0 eV (Fe^{3+}) in agreement with literature reports.[84] The Fe^{3+}/Fe^{2+} ratio was estimated to be approx. 2:1, typical of magnetite. The formation of Fe_3O_4 rather than Fe_2O_3 may be attributed to the use of chitosan as a chelating agent. Chitosan also behaves as an environmentally friendly reducing and stabilising agent, due to the presence of amino and hydroxyl groups on the chain. [85–88] This occurs as glucose, a key building block of chitosan, is a reducing sugar. Glucose alone can reduce metal ions[89], with $-CH_2OH$ groups of glucose within chitosan reducing metal ions.[86] Alternatively, in an acidic solution, chitosan may be

hydrolysed to form D-glucosamine, which can also reduce metals.[86] Through either mechanism, a mixture of Fe^{3+} and Fe^{2+} metal ions are formed. In the correct ratio (1 Fe^{2+}: 2 Fe^{3+}), Fe_3O_4 forms after thermal oxidation.[90] Thus, the formation of Fe_3O_4 can be explained by; **1)** an initial reduction of approx. ⅓ of the Fe^{3+} ions by chitosan, followed by **2);** an oxidation of the Fe^{2+}/Fe^{3+} mixture. The C1s peak is nominal demonstrating the effective removal of biopolymeric material during calcination, and is consistent with extraneous carbon species adsorbed during sample preparation (**Figure S17** in section **3.8 Appendix**).

3.5.2. PROTUBERANCE GROWTH IN BLEND THIN-FILMS

Feature diameter determines the properties of a surface, such as pattern transferability, hydrophobicity, etc. SDs can be used provide insight into film features and their growth mechanisms[52]. This allows control of feature formation to optimise films for specific applications. Protuberance diameter data was extracted from AFM images and presented as SDs in normalized frequency histograms (**Figure 3.5**). Information about pore diameter and mechanism of pore formation can be found in in section **3.8 Appendix** (**Figure S3.19**). All blends exhibit multimodal SDs with protuberances of large diameter at low spin speeds. Increasing spin speed reduces the number of modes and shifts population weight to narrower diameters, further indicating a nucleation and growth process. This also indicates that faster spin speeds, up to certain thresholds, produce more homogenously distributed features of more uniform diameter. This is crucial to production of effective patterned thin films. The 2:1 BSA-Ch blend at 4000 rpm (**Figure 3.5b**) is an exception to the above, exhibiting a bimodal SD with peaks at 1.3 µm and 1.5 µm protuberance diameters. This is likely due to shear effects at higher spin speeds.

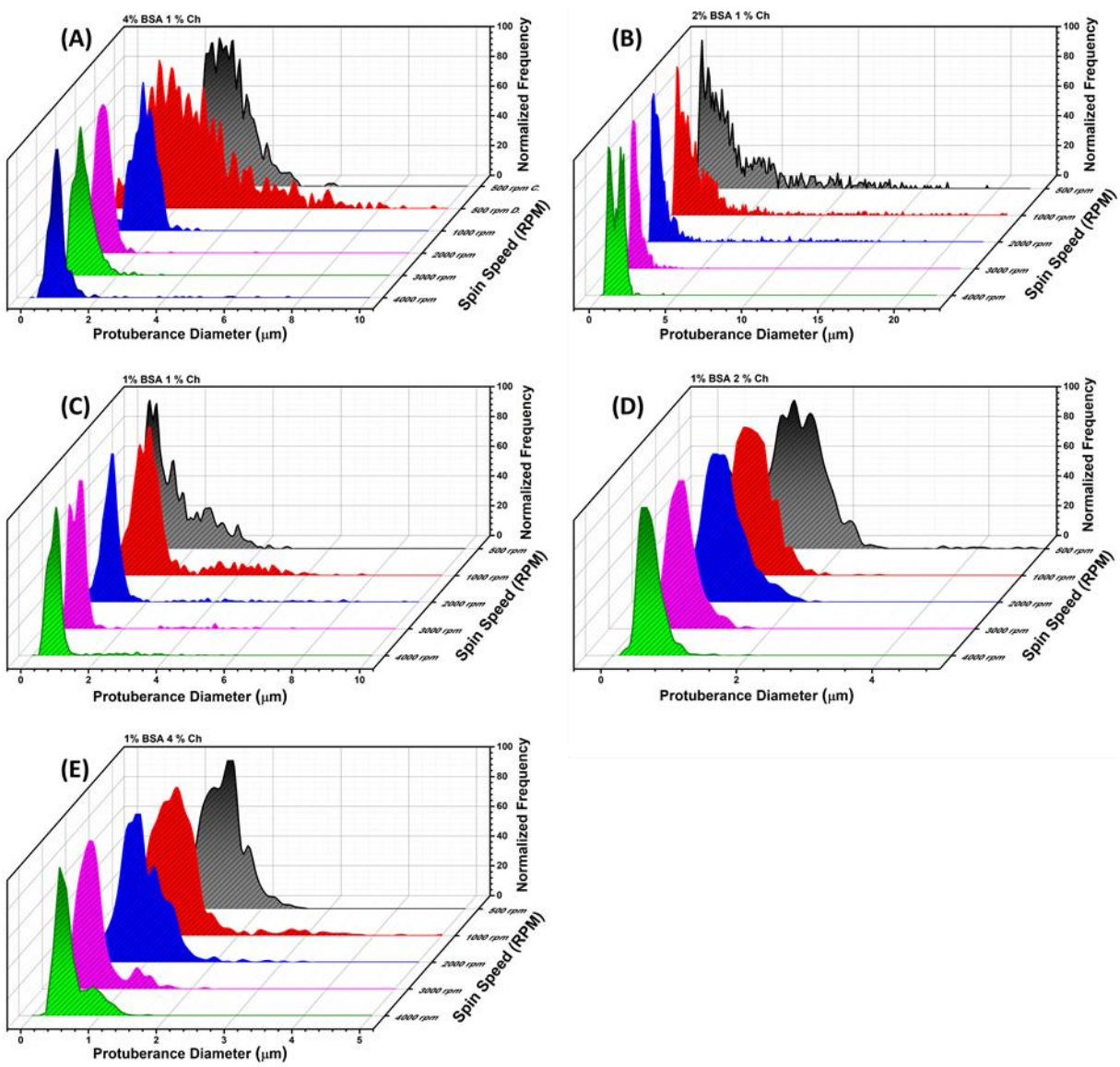


Figure 3.5: *Statistical analysis of BSA-Ch blends for protuberances and frequency of protuberance sizes. Each curve based on approx. 1000 protuberance diameter measurements. All but the 4:1 blend refers to protuberance measurements contained within the matrix, with the 4:1 blend data displaying protuberance data for the continuous and discontinuous (salami structure) domain.* ***A – E*** *displays feature frequency vs diameter of observed features for 4:1, 2:1, 1:1, 1:2 and 1:4 blends respectively.*

Ostwald ripening occurs by the transfer of material from smaller features to larger features by diffusion. The result is smaller features reducing in diameter while larger features increase in diameter.[52] This is distinct from coalescence, where multiple spherical features merge to form a larger version of the feature with lower surface area to volume ratio. Ostwald ripening results in broader SDs and is undesirable. SDs arising from these processes have

distinct identifiable characteristics. Curve fitting may be used to determine the modality of the SD (either unimomodal or polymodal), identify the mode diameter (Mo), and centre of gravity (Xc) of the identified peaks.[91] Typically, this includes the fitting of a lognormal curve to the SD. [52,91–94] Lognormal peak fitting was achieved using the non-linear least squares method.[94,95]

The 4:1 blend exhibits coalescence characteristics; increased feature diameter and peak broadening corresponding to longer evaporation times (**Figure 3.6a** and **b**). Additionally, the SD transitions from a bimodal distribution to unimodal distribution.[96] In contrast, the 1:4 BSA-Ch blend exhibits Ostwald ripening characteristics; feature diameter increases with longer evaporation time (**Figure 3.6c** and **d**), but formation of an extra peak (at approx. 0.3 µm) is observed with longer drying time (Peak 1, **Figure 3.6d**), indicating production of smaller particles, characteristic of Ostwald ripening. Increasing the concentration of Ch increased the continuous phases viscosity, resulting in Ostwald ripening being the dominant growth mechanism.[33]

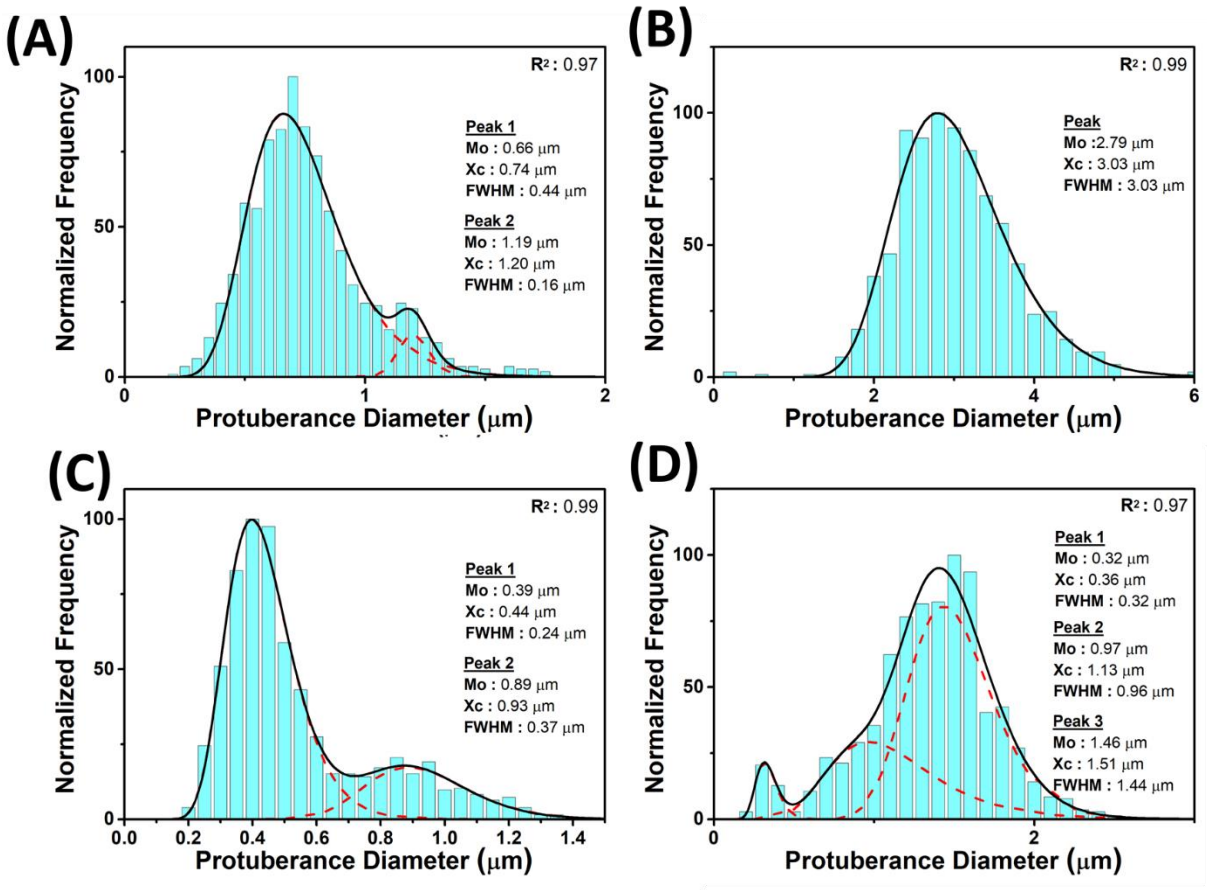


***Figure 3.6**: Protuberance SD of **A)** 4:1 BSA-Ch blend, 4000 rpm deposition, **B)** 4:1 BSA-Ch blend, 500 rpm deposition, **C)** 1:4 BSA-Ch blend, 4000 rpm deposition and **D)** 1:4 BSA-Ch blend, 500 rpm deposition. The black curve (solid) denotes the best unimodal or*

polymodal fit with the distribution. The deconvouted peaks, shown in red (dashed), show the separate populations in the SD.

These results show sub-micron features may be achieved using industrial standard deposition techniques. This technique produces rapid pattern realisation, without requiring extensive environmental controls such as temperature or humidity regulation. Feature diameter and frequency/area are substantially similar to synthetic polymer blends. This means that biopolymer blends could be incorporated into existing production processes for applications where biopolymers offer a distinct advantage, with all the environmental and economic benefits that come with using renewable resources. Furthermore, assignment of the protein and polysaccharide domain was possible due to selective etching and metal incorporation. Both techniques show promise as a method of identification of each domain (inaccessible to typical staining techniques at such a small scale). This is simply achieved by the use of a crosslinking agent, aqueous buffer and cheap metal additive, avoiding the use of expensive or specialist enzymes for identification. The attraction of these techniques is the ability to identify each domain without reliance on highly sensitive surface specific methods. Furthermore, these techniques compliment other facile surface probing techniques such as water contact angle measurements, which show clear differences when analysing the various surfaces encountered (**Figure S3.20** in section **3.8 Appendix**). Though incorporation and etching provides insight into the internal structure (and thereby formation mechanism) of the film, they do little to inform us of the chemical state of the crosslinked blend at the interface. Higher sensitivity ATR-FTIR would be required to determine if crosslinking occurs at the interface. Deconvolution of the SD clearly shows the presence of 2 growth mechanisms (Ostwald ripening and coalescence). Understanding of the growth mechanisms is invaluable when choosing protein:polysaccharide ratios for surface patterning. Selective incorporation of a metal salt could further be enhanced by use of other metal salt derivatives, varying weight percentage of the salt type or varying contact time with the blend film. It would be interesting to see if other salts could show preference to the protein domain when incorporating into the blend film.

3.6. CONCLUSION

Spin speed and blend ratio are major factors when determining feature diameter, growth mechanism and morphology. Blends generally showed a decrease in feature diameter and

roughness, while increasing in features per area with increasing spin speeds and polysaccharide content. Faster drying times (high spin speeds) generally resulted in smaller features, while longer drying times (low spin speeds) resulted in larger features. Simply put, faster spin speeds increase the evaporation rate, limiting the amount of time features have to grow. Increasing viscosity by increasing the relative Ch ratio reduced feature diameter due to lowered polymer mobility. As Ch content is increased, it creates a viscous, honey-like matrix in which BSA domain growth is hindered. Faster spin speeds resulted in more monodisperse blend SD's, unless banding occurred due to shear effects at high speed. Protein:polysaccharide ratio played an important role in determining morphology. Increasing the relative BSA ratio resulted in larger BSA domains, and banding of the BSA domain at high shear due to the difference in viscosity between the two phases.[18] Selective etching and selective incorporation of the metal salts in the Ch domain allowed for protuberances to be assigned as the BSA domain, a first for biopolymer blends. Coalescence was inhibited in 1:4 BSA-Ch blends due to the increased viscosity of the blend, with feature growth described by Ostwald ripening. 4:1 blends grew by a coalesence mechanism. 1:2 and 1:4 BSA-Ch blends have the smallest circular protuberances. This is attributable to the blend solutions high viscosity and low amount of BSA to form a discontinuous phase. The 1:1 blend smaller, circular features decrease in diameter, while larger ovoid features increase in diameter at higher spin speeds (i.e. high shear). This shows inhibited growth of the film morphology at higher spin speeds, and (similar to the 2:1 blend at 1000 rpm) an attempt to phase invert its morphology. Porous films are formed in the 4:1 BSA-Ch blend. Pores decrease in diameter with increasing spin speed. Pores are produced from a solvent rich phase. The 2:1 blend phase inverts at high spin speeds. After phase inversion, pores increase in diameter with increasing spin speed due to high shear elongating their domains.

This work demonstrates that protein-polysaccharide blends can be used to rapidly produce biopolymer thin films with sub-micron patterns, all without requiring extracting, refinement and production of synthetic polymer precursors. Due to their patterns, these unique biopolymer thin-films present a vast spectrum of possible applications. These range from simple applications including traditional packaging alternatives and smart foods production, to more complex applications such as hydrophobic textile coatings, lithographic templates, antireflective coatings, and state-of-the-art hierarchal designs used in biomedicine or responsive membranes.[22,33] Feature growth mechanisms were identified through analysis of the SD. We did not find any previous attempts into the literature to determine the growth mechanism, which may be one reason biopolymer blends thus far have had such large feature diameters. Not only do these blends use environmentally benign and economically cheap

biopolymers, but they have feature diameters on a scale with those of synthetic polymer blends, while utilizing industrially viable methods. This bottom-up method allows for instant pattern production without the need for complex equipment and techniques such as e-beam lithography. Patterns may be produced using benchtop equipment, without the long annealing times associated with synthetic polymers. Biopolymer blends are projected to play a pivotal in future manufacturing of biomedical, electronic, sensor and optical components.[22,32,33] Research into the properties of biopolymer blends thin-film surface morphologies is an emerging field, and our method for producing these blends in a controlled manner is a progressive step in the adoption of these films in modern technologies.

3.7. REFERENCES

(1) OECD. Future Technology Trends. In *OECD Science, Technology, and Innovation Outlook, 2016*; pp 77–125.

(2) López, A. B.; De La Cal, J. C.; Asua, J. M. Highly Hydrophobic Coatings from Waterborne Latexes. *Langmuir* 2016, **32** (30), 7459–7466. https://doi.org/10.1021/acs.langmuir.6b01072.

(3) Mokarian-Tabari, P.; Senthamaraikannan, R.; Glynn, C.; Collins, T. W.; Cummins, C.; Nugent, D.; O'Dwyer, C.; Morris, M. A. Large Block Copolymer Self-Assembly for Fabrication of Subwavelength Nanostructures for Applications in Optics. *Nano Lett*. 2017, **17** (5), 2973–2978. https://doi.org/10.1021/acs.nanolett.7b00226.

(4) Alizadeh-Birjandi, E.; Kavehpour, H. P. Plant Leaves Icephobicity. *J. Coatings Technol. Res.* 2017. https://doi.org/10.1007/s11998-017-9988-4.

(5) Fu, Y. F.; Yuan, C. Q.; Bai, X. Q. Marine Drag Reduction of Shark Skin Inspired Riblet Surfaces. *Biosurface and Biotribology* 2017, **3** (1), 11–24. https://doi.org/10.1016/j.bsbt.2017.02.001.

(6) Borah, D.; Rasappa, S.; Senthamaraikannan, R.; Holmes, J. D.; Morris, M. A. Tuning PDMS Brush Chemistry by UV-O3 Exposure for PS-b-PDMS Microphase Separation and Directed Self-Assembly. *Langmuir* 2013, **29** (28), 8959–8968. https://doi.org/10.1021/la401561k.

(7) Blackstock, J. C. Carbohydrates. In *Guide to Biochemistry*; Blackstock, J. C., Ed.; Butterworth-Heinemann: Glasgow, 1989; pp 20–31. https://doi.org/10.1016/B978-0-7236-1151-6.50009-1.

(8) Whistler, R. L. Solubility of Polysaccharides and Their Behavior in Solution. In *Carbohydrates in Solution*; Horace S. Isbell, Ed.; Amer Chemical Society, 1973; pp 242–255. https://doi.org/10.1021/ba-1971-0117.ch014.

(9) García, M. C. Drug Delivery Systems Based on Nonimmunogenic Biopolymers. *In Engineering of Biomaterials for Drug Delivery Systems*; Parambath, A., Ed.; Woodhead Publishing: Swanston, Cambridge, 2018; pp 317–344. https://doi.org/10.1016/B978-0-08-101750-0.00012-X.

(10) Ma, X.; Sun, X.; Hargrove, D.; Chen, J.; Song, D.; Dong, Q.; Lu, X.; Fan, T.-H.; Fu, Y.; Lei, Y. A Biocompatible and Biodegradable Protein Hydrogel with Green and Red Autofluorescence: Preparation, Characterization and In Vivo Biodegradation Tracking and Modeling. *Sci. Rep*. 2016, **6**, 19370. https://doi.org/10.1038/srep19370.

(11) Picout, D. R.; Ross-Murphy, S. B. Rheology of Biopolymer Solutions and Gels. *Sci. World J.* 2003, **3**, 105–121. https://doi.org/10.1100/tsw.2003.15.

(12) de Jong, S.; van de Velde, F. Charge Density of Polysaccharide Controls Microstructure and Large Deformation Properties of Mixed Gels. *Food Hydrocoll*. 2007, **21** (7), 1172–1187. https://doi.org/10.1016/j.foodhyd.2006.09.004.

(13) Gengec, N. A.; Cengiz, U.; Erbil, H. Y. Superhydrophobic Perfluoropolymer/Polystyrene Blend Films Induced by Nonsolvent. *Appl. Surf. Sci*. 2016, **383**, 33–41. https://doi.org/10.1016/J.APSUSC.2016.04.160.

(14) Xavier, P.; Rao, P.; Bose, S. Nanoparticle Induced Miscibility in LCST Polymer Blends: Critically Assessing the Enthalpic and Entropic Effects. *Phys. Chem. Chem. Phys*. 2016, **18** (1), 47–64. https://doi.org/10.1039/C5CP05852J.

(15) van de Velde, F.; de Hoog, E. H. A.; Oosterveld, A.; Tromp, R. H. Protein-Polysaccharide Interactions to Alter Texture. *Annu. Rev. Food Sci. Technol*. 2015, **6** (1), 371–388. https://doi.org/10.1146/annurev-food-022814-015558.

(16) Butler, M. F.; Heppenstall-Butler, M. Phase Separation in Gelatin/Dextran and Gelatin/Maltodextrin Mixtures. *Food Hydrocoll*. 2003, **17** (6), 815–830. https://doi.org/10.1016/S0268-005X(03)00103-6.

(17) Hirose, A.; Shimada, K.; Hayashi, C.; Nakanishi, H.; Norisuye, T.; Tran-Cong-Miyata, Q. Polymer Networks with Bicontinuous Gradient Morphologies Resulting from the Competition between Phase Separation and Photopolymerization. *Soft Matter* 2016, **12** (6), 1820–1829. https://doi.org/10.1039/c5sm02399h.

(18) Wolf, B.; Scirocco, R.; Frith, W. J.; Norton, I. T. Shear-Induced Anisotropic Microstructure in Phase-Separated Biopolymer Mixtures. *Food Hydrocoll.* 2000, **14** (3), 217–225. https://doi.org/10.1016/S0268-005X(99)00062-4.

(19) Norton, I. T.; Frith, W. J. Microstructure Design in Mixed Biopolymer Composites. *Food Hydrocoll*. 2001, **15** (4–6), 543–553. https://doi.org/10.1016/S0268-005X(01)00062-5.

(20) Firoozmand, H.; Rousseau, D. Microstructure and Elastic Modulus of Phase-Separated Gelatin–Starch Hydrogels Containing Dispersed Oil Droplets. *Food Hydrocoll.* 2013, **30** (1), 333–342. https://doi.org/10.1016/J.FOODHYD.2012.06.010.

(21) Hoeger, I. C.; Filpponen, I.; Martin-Sampedro, R.; Johansson, L.-S.; Österberg, M.; Laine, J.; Kelley, S.; Rojas, O. J. Bicomponent Lignocellulose Thin Films to Study the Role of Surface Lignin in Cellulolytic Reactions. *Biomacromolecules* 2012, **13** (10), 3228–3240. https://doi.org/10.1021/bm301001q.

(22) Nady, N.; Kandil, S. H. Novel Blend for Producing Porous Chitosan-Based Films Suitable for Biomedical Applications. *Membranes (Basel)*. 2018, **8** (1), 2. https://doi.org/10.3390/membranes8010002.

(23) Trommer, K.; Morgenstern, B.; Gähr, F.; Hermanutz, F. Sub-Micrometer Structured Textile Coatings Generated From Cellulose Based Polymer Blends. *Lenzinger Berichte* 2009, **87**, 151–161.

(24) Taajamaa, L.; Rojas, O. J.; Laine, J.; Yliniemi, K.; Kontturi, E. Protein-Assisted 2D Assembly of Gold Nanoparticles on a Polysaccharide Surface. *Chem. Commun*. 2013, **49** (13), 1318–1320. https://doi.org/10.1039/c2cc37288f.

(25) Claro, P. I. C.; Neto, A. R. S.; Bibbo, A. C. C.; Mattoso, L. H. C.; Bastos, M. S. R.; Marconcini, J. M. Biodegradable Blends with Potential Use in Packaging: A Comparison of PLA/Chitosan and PLA/Cellulose Acetate Films. *J. Polym. Environ*. 2016, **24** (4), 363–371. https://doi.org/10.1007/s10924-016-0785-4.

(26) Taajamaa, L.; Rojas, O. J.; Laine, J.; Kontturi, E. Phase-Specific Pore Growth in Ultrathin Bicomponent Films from Cellulose-Based Polysaccharides. *Soft Matter* 2011, **7** (21), 10386. https://doi.org/10.1039/c1sm06020a.

(27) Chen, F.; Monnier, X.; Gällstedt, M.; Gedde, U. W.; Hedenqvist, M. S. Wheat Gluten/Chitosan Blends: A New Biobased Material. *Eur. Polym. J.* 2014, **60**, 186–197. https://doi.org/10.1016/J.EURPOLYMJ.2014.09.007.

(28) Chen, F.; Gällstedt, M.; Olsson, R. T.; Gedde, U. W.; Hedenqvist, M. S. A Novel Chitosan/Wheat Gluten Biofoam Fabricated by Spontaneous Mixing and Vacuum-Drying. *RSC Adv*. 2015, **5** (114), 94191–94200. https://doi.org/10.1039/C5RA18569F.

(29) Walha, F.; Lamnawar, K.; Maazouz, A.; Jaziri, M. Rheological, Morphological and Mechanical Studies of Sustainably Sourced Polymer Blends Based on Poly(Lactic Acid) and Polyamide 11. *Polymers (Basel)*. 2016, **8** (3). https://doi.org/10.3390/polym8030061.

(30) Cao, W.; Wang, A.; Jing, D.; Gong, Y.; Zhao, N.; Zhang, X. Novel Biodegradable Films and Scaffolds of Chitosan Blended with Poly(3-Hydroxybutyrate). *J. Biomater. Sci. Polym. Ed.* 2005, **16** (11), 1379–1394. https://doi.org/10.1163/156856205774472308.

(31) Czibula, C.; Teichert, G.; Nau, M.; Hobisch, M.; Palasingh, C.; Biesalski, M.; Spirk, S.; Teichert, C.; Nypelö, T. Design of Friction, Morphology, Wetting, and Protein Affinity by Cellulose Blend Thin Film Composition. *Front. Chem*. 2019, **7** (Article 239), 1–10. https://doi.org/10.3389/fchem.2019.00239.

(32) Gopishetty, V.; Roiter, Y.; Tokarev, I.; Minko, S. Multiresponsive Biopolyelectrolyte Membrane. *Adv. Mater*. 2008, **20** (23), 4588–4593. https://doi.org/10.1002/adma.200801610.

(33) Hu, X.; Cebe, P.; Weiss, A. S.; Omenetto, F.; Kaplan, D. L. Protein-Based Composite Materials. *Mater. Today* 2012, **15** (5), 208–215. https://doi.org/10.1016/S1369-7021(12)70091-3.

(34) Banta, R. A.; Collins, T. W.; Curley, R. A.; Young, P. W.; Holmes, J. D.; Flynn, E. J. Nanopatterned Protein-Polysaccharide Thin Films by Humidity Regulated Phase Separation. *J. Colloid Interface Sci.* 2018, **532**, 171–181. https://doi.org/10.1016/J.JCIS.2018.07.109.

(35) Jovanović, G. D.; Klaus, A. S.; Nikšić, M. P. Antimicrobial Activity of Chitosan Coatings and Films against Listeria Monocytogenes on Black Radish. *Rev. Argent. Microbiol.* 2016, **48** (2), 128–136. https://doi.org/10.1016/j.ram.2016.02.003.

(36) Teixeira, M. do C.; Santini, A.; Souto, E. B. Delivery of Antimicrobials by Chitosan-Composed Therapeutic Nanostructures. In *Nanostructures for Antimicrobial Therapy: Nanostructures in Therapeutic Medicine Series*; Ficai, A., Grumezescu, A. M., Eds.; Elsevier, 2017; pp 203–222. https://doi.org/10.1016/B978-0-323-46152-8.00008-1.

(37) Saha, B.; Chakraborty, S.; Das, G. A Rational Approach for Controlled Adsorption of Metal Ions on Bovine Serum Albumin−Malachite Bionanocomposite. *J. Phys. Chem. C* 2010, **114** (21), 9817–9825. https://doi.org/10.1021/jp1003243.

(38) Oliveira, M.; Simoni, J. A.; Airoldi, C. Chitosan Metal-Crosslinked Beads Applied for n-Alkylmonoamines Removal from Aqueous Solutions – a Thermodynamic Study. *J. Chem. Thermodyn.* 2014, **73**, 197–205. https://doi.org/10.1016/J.JCT.2013.12.030.

(39) Hernández, R. B.; Franco, A. P.; Yola, O. R.; López-Delgado, A.; Felcman, J.; Recio, M. A. L.; Mercê, A. L. R. Coordination Study of Chitosan and Fe^{3+}. *J. Mol. Struct*. 2008, **877** (1–3), 89–99. https://doi.org/10.1016/J.MOLSTRUC.2007.07.024.

(40) Guo, X.; Liu, L.; Zhuang, Z.; Chen, X.; Ni, M.; Li, Y.; Cui, Y.; Zhan, P.; Yuan, C.; Ge, H.; Wang, Z.; Chen, Y. A New Strategy of Lithography Based on Phase Separation of Polymer Blends. *Sci. Rep*. 2015, **5** (Article 15947). https://doi.org/10.1038/srep15947.

(41) Donie, Y. J.; Smeets, M.; Egel, A.; Lentz, F.; Preinfalk, J. B.; Mertens, A.; Smirnov, V.; Lemmer, U.; Bittkau, K.; Gomard, G. Light Trapping in Thin Film Silicon Solar Cells via Phase Separated Disordered Nanopillars. *Nanoscale* 2018, **10** (14), 6651–6659. https://doi.org/10.1039/C8NR00455B.

(42) Dhillon, G. S.; Kaur, S.; Brar, S. K.; Verma, M. Green Synthesis Approach: Extraction of Chitosan from Fungus Mycelia. *Critical Reviews in Biotechnology*. December 2013, pp 379–403. https://doi.org/10.3109/07388551.2012.717217.

(43) And, D. J. M.; Hardy, J. J. E. Applications of Functionalized Chitosan in Catalysis. *Ind. Eng. Chem*. Res. 2005, **44** (23), 8499–8520. https://doi.org/10.1021/IE050007V.

(44) Van De Witte, P.; Dijkstra, P. J.; Van Den Berg, J. W. A.; Feijen, J. Phase Separation Processes in Polymer Solutions in Relation to Membrane Formation. *Elsevier J. Membr. Sci.* 1996, **117**, 1–31.

(45) Sperling, L. H. Concentrated Solutions, Phase Separation Behavior, and Diffusion. In *Introduction to Physical Polymer Science*; John Wiley & Sons, Inc.: Hoboken, NJ, USA, 2005; pp 145–195. https://doi.org/10.1002/0471757128.ch4.

(46) Vonka, M.; Kosek, J. Modelling the Morphology Evolution of Polymer Materials Undergoing Phase Separation. *Chem. Eng. J.* 2012, **207**, 895–905. https://doi.org/10.1016/j.cej.2012.06.091.

(47) Voigt, M.; Chappell, J.; Rowson, T.; Cadby, A.; Geoghegan, M.; Jones, R. A. L.; Lidzey, D. G. The Interplay between the Optical and Electronic Properties of Light-Emitting-Diode Applicable Conjugated Polymer Blends and Their Phase-Separated Morphology. *Org. Electron*. 2005, **6** (1), 35–45. https://doi.org/10.1016/J.ORGEL.2005.02.002.

(48) Aschenbrenner, O.; Supasitmongkol, S.; Taylor, M.; Styring, P. Measurement of Vapour Pressures of Ionic Liquids and Other Low Vapour Pressure Solvents. *Green Chem.* 2009, **11** (8), 1217. https://doi.org/10.1039/b904407h.

(49) Nesmeyanov, A. N.; Kikxadze, E. V. Concentration of Proteins as a Result of the Phase Separation of Water-Protein-Polysaccharide Systems Part 1. Phase Equilibria in Water-Milk Proteins-Plysaccharide Systems. *Nahrung* 1986, **30** (6), 591–599.

(50) Nesmeyanov, A. N.; Zhuravskaya, N. A.; Kiknadze, E. V; Tolstoguzov, V. B. Concentration of Proteins as a Result of the Phase Separation of Water-Protein-Polysaccharide Systems Part 2. Concentration of Milk Proteins. *Nahrung* 1986, **30** (6), 601–613.

(51) Fang, Y.; Li, L.; Inoue, C.; Lundin, L.; Appelqvist, I. Associative and Segregative Phase Separations of Gelatin/κ-Carrageenan Aqueous Mixtures. *Langmuir* 2006, **22** (23), 9532–9537. https://doi.org/10.1021/la061865e.

(52) Dimitrova, L. M.; Boneva, M. P.; Danov, K. D.; Kralchevsky, P. A.; Basheva, E. S.; Marinova, K. G.; Petkov, J. T.; Stoyanov, S. D. Limited Coalescence and Ostwald Ripening in Emulsions Stabilized by Hydrophobin HFBII and Milk Proteins. *Colloids Surfaces A Physicochem. Eng. Asp.* 2016, **509**, 521–538. https://doi.org/10.1016/J.COLSURFA.2016.09.066.

(53) Huang, C.; Moosmann, M.; Jin, J.; Heiler, T.; Walheim, S.; Schimmel, T. Polymer Blend Lithography: A Versatile Method to Fabricate Nanopatterned Self-Assembled Monolayers. *Beilstein J. Nanotechnol*. 2012, **3**, 620–628. https://doi.org/10.3762/bjnano.3.71.

(54) Sprenger, M.; Walheim, S.; Budkowski, A.; Steiner, U. Hierarchic Structure Formation in Binary and Ternary Polymer Blends. *Interface Sci*. 2003, **11** (2), 225–235. https://doi.org/10.1023/A:1022182930454.

(55) Cui, L.; Wang, H.; Ding, Y.; Han, Y. Tunable Ordered Droplets Induced by Convection in Phase-Separating P2VP/PS Blend Film. *Polymer (Guildf).* 2004, **45** (24), 8139–8146. https://doi.org/10.1016/J.POLYMER.2004.09.065.

(56) Xue, L.; Zhang, J.; Han, Y. Phase Separation Induced Ordered Patterns in Thin Polymer Blend Films. *Prog. Polym. Sci.* 2012, **37** (4), 564–594. https://doi.org/10.1016/J.PROGPOLYMSCI.2011.09.001.

(57) Huang, C.; Förste, A.; Walheim, S.; Schimmel, T. Polymer Blend Lithography for Metal Films: Large-Area Patterning with over 1 Billion Holes/Inch^2. *Beilstein J. Nanotechnol.* 2015, **6,** 1205–1211. https://doi.org/10.3762/bjnano.6.123.

(58) Filippone, G.; Netti, P. A.; Acierno, D. Microstructural Evolutions of LDPE/PA6 Blends by Rheological and Rheo-Optical Analyses: Influence of Flow and Compatibilizer on Break-up and Coalescence Processes. *Polymer (Guildf).* 2007, **48** (2), 564–573. https://doi.org/10.1016/j.polymer.2006.11.050.

(59) Jůza, J.; Fortelný, I. Flow-Induced Coalescence: Evaluation of Some Approximations. *Macromol. Symp.* 2017, **373** (1), 1–10. https://doi.org/10.1002/masy.201600097.

(60) Fortelný, I.; Jůza, J.; Dimzoski, B. Coalescence in Quiescent Polymer Blends with a High Content of the Dispersed Phase. *Eur. Polym. J.* 2012, **48** (7), 1230–1240. https://doi.org/10.1016/J.EURPOLYMJ.2012.04.017.

(61) Roy, S.; Sharma, A. Self-Organized Morphological Evolution and Dewetting in Solvent Vapor Annealing of Spin Coated Polymer Blend Nanostructures. *J. Colloid Interface Sci*. 2015, **449**, 215–225. https://doi.org/10.1016/J.JCIS.2014.12.095.

(62) Ji-Seon, K.; Ho, P. K. H.; Murphy, C. E.; Friend, R. H. Phase Separation in Polyfluorene-Based Conjugated Polymer Blends: Lateral and Vertical Analysis of Blend Spin-Cast Thin Films. *Macromolecules* 2004, **37** (8), 2861–2871. https://doi.org/10.1021/MA035750I.

(63) Ghoshal, T.; Maity, T.; Senthamaraikannan, R.; Shaw, M. T.; Carolan, P.; Holmes, J. D.; Roy, S.; Morris, M. A. Size and Space Controlled Hexagonal Arrays of Superparamagnetic Iron Oxide Nanodots: Magnetic Studies and Application. *Sci. Rep*. 2013, **3** (1), Article No. 2772. https://doi.org/10.1038/srep02772.

(64) Guibal, E.; Vincent, T.; Navarro, R. Metal Ion Biosorption on Chitosan for the Synthesis of Advanced Materials. J. Mater. Sci. 2014, **49** (16), 5505–5518. https://doi.org/10.1007/s10853-014-8301-5.

(65) Mohanasrinivasan, V.; Mishra, M.; Paliwal, J. S.; Singh, S. K.; Selvarajan, E.; Suganthi, V.; Subathra Devi, C. Studies on Heavy Metal Removal Efficiency and Antibacterial Activity of Chitosan Prepared from Shrimp Shell Waste. *3 Biotech* 2014, **4** (2), 167–175. https://doi.org/10.1007/s13205-013-0140-6.

(66) Varma, A.; Deshpande, S.; Kennedy, J. Metal Complexation by Chitosan and Its Derivatives: A Review. *Carbohydr. Polym*. 2004, **55** (1), 77–93. https://doi.org/10.1016/J.CARBPOL.2003.08.005.

(67) Guibal, E. Interactions of Metal Ions with Chitosan-Based Sorbents: A Review. *Sep. Purif. Technol*. 2004, **38** (1), 43–74. https://doi.org/10.1016/J.SEPPUR.2003.10.004.

(68) Horzum, N.; Boyacı, E.; Eroğlu, A. E.; Shahwan, T.; Demir, M. M. Sorption Efficiency of Chitosan Nanofibers toward Metal Ions at Low Concentrations. *Biomacromolecules* 2010, **11** (12), 3301–3308. https://doi.org/10.1021/bm100755x.

(69) Okur, H. I.; Hladílková, J.; Rembert, K. B.; Cho, Y.; Heyda, J.; Dzubiella, J.; Cremer, P. S.; Jungwirth, P. Beyond the Hofmeister Series: Ion-Specific Effects on Proteins and Their Biological Functions. *J. Phys. Chem. B* 2017, **121** (9), 1997–2014. https://doi.org/10.1021/acs.jpcb.6b10797.

(70) Braun, M. K.; Sauter, A.; Matsarskaia, O.; Wolf, M.; Roosen-Runge, F.; Sztucki, M.; Roth, R.; Zhang, F.; Schreiber, F. Reentrant Phase Behavior in Protein Solutions Induced by Multivalent Salts: Strong Effect of Anions Cl^- Versus NO_3^-. *J. Phys. Chem. B* 2018, **122** (50), 11978–11985. https://doi.org/10.1021/acs.jpcb.8b10268.

(71) Senthil Kumar, R.; Rajkumar, P. Characterization of Minerals in Air Dust Particles in the State of Tamilnadu, India through FTIR, XRD and SEM Analyses. *Infrared Phys. Technol.* 2014, **67**, 30–41. https://doi.org/10.1016/J.INFRARED.2014.06.002.

(72) Young, T. F.; Chen, C. P.; Liou, J. F.; Yang, Y. L.; Chang, T. C. Study on the Si–Si Vibrational States of the Near Surface Region of Porous Silicon. *J. Porous Mater.* 2000, **7** (1/3), 339–343. https://doi.org/10.1023/A:1009622601723.

(73) Girsova, M. A.; Golovina, G. F.; Anfimova, I. N.; Arsent'ev, M. Y.; Antropova, T. V. Structure and Spectral Properties of the Silver-Containing High-Silica Glasses. *J. Phys. Conf. Ser*. 2016, **741** (1), 1–5. https://doi.org/10.1088/1742-6596/741/1/012144.

(74) Garidel, P.; Schott, H. Fourier-Transform Midinfrared Spectroscopy for Analysis and Screening of Liquid Protein Formulations, Part 1. *BioProcess Tech.* 2006, **4** (5), 40–46.

(75) Smith, J. R.; Cicerone, M. T.; Meuse, C. W. Tertiary Structure Changes in Albumin upon Surface Adsorption Observed via Fourier Transform Infrared Spectroscopy. *Langmuir* 2009, **25** (8), 4571–4578. https://doi.org/10.1021/la802955w.

(76) Murugaraj, P.; Mainwaring, D. E.; Tonkin, D. C.; Al Kobaisi, M. Probing the Dynamics of Water in Chitosan Polymer Films by Dielectric Spectroscopy. *J. Appl. Polym*. Sci. 2011, **120** (3), 1307–1315. https://doi.org/10.1002/app.33163.

(77) Guo, L.; Liu, G.; Hong, R.-Y.; Li, H.-Z. Preparation and Characterization of Chitosan Poly(Acrylic Acid) Magnetic Microspheres. *Mar. Drugs* 2010, **8** (7), 2212–2222. https://doi.org/10.3390/md8072212.

(78) Monvisade, P.; Siriphannon, P. Chitosan Intercalated Montmorillonite: Preparation, Characterization and Cationic Dye Adsorption. *Appl. Clay Sci.* 2009, **42** (3–4), 427–431. https://doi.org/10.1016/J.CLAY.2008.04.013.

(79) Al-Remawi, M. M. A. Properties of Chitosan Nanoparticles Formed Using Sulfate Anions as Crosslinking Bridges. *Am. J. Appl. Sci*. 2012, **9** (7), 1091–1100.

(80) Kunjachan, S.; Gupta, S.; Dwivedi, A. K.; Dube, A.; Chourasia, M. K. Chitosan-Based Macrophage-Mediated Drug Targeting for the Treatment of Experimental Visceral Leishmaniasis. *J. Microencapsul.* 2011, **28** (4), 301–310. https://doi.org/10.3109/02652048.2011.559281.

(81) Yang, T.-C.; Saraswat, K. C. Effect of Physical Stress on the Degradation of Thin SiO_2 Films Under Electrical Stress. *IEEE Trans. Electron Devices* 2000, **47** (4), 746–755.

(82) Matteini, F.; Tütüncüoğlu, G.; Rüffer, D.; Alarcón-Lladó, E.; Fontcuberta i Morral, A. Ga-Assisted Growth of GaAs Nanowires on Silicon, Comparison of Surface SiO_x of Different *Nature. J. Cryst. Growth* 2014, **404**, 246–255. https://doi.org/10.1016/j.jcrysgro.2014.07.034.

(83) Ghoshal, T.; Ntaras, C.; O'Connell, J.; Shaw, M. T.; Holmes, J. D.; Avgeropoulos, A.; Morris, M. A. Fabrication of Ultra-Dense Sub-10 Nm in-Plane Si Nanowire Arrays by Using a Novel Block Copolymer Method: Optical Properties. *Nanoscale* 2016, **8** (4), 2177–2187. https://doi.org/10.1039/c5nr07085f.

(84) Prakash, R.; Choudhary, R. J.; Chandra, L. S. S.; Lakshmi, N.; Phase, D. M. Electrical and Magnetic Transport Properties of Fe3O4 Thin Films on GaAs (100) Substrate. *J. Phys. Condens. Matter* 2009, **19** (48), 486212. https://doi.org/10.1088/0953-8984/19/48/486212.

(85) Di Carlo, G.; Curulli, A.; Toro, R. G.; Bianchini, C.; De Caro, T.; Padeletti, G.; Zane, D.; Ingo, G. M. Green Synthesis of Gold-Chitosan Nanocomposites for Caffeic Acid Sensing. Langmuir 2012, **28** (12), 5471–5479. https://doi.org/10.1021/la204924d.

(86) Huang, H.; Yang, X. Synthesis of Chitosan-Stabilized Gold Nanoparticles in the Absence/Presence of Tripolyphosphate. *Biomacromolecules* 2004, **5** (6), 2340–2346. https://doi.org/10.1021/bm0497116.

(87) Wang, B.; Chen, K.; Jiang, S.; Reincke, F.; Tong, W.; Wang, D.; Gao, C. Chitosan-Mediated Synthesis of Gold Nanoparticles on Patterned Poly(Dimethylsiloxane) Surfaces. *Biomacromolecules* 2006, **7** (4), 1203–1209. https://doi.org/10.1021/bm060030f.

(88) Wei, D.; Qian, W.; Shi, Y.; Ding, S.; Xia, Y. Mass Synthesis of Single-Crystal Gold Nanosheets Based on Chitosan. *Carbohydr. Res.* 2007, **342** (16), 2494–2499. https://doi.org/10.1016/j.carres.2007.07.001.

(89) Raveendran, P.; Fu, J.; Wallen, S. L. Completely "Green" Synthesis and Stabilization of Metal Nanoparticles. *J. Am. Chem. Soc.* 2003, **125** (46), 13940–13941. https://doi.org/10.1021/ja029267j.

(90) Sun, X.; Zheng, C.; Zhang, F.; Yang, Y.; Wu, G.; Yu, A.; Guan, N. Size-Controlled Synthesis of Magnetite (Fe3O4) Nanoparticles Coated with Glucose and Gluconic Acid from a Single Fe(III) Precursor by a Sucrose Bifunctional Hydrothermal Method. *J. Phys. Chem. C* 2009, **113** (36), 16002–16008. https://doi.org/10.1021/jp9038682.

(91) Shih, C.-Y.; Streubel, R.; Heberle, J.; Letzel, A.; Shugaev, M. V.; Wu, C.; Schmidt, M.; Gökce, B.; Barcikowski, S.; Zhigilei, L. V. Two Mechanisms of Nanoparticle Generation in Picosecond Laser Ablation in Liquids: The Origin of the Bimodal Size Distribution. *Nanoscale* 2018, **10** (15), 6900–6910. https://doi.org/10.1039/C7NR08614H.

(92) Prieto, I.; Kozak, R.; Skibitzki, O.; Rossell, M. D.; Zaumseil, P.; Capellini, G.; Gini, E.; Kunze, K.; Rojas Dasilva, Y. A.; Erni, R.; Schroeder, T.; Känel, H. von. Bi-Modal Nanoheteroepitaxy of GaAs on Si by Metal Organic Vapor Phase Epitaxy. *Nanotechnology* 2017, **28** (13), 135701. https://doi.org/10.1088/1361-6528/aa5ec4.

(93) Morgan, T. T.; Goff, T. M.; Adair, J. H. The Colloidal Stability of Fluorescent Calcium Phosphosilicate Nanoparticles: The Effects of Evaporation and Redispersion on Particle Size Distribution. *Nanoscale* 2011, **3** (5), 2044–2053. https://doi.org/10.1039/c0nr00995d.

(94) Wallecan, J.; McCrae, C.; Debon, S. J. J.; Dong, J.; Mazoyer, J. Emulsifying and Stabilizing Properties of Functionalized Orange Pulp Fibers. *Food Hydrocoll*. 2015, **47**, 115–123. https://doi.org/10.1016/J.FOODHYD.2015.01.009.

(95) Ha, W. N.; Shakibaie, F.; Kahler, B.; Walsh, L. J. Deconvolution of the Particle Size Distribution of ProRoot MTA and MTA Angelus. *Acta Biomater. Odontol. Scand*. 2016, **2** (1), 7–11. https://doi.org/10.3109/23337931.2015.1129611.

(96) Ziegler, V. E.; Wolf, B. A. Bimodal Drop Size Distributions during the Early Stages of Shear Induced Coalescence. *Polymer (Guildf).* 2005, **46** (22), 9265–9273. https://doi.org/10.1016/J.POLYMER.2005.07.055.

(97) Rezaei Kolahchi, A.; Carreau, P. J.; Ajji, A. Surface Roughening of PET Films through Blend Phase Coarsening. *ACS Appl. Mater. Interfaces* 2014, **6** (9), 6415–6424. https://doi.org/10.1021/am4058259.

(98) Reddy, A. B.; Reddy, G. S. M.; Sivanjineyulu, V.; Jayaramudu, J.; Varaprasad, K.; Sadiku, E. R. Chapter 17 Design and Applications of Nanostructured Polymer Blends and Nanocomposite Systems, 1st ed.; Thomas, S., SHanks, Ro., Chandrasekharakurup, S., Eds 1st; pp 385-411 *Elsevier Inc*., 2016. https://doi.org/10.1016/B978-0-323-39408-6.00016-9.

(99) Jara, F.; Pérez, O. E.; Pilosof, A. M. R. Impact of Phase Separation of Whey Proteins/Hydroxypropylmethylcellulose Mixtures on Gelation Dynamics and Gels Properties. *Food Hydrocoll.* 2010, **24** (6–7), 641–651. https://doi.org/10.1016/J.FOODHYD.2010.03.005.

(100) Kimura, N.; Kawazoe, K.; Nakanishi, H.; Norisuye, T.; Tran-Cong-Miyata, Q. Influences of Wetting and Shrinkage on the Phase Separation Process of Polymer Mixtures Induced by Photopolymerization. *Soft Matter* 2013, **9** (35), 8428. https://doi.org/10.1039/c3sm51203g.

(101) Geldhauser, T.; Walheim, S.; Schimmel, T.; Leiderer, P.; Boneberg, J. Influence of the Relative Humidity on the Demixing of Polymer Blends on Prepatterned Substrates. *Macromolecules* 2010, **43** (2), 1124–1128. https://doi.org/10.1021/ma9022058.

(102) Zhang, H.; Wang, F. Analysis of Surface Wettability of Synthetic Magnetite. *J. Wuhan Univ. Technol. Mater. Sci. Ed.* 2014, **29** (4), 679–683. https://doi.org/10.1007/s11595-014-0979-3.

3.8. APPENDIX

3.8.1. SOLUTION PREPARATION

Prior to dissolution, proteins, and polysaccharides were dried overnight at room temperature under vacuum. Biopolymer stock solutions were made by solubilising Ch and BSA in 90% FA at 5 w/v%, 10 w/v%. These solutions were stirred in a closed vessel for 3 h at room temperature. The solutions were then centrifuged at 13,000 rpm in a Beckman Coulter Avanti J-26XPI centrifuge at 18 ºC for 15 min and decanted. Following this, stock solutions were stored at -20 ºC for further use or used immediately. Stock solutions were diluted with fresh FA and/or mixed with each other to produce coating solutions.

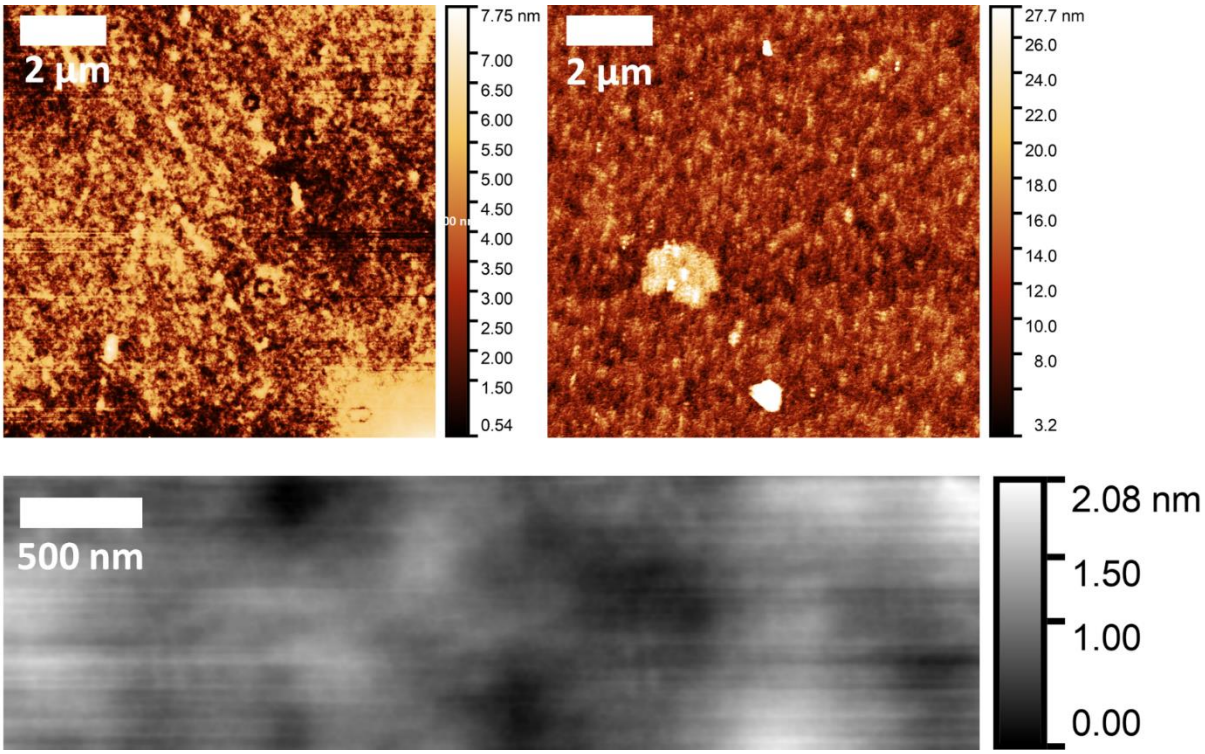


Figure S3.1: *AFM images showing results of casting neat thin-films at 65% relative humidity at 2000 rpm prepared in the same manner as BSA-Ch blends. Biopolymer AFM images are red, glass substrate AFM image is grey. Shows 1% BSA film (left), 1% chitosan film (right) and glass substrate (bottom).* ***Scale bars top left hand corner of each image.***

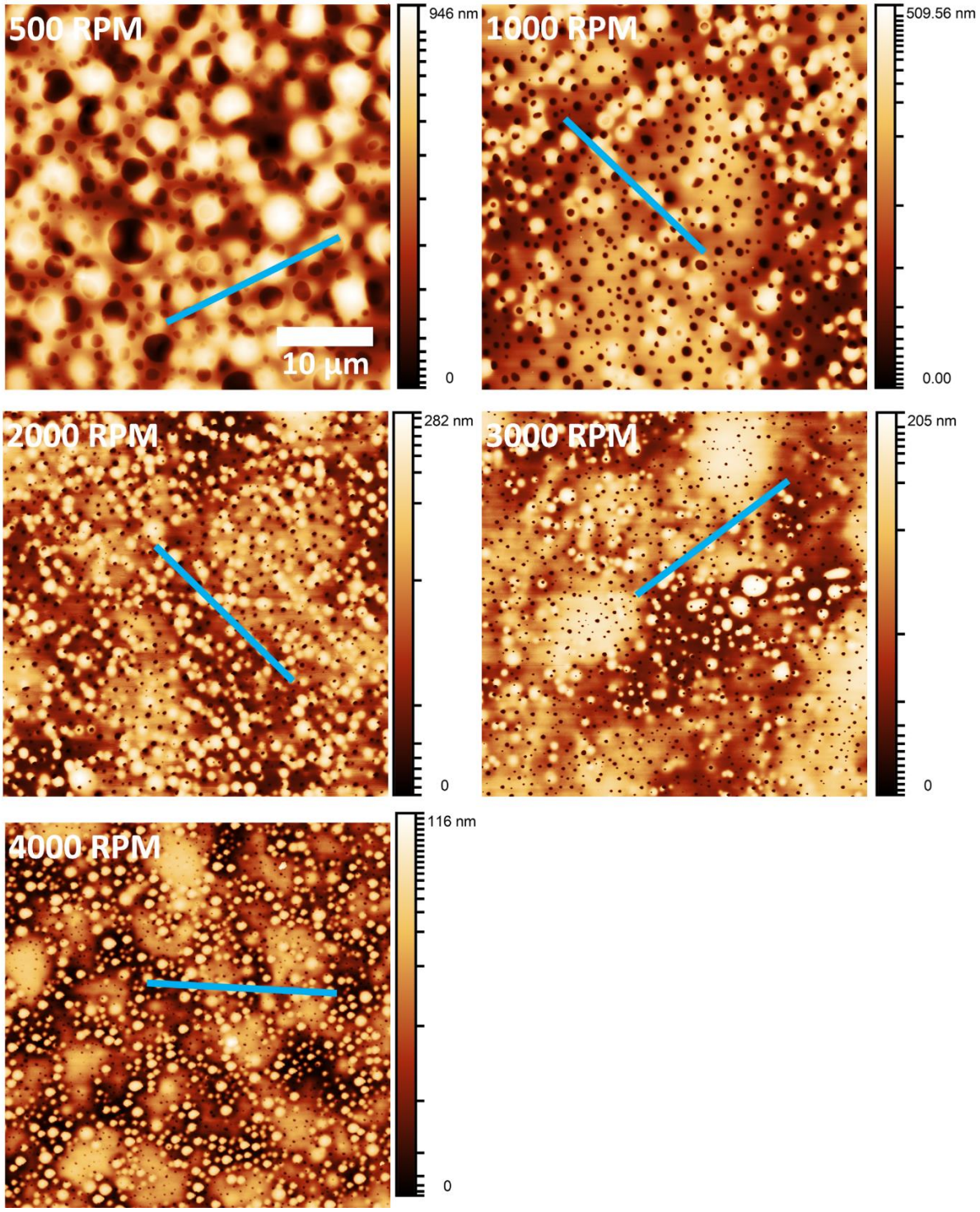


Figure S3.2: *AFM images depicting the effect spin speed in ambient air (65% RH) for the 4:1 BSA-Ch blend. Each image is 40 µm × 40 µm area (scale bar 10 µm, shown in the 500 rpm image). Line profile denoted by blue line.*

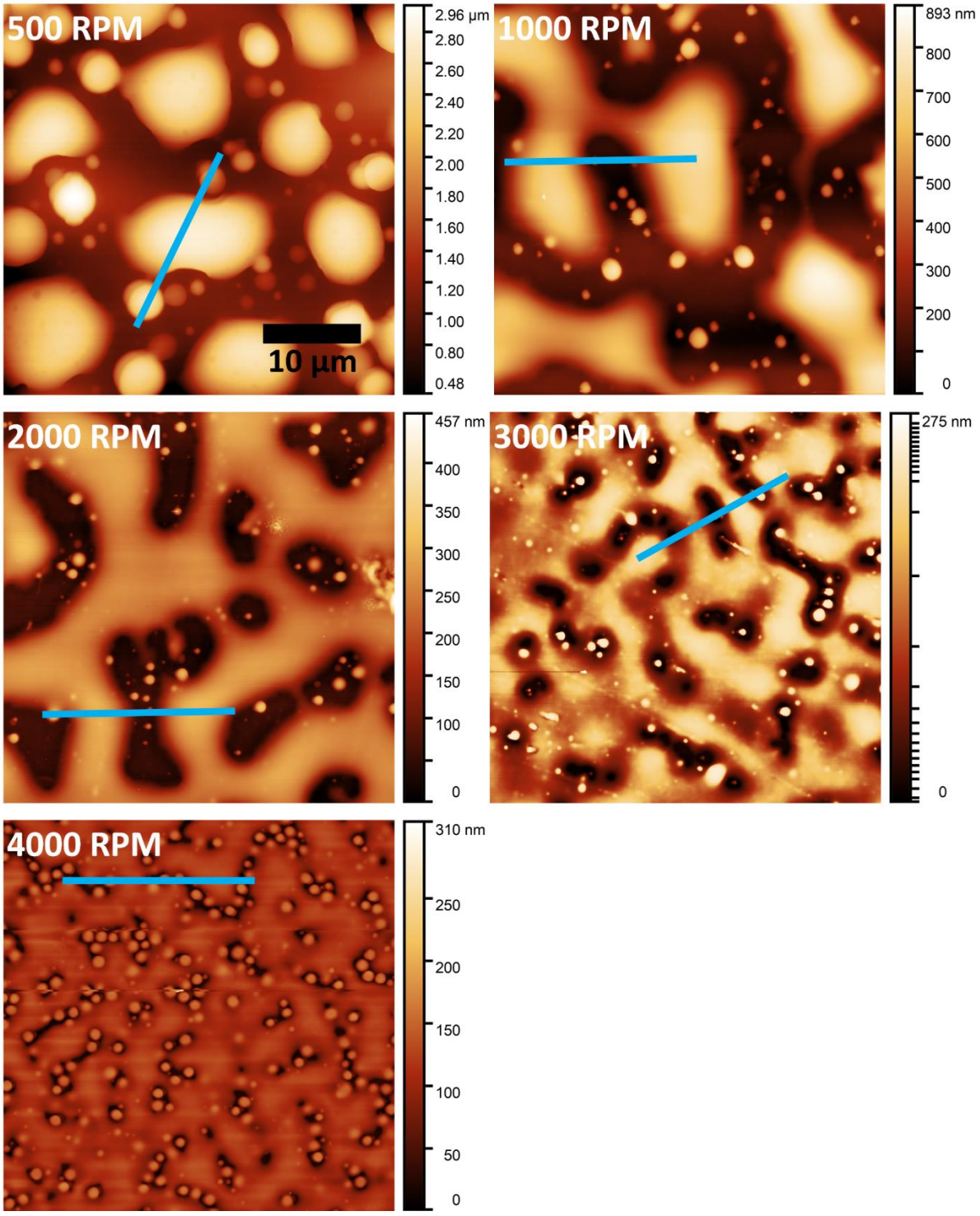


Figure S3.3: *AFM images depicting the effect spin speed in ambient air (65% RH) for the 4:1 BSA-Ch blend. Each image is 40 µm × 40 µm area (scale bar 10 µm, shown in the 500 rpm image). Line profile denoted by blue line.*

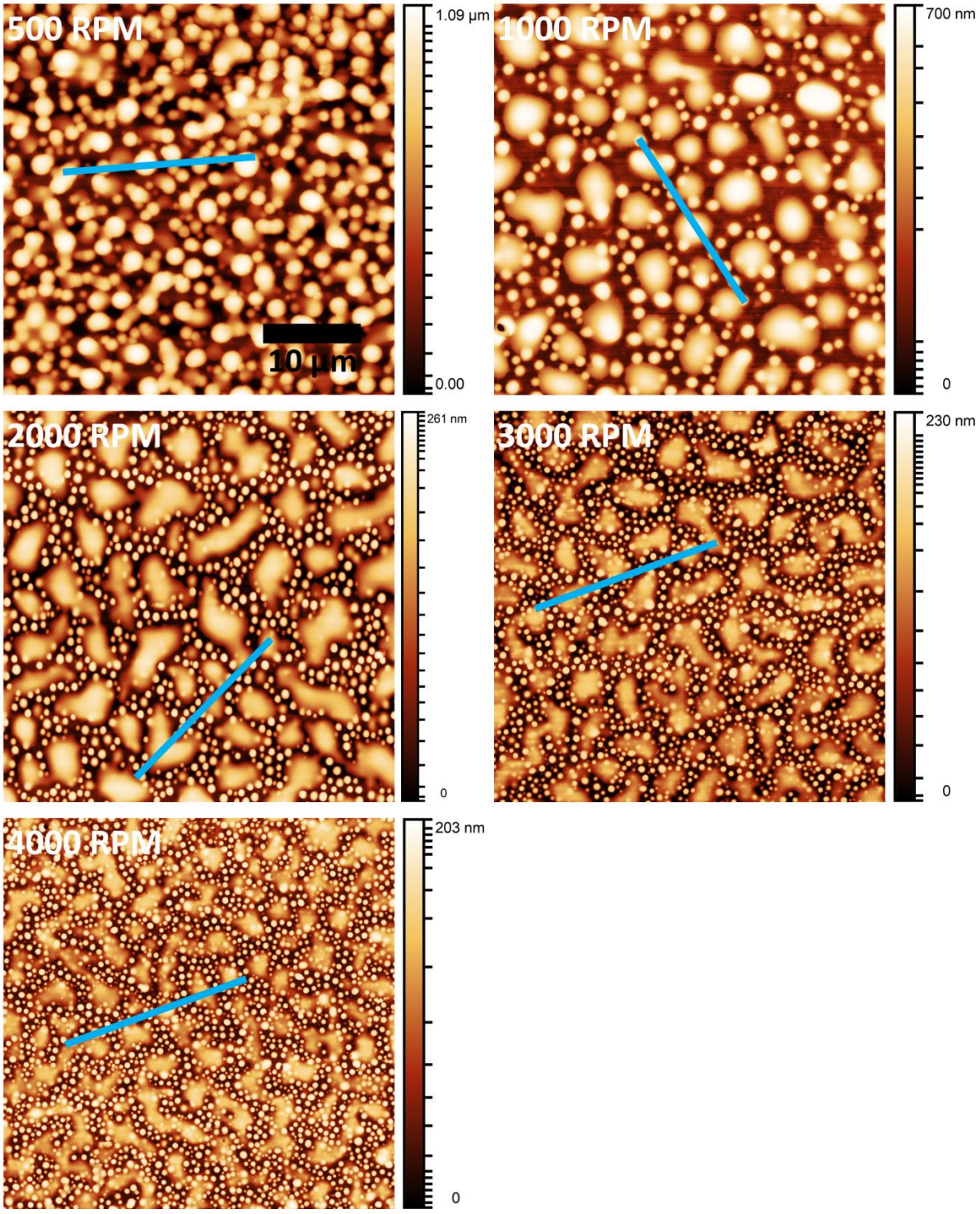


Figure S3.4: *AFM images depicting the effect spin speed in ambient air (65% RH) for the 1:1 BSA-Ch blend. Each image is 40 µm × 40 µm area (scale bar 10 µm, shown in the 500 rpm image). Line profile denoted by blue line.*

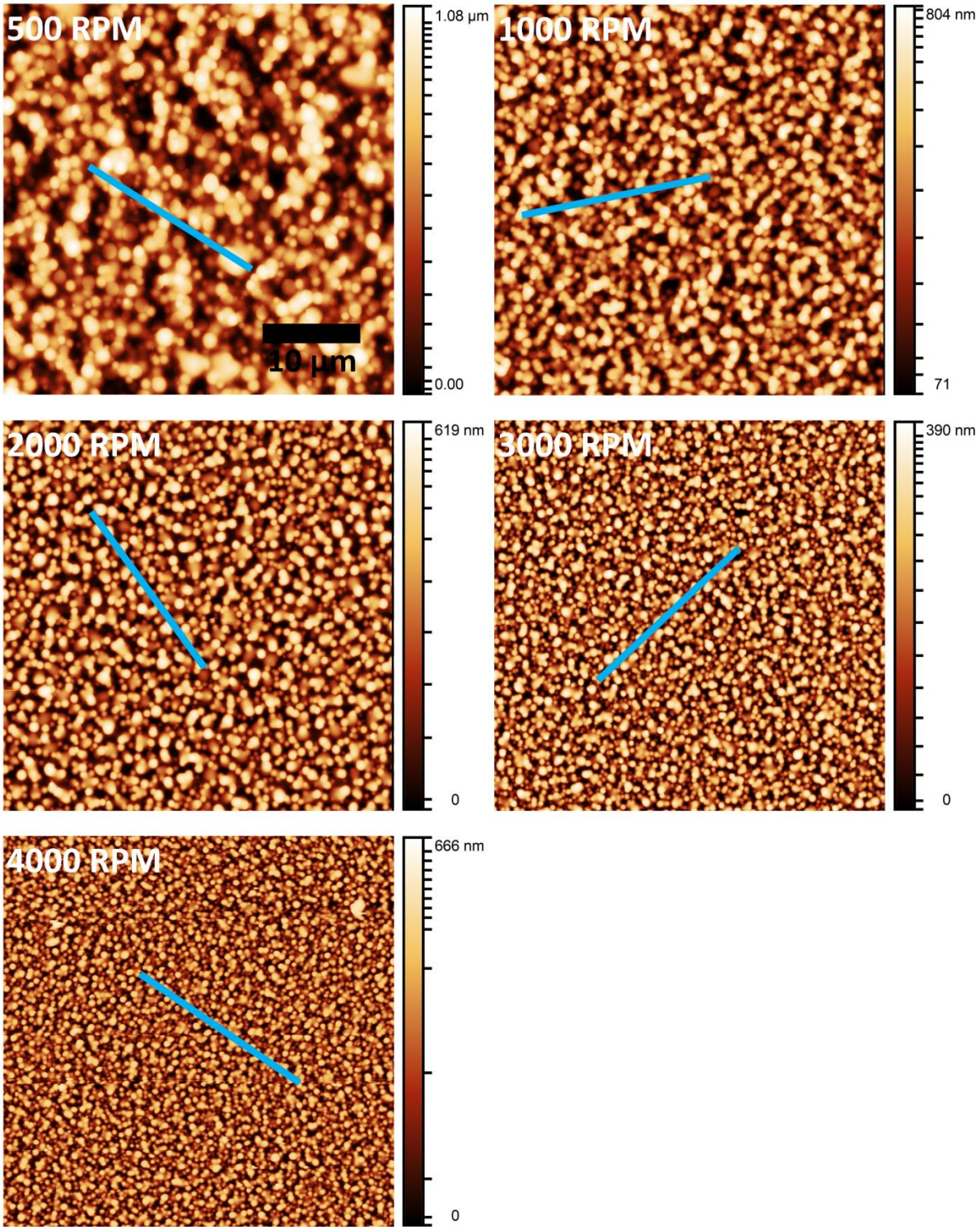


Figure S3.5: *AFM images depicting the effect spin speed in ambient air (65% RH) for the 1:2 BSA-Ch blend. Each image is 40 µm × 40 µm area (scale bar 10 µm, shown in the 500 rpm image). Line profile denoted by blue line.*

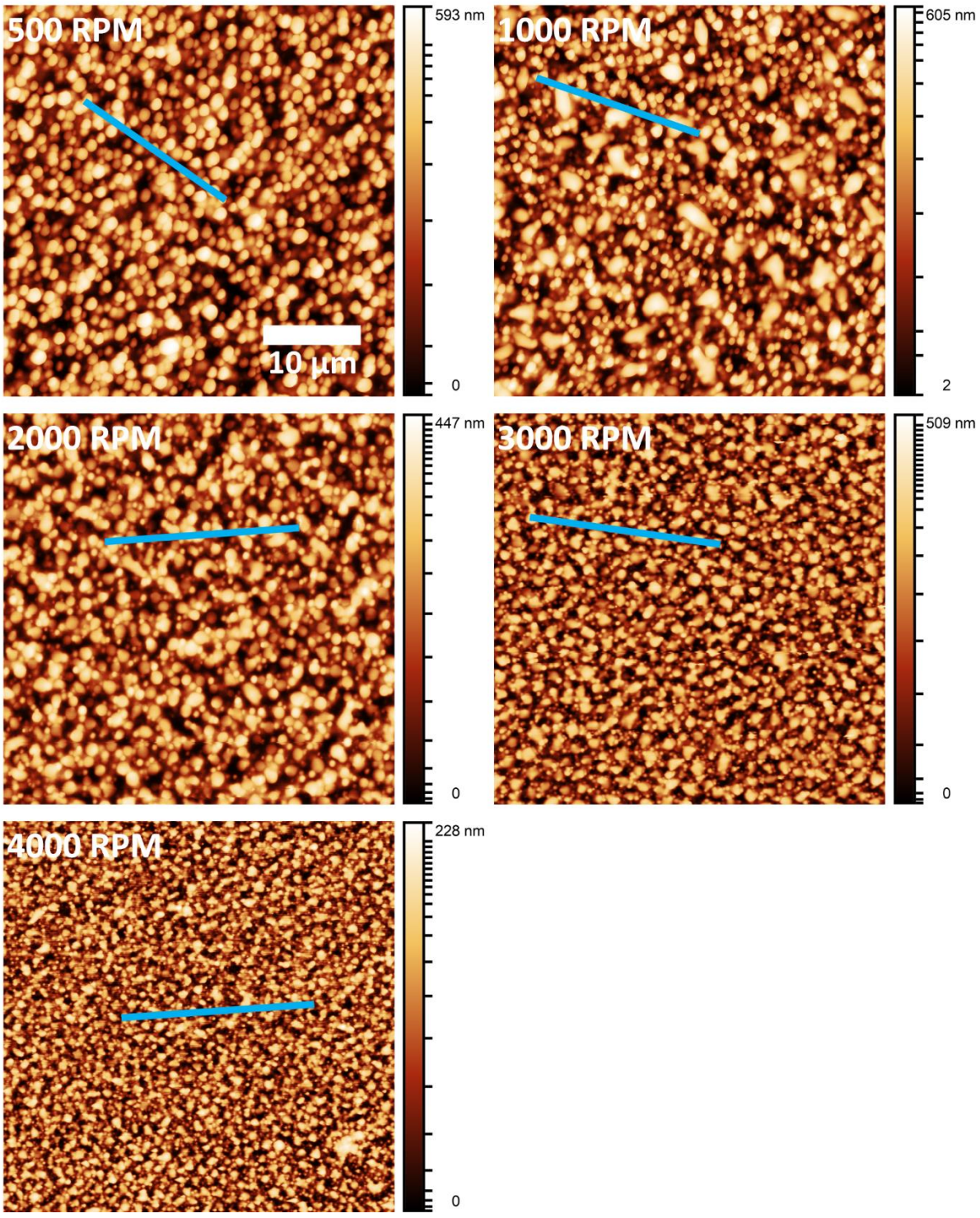


Figure S3.6: *AFM images depicting the effect spin speed in ambient air (65% RH) for the 1:2 BSA-Ch blend. Each image is 40 µm × 40 µm area (scale bar 10 µm, shown in the 500 rpm image). Line profile denoted by blue line.*

4% : 1%

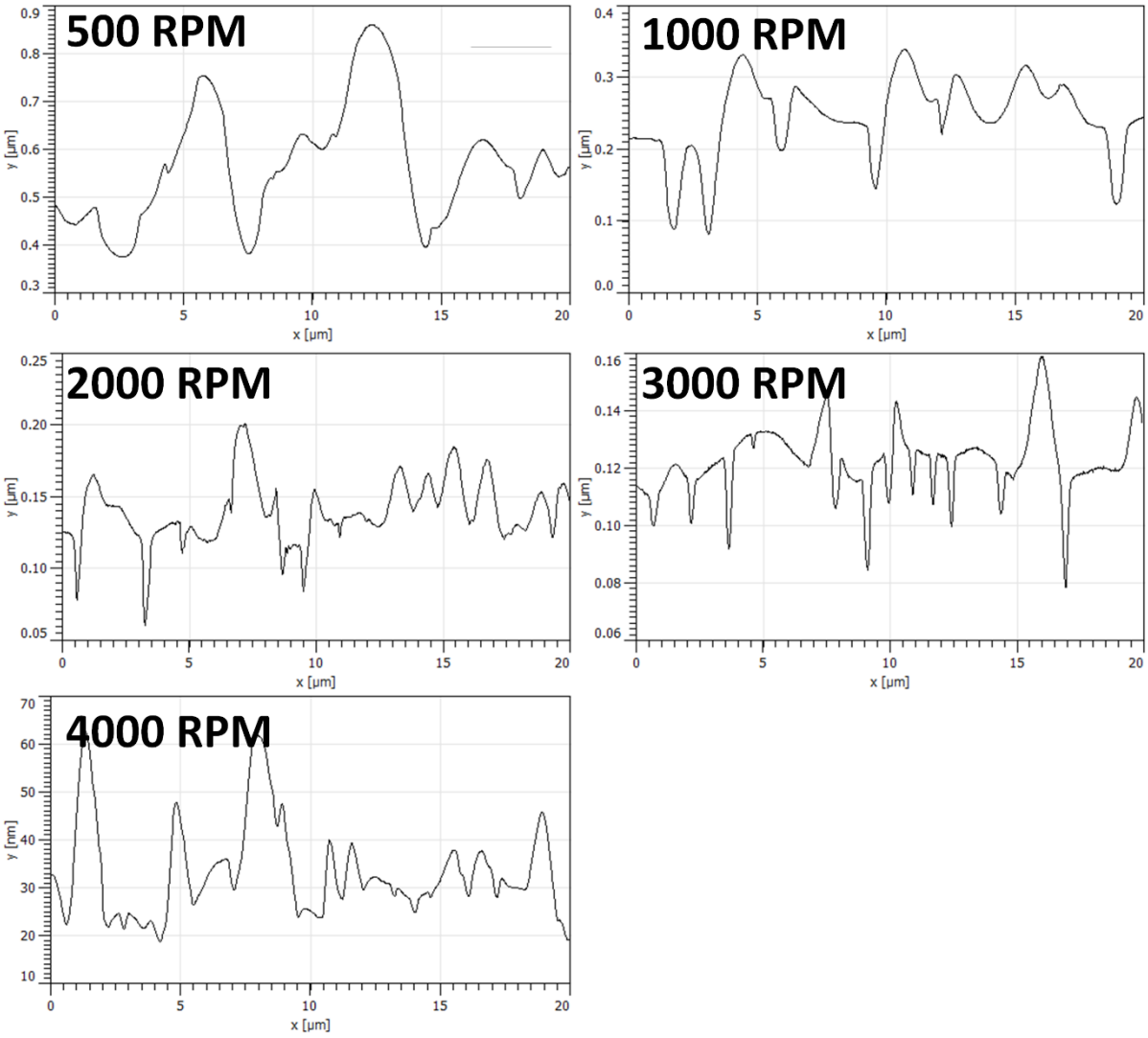


Figure S3.7: *20 µm line profiles for all 4:1 BSA-Ch.*

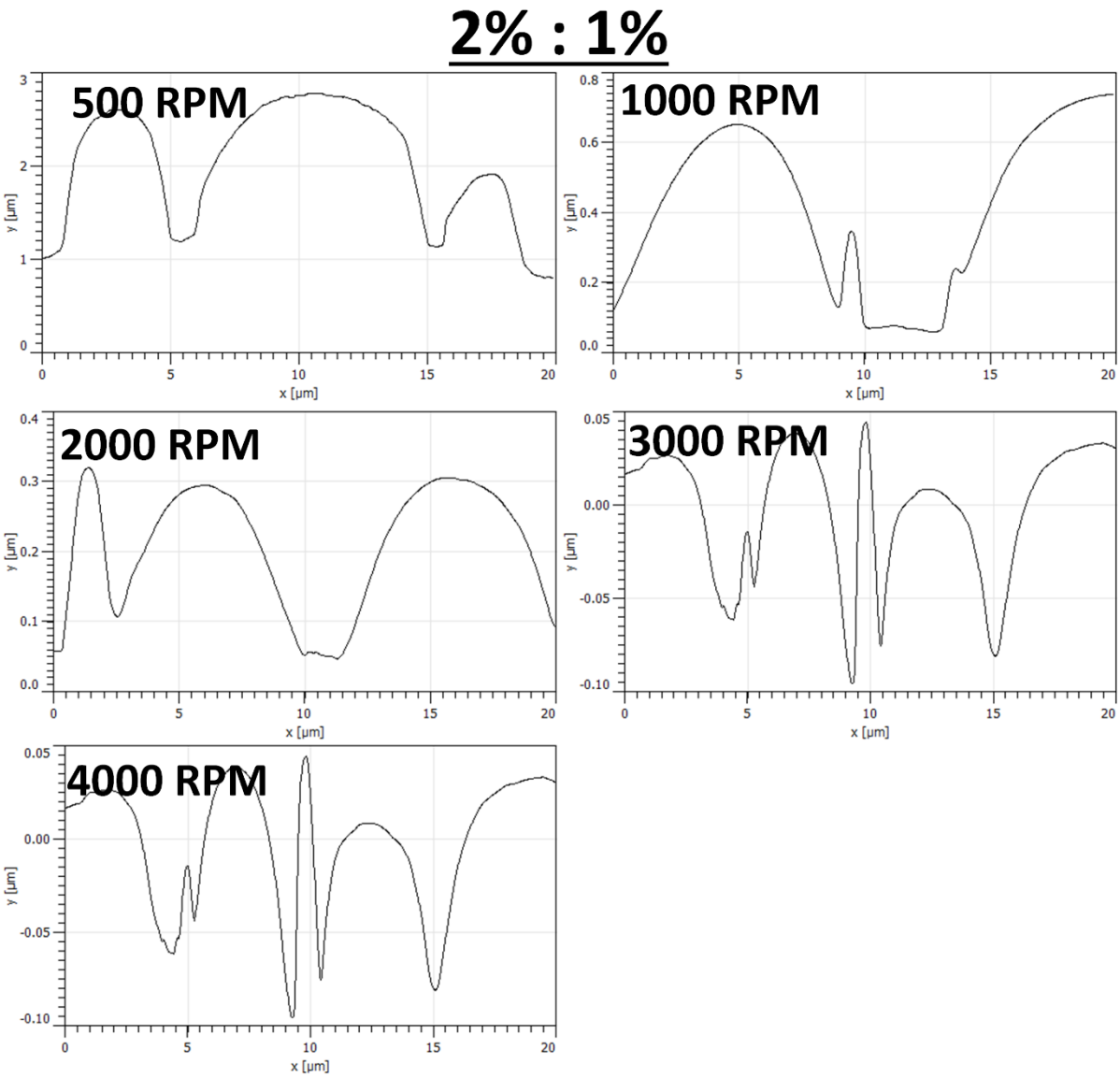


Figure S3.8: *20 µm line profiles for all 2:1 BSA-Ch.*

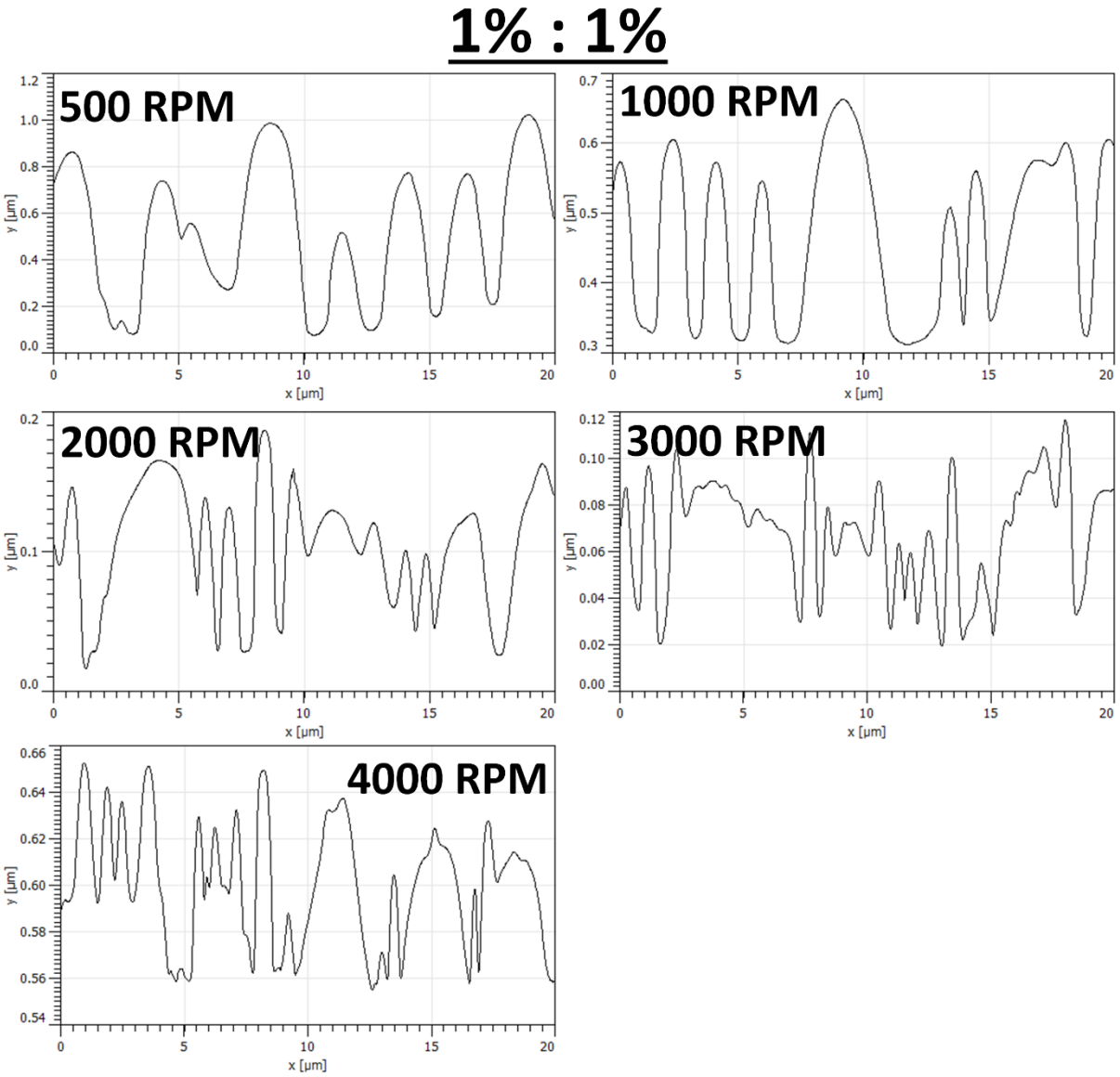


Figure S3.9: *20 µm line profiles for all 1:1 BSA-Ch.*

1% : 2%

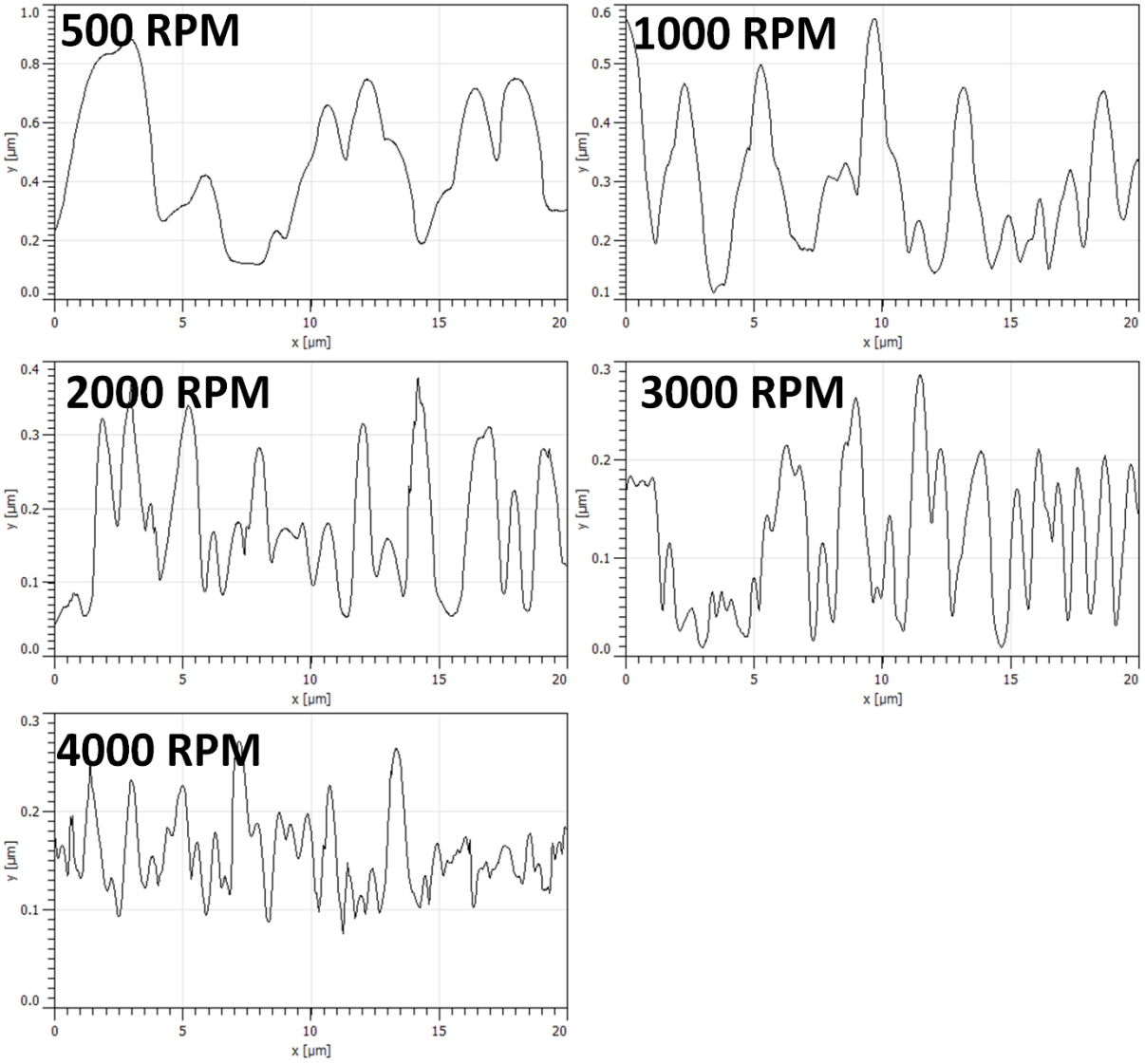


Figure S3.10: *20 µm line profiles for all 1:2 BSA-Ch.*

1% : 4%

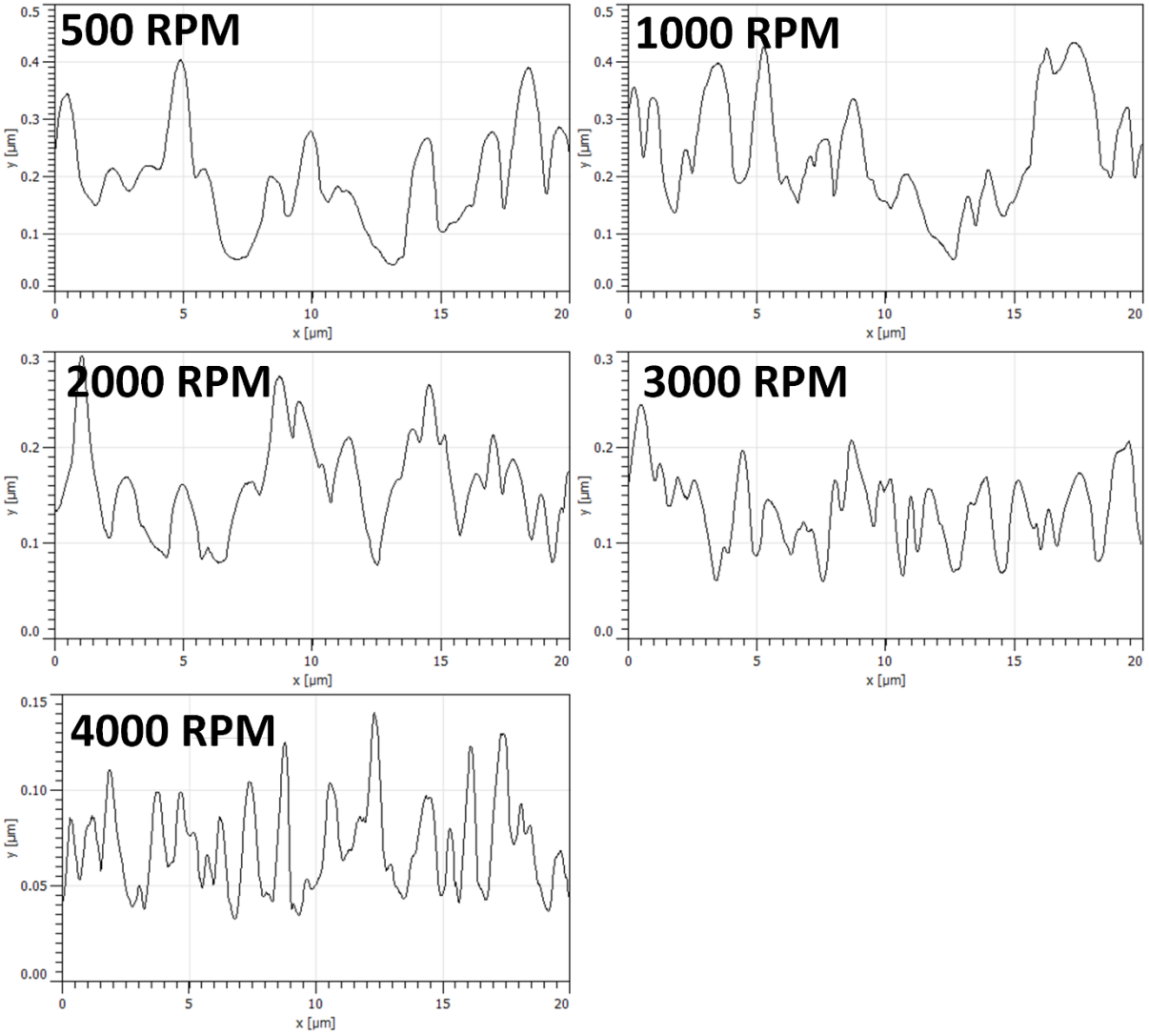


Figure S3.11: *20 µm line profiles for all 1:4 BSA-Ch.*

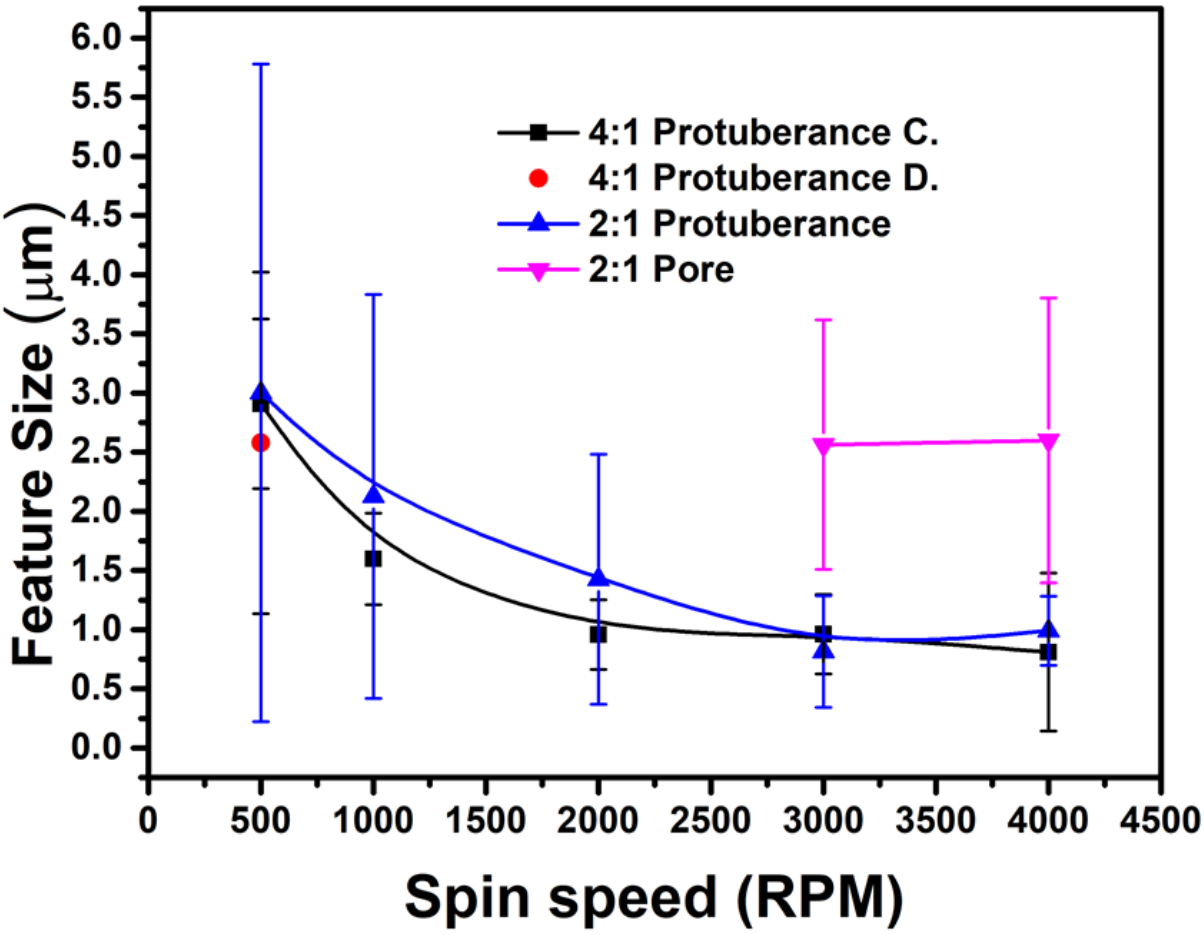


Figure S3.12: *Statistical analysis of BSA-Ch blends feature diameter plotted against spin speed. All but the 2:1 blend refers to protuberance measurements, with the 2:1 blend data displaying both protuberance and pore data separately. The circular legend for the 4:1 blend refers to feature diameter in the discontinuous domain, i.e. salami structure regions.*

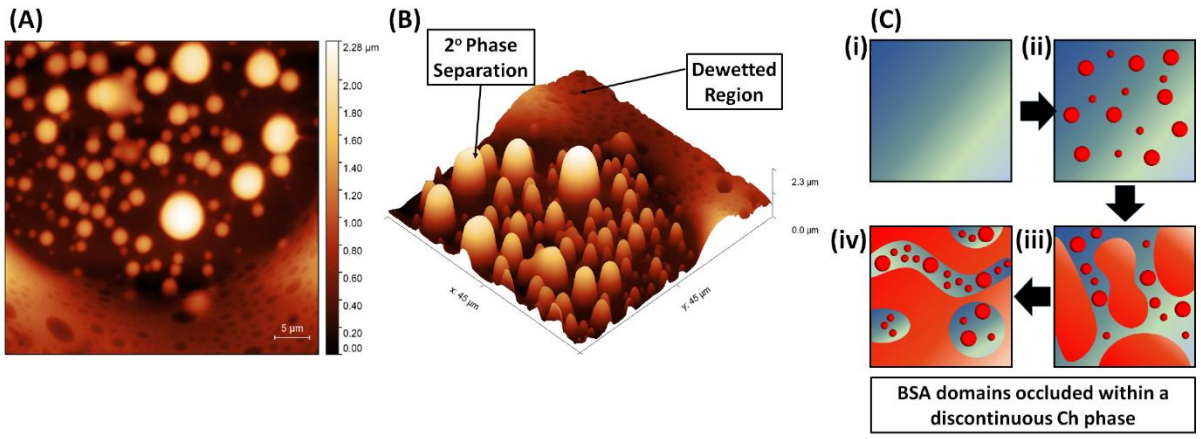


***Figure S3.13: A** and **B)** 2D and 3D AFM images of 4:1 BSA-Ch blend salami structures, inset scale bar 5 µm. **C)** Mechanism of occlusion of the discontinuous phase. **Figure S3.14 (i)** shows homogenous solution before phase separation, **(ii)** shows blend phase separation, **(iii)** shows elongated structures which may result from coalescence or high shear forces and **(iv)** phase occlusion and adoption of salami structure.*

3.8.2. GENERAL TRENDS IN BLEND THIN-FILMS

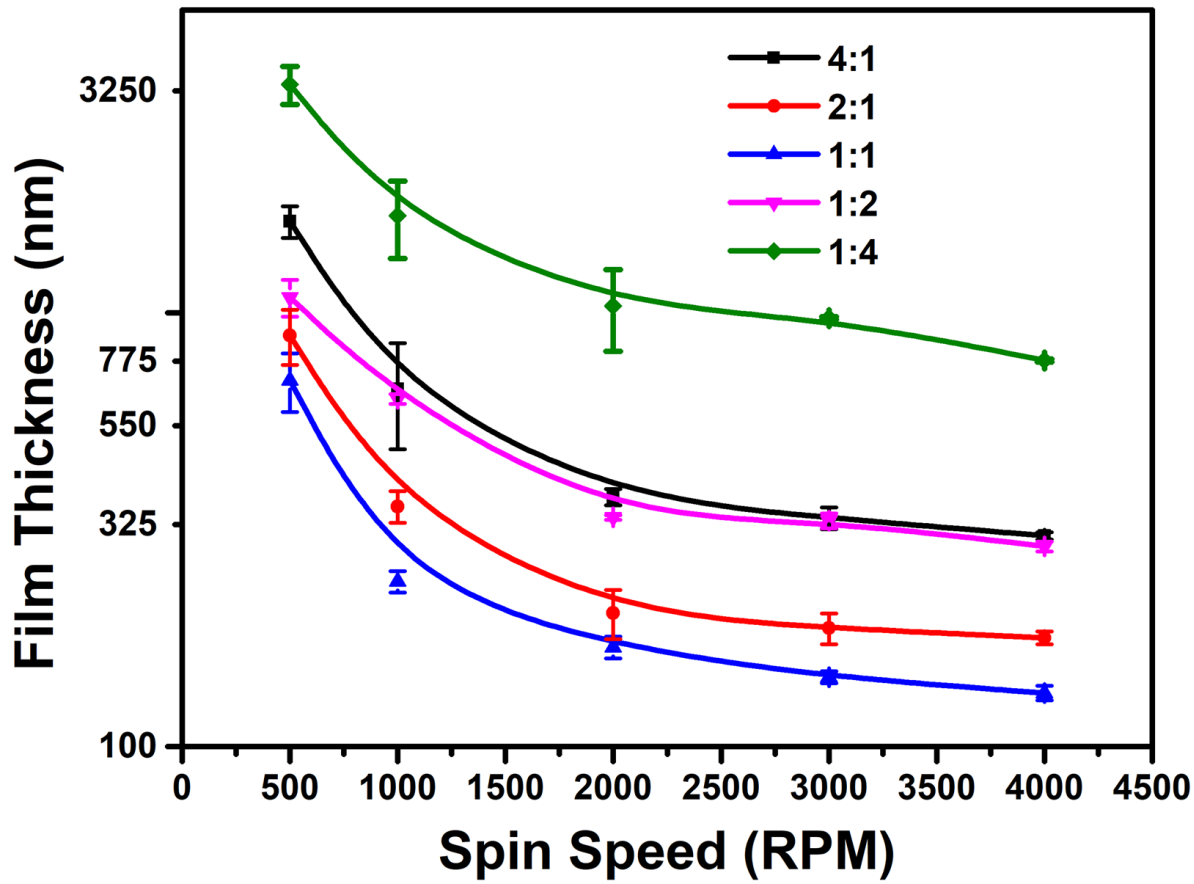


Figure S3.15: *Plots the average film thickness (nm) vs spin speed (rpm) for all BSA-Ch blends.*

Figure S3.15 shows the average film thickness of BSA-Ch blends. 1:1 BSA-Ch films are the thinnest, due to low solution viscosity. Doubling the BSA wt% in the 2:1 BSA-Ch blends increases film thickness due to increased solution viscosity. As Ch produces more viscous solutions in formic acid, the 1:2 BSA-Ch blend produces thicker films than the 1:1 or 2:1 BSA-Ch blends. Similarly, the 4:1 BSA-Ch blend is thicker than the 2:1 BSA-Ch blend. However, at higher spin speeds (≥ 2000 rpm) 1:2 BSA-Ch blends have equivalent film thickness measurements to 4:1 BSA-Ch blends. This is most likely due to faster evaporation during spin coating resulting in more viscous solutions. This, in turn, would result in more Ch retained on the substrate. As the most viscous solution, the 1:4 BSA-Ch films are the thickest. All blends (with the exception of the 1:4 BSA-Ch blend) achieved minimal reduction in film thickness with speeds exceeding 2000 rpm. The 4:1 BSA-Ch blend was the only blend to result in salami structure formation.

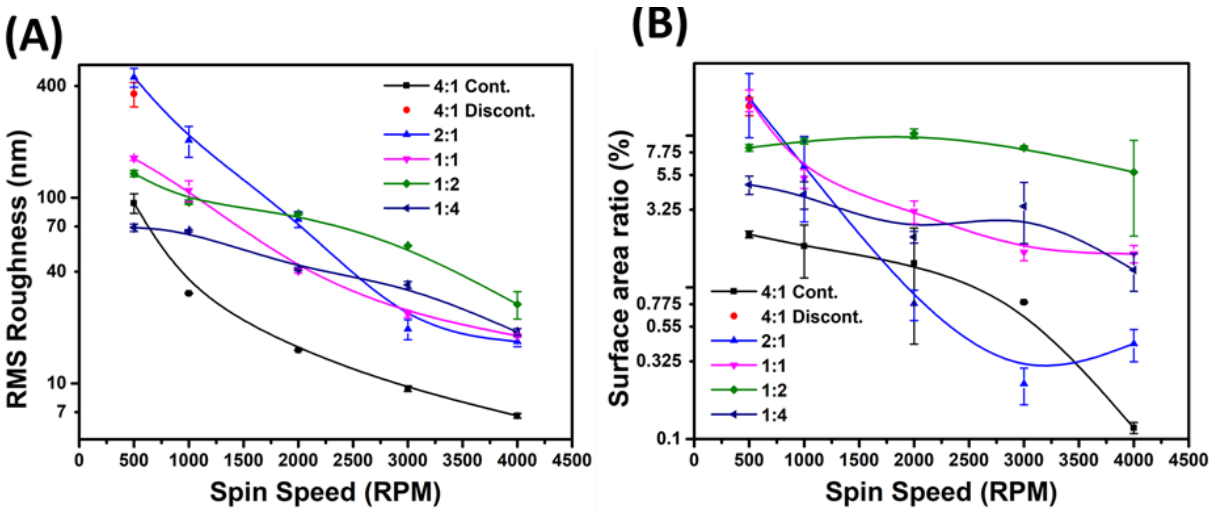


Figure S3.16: A) *Plots the RMS roughness vs spin speed for all BSA-Ch blends.* ***B)*** *Plots the surface area ratio (%) vs spin speed for all BSA-Ch blends.*

Figure S3.16 shows the BSA-Ch blend film RMS roughness as a function of spin speed for all samples. RMS of polymer blends can affect coating properties such as hydrophobicity[23] and wettability[97] and bacterial adhesion.[31] Therefore, tailorable RMS is desirable. In all blends, roughness decreased with increased spin speed. Slopes of the 4:1 BSA-Ch blend were similar to the 2:1 blend, showing the sharpest reduction in RMS roughness from 500 rpm to 2000 rpm. For the 4:1 blend, this is likely due to a reduction in the diameter of all features as rpm increases. By contrast, the 2:1 blend loses large, tall features in favour of a smooth continuous BSA domain. At 4:1, 1:1, 1:2 and 1:4 ratios, protuberances become oblate, pancake-like structures with increasing spin speed, thereby reducing RMS roughness. This also occurs in the 2:1 BSA blend, but to a lesser degree. Transitions in spin speed from 500 rpm to 1000 rpm reduced protuberance height from 4 μm to 600 nm resulting in the largest decrease in RMS roughness (242 nm, **Figure S3.16A**). However, a smooth continuous domain appears to be the predominant feature when determining RMS roughness for this blend.

Figure S3.16B plots surface area ratio (%) as a function of rotational speed in spin coating. In general, surface area ratio (%) is reduced with increased spin speed due to the reduced height of the structures. This result shows that aspect ratio of features can be tuned, allowing broader applicability. Higher aspect ratios are particularly useful for enhancing anti-reflective properties. This aligns with previous data seen with RMS roughness in **Figure S3.16A**. The 1:2 blend deviates from the general observation by increasing surface area ratio (%) with spin

speed. This is due to interconnects (necks) forming between individual protuberances. As spin speed is increased from 500 rpm to 1000 rpm (**Figure 3.1**, D1 and D2), protuberance growth is inhibited by faster spin speed (**Figure 3.2a**). Protuberances however appear interconnected by a wall structure, referred to as a neck (i.e. inhibited coalescence).[58] As viscosity increases (due to increased concentration of the continuous phase) coalescence is supressed. This is to be expected as the adoption of a spheroidal shape is impeded.[40] These structures become more numerous as spin speed increases to 2000 rpm (**Figure 3.1**, D3) and growth is further inhibited. These interconnects increase the surface area ratio (%) of the sample. This is further supported by interconnects becoming less prominent at speeds exceeding 2000 rpm, though not totally removed (**Figure 3.1**, D4 and D5). In contrast to 4:1, 2:1 and 1:1 blends, the 1:2 blend features are compacted together and are not as well resolved from one another.

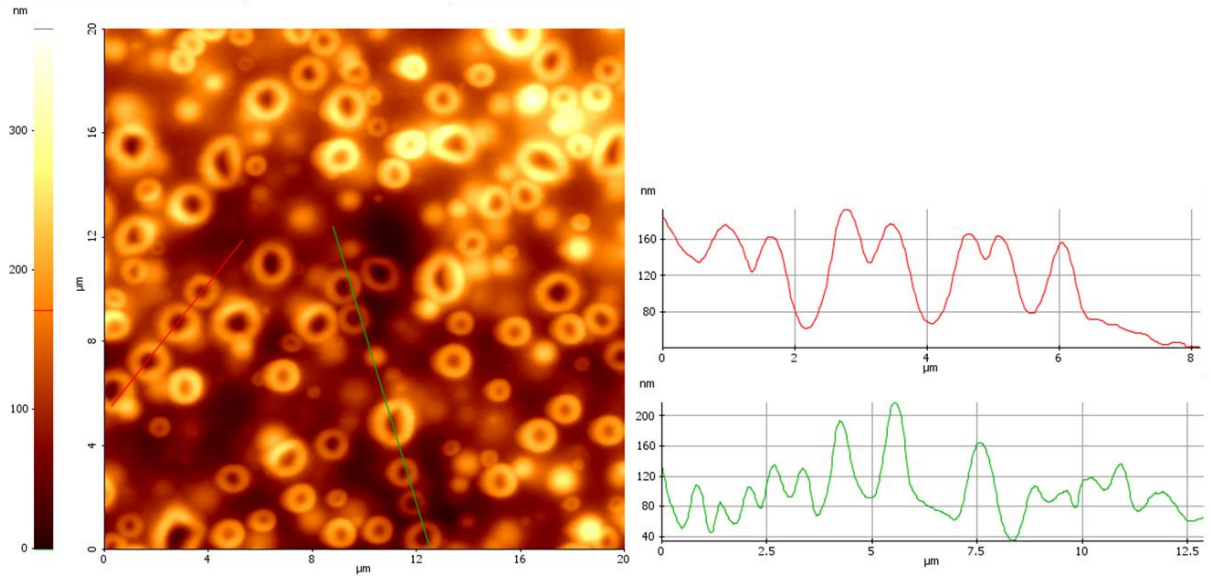


Figure S3.17: *AFM images and surface profiles of 1:4 BSA-Ch blends, 500 rpm on planar silicon substrates. Sample was etched using buffered solutions contained 200 mM Tris-HCl, pH 8.8 for 20 hrs after crosslinking with 20 wt% glutaraldehyde for 20 hr.*

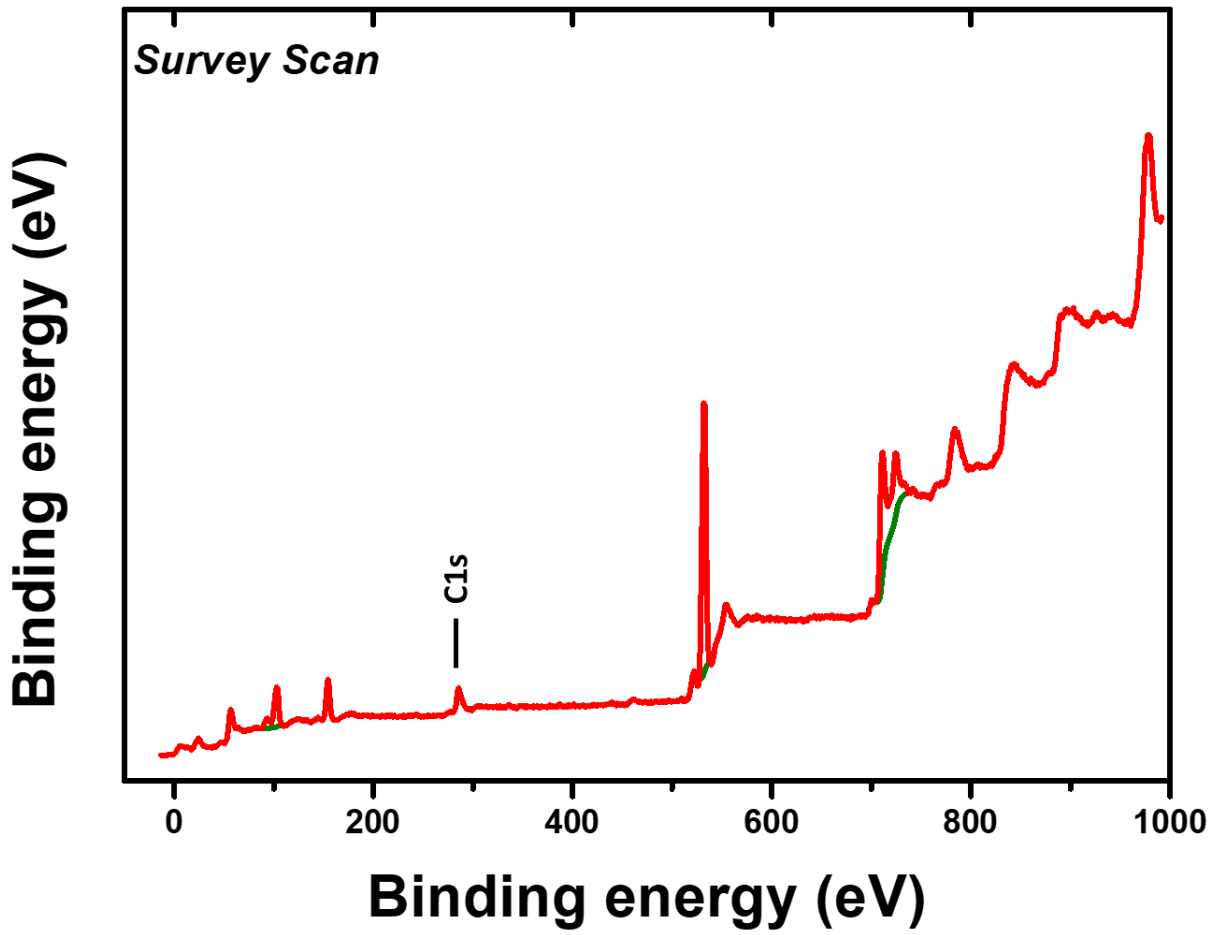
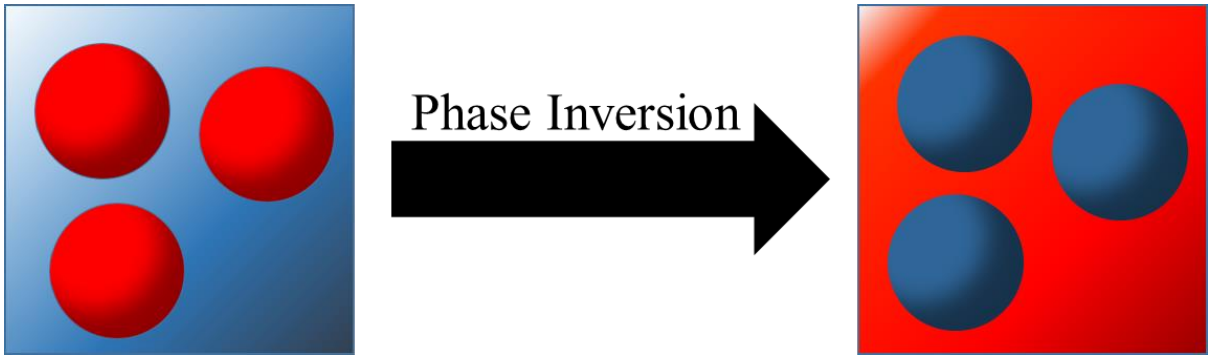


Figure S3.18: *Survey spectra of porous iron oxide matrix following calcination treatment.*

3.8.3. PORE GROWTH IN BLEND THIN-FILMS

At biopolymer ratio of 4 w/v% BSA to 1 w/v% Ch, across all spin speeds (**Figure 3.1**, Column A and **Figure S3.2**), pores (spherical holes) formed. Two relationships between pores and spin speed were observed: as spin speed increased, the mean pore diameter (**Figure 3.2a**) decreased and the number of pores per unit area (pores / μm^2, **Figure 3.2b**) increased. The mean pore diameter dropped from 1.14 μm (500 rpm) to 0.25 μm (4000 rpm), **Figure 3.2a**. Thus, pore formation at this biopolymer ratio occurs via an inhibited growth mechanism, i.e. a decrease in pore diameter with faster solvent removal.[23,34,40] The mechanisms of pore formation vary for each blend, unlike protuberances which show a consistent formation mechanism. The 2:1 BSA-Ch blend only forms "pseudo pores" (discontinuous indented regions caused by dewetting and phase inversion) at spin speeds ≥3000 rpm (**Scheme S3.1**), unlike in the 4:1 blend. [15,18,19,34,98,99] An increase in spin speed increased pore diameter and decreased the numbers of pores per area (**Figure 3.1**, Column B and **Figure S3.3**). This is in contrast to the trend observed with the 4:1 BSA-Ch blend which showed a decrease in pore diameter and an increase in pores per area with increased spin speed (**Figure 3.1**, Column A) which suggests a secondary phase inversion rather than salami structure formation.[17,100]



Scheme S3.1: *Pore forming process for the 2:1 blend. With sufficient BSA in the blend, the film phase inverts, so that the continuous phase comprises of BSA (red), while the discontinuous phase now comprises of Ch (blue), forming a porous array.*

Irregularly shaped pseudo pores are generated at ≥3000 rpm as phase inversion occurs (**Figure 3.1**, B3) due to the BSA component forming a continuous phase. Differences between the protein and polysaccharide phase viscosities at the 2:1 blend ratio, and strong shear forces at high spin speeds are the cause of phase inversion and phase elongation.[1898] These shear stress effects also contribute to the increased pore diameter, the decreased number of features/area, and the irregular pore shapes.[18,34] The pseudo pores observed in the 2:1 BSA-Ch blend are much larger than that of the pores caused by solvent-rich phase evaporation in the

4:1 blend (**Figure 3.1** Column A and B, **Figure 3.2A**). This is due to pseudo pores arising during the BSA continuous phase formation and shear effects in the 2:1 blend, whereas "true" pores in the 4:1 blend appear to be formed from a solvent rich phase and solvent evaporation upon film vitrification. [53]

Figure 3.1, image B5 shows that 4000 rpm yields small, circular pores. The larger pores form longer continuous phases resulting in a minor increase of mean pore diameter. This indicates that the 2:1 BSA-Ch blend pore growth mechanism differs to that of the 4:1 blend, resulting from the formation of a continuous BSA phase.

Pore diameter data was also extracted from AFM images and the corresponding normalized frequency histograms are shown in **Figure S3.19**. The 4:1 BSA-Ch blend pores exhibited similar growth patterns to protuberances. At low spin speeds, the blends exhibit multimodal SDs over a broad diameter range. Increasing spin speed reduces the number of modes and population weight shifts to a smaller diameter (**Figure S3.19a**). This suggests that the pores, like the protuberances, develop via nucleation and growth. The 2:1 BSA-Ch blend produces a multimodal pore SD at high spin speeds (**Figure S3.19b**). These pores are irregularly shaped and do not form via the same process as 4:1 BSA-Ch blend pores **Figure 3.1**, Column A).[26] They are caused by the BSA phase inverting and forming a continuous domain.[15] As such, increasing spin speed to 4000 rpm does little to shift the pore diameter, though the blend exhibits more pronounced peaks at 1.4 µm, 1.8 µm, 2.4 µm and 2.8 µm. It must be stated, however, that phase separation of polymer blends at high humidity and resulting pore formation is poorly understood.[26] Furthermore, humidity is not typically monitored, regulated or even discussed in the majority of polymer blend literature.[101] If pores are the desired morphological structure, removal of the discontinuous domain may be a more reliable manner of achieving a porous matrix.[57]

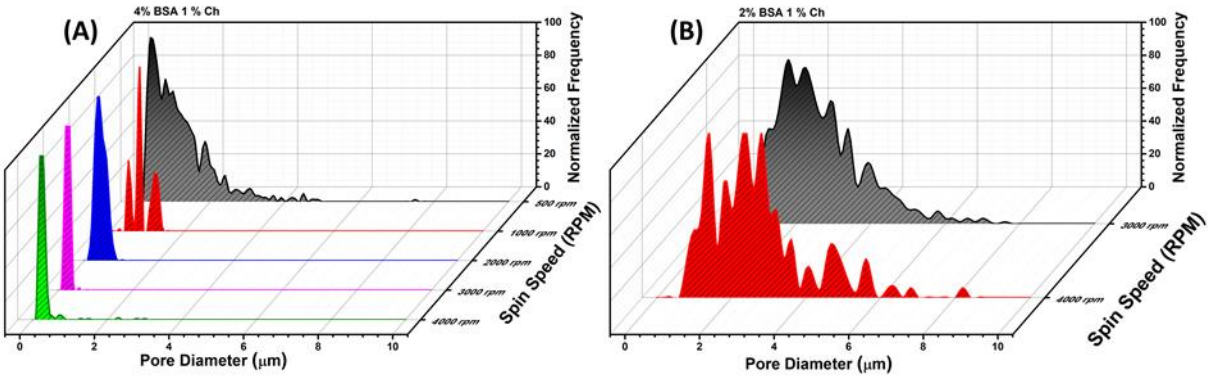


Figure S3.19: *Statistical analysis of BSA-Ch blends for feature diameter and frequency of feature diameters.* ***A)*** *Displays feature frequency vs diameter of observed features for the 4:1 blends and* ***B)*** *displays feature frequency vs diameter of observed features for the 2:1 blends respectively.*

3.8.4. WATER CONTACT ANGLE

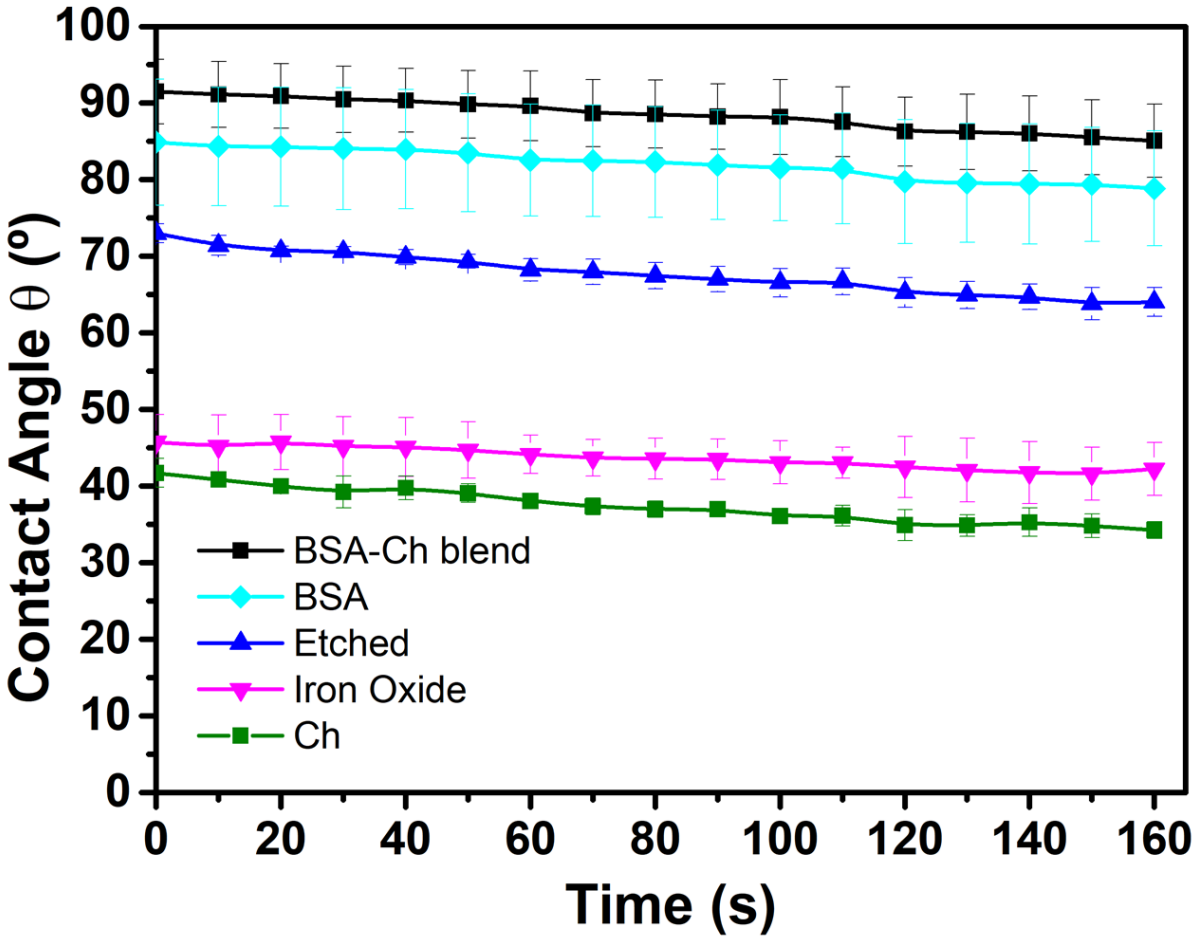


Figure S3.20: *Displays plot of average receding contact angle as a function of time for BSA, Ch, BSA-Ch blend, Tris-HCl etched blend and porous iron oxide matrix.*

Figure S3.20 shows water contact angles of the various relevant surfaces to confirm chemical and morphological changes in the samples with processing. This is to done to confirm the removal of BSA and the formation of a metal oxide on the surface to demonstrate correct assignment of each domain. All tested surfaces displayed a reduction in measured contact angle after 160 s. The 1:1 BSA-Ch blend exhibited the largest water contact angle, starting at 92º receding to 85º. This is unsurprising due to the rough nature of the blend surface and the incorporation of BSA, which is shown to have the second largest contact angle (85º – 79 º).[13] While on its own, water contact angle measurements do not confirm the removal of BSA or formation of the metal oxide, these results compliment the findings of the etching, metal incorporation, FTIR and XPS.

The porous Ch matrix (73º – 64 º) has a higher contact angle than the pristine Ch surface (42º – 32 º): This is due to surface roughening caused by the pores. The reduction in the contact angle, compared to the 1:1 BSA–Ch, confirms the successful removal of BSA from the blend. Finally, the water contact angle of the iron oxide film (46º – 42 º) indicates magnetite composition, with the increased roughness and presence of pores contributing to a slightly larger contact angle than the literature.[102] The changes in the morphology and surface chemistry are as expected, and support the data seen in the FTIR and XPS spectra (**Figure 3.4**).

Chapter 4

Biopolymer Metal Inclusion Lithography (BioMIL): A simple, renewable method to produce metal oxide masks

Submitted for publication – ACS Applied Materials & Interfaces

4.1. ABSTRACT

Patterned thin films (PTFs) films are essential to the commonplace technologies of modern life, and have a crucial role in a host of current and emerging critical technologies across a broad range of industries. Contemporary PTFs rely on unsustainable and relatively ineffective petrochemical polymers. These generate pollution; come from dwindling, finite resources; and are suboptimal for making the structures needed for certain advanced applications – particularly broadband anti-reflective (AR) materials, where biomimicry of the AR structures of butterfly wings is the goal. Here we describe the first successful development of an uncomplicated, cheap, sustainable fabrication process for patterned metal templates with tessellated, sub-micron scale structures, like those of butterfly wings, and their transfer to a substrate by wet etching: *Biopolymer metal-inclusion lithography* (BioMIL). Patterning is achieved through phase separation a biopolymer blend, creating a PTF then used as a template for a metal precursor. Biopolymer template morphology is readily controllable and transfer to metals makes for more robust materials, opening up other applications, such as lithography. BioMIL is simple - not requiring enzymes, master templates, or thermal deposition of metals, while selective metal incorporation into a chosen pattern domain is easily achieved. Transfer of metal patterns was done by wet etching, showing these biopolymer templates could replace synthetic polymer blends as pattern-transfer agents.

4.2. INTRODUCTION

The production of patterned surfaces plays a pivotal role in a vast number of current and emerging technologies. Micro and nanostructured surfaces have found applications in textiles[1], optical components[2], self-cleaning/hydrophobic surfaces[3,4], fluid engineering[5–7], anti-reflective (AR) surfaces[2,8–10], gas sensors[8], food texturing[11–16], edible coatings[17], packaging[18,19], lithographic masks[20–24] and in medical technologies.[25–32] These patterns are often dot arrays, nanopillars, or porous materials. AR surfaces have attracted a great deal of research focus for their uses in photonics, smart devices, and renewable energy technologies. Broadband AR surfaces are an acme of AR technology. Nature, as is often the case, has evolved broadband AR materials superior to anything we can produce artificially. Such natural AR technology is epitomised by butterfly wings. Making synthetic broadband AR materials that are equivalent, to nature's finest AR surfaces is a primary objective of research in this area. This is a technical challenge greater than any in other areas of patterned or structured surfaces research. Currently, synthetic block co-polymer (BCP) based AR materials have not managed to produce, at scale,

an adequate equivalent of butterfly wings. By turning to nature, and using naturally occurring polymers – biopolymers – to replicate the structures of butterfly wings, reliable, cleaner, more sustainable production of materials with the necessary structures and scale for broadband AR materials is feasible.

Butterfly wings contain a porous, quasi-honeycomb-array (tessellated), which confer super light trapping properties.[33] These pores are random in size, shape, spacing, and pores/area. Pore diameter appears to range from 300 – 800 nm.[34–37] Evolution is a, slow, imperfect process, and so it can be refined. Nature has not settled on either pores or pillars for butterfly wing AR structures. However, we can ascertain that porous structures are the best option for artificial AR materials for a few reasons: pillars are subject to capillary forces causing aggregation, increasing reflectivity;[2] are easily contaminated and broken, and have no easy means of restoration.[38] Porous structures are stronger than pillar structures, use less material than pillar based surfaces to form structures[37], and do not require the precise, sub-100 nm block copolymers (BCPs) patterns needed to produce pillars. Many methods are used to produce porous structures on substrates where limitations exist due to the number of defects, feature size restrictions, cost, and controllability.[9] Synthetic BCPs and homopolymers are traditionally used, either as device components or in critical production steps. But BCPs are expensive; petrochemically derived; have complex and inefficient manufacturing syntheses; and require long process times.[2,39] This has led to investigations of polymer blends as a simple, low-cost, bottom-up, alternative in AR surface production, and in patterned/structured surface production generally.[1,8–10] This opens up the possible use of biopolymer blends to the same ends.

Most research into polymer blends for patterned surface production employs environmentally damaging, synthetic polymer blends. Biopolymers have not been adopted, seemingly as a result of the complexity of their phase separations, and their wide variation in functional groups. We previously demonstrated the benefits of biopolymer blends in producing patterned thin-films (PTFs).[40,41] PTFs can be produced from biopolymer blends by controlling the phase separation process of the blend.[40,41] This is done by controlling their drying processes. As solvent evaporates, the precipitating polymers phase separate. The manner in which this separation occurs determines the final PTF, allowing for controllable production of surface structures and their patterns. Adjusting experimental parameters such as blend deposition speed and ambient relative humidity, determines the growth mechanisms, and structure scales in the PTF. Here, we demonstrate that the same methods can be applied to AR surface production to develop a new biopolymer based process called, *biopolymer metal inclusion lithography* (*BioMIL*). BioMIL is similar to conventional metal polymer blend lithography (metal-PBL). It can readily

produce metal patterns with the > 100 nm feature sizes needed for broadband AR surfaces that are, thus far, beyond the reach of BCPs. BioMIL also allows for varied morphology, without the need for solvent annealing, or brush layers.[9,10,42] Traditional metal-PBL first requires selective polymer dissolution by solvent annealing, subsequent metal deposition, and lift-off of the final polymer layer under the metal deposition to achieve a metal pattern. But, BioMIL, by using biopolymer PTFs, achieves metal incorporation into a specific domain, similar to the metal incorporation of BCP's, resulting in a simple, clean, process, without the need for complex processing techniques or large capital investments.

Our biopolymer blend is composed of a protein, bovine serum albumin (BSA) and a polysaccharide, chitosan (Ch) with BSA forming the discontinuous domain. Metal-PBL has historically relied on synthetic polymers such as polystyrene (PS) and poly(methyl methacrylate) (PMMA)[8], or PS and polyethylene glycol (PEG)[9] to form immiscible blends. One of the polymers is selectively solubilized/removed, and metal is thermally deposited on the remaining PTF, followed by removal of the polymer situated under the metal to produce either a metallic porous matrix or, inversely, a dot array.[10] In BCP patterning, metal is typically incorporated into a single domain by selective inclusion of the metal.[43] By using a biopolymer blend instead, and selecting Ch as a component, we can utilize the metal binding capacity of Ch to direct the growth of a metal film mirroring the Ch domain.[44–47] Specifically, the amino group of Ch is responsible for the chelating ability of metal cations.[44,45,48,49] In comparison, BSA is a protein comprised of 583 amino acids (AAs).[50] Selective adsorption of soft metal ions occurs due to the hard-soft acid base (HSAB) principle due to the imidazole and thiol containing AAs.[51] Using a protein-polysaccharide blend is closer to the approach used in BCP's than the more complicated techniques used in metal-PBL. BioMIL surpasses metal-PBL in terms of simplicity, cost, time and required infrastructure. BioMIL exemplifies how biopolymer blends could replace existing synthetic polymer technologies. Additionally, the initial morphology of the PTF and the chemistry of each domain will determine the metal oxides features. This makes BioMIL a simpler process than traditional metal-PBL, as well as being more sustainable, cheaper, cleaner, and better able to produce surface structures at the scales needed to manufacture broadband AR materials.

4.3 RESULTS AND DISCUSSION

4.3.1. FABRICATION OF METAL OXIDE HARD MASK PATTERNS

Biopolymer pattern formation and growth mechanisms have been extensively discussed in our previous work.[40,41] To produce effective metal masks for production of broadband AR surfaces, metals must be incorporated selectively into a specific biopolymer phase after phase separation. Therefore, initially, a variety of metals were incorporated (3000 rpm, 60% RH) into the patterns of a 1:1 BSA-Ch blend biopolymer template, in order to determine which, if any, could be incorporated most selectively (**Figure 4.1)**. Porous structures were desired as they are more robust and more easily cleaned when transferred, and exhibit enhanced mechanical properties.

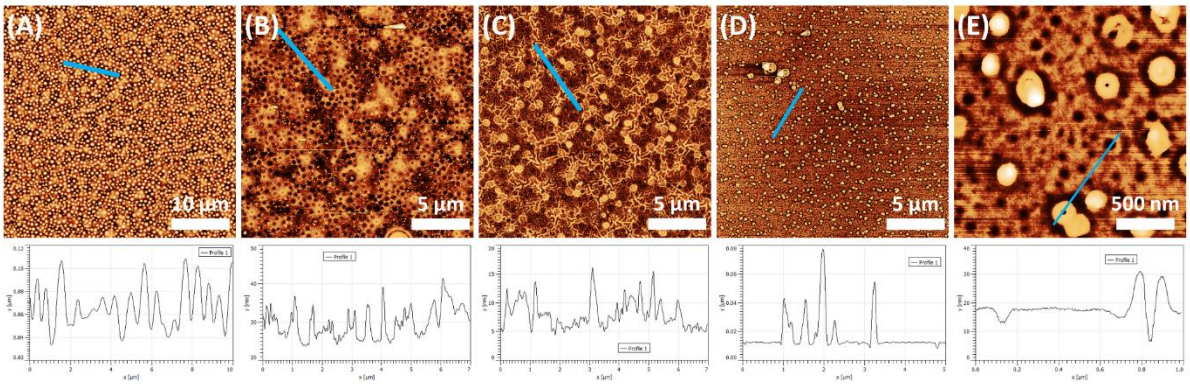
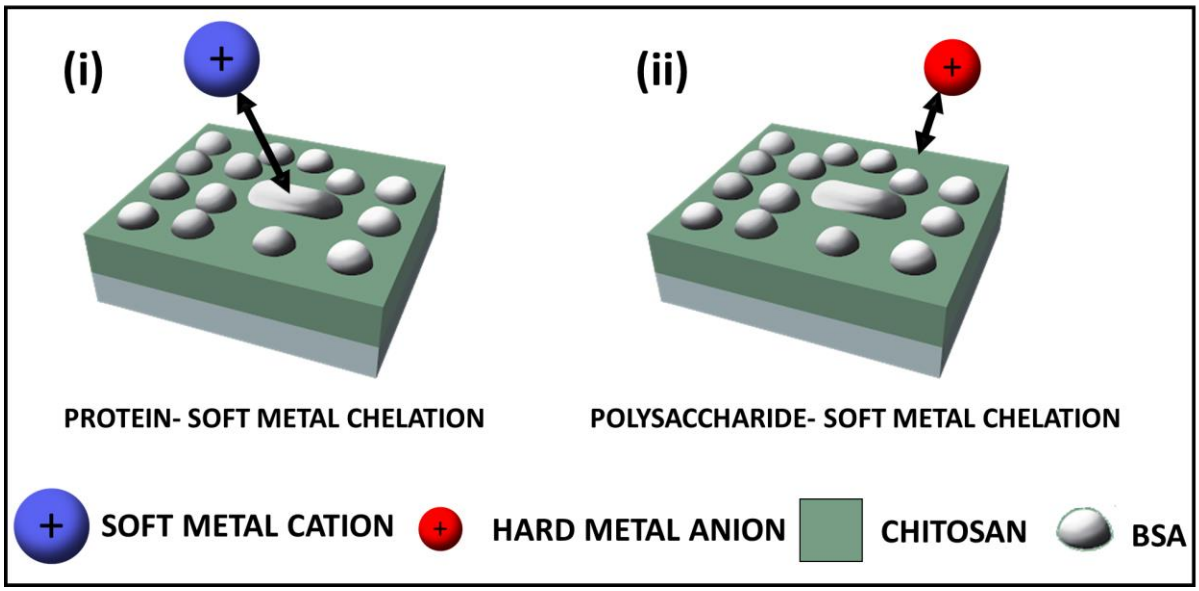


Figure 4.1: *AFM images and surface profiles (blue lines) of biopolymer template and resulting metal structures. Scale bar bottom right of image.* ***A)*** *Refers to the biopolymer template 1:1 BSA-Ch blend, 3000 rpm, 60% RH on planar silicon substrates. Nanoporous metal templates were prepared with alternative precursors (1 w/w%-EtOH).* ***B)*** *1 w/w% $FeCl_3$ anhydrous precursor,* ***C)*** *1 w/w% $Al(NO3)_3.9H_2O$ precursor, and* ***D*** *and* ***E)*** *1 w/w% $AgNO_3$ respectively.*

Figure 4.1 shows the AFM of the 1:1 BSA-Ch template (**Figure 4.1a**) and oxide patterns (**Figure 4.1b, c, d** and **e**) generated by spin coating of 1 wt% metal precursor in EtOH solutions (1 wt% precursor-EtOH). Anhydrous EtOH was used as solvent to limit any effect water may have on the biopolymer template (the protein domain is water soluble). BSA spheres (**Figure 4.1a**) were 0.51 ± 0.47 µm in diameter with 3.62 ± 0.10 spheres/µm^2. This diameter is small for a biopolymer blend,[5,11,52–54] and comparable to, or even smaller than, feature sizes of synthetic blends, indicating viability as patterning agents.[4,9,10,55,56] **Figure 4.1b** clearly shows an iron oxide porous matrix, in good agreement to previous work.[41] Mean pore diameter was

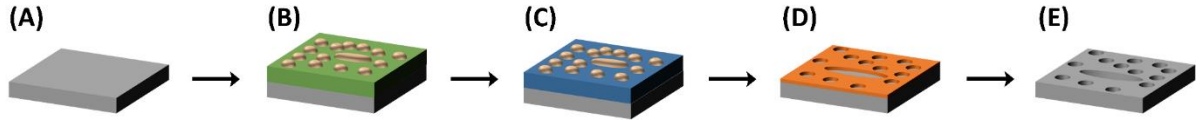
0.34 ± 0.15 µm, with 2.47 ± 0.10 pores/µm^2. This was achieved without glutaraldehyde, which was previously used to slow metal binding to the Ch domain. This removes the need to pre-process the biopolymer template with an environmentally unfriendly precursor.[41]

Figure 4.1c, **d** and **e** show the $Al(NO_3)_3.9H_2O$ precursor and $AgNO_3$ precursor produced a mixed morphology of pores and spheres. All samples in **Figure 4.1** had the same metal ion solution - biopolymer template contact times, indicating non-specific binding to both the BSA and Ch domain occurred – not ideal, given our objectives to produce reproducible, porous, metal films with a consistent morphology. BSA binds to mononuclear and polynuclear metals[57], and binds to soft and borderline metals through its Cys and His residues (**Scheme 4.1**).[51] Some of these suggested AA-metal complexes are shown in **Scheme S4.1**, in section **Appendix 4.7**.[58,59] The pores produced using the Ag precursor had a mean diameter of 0.12 ± 0.07 µm, with 31.15 ± 5.11 pores/µm^2. These pores are smaller and more frequent than protuberances created by the biopolymer template features. The metal spheres formed on the surface were 0.21 ± 0.07 µm, with 2.47 ± 0.09 spheres/µm^2. This suggests that the Ag^+ (a soft metal cation) may preferentially bind to the BSA domain to produce metal spheres, while pores formed through another mechanism.



Scheme 4.1: *Shows the directional binding of hard and soft metals to the blend film.* ***(i)*** *Shows the binding of soft metal cations to the protein domain (BSA).* ***(ii)*** *Shows the binding of hard metals to the polysaccharide domain (Ch).*

The smaller sphere size may result from the finite number of binding sites that exist in BSA, when compared to chitosan. Binding of different cations to specific domains is supported by the hard-soft acid base (HSAB) principle, which suggests that amine ligands will bond preferentially to hard acids (Fe^{3+}), while binding to soft acids (Ag^{+}) is unfavourable. This is consistent with our results in **Figure 4.1**.[60] Knowing this, we can appropriately choose metal precursors which only incorporate into the polysaccharide domain (**Scheme 4.2**). The coordination of metal cations with Ch is well documented[61,62], with example structures shown in **Scheme S4.2**. **Figure 4.1e** shows that some particles form with a crater in the middle. This morphology can occur when using $AgNO_3$; gases produced during thermal annealing lead to explosive decomposition creating "nanorings".[63] Overall, **Figure 4.1** indicates soft cations may provide a path to forming dot arrays, while hard cations provide a means of producing porous matrices. The mixed porous/particulate morphology in the Ag and Al templates present a challenge in developing either purely porous or purely dot array masks.



Scheme 4.2: *Schematic illustration of the fabrication of porous metal matrix on substrate the substrate.* ***(A)*** *Substrate after cleaning.* ***(B)*** *1:1 BSA–Ch blend thin film after spin coating.* ***(C)*** *Metal precursor solution incorporated into the template.* ***(D)*** *Porous metal oxide matrix formed after annealing and calcination treatment.* ***(E)*** *Porous silicon generated by the silicon etch process.*

The Al product contained cracks between pores. Water loss during annealing was the culprit.[64,65] This is likely exacerbated by broad distribution in feature size compared to monodisperse BCP systems as polydisperse feature sizes results in more drying stress.[64] These initial tests suggest that to generate a porous matrix suitable for pattern transfer, with no cracking, an un-hydrated metal salt with a hard cation should be used. This limits metal precursors to unhydrated metals, as cracking is detrimental to final thin film surface properties.[64] With this in mind, the Fe precursor gave the most promising results. $FeCl_3$ allowed for selective metal incorporation into the Ch domain. Using metal incorporation rather than thermal deposition eliminates the need for selective removal of one domain, deposition onto the patterned film, and subsequent removal of the final polymer as is typical in current PBL.[8,10,42] This reduces the number of steps required for metal incorporation, the need for

expensive equipment, and is more similar to industrial standard BCP metal incorporation. Such methods could be easily substituted into existing manufacturing protocols.

4.3.1.1 $FeCl_3$ Precursor

Figure 4.2 shows the surface morphology of porous iron oxide films, produced using increasing metal ion solution – biopolymer template contact time. **Figure 4.2a** shows large pores, as in **Figure 4.1b**. Increased contact time resulted in mesa formation (a localized flat topped region with an abrupt change in slope at the boundary, **Figure 4.2b**). Inhomogeneity in pores/area, depth, and mean diameter are poor characteristics in a hard mask, resulting in inconsistent pattern transfer. Additionally, mesa formation results in regions of different characteristics. Mean pore diameter in the lower (darker) region of the mesa is 0.41 ± 0.39 µm with 2.31 ± 0.25 pores/µm^2, while higher (brighter) region has mean diameter of 0.16 ± 0.09 µm, with 2.78 ± 0.65 pores/µm^2. The formation of a mesa, and the reduction of pore density and size in the upper mesa region suggests that increased contact time overfilled the biopolymer template.[66] Pores in the upper portion of the mesa are much deeper compared to the lower portion, indicating more Fe^{3+} uptake with increased time. Increasing metal contact time to 60 s results in no discernible mimicry of the biopolymer template pattern. With increasing time, mesas become large enough to be observed even by optical microscope, **Figure S4.1**. Increasing metal ion solution contact time increases the amount of metal bound by the Ch domain. This occurs until no free sites exist and metal is deposited on the surface (**Figure 4.2**). In summary, minimising Ch-metal ion binding time provides the most homogenous metal template when using $FeCl_3$. Homogeneity and timely production are both desirable traits in metal mask production. Reducing the time Ch has to bind to the metal prevents random deposition onto the surface. At 15 s, no binding was observed to the BSA domain, while pores were still observed in the upper portions of the mesa. This shows that $FeCl_3$ has no affinity for the BSA domain, showing high selectivity for the Ch domain. This is crucial for selective metal incorporation.

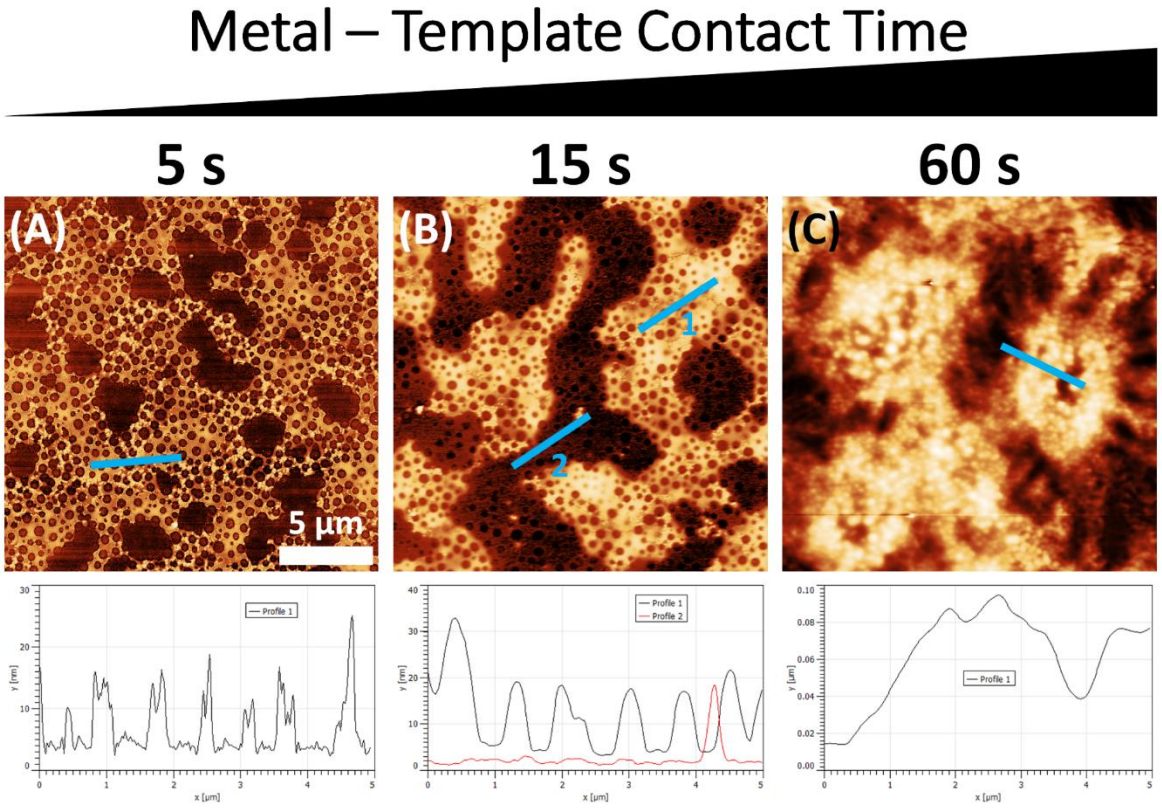


Figure 4.2: *AFM images displaying surface morphology and line profiles (blue), showing the growth nanoporous iron oxide matrix prepared with different biopolymer template–metal solution contact times. All images 20 x 20 µm, scale bar provided in image* ***A****. FeCl3-EtOH solution stirred for 30 min.* ***A – C)*** *display iron patterns generated with using 5 s, 15 s and 60 s respectively.*

Wt% of the $FeCl_3$ precursor was also varied, with a 5 s metal ion solution – biopolymer template contact time. **Figure 4.3** shows the morphology and line profiles of porous iron oxide films generated with increasing concentration of the metal precursor. **Figure 4.3a** shows no pores were generated using 0.1 wt% $FeCl_3$. Increasing this to 0.2 wt%, **Figure 4.3b**, formed regions with minor mesas and ill-defined pores. 0.4 wt% $FeCl_3$, **Figure 4.3c**, produced larger mesas, along with the first evidence for well-defined pores. Upper mesa regions contained pores with a mean diameter 0.29 ± 0.08 µm with 2.68 ± 0.14 pores/μm^2, while lower regions had a mean pore diameter of 0.33 ± 0.11 µm, with 3.23 ± 0.08 pores/μm^2. This shows upper portions of the mesa suffer from partial overfilling, reducing mean diameter and the number of features/area as with **Figure 4.2b**. Again, the lack of pore formation and inhomogeneity of the matrix prove that a minimum metal concentration is required to form a suitable metal mask. This suggests a minimum metal ion concentration threshold must be surpassed for sufficient pattern adoption. This is unsurprising as metal binding rates vary with increasing metal ion concentration in

sorbent Ch materials.[44] **Figure 4.3e**, produced pores with a mean diameter of 0.26 ± 0.10 µm with 3.6 ± 0.17 pores/µm^2. Varying the wt% of the metal ion precursor also resulted in mesa formation in the metal oxide. However, the mesas formed in **Figure 4.3** are also much smaller in height than in **Figure 4.2**, indicating that varying wt% produces subtler changes in morphology. Again, this is similar to the metal inclusion mechanism of PS-*b*-PEO BCP films. Thus, the same techniques used to refine metal masks with BCP films are transferable to biopolymer blends. For new technologies such as this to be adopted, easy integration into existing manufacturing processes is essential.

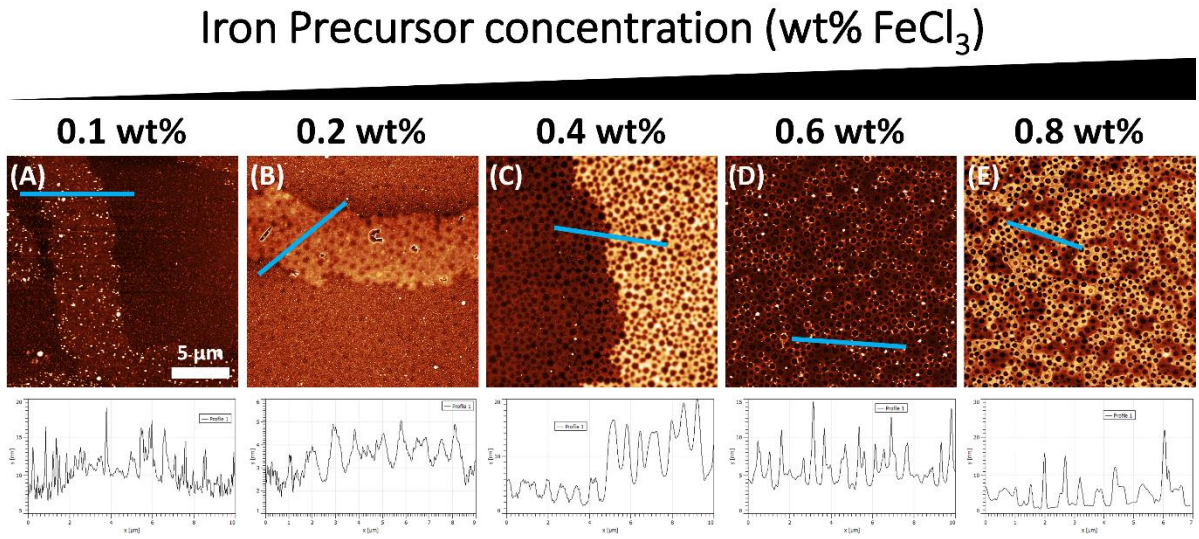


Figure 4.3: *Surface morphology and line profiles (blue) showing the growth nanoporous iron oxide matrix prepared with different concentrations of $FeCl_3$–EtOH solution stirred for 30 min. All images 20 x 20 µm, scale bar provided in image* ***A****.* ***A – E)*** *display iron patterns generated with 0.1 w/w%, 0.2 w/w%, w/w%, 0.6 w/w% and 0.8 w/w% respectively.*

4.3.1.2 $Fe(NO_3)_3.9H_2O$ PRECURSOR

To avoid over-flooding of the biopolymer template, as observed above, the Fe precursor anion, concentration, and metal contact time with the biopolymer template were varied. 1 wt% $Fe(NO_3)_3.9H_2O$–EtOH solutions were contacted with 1:1 BSA-Ch blend biopolymer templates (produced at 3000 rpm and 60% RH). Metal ion solution contact time was varied from 2.5 s to 60 s before spin-coating. The patterns generated from $Fe(NO_3)_3.9H_2O$ deviate from those of the $FeCl_3$ precursor and are more akin to those of Al oxide (**Figure 4.1c**), showing spherical particles and undesired cracking of the matrix.

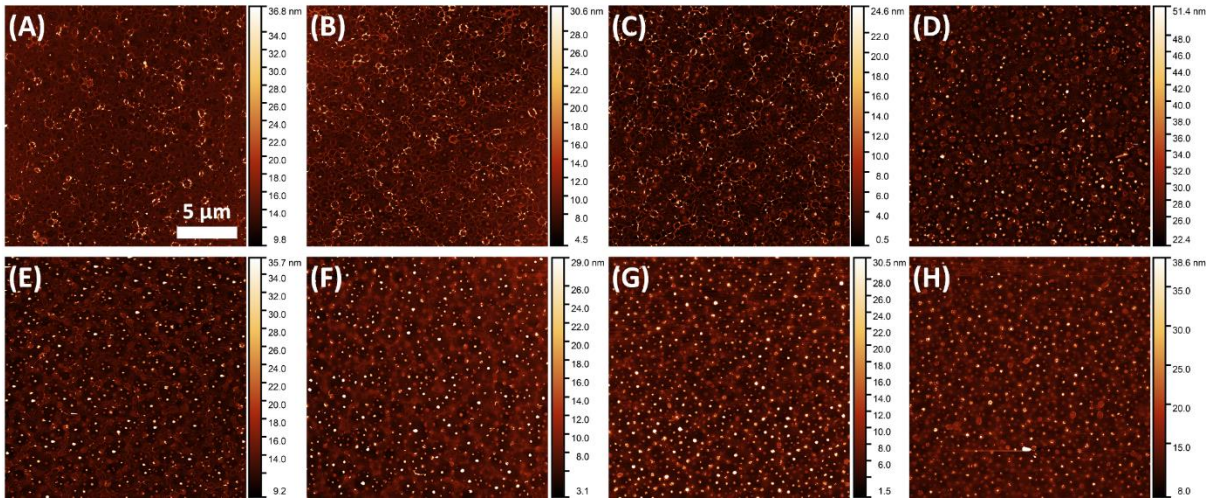


Figure 4.4: *AFM images and z scales of iron oxide matrix prepared with different biopolymer template–metal solution contact times. 1 w/w% Fe(NO3)3.9H2O – EtOH solution stirred for 30 min. All images 20 x 20 µm, scale bar provided in image A.* ***A – H)*** *display iron patterns generated with using 2.5 s, 5 s, 7.5 s, 10 s, 15 s, 30 s, 45 s and 60 s biopolymer template–metal solution contact time respectively. Annealing and calcination was performed with a preheated furnace (700 °C) for 1hr.*

Cracking is evident from 2.5 s (**Figure 4.4a)** until 15 s (**Figure 4.4e**). From 30 s (**Figure 4.4f**), cracked pores are mostly replaced with spherical particles. Larger metal discontinuous domains occur at 30 s, similar to that of the coalesced BSA regions (**Figure 4.1a)**. Metal particle size increased as contact time with the metal solutions increased from 30 s to 60 s. From 30 s – 45 s contact time, mean particle diameter increased from 0.23 ± 0.11 µm, with 3.35 ± 0.08 µm particles/µm^2 to 0.30 ± 0.12 µm, with 3.65 ± 0.41 particles/µm^2. At 60 s a decrease to mean particle diameter 0.27 ± 0.14 µm, with 3.29 ± 0.54 particles/µm^2 was seen. The number of metal particles/area matches the number of BSA spheres imbedded in the Ch domain, showing

good adoption of the biopolymer template pattern. The metal particle diameter was smaller than BSA domain size in **Figure 4.1a**. As BSA is not comprised solely from metal binding residues, i.e. repeating His and Cys residues, there are fewer sites for metal ions to bind to, unlike Ch or, synthetic polymers such as PEO. This lack of metal ions in the BSA domains reduced particle diameter. But this is useful, as only metal binding to the Ch domain is desired. The lack (and type) of metal binding sites in BSA inhibit hard metal binding.

The formation of particle arrays seems contrary to the HSAB mechanism, as the hard Fe^{3+} cation is still in use. It implies that changes in the metal template morphology result from the metal salts anion, NO_3^-. Anions can affect the metal binding ability of proteins. Cl^- has a weak affinity for proteins, while NO_3^- has a slightly stronger affinity for proteins, according to the Hofmeister series.[67,68] The stronger affinity for the NO_3^- results in enhanced attraction between the protein and cation.[69] This results in the BSA domain being filled with the metal cation. In short, specific anions can behave as a metal chaperone, shuttling metals to the BSA domain through Coulomb interactions.[70,71] In addition to HSAB theory. the Hofmeister effect may explain the particles formed in **Figure 4.4** and **Figure 4.1c**, **d** and **e** using the $Al(NO_3)_3.9H_2O$ and $AgNO_3$ precursor sample. Just as longer binding times must be avoided with the $FeCl_3$ precursor to prevent mesa formation, longer metal inclusion times must be avoided with $Fe(NO_3)_3.9H_2O$ to prevent protein binding. Rather than the Cl^- anion preventing protein binding of metal, protein binding of the metal ion must be avoided kinetically. This allows for the use of hydrated, atmospherically stable precursors such as $Fe(NO_3)_3.9H_2O$, while controlling which domain incorporates metal. This greatly increases the range of suitable metal compounds. For technologies like this to be adopted, broad choice of precursor compounds is essential for facile integration into existing industrial processes.

To compare cation uptake of the $Fe(NO_3)_3.9H_2O$ precursor to the $FeCl_3$ precursor, wt% of the $Fe(NO_3)_3.9H_2O$ precursor was varied (**Figure 4.5**) from 0.6 wt% to 2 wt%. Unlike the $FeCl_3$ precursor, pattern adoption did not occur until 1 wt% (**Figure 4.3c**). This morphology, like **Figure 4.1c** and **Figure 4.4d** and **e**, contained both metal pores and metal particles. Increasing the concentration of the metal precursor to 2 wt% produced a well-defined particle matrix (**Figure 4.5e**) with no pores present. Metal particles were 0.44 ± 0.31 μm in mean diameter, with 2.04 ± 0.25 particles/μm^2. The 1 wt% and 1.2wt% oxide films both exhibited cracking of the pore walls, similar to the Al precursor (**Figure 4.1c**) and Fe precursor in **Figure 4.4**. As both precursors were hydrated, this is likely due capillary pressure of water menisci exceeding the strength of the metal matrix during water loss.[64,65] Cracked pores reduce the fidelity of the metal mask to the biopolymer template and result in poor pattern transfer, both negatively

impacting metal film performance.[64,65] Increasing the metal precursor concentration results in more anions binding to the protein surface, resulting in a negatively charged protein-anion complex. This results in a stronger affinity of the protein to the Fe^{3+} cations to decrease the surface charge.[69] Chaperoning is again due to anions delivering metal cations to the protein surface through Coulomb interactions.[70,71] As such, rather than large mesas being formed in the Ch domain, the protein is filled with the metal cation (**Scheme S4.3**). While $Fe(NO_3)_3.9H_2O$ did not suffer from mesa formation as with the $FeCl_3$ products, increased metal concentration resulted in increased metal binding to the protein domain, producing a non-porous matrix. As the aim is to produce a porous metal matrix, low concentrations of the NO_3^- precursor or short incorporation times are required to selectively incorporate metal into the polysaccharide domain when using a metal nitrate precursor. However, this does demonstrate that a dot matrix surface pattern could be achieved by selective metal incorporation into the protein domain, if one takes advantage of the Hofmeister effect and appropriately chosen biopolymers and metal precursors.

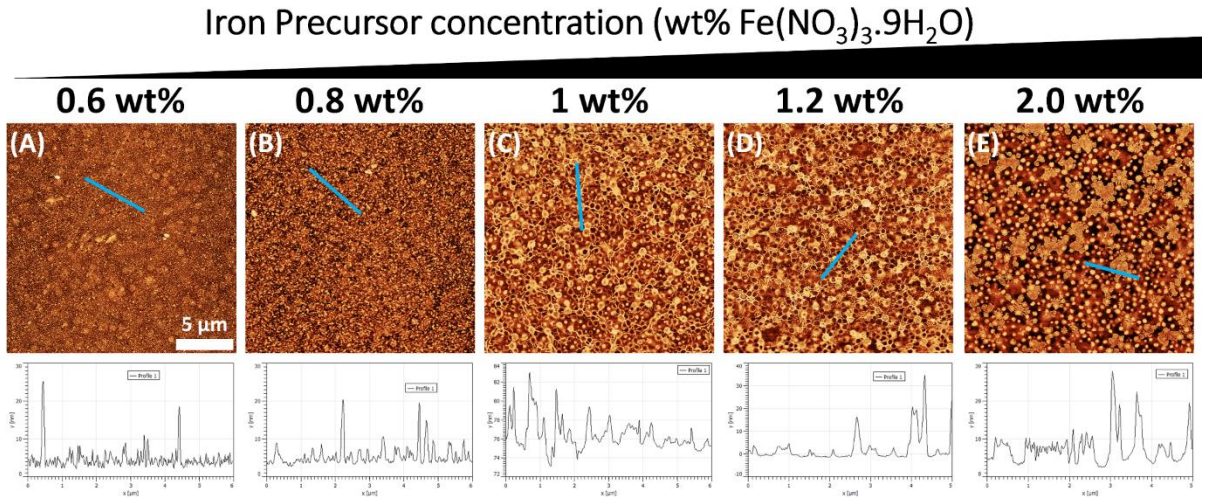


Figure 4.5: *AFM images and line profiles (blue) of iron oxide matrix prepared with different metal solution concentrations, stirred for 30 min. All images 20 x 20 µm, scale bar provided in image* ***A****.* ***A – E)*** *display iron patterns generated with using 0.6 w/w%, 0.8 w/w%, 1 w/w%, 1.2 w/w% and 2 w/w% $Fe(NO_3)_3.9H_2O$–EtOH solution respectively. Annealing and calcination was performed with a preheated furnace (700 °C) for 1 hr.*

4.3.2. SPEED AND HUMIDITY VARIATION

To improve pore packing and metal incorporation, metal matrices were produced by varying humidity and spin speed when forming the biopolymer template. A range of metal precursors

were used to produce a porous matrix with a range of applications discussed in the introduction. Cracking of pores in the metal mask was a problem, as outlined above. Based on the literature, if capillary pressure was the cause, then reducing the evaporation rate of residual water should result in a reduction or absence of cracks.[64,65] To achieve this, rather than using a preheated furnace, samples were brought to a 1hr hot hold of 160 ºC at a ramp rate of 20 ºC/min. Samples were then heated up to 700 ºC, at a ramp rate of 20 ºC/min. This was done to remove residual water before formation of the metal oxide. This successfully reduced cracking of the pores in the masks and increased transfer fidelity, as shown in **Figure 4.6**. To achieve tiling/Voronoi tessellation (the formation of quasi-honeycomb arrays, with tri-junctions at pore interfaces) to mimic the morphology of butterfly wings, the humidity was reduced during blend casting.

To determine if a slower heating ramp rate reduced metal oxide cracking, metal precursors $Fe(NO_3)_3.9H_2O$, $Ce(NO_3)_3.6H_2O$, $Cu(NO_3)_2.3H_2O$, $Ni(NO_3)_2.6H_2O$, and $Al(NO_3)_3.9H_2O$ were used for inclusion; all hydrated metal nitrate precursors of varying metal hardness. **Figure 4.6** shows the morphology and line profiles of the metal oxide films. XPS survey and core level spectra are shown in **Figure S4.2** and **Figure S4.3** respectively. Only the Al and Cu precursors produced a particulate/porous matrix. All others produced a purely porous matrix. The Fe, Al, Ni, and Cu samples all exhibited tiling after incorporation into the biopolymer template, and annealing. This is the first evidence that biopolymer blends may be used to form honeycomb metal masks, and emulate the pores of butterfly wings. Our experiments show that tessellation became more prominent with reduced humidity **(Figure S4.1, Figure S4.4, & Figure S4.5**), consistent with the literature.[72]

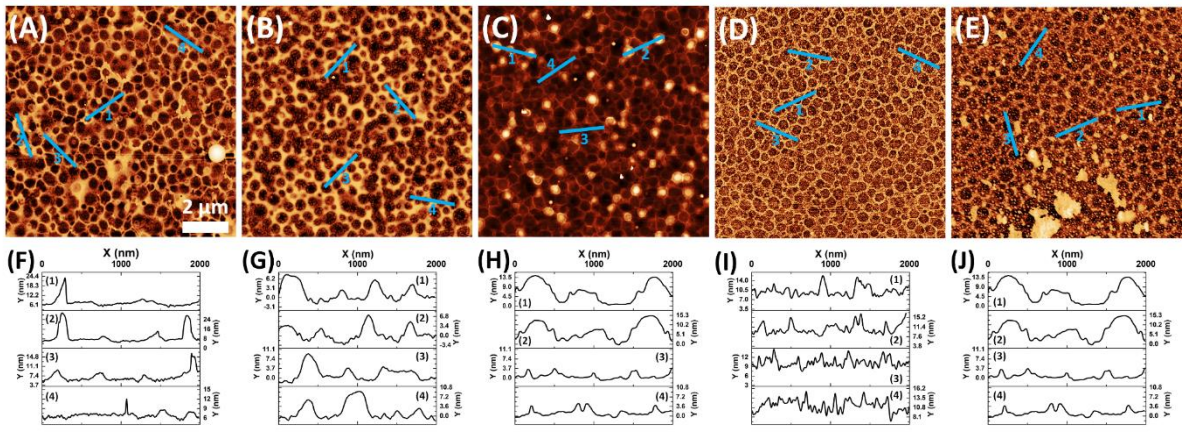


Figure 4.6: *AFM images and 2 µm surface profiles (blue lines) of nanoporous metal structures. Metal templates produces with biopolymer template (1:1 BSA-Ch, 4000 RPM, 20% RH) on planar silicon substrates, annealed and calcined at 700ºC. Nanoporous metal*

templates were prepared with alternative precursors (1 w/w%-EtOH). ***(A, F)*** *Fe_2O_3,* ***(B, G)*** *Ce_2O_3,* ***(C, H)*** *Al_2O_3,* ***(D, I)*** *NiO, and* ***(E, J)*** *CuO respectively*

None of the walls exhibited the cracking seen in the previous hydrated metal precursors (**Figure 4.1c**, **Figure 4.4a – e, Figure 4.5c and d).** This confirmed the removal of water pre-calcination was the key factor in preventing crack formation. This allows for the use of hydrated precursors (stable at ambient humidity) without compromising the metal oxide morphology through cracking, improving the number of precursors available to this technique. XPS (**Figure S4.3 a – f**) confirmed the presence of α-Fe_2O_3[73], Ce_2O_3[74], Al_2O_3[75], NiO[76] CuO[77] respectively.
Binding of the metal precursor to the biopolymer can be determined from the domain in which the metal resides post calcination, wall height and wall thickness. Fe^{3+} and Ce^{3+} are hard acids using the HSAB principle, and thus, bind well to the Ch domain but not the BSA domain, as seen in **Figure 4.6a** and **b**.[78] Ni^{2+} is considered a borderline acid, which is reflected in the low wall height and thin walls indicating low metal uptake by the Ch domain, as seen in **Figure 4.6**and **i.**[78] Al^{3+} and Cu^{2+} are considered hard and borderline hard acids respectively.[78,79] The 0 precursor binds less with the Ch in the allotted time than other hard cations, similar to the Ni^{2+} ion. The unbound metal ions result in random Cu oxide formation over the substrate. Localised agglomerates of particles are produced by this, which has also been seen in PS-*b*-PEO BCP films over a critical Cu precursor concentration.[73] This debris makes the sample unsuitable for pattern transfer. Al produced a mixed porous/particulate matrix (**Figure 4.6c** and **h**). Particles were restricted to within the BSA domain indicating binding to the protein. As such, no secondary growth mechanisms are likely to be the cause of the formation of metal oxide particles, and the metal anion is responsible for protein binding. This means that by choosing an appropriate biopolymer blend and an appropriate the metal precursor, the metal can be selectively incorporated into a chosen phase, and the resulting film properties can be more effectively controlled. Particle formation did not occur in every pore. This can be attributed to the hardness of Al^{3+}, the enhanced Hofmeister effect occurring in a limited time (5 s),[67–69] and small BSA domains limiting the probability of nucleation within this time period.[80] To form purely porous structures, particle formation (promoted by the Hofmeister effect) must be avoided kinetically and chemically, to ensure a homogenous pattern for transfer.
None of the walls exhibited the cracking seen in the previous hydrated metal precursors (**Figure 4.1c**, **Figure 4.4a – e, Figure 4.5c and d).** This confirmed the removal of water pre-calcination was the key factor in preventing crack formation. This allows for the use of hydrated

precursors (stable at ambient humidity) without compromising the metal oxide morphology through cracking, improving the number of precursors available to this technique. XPS (**Figure S4.3 a – f**) confirmed the presence of α-Fe_2O_3[73], Ce_2O_3[74], Al_2O_3[75], NiO[76] CuO[77] respectively. α-Fe_2O_3 was also confirmed using FTIR (**Figure S4.6a**) and Raman spectroscopy (**Figure S4.6b)**, see **4.7 Appendix** .

There are numerous advantages to tessellated geometries; they provide greater mechanical strength than spheroidal features, while economically encapsulating a material (honey, air, etc.) with minimal wall material. In other words, greater strength with less material. Voronoi tessellation in polymer blends seem elusive in the literaure[72], but in reality they occur regularly but are often unassigned.[1,9,25,81–85] Tessellation is the result of the formation of tri-junctions with angles of 120° occurring at each vertex in close packed systems of spheroidal cells. This is due to attempts by the system to reduce surface energy along the plane.[86–88] Our experiments show that tessellation became more prominent with reduced humidity **(Figure 4.7, Figure S4.1, & Figure S4.5**), consistent with the literature.[72]

Tessellated pores are advantageous, as it is this morphology which provides butterfly wings with their unparalleled AR properties.[33] Both porous silicon and butterfly wings with sub-micron pores are antrireflective.[33,89] This is attributed to the increase in the optical path length. Butterfly wings with honeycomb structures are significantly less reflective than those with cross ribbing structures. Butterfly wings take advantage of refraction, like a fibre optic cable. The wing material has a high refractive index, meaning they can take advantage of total internal reflections. i.e. when light enters the material, it is continuously reflected, until absorbed.[90] Honeycomb structures can also diffract light, increasing the amount of light scales absorb.[91] The role of periodic ridges which surround the pores of butterfly wings is subjected to debate, Some evidence supports that these ridges increase light absorption by funnelling light into the pores.[92] However, other evidence suggests these ridges have an inconsequential effect on broadband light absorption in the visible range.[93] Both can be true, as feature dimensions in different species appear to play a key role.[94] Regardless, honeycomb pores are regarded as a key feature in antireflectivity. This is a different mechanism to how nanostructured silicon

absorbs light. Nanostructured materials behave as if they have a gradient refractive index, progressively bending light until absorbed. [95]

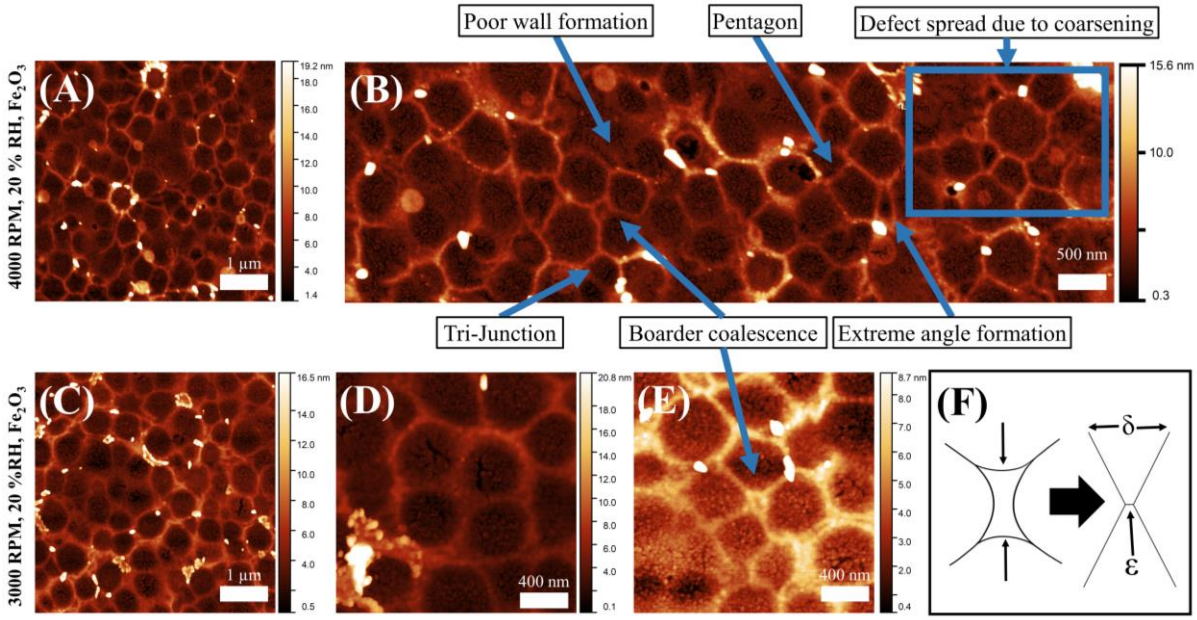
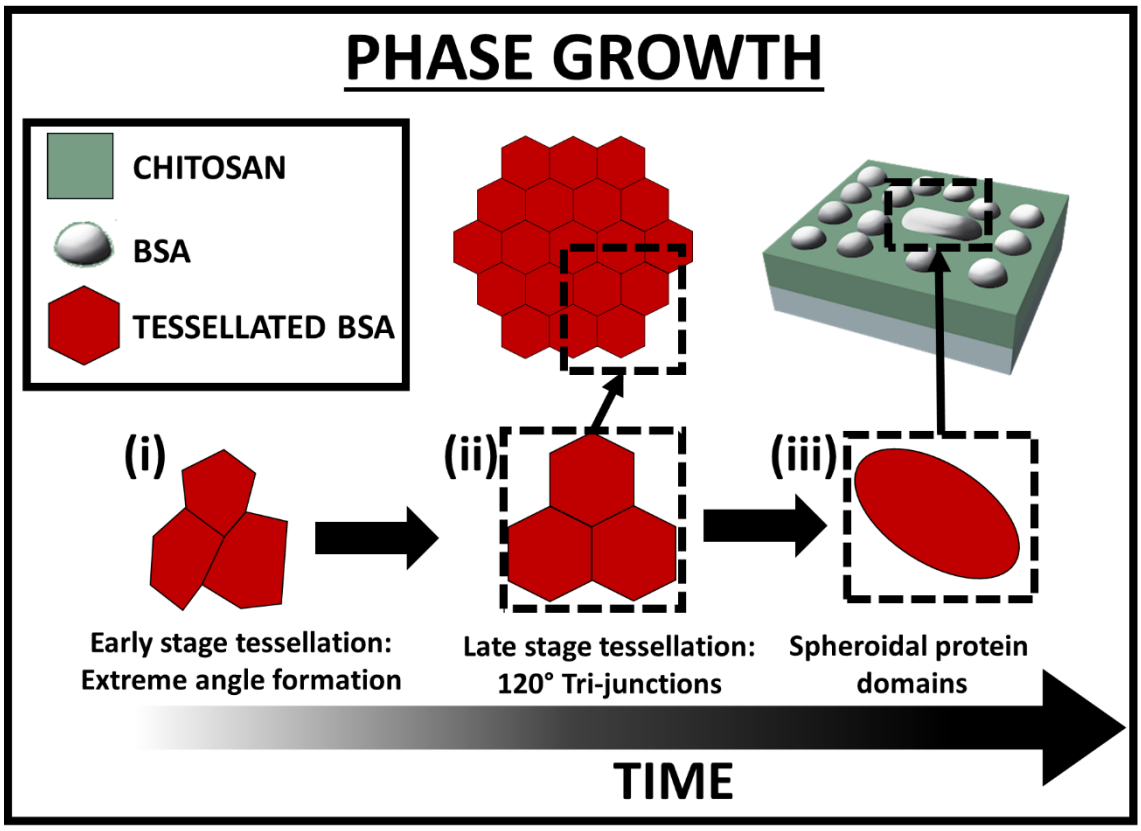


Figure 4.7: *Shows AFM images of metal masks generated using biopolymer templates cast at reduced humidity (20% RH). Masks were produced using metal incorporation of $Fe(NO_3)_3.9H_2O$, subsequent annealing at 160 °C for 2 hr to remove any water, and calcination at 700 °C for 1 hour to remove biopolymer template.* ***(A, B)*** *AFM images of Fe_2O_3 metal masks generated from 1:1 BSA-Ch biopolymer template, cast at 4000 RPM.* ***(B)*** *Provides an enhanced view of the tessellated morphology, and variance found within.* ***(C-E)*** *AFM images of Fe_2O_3 metal masks generated from 1:1 BSA-Ch biopolymer template, cast at 3000 RPM.* ***(F)*** *Scheme for "border coalescence", driving the formation of metastable quad-junctions observed in* ***(B)*** *and* ***(E)****, a metastable structure resulting from structure observed in* ***(D)****.*

Figure 4.7 shows the formation of a quasi-honeycomb hole array when humidity was lowered to 20% RH.[37] Tessellation of the BSA domains results from an increased evaporation rate of the solvent, allowing less time for feature development, essentially pausing development in an earlier, tessellated form.[72] With the median interior angle at approx. 120° **(Figure S4.5)**, the BSA wall tensions approach near uniformity with slower solvent removal. **Figure 4.7b** provides more information on structural formation. Less discrete wall formation results in larger voids. These poorly defined walls occurred when biopolymer templates were cast at 4000 rpm (**Figure 4.7 & Figure S4.7e**). This is attributed to thinner biopolymer template films, which meant there was less material overall and so, less Ch to incorporate the precursor in the allotted time. Additionally, while this morphology is referred to in the literature as quasi-

honeycomb hole array, many of these pores are not hexagonal. Rather these pores can be made with *n* border walls (e.g. n = 5, pentagonal). The spreading of defects occurs in regions where coalescence occurs.[96] This can result in the adoption of energetically unfavourable angles, and increases disorder within the array. This is evidenced in **Figure 4.7c**, where pores are formed with wide internal pore walls (**Figure 4.7d**). During tessellation, border coalescence results in the formation of metastable fourfold vertices, **Figure 4.7e**. As this is a 2D, rather than 3D, honeycomb array, it is not constrained by Plateau's requirement for threefold vertices. Thus, pores can either form quad-junctions, or two tri-junctions with minimal separation of the threefold vertices (ε), (**Figure 4.7e & f**.[97] This supports that faster drying of the biopolymer blends results in tessellated structures (**Scheme 4.3**).



Scheme 4.3: *Scheme detailing pattern development blend films.* ***(i)*** *Contacting BSA domains deform to adopt polygonal morphologies.* ***(ii)*** *With longer drying times, morphologies adopt tri-junctions with internal angles averaging 120°.* ***(iii)*** *Further growth of the BSA domains sees the collapse of polygonal features via coalescence, and the adoption of a spheroidal morphology.*

Tessellation of the BSA domains results from an increased evaporation rate of the solvent, allowing less time for feature development, essentially pausing development in an earlier,

tessellated form.[72] With the median interior angle at approx. 120° **(Figure S4.5)**, the BSA wall tensions approach near uniformity with aging. The biopolymer blend film (cast at 4000 rpm, 20% RH) produces a metal mask, **(Figure 4.7a & Figure S4.5b)** which contains more extreme internal angles, resulting in a higher population in the first mode (data value that occurs most often), compared to the film cast at 3000 rpm at 20% RH (**Figure 4.7c** & **Figure S4.5a**). Newly formed vertices result in more extreme tessellation values. A longer evaporation time resulted in relaxation of the structures and adoption of 120° tri-junctions.[98] This effect can be observed in the 4000 rpm film, which dried more quickly, and a broader distribution of interior angles is seen, because the vertices in the 4000rpm film are younger. This is unsurprising, as Voronoi tessellation is deeply rooted in nucleation and growth processes.[99]

4.3.2.1 *α-Fe_2O_3 MASK ETCHING AND ANALYSIS*

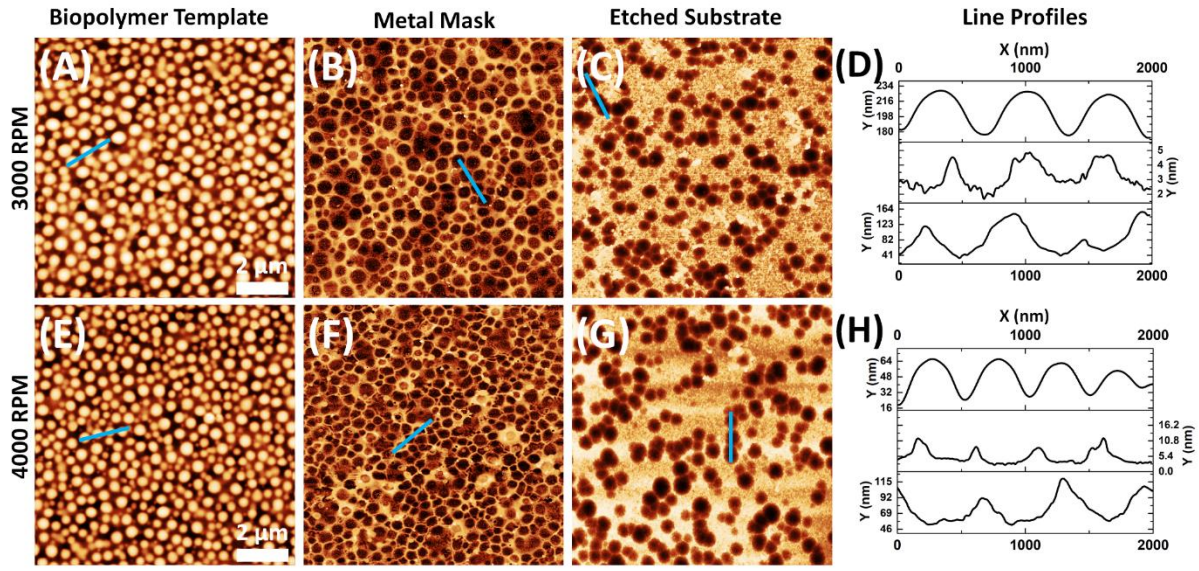


Figure 4.8: *Each image is 10 x 10 µm, 2 µm scale bar provided in image* ***A*** *and* ***E,*** *and line profiles denoted by a blue line.* ***(A, E)*** *AFM images of 1:1 BSA-Ch biopolymer template, 20% RH, cast at 3000 RPM and 4000 RPM respectively.* ***(B, F)*** *AFM images of Fe_2O_3 metal masks generated from biopolymer templates* ***(A)*** *and* ***(E)****, following metal incorporation of $Fe(NO_3)_3.9H_2O$, and subsequent annealing at 160 °C for 2 hr and calcination at 700 °C for 1 hour.* ***(C, G)*** *AFM images of substrates post-etching samples* ***(B)*** *and* ***(F)*** *with $NH_4F/HNO_3/H_2O$ solutions for 5 min.* ***(D, G)*** *line profiles of samples* ***(A, B, C)*** *and* ***(E, F, G)*** *respectively.*

α-Fe_2O_3 is typically used as a mask for pattern transfer. The α-Fe_2O_3 sample also had the least amount of defects (particle formation), and was well-defined in **Figure 4.6a**, so the Fe_2O_3 mask

was used for further processing (i.e. etching). **Figure 4.8** shows the biopolymer template, metal mask and subsequent etching of the silicon substrate with $NH_4F/HNO_3/H_2O$. Biopolymer templates were produced at 3000 rpm and 4000 rpm at 20% RH (**Figure 4.8a** and **e**). Metal masks were produced, as in **Figure 4.6**, using 1 wt% $Fe(NO_3)_3.9H_2O$, with low temperature heating (160 ºC) for 1 hr before calcination (700 ºC) for 1 hr, using a ramp rate of 20 ºC/min (**Figure 4.8b** and **f**). The mask-substrate assembly was then treated with $NH_4F/HNO_3/H_2O$ solution for 5 min (**Figure 4.8c** for 1:1 BSA-Ch 3000 rpm 20% RH metal template, and **Figure 4.8g** for 1:1 BSA-Ch 4000 rpm 20%), to transfer the mask pattern to the Si substrate. Though not all pores transferred, later discussed, transferred pores retained a polygonal morphology, showing excellent the fidelity of pores that transferred.

Figure 4.8b and **f** (shown in more detail in **Figure S4.7**) shows differences in metal masks produced using biopolymer templates coated at different spin speeds, at 20% RH. Discussed briefly earlier, as with **Figure 4.6**, the **Figure 4.8** metal masks show tessellation. Casting biopolymer blends at 3000 rpm meant a slower solvent evaporation rate which allowed structures to age more. Thus, pores could adopt the desired relaxed structures with angles of approximately 120° (**Figure 4.8a-b**, **Figure S4.5b**, & **Figure S4.7a-c**). A small number of extreme interior angles were observed in peak 1 of **Figure S4.5b**. Shorter drying times permit less aging and so produce more acute and obtuse interior angles (**Figure S4.5a** peak 1 and **Figure S4.7a**).[72,98] 4000 rpm blends were also less homogenous across the sample than 3000 rpm blends (**Figure S4.7**). Sparse partial mesa formation was observed in Fe_2O_3 matrices, when biopolymer templates were cast at 3000 rpm (**Figure S4.7b**), attributed to the thicker deposit of the biopolymer template. Both masks created using 3000 and 4000 rpm blends had pores of sub-100 nm diameters in between larger pores. Finally, metal masks produced using the 4000 rpm blend exhibited undesired deformation of the pore wall, non-connective wall structures and slightly jagged regions (**Figure S4.7f**). Pores producing using 3000 rpm biopolymer blend were not as deformed (**Figure S4.7c**). It is possible that the acute angle of some of the pore walls (**Figure S4.5**) causes strain during oxide formation, and may result in this deformation.

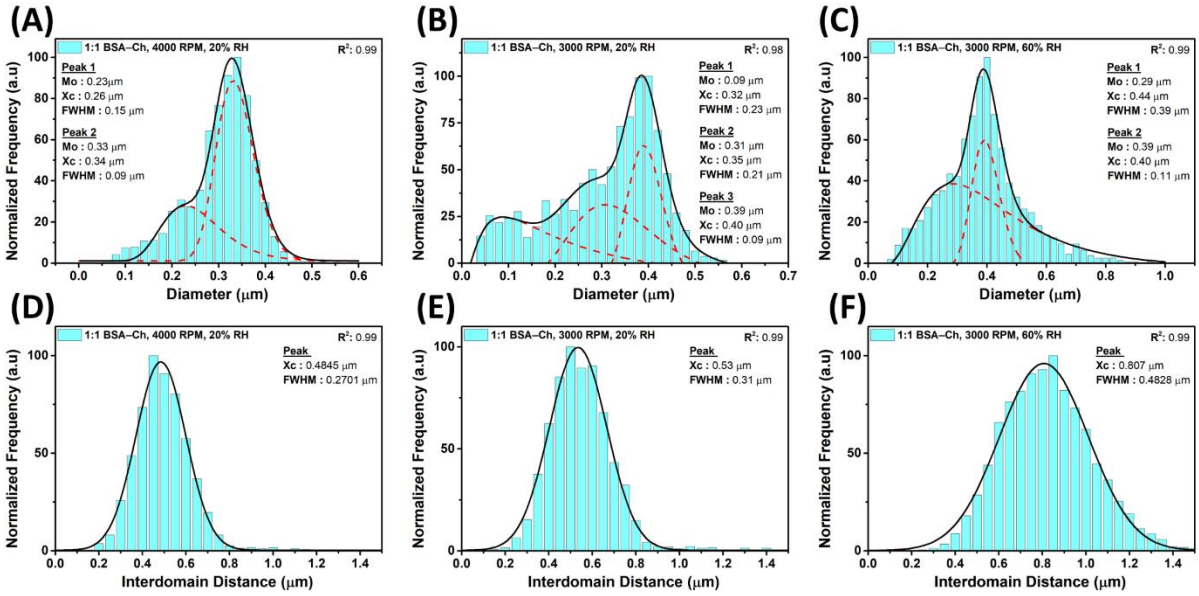


Figure 4.9: *Statistical analysis of 1:1 BSA-Ch blends. Each curve is based on approximately 1000 diameter measurements performed with Gwyddion, and interdomain distance performed with ImageJ. PSD's were fitted with log-normal curves, while interdomain distances were fitted Gaussian curves. The black curve (solid) denotes the best polymodal fit with the distribution, while the deconvouted peaks, shown in red (dashed), show the separate populations in the PSD.* ***A*** *and* ***D)*** *display the normalized PSD and interdomain distance of biopolymer blends cast at 4000 rpm and 20% RH.* ***(B, E)*** *corresponds to the PSD and interdomain distance biopolymer blends cast at 3000 rpm, 20% RH.* ***C, F)*** *corresponds to the PSD and interdomain distance of biopolymer blends cast at 3000 rpm, 60% RH.*

Figure 4.9 shows the particle size distributions (PSDs) and interdomain distances for the 1:1 BSA-Ch biopolymer templates cast at; 3000 rpm 60% RH (**Figure 4.9a** & **d**); 3000 rpm 20% RH (**Figure 9b** &**d**); and 4000 rpm 20% RH (**Figure 4.9c** & **f**). Analysis of the BSA domain size and interdomain spacing provides insight into the growth mechanism of the biopolymer blend, and the expected morphology following metal inclusion and etching. This provides greater understanding of the growth mechanism and, thereby, control of the biopolymer and metal template. At 20% RH, reducing spin speed from 4000 rpm to 3000 rpm resulted in a reduction of the domain size of smaller BSA spheres, while increasing the size of the larger BSA spheres (**Figure 4.9a** and **b**). The mean diameter of BSA spheres increased from 0.29 ± 0.08 µm to 0.54 ± 0.23 µm. The number of BSA spheres/area reduced slightly from 4.99 ± 0.13 spheres/µm ^{2} to 4.66 ± 0.48 spheres/µm^2. The interdomain distance of the BSA remains the same, approximately 0.5 ± 0.23 µm. The growth of larger particles, with a reduction in size of

smaller particles, and little-to-no change to the interdomain distance between particles describes a diffusion process (i.e. Ostwald ripening, **Figure 4.9d** and **e**), indicating Ostwald ripening is dominant in this blend when reducing spin speed.[100,101] This supports the formation of more acute and obtuse interior angles earlier in the growth process (**Figure S4.5**). However, increasing humidity to 60%, as with the initial templates, results in an increase in size of both smaller and larger features, which is evident in the modal shift observed in **Figure 4.9c**. Mean particle diameter is increased to 0.51 ± 0.47 µm. The large variation in size results from features in this blend exceeding 5 µm. BSA spheres/area is further reduced to 3.62 ± 0.10 spheres/µm^2. This results in a larger interdomain spacing observed in **Figure 4.9f**, 0.82 ± 0.35 µm. This indicates that increasing the humidity results in coalescence of BSA domains.[100–102]

To achieve smaller feature sizes used in pattern transfers to produce AR coatings,[9] inhibition of coalescence (growth by Ostwald ripening) is required. Any deviations from the modes of the diameter, mean diameter, features/area, loss of tessellation, or feature spacing from the biopolymer template will indicate the efficacy of the metal patterning (**Figure S4.8**) and subsequent etching (**Figure S4.9**). An in-depth discussion of such can be found in the **SI**. Numerous mechanisms involve the removal of water in some form or another, or the overfilling of pores. However, the strain caused by such extreme interior angles formed by the pores likely plays a role, e.g. peak 1 in **Figure S4.5a,** & **Figure S4.7 d – f**. In contrast, larger pores appear in the metal oxide SD's, attributed to regions of poor metal uptake observable in **Figure 4.7** and **Figure 4.8**. The increase in interpore spacing is ascribed to the number of pores transferred to the substrate, likely caused by limited perforation of the BSA domains to the substrate.[9]

Though the number of transferred pores approaches the theoretical number of transferable pores made through synthetic polymer blends, features that are not transferred affect the interpore spacing. This would likely affect the homogeneity of characteristics across the substrate, and is undesirable when uniform homogeneous pattern is required.[103] The lack of complete pattern transfer likely results from a mixed lateral and vertical phase morphology, exhibited by a majority of polymer blends and why most have not been used as lithographic masks.[8,42] However, the use of polymer blends rather than BCPs is more cost effective, increases the number of materials available (compared to producing new BCPs), allows for more flexibility with a range of patterns sizes and shapes, simple multiscale patterning in a single step ≥ 100 nm patterns due to the lack of block length restrictions.[2,9,104]

Huang *et al* produced metal masks through spin-casting of PS/PMMA blends and deposition of metal via thermal evaporation. This achieved a porous metal matrix with pores between 200 – 800 nm with an average of 400 nm. The largest number of pores/area in the metal mask was

2.2 holes/μm^2.[10] Guo *et al* achieved similar results with PS/PEG blend. Typical pore diameters ranged from 200 – 400 nm, spaced 100 nm apart. Pores/area ranged from 0.7 holes/μm^2 to 13.1 pores/μm^2. However, high pore/area films were not homogenously porous, while larger pore films exhibited bimodal PSDs.[9] As the number of pores actually transferred to the substrate in our work exceed the theoretical maximum number of pores that could be transferred by Huang *et al*, biopolymer blends show they are a viable candidate for metal templating.

Finally, the dielectric constant and donor number of the solvent appear to affect metal uptake rate (**Figure S4.10**, discussed in **SI**). The strength of hydration of the anion appears to play a role in chaperoning the anion to protein functional groups rather than the backbone (**Figure S4.11**, discussed in **SI**), thereby chaperoning the metal to the protein domain. Finally, very little metal can be adsorbed by the Ch domain if the anion and cation do not promote chelation (**Figure S4.12** discussed in **SI**) resulting in no metal oxide pattern development.

4.4. EXPERIMENTAL

4.4.1. BIOPOLYMERS, CASTING SOLUTIONS AND SUBSTRATE

Low molecular weight chitosan (50-190 kDa, 75% deacetylation) and bovine serum albumin (lyophilised powder, ≥ 96%, molecular weight ~66 kDa) were purchased from Sigma Aldrich. Substrates used all cases were planar substrates, highly polished single-crystal silicon <100> wafers (p-type, boron) with a native oxide layer of ~2 nm, were used. Stock and working solutions were prepared as reported in our previous work.[41] Films were cast using a spin coater (*Speciality Coating Systems, 6800 Spin Coater Series*). The substrate was spun for 30 s (ramp time 5 s, dwell 25 s). Casting solutions contained 1 w/v% BSA 1 w/v% Ch (1:1 blend ratio). Biopolymer films were cast at 60% and 20% relative humidity (RH). 20% RH was achieved by a custom-built humidity controlled spin coating chamber. Temperature and humidity were monitored using a *HOBO MX Temp/RH Logger* sensor.

4.4.2. METAL INCLUSION

All metal precursors were purchased from Sigma-Aldrich and used as received. Metal reagents included $AgNO_3$, $Al(NO_3)_3.9H_2O$, $FeCl_3$, $Fe(CO_2CH_3)_2$, $Fe(acac)_2$, $Fe(acac)_3$, $Fe(NO_3)_3.9H_2O$, $Ce(NO_3)_3.6H_2O$, $CuCl_2$, $Cu(CO_2CH_3).H_2O$, $Cu(SO_4).H_2O$, $Cu(NO_3)_2.3H_2O$, $Ni(NO_3)_2.6H_2O$, and $NiCl_2.6H_2O$. Before metal inclusion, metals were dissolved in anhydrous EtOH. Experiments with other solvents (such as dH_2O, acetone, and isopropyl alcohol may be found

in **4.7 Appendix.** Substrates were cleaned using acetone and EtOH for 30 min via ultrasonication, and were dried using a nitrogen stream. Metal inclusion was achieved by exposing the biopolymer blend film to 0.5 mL of metal solution for a set amount of time before spin coating, with inclusion times for the Fe precursors ranging from 2.5 s to 60 s. The wt% of the Fe precursors was varied from 0.1 wt% - 1.2 wt%. Metal inclusion was performed at 3000 rpm (ramp time 5 s, dwell 25 s) at ambient humidity (60% RH).

After metal inclusion, incorporated films were then placed into furnace, and calcined at 700 ºC for 1 hr, to remove the biopolymer template, and oxidize the metal precursor. The furnace was either: **1)** preheated to 700 °C for rapid calcination or; **2)** samples were heated to 160 °C for 1 hr, with a ramp rate of 20 °C/min, to remove water before calcination. After calcination, samples were removed, and allowed to cool to room temperature before further processing or analysis.

Samples were then placed into a cold furnace, heated to 700 °C (with a 20 °C/min ramp) and left for 1 hr before removal. Selected metal oxides were etched using NH_4F (0.5 g), dH_2O (12.6 mLs) and 70% HNO_3 (8.3 mLs).

4.4.3. CHARACTERIZATION

Surface topographies were imaged by atomic force microscopy (AFM) in non-contact mode using a Park Systems, XE-100 instrument. Images were analysed using *Park XEI*, *Gwyddion*, and *ImageJ*, and resulting data analysed using *Origin*.[41] Inter-domain distances were determined using ImageJ, and fitted with Gaussian curves.[102,106,107] Voronoi tessellation (used to determine inter-domain distance) was analysed using ImageJ, using the method developed by Corson *et al*.[98] Feature diameter, features/area, and inter-domain distance were represented as mean±standard deviation, using approx. 1000 features. Infrared spectra of the substrate, biopolymer blend and iron oxide were recorded using a PerkinElmer Spectrum 2 FT-IR spectrometer. 64 scans were collected and averaged in the range of 400 – 4000 cm^{-1}. with a resolution of 4 cm^{-1}. Elmer Spectrum v5.0.1 software was used to perform baseline corrections. X-Ray photoelectron spectroscopy (XPS) on metal oxides were performed using an *Oxford Applied Research Escabase XPS* system with a non-monochromated Al Kα x-ray source operated at 200 W. This is further detailed in our previous work.[41] XPS data was processed using *CasaXPS* software with a *Shirley* background correction applied and peaks fitted to Voigt profiles. Raman spectra of the Si substrate and iron oxide sample were collected using a *Renishaw InVia Raman Spectrometer* using a 40 mW Ar^+ laser at 514 nm excitation, with the beam focused onto the samples using a 50 x objective lens. Spectra were collected using a

RenCam CCD camera and plotted using Origin. biopolymer blends could replace existing synthetic polymer technologies in a simple manner.

4.5. CONCLUSION

Evolutionary processes have sculpted nanoscale structure in the wings of butterflies, rendering them optimally reflective for their niche. BioMIL is the first method that allows us to mimic those structures by fabricating metallic, tessellated features, in a bottom-up process. It is also the first description of how to selectively incorporate a metal into one biopolymer (a polysaccharide), while avoiding incorporation into another (a protein). This opens up a source of green materials for bottom-up manufacturing of metallic structures, and provides a means to create these intricate biological patterns.

The morphologies of the biopolymer templates we used here can be readily modified by controlling ambient humidity, or deposition spin speed. To achieve feature sizes suitable for AR surfaces[9], features were grown by Ostwald ripening rather than coalescence mechanisms **(Figure 9)**. The binding of cations to either the protein or polysaccharide domain follows the HSAB principle. Additionally, specific anions, such as NO_3^-, behave as chaperones, shuttling metals to the protein (BSA) domain.[70,71] Increasing the precursor concentration enhanced chaperoning of metal to the protein domain, when using a more strongly hydrated anion. As more anions bind to the protein surface, the protein-anion complex becomes more negatively charged, enhancing the affinity of the protein domain for the Fe^{3+} cations, allowing for even more selective metal incorporation. This is a significant advantage as Fe is one of the most commonly used metals industrially in metal-PBL type processes.[69] Undesired metal chelation to the protein domain can be avoided by reducing metal ion solution – biopolymer template contact times, or by reducing the wt% of the metal ion solution. Similarly, limiting the contact time of the metal ion solution with the biopolymer template prevents the formation of problematic mesa structures.

Typically, metal-PBL methods require selective removal of one polymer domain, then thermal deposition of a metal, followed by removal of the final polymer domain, to produce a metal mask.[8,10,42] BCP patterning is more efficient; metal is typically incorporated into a single domain by selective inclusion of the metal into that domain.[43] Our BioMIL process makes use of the greater efficiencies in BCP patterning based methods, and enhances them with the advantages found in biopolymers. By using a biopolymer blend instead of synthetic BCPs, and by selecting Ch as one of the components, BioMIL makes use of the metal binding capacity of

Ch to promote the growth of a metal film that mirrored the Ch domain.[44–47] Common problems like cracking in the resultant metal mask were prevented by the use of an unhydrated metal precursor, or the removal of water through a simple bake (160 °C) before annealing.

By using a wet etch ($NH_4F/HNO_3/H_2O$ solution), a maximum of 53% of pores could be transferred to the substrate. This results from a mixed lateral and vertical internal phase morphology.[8,42] Pore wall aspect ratio could be improved by modifying the deposition speed of the metal precursor, or through the $FeCl_3$ precursor mesa formation mechanism, which may help reduce the effects of mask erosion during lithography. Pores of this size could be used as optical filters, anisotropic etching masks and hierarchical patterns for cell adhesion studies.[10] Numerous optical and optoelectronic technologies derive their properties from the average surface morphology, making blends an ideal candidate.[9] Etched silicon solar cells with irregular pores approximately 100 nm deep can reduce reflection loss to as much as 2.1%.[105]. This would reduce the effects of mask erosion during lithography. Etching could be improved by using an anisotropic reactive ion etch, or refinement of BSA perforation to the substrate.[9] This method could be used to produce porous surfaces for optical filters, anisotropic etching masks and hierarchical patterns for cell adhesion studies.[10] The number of pores successfully transferred to the substrate in this work outperform the theoretical maximum number of pores which could be theoretically transferred by Huang *et al*, emphasising the potential of the BioMIL process for pattern transfer applications.[9] Pore transference could be further improved by the use of reactive ion etches to expose the Si substrate before pattern transfer of the metal mask to the silicon. This could achieve up to 570 million pores/cm^2, which exceeds most synthetic polymer PBL pores/area.

Arguably the most promising finding in this work is that by maintaining low humidity environments and high spin speeds, our BioMIL process produced tessellated structures. Analysis of the tessellation patterns and the PSD of the protein domains indicated an inhibited growth mechanism. This is the first evidence that metal adsorption into a polymer blend of any type can produce tessellated features. The highly AR structures of butterfly wings are tessellated, and their successful replication in synthetic materials has long been sought. The range of feature sizes, tessellated morphologies, and pores/area seen in this work are the closest replication of the porous butterfly wing structure to date using a bottom-up approach.[33–37]

Reflecting on our findings, though the theory behind BioMIL is more complex than that of metal-PBL, its methods are simpler, as scalable, and more affordable. The biopolymers that underpin the process are renewable, biodegradable, and can be sourced from the wastes of other industries as part of a circular economy. The phase separation processes that determine the

patterns of the metal masks occur within a minute, and metal incorporation can also be performed in under a minute, making for rapid production. Processing conditions allow for total control of the metal oxide morphology. The BioMIL process is a feasible, economical, more controllable, cleaner, more sustainable, and potentially superior alternative to synthetic polymer based metal-PBL process, and holds great promise for future sustainable technologies.

4.6. REFERENCES

(1) Trommer, K.; Morgenstern, B.; Gähr, F.; Hermanutz, F. Sub-Micrometer Structured Textile Coatings Generated From Cellulose Based Polymer Blends. *Lenzinger Berichte* 2009, **87**, 151–161.

(2) Mokarian-Tabari, P.; Senthamaraikannan, R.; Glynn, C.; Collins, T. W.; Cummins, C.; Nugent, D.; O'Dwyer, C.; Morris, M. A. Large Block Copolymer Self-Assembly for Fabrication of Subwavelength Nanostructures for Applications in Optics. *Nano Lett*. 2017, **17** (5), 2973–2978. https://doi.org/10.1021/acs.nanolett.7b00226.

(3) Bhushan, B.; Jung, C.; Koch, K. Self-Cleaning Efficiency of Artificial Superhydrophobic Surfaces. *Langmuir* 2009, **25** (5), 3240–3248. https://doi.org/10.1021/la803860d.

(4) Gengec, N. A.; Cengiz, U.; Erbil, H. Y. Superhydrophobic Perfluoropolymer/Polystyrene Blend Films Induced by Nonsolvent. *Appl. Surf. Sci*. 2016, **383**, 33–41. https://doi.org/10.1016/J.APSUSC.2016.04.160.

(5) Gopishetty, V.; Roiter, Y.; Tokarev, I.; Minko, S. Multiresponsive Biopolyelectrolyte Membrane. *Adv. Mater*. 2008, **20** (23), 4588–4593. https://doi.org/10.1002/adma.200801610.

(6) Tokarev, I.; Gopishetty, V.; Minko, S. Highly Porous 3D Fibrous Nanostructured Bioplolymer Films with Stimuli-Responsive Porosity via Phase Separation in Polymer Blend. *ACS Appl. Mater. Interfaces* 2015, **7** (23), 12463–12469. https://doi.org/10.1021/am5076327.

(7) Gopishetty, V.; Tokarev, I.; Minko, S. Biocompatible Stimuli-Responsive Hydrogel Porous Membranes via Phase Separation of a Polyvinyl Alcohol and Na-Alginate Intermolecular Complex. *J. Mater. Chem*. 2012, **22** (37), 19482–19487. https://doi.org/10.1039/c2jm31778h.

(8) Huang, C.; Moosmann, M.; Jin, J.; Heiler, T.; Walheim, S.; Schimmel, T. Polymer Blend Lithography: A Versatile Method to Fabricate Nanopatterned Self-Assembled Monolayers. *Beilstein J. Nanotechnol*. 2012, **3**, 620–628. https://doi.org/10.3762/bjnano.3.71.

(9) Guo, X.; Liu, L.; Zhuang, Z.; Chen, X.; Ni, M.; Li, Y.; Cui, Y.; Zhan, P.; Yuan, C.; Ge, H.; Wang, Z.; Chen, Y. A New Strategy of Lithography Based on Phase Separation of Polymer Blends. *Sci. Rep.* 2015, **5** (Article 15947). https://doi.org/10.1038/srep15947.

(10) Huang, C.; Förste, A.; Walheim, S.; Schimmel, T. Polymer Blend Lithography for Metal Films: Large-Area Patterning with over 1 Billion Holes/Inch^2. *Beilstein J. Nanotechnol*. 2015, **6**, 1205–1211. https://doi.org/10.3762/bjnano.6.123.

(11) Norton, I. T.; Frith, W. J. Microstructure Design in Mixed Biopolymer Composites. *Food Hydrocoll*. 2001, **15** (4–6), 543–553. https://doi.org/10.1016/S0268-005X(01)00062-5.

(12) Foegeding, E. A. Rheology and Sensory Texture of Biopolymer Gels. *Curr. Opin. Colloid Interface Sci*. 2007, **12** (4–5), 242–250. https://doi.org/10.1016/J.COCIS.2007.07.001.

(13) Dekkers, B. L.; Boom, R. M.; van der Goot, A. J. Structuring Processes for Meat Analogues. *Trends Food Sci. Technol*. 2018, **81**, 25–36. https://doi.org/10.1016/J.TIFS.2018.08.011.

(14) Stieger, M.; van de Velde, F. Microstructure, Texture and Oral Processing: New Ways to Reduce Sugar and Salt in Foods. *Curr. Opin. Colloid Interface Sci*. 2013, **18** (4), 334–348. https://doi.org/10.1016/j.cocis.2013.04.007.

(15) DeMars, L. L.; Ziegler, G. R. Texture and Structure of Gelatin/Pectin-Based Gummy Confections. *Food Hydrocoll*. 2001, **15** (4–6), 643–653. https://doi.org/10.1016/S0268-005X(01)00044-3.

(16) Moore, M. M.; Schober, T. J.; Dockery, P.; Arendt, E. K. Textural Comparisons of Gluten-Free and Wheat-Based Doughs, Batters, and Breads. *Cereal Chem. J*. 2004**, 81** (5), 567–575. https://doi.org/10.1094/CCHEM.2004.81.5.567.

(17) Abugoch, L. E.; Tapia, C.; Villamán, M. C.; Yazdani-Pedram, M.; Díaz-Dosque, M. Characterization of Quinoa Protein–Chitosan Blend Edible Films. *Food Hydrocoll*. 2011, **25** (5), 879–886. https://doi.org/10.1016/J.FOODHYD.2010.08.008.

(18) Wang, L.; Auty, M. A. E.; Kerry, J. P. Physical Assessment of Composite Biodegradable Films Manufactured Using Whey Protein Isolate, Gelatin and Sodium Alginate. *J. Food Eng*. 2010, **96** (2), 199–207. https://doi.org/10.1016/J.JFOODENG.2009.07.025.

(19) Sébastien, F.; Stéphane, G.; Copinet, A.; Coma, V. Novel Biodegradable Films Made from Chitosan and Poly(Lactic Acid) with Antifungal Properties against Mycotoxinogen Strains. *Carbohydr. Polym*. 2006, **65** (2), 185–193. https://doi.org/10.1016/J.CARBPOL.2006.01.006.

(20) Kargl, R.; Mohan, T.; Köstler, S.; Spirk, S.; Doliška, A.; Stana-Kleinschek, K.; Ribitsch, V. Functional Patterning of Biopolymer Thin Films Using Enzymes and Lithographic Methods. *Adv. Funct. Mater*. 2013, **23** (3), 308–315. https://doi.org/10.1002/adfm.201200607.

(21) Caillau, M.; Crémillieu, P.; Laurenceau, E.; Chevolot, Y.; Leclercq, J.-L.; Alekseev, S.; Chevalier, C.; Delair, T. Fifty Nanometer Lines Patterned into Silica Using Water Developable Chitosan Bioresist and Electron Beam Lithography. *J. Vac. Sci. Technol. B Nanotechnol. Microelectron. Mater. Process. Meas. Phenom.* 2017, **35** (60GE01). https://doi.org/10.1116/1.4996870.

(22) Pal, R. K.; Yadavalli, V. K. Silk Protein Nanowires Patterned Using Electron Beam Lithography. Nanotechnology 2018, 29 (33), 335301. https://doi.org/10.1088/1361-6528/aac855.

(23) Kim, S.; Marelli, B.; Brenckle, M. A.; Mitropoulos, A. N.; Gil, E.-S.; Tsioris, K.; Tao, H.; Kaplan, D. L.; Omenetto, F. G. All-Water-Based Electron-Beam Lithography Using Silk as a Resist. Nat. Nanotechnol. 2014, 9 (4), 306–310. https://doi.org/10.1038/nnano.2014.47.

(24) Dore, C.; Osmond, J.; Mihi, A. A Water-Processable Cellulose-Based Resist for Advanced Nanofabrication. Nanoscale 2018, 10 (37), 17884–17892. https://doi.org/10.1039/C8NR04851G.

(25) Nady, N.; Kandil, S. H. Novel Blend for Producing Porous Chitosan-Based Films Suitable for Biomedical Applications. *Membranes (Basel).* 2018, **8** (1), 1–18. https://doi.org/10.3390/membranes8010002.

(26) Fukuhira, Y.; Kitazono, E.; Hayashi, T.; Kaneko, H.; Tanaka, M.; Shimomura, M.; Sumi, Y. Biodegradable Honeycomb-Patterned Film Composed of Poly(Lactic Acid) and Dioleoylphosphatidylethanolamine. *Biomaterials* 2006, **27** (9), 1797–1802. https://doi.org/10.1016/j.biomaterials.2005.10.019.

(27) Czibula, C.; Teichert, G.; Nau, M.; Hobisch, M.; Palasingh, C.; Biesalski, M.; Spirk, S.; Teichert, C.; Nypelö, T. Design of Friction, Morphology, Wetting, and Protein Affinity by Cellulose Blend Thin Film Composition. *Front. Chem*. 2019, **7** (Article 239), 1–10. https://doi.org/10.3389/fchem.2019.00239.

(28) Hu, X.; Wang, X.; Rnjak, J.; Weiss, A. S.; Kaplan, D. L. Biomaterials Derived from Silk–Tropoelastin Protein Systems. *Biomaterials* 2010, **31** (32), 8121–8131. https://doi.org/10.1016/j.biomaterials.2010.07.044.

(29) Hu, X.; Park, S.-H.; Gil, E. S.; Xia, X.-X.; Weiss, A. S.; Kaplan, D. L. The Influence of Elasticity and Surface Roughness on Myogenic and Osteogenic-Differentiation of Cells on Silk-Elastin Biomaterials. *Biomaterials* 2011, **32** (34), 8979–8989. https://doi.org/10.1016/J.BIOMATERIALS.2011.08.037.

(30) Skopinska-Wisniewska, J.; Sionkowska, A.; Kaminska, A.; Kaznica, A.; Jachimiak, R.; Drewa, T. Surface Characterization of Collagen/Elastin Based Biomaterials for Tissue Regeneration. *Appl. Surf. Sci*. 2009, **255** (19), 8286–8292. https://doi.org/10.1016/J.APSUSC.2009.05.127.

(31) Yoo, C. R.; Yeo, I.-S.; Park, K. E.; Park, J. H.; Lee, S. J.; Park, W. H.; Min, B.-M. Effect of Chitin/Silk Fibroin Nanofibrous Bicomponent Structures on Interaction with Human

Epidermal Keratinocytes. *Int. J. Biol. Macromol*. 2008, **42** (4), 324–334. https://doi.org/10.1016/J.IJBIOMAC.2007.12.004.

(32) Lee, K.-G.; Kweon, H.; Yeo, J.-H.; Woo, S.-O.; Lee, J.-H.; Hwan Park, Y. Structural and Physical Properties of Silk Fibroin/Alginate Blend Sponges. *J. Appl. Polym. Sci*. 2004, **93** (5), 2174–2179. https://doi.org/10.1002/app.20714.

(33) Han, Z.; Li, B.; Mu, Z.; Yang, M.; Niu, S.; Zhang, J.; Ren, L. An Ingenious Super Light Trapping Surface Templated from Butterfly Wing Scales. *Nanoscale Res. Lett*. 2015, **10** (1), Article Number: 344. https://doi.org/10.1186/s11671-015-1052-7.

(34) Zhang, W.; Zhang, D.; Fan, T.; Gu, J.; Ding, J.; Wang, H.; Guo, Q.; Ogawa, H. Novel Photoanode Structure Templated from Butterfly Wing Scales. Chem. Mater. 2009, **21** (1), 33–40. https://doi.org/10.1021/cm702458p.

(35) Zhang, Z.; Yu, K.; Lou, L.; Yin, H.; Li, B.; Zhu, Z. Morphology-Controlled Synthesis of ZnO Replicas with Photonic Structures from Butterfly (Papilio Paris) Wing Scales for Tunable Optical Properties. *Nanoscale* 2012, **4** (8), 2606. https://doi.org/10.1039/c2nr30284e.

(36) Siddique, R. H.; Donie, Y. J.; Gomard, G.; Yalamanchili, S.; Merdzhanova, T.; Lemmer, U.; Hölscher, H. Bioinspired Phase-Separated Disordered Nanostructures for Thin Photovoltaic Absorbers. *Sci. Adv*. 2017, **3** (10), e1700232. https://doi.org/10.1126/sciadv.1700232.

(37) Liu, H.; QibinZhao; Zhou, H.; Ding, J.; Zhang, D.; Zhu, H.; Fan, T. Hydrogen Evolution via Sunlight Water Splitting on an Artificial Butterfly Wing Architecture. *Phys. Chem. Chem. Phys.* 2011, **13** (23), 10872. https://doi.org/10.1039/c1cp20787c.

(38) Diao, Z.; Hirte, J.; Chen, W.; Spatz, J. P. Inverse Moth Eye Nanostructures with Enhanced Antireflection and Contamination Resistance. *ACS Omega* 2017, **2** (8), 5012–5018. https://doi.org/10.1021/acsomega.7b01001.

(39) Feng, H.; Lu, X.; Wang, W.; Kang, N.; Mays, J. W. Block Copolymers: Synthesis, Self-Assembly, and Applications. *Polymers (Basel)*. 2017, **9** (494), 1–31. https://doi.org/10.3390/polym9100494.

(40) Banta, R. A.; Collins, T. W.; Curley, R. A.; Young, P. W.; Holmes, J. D.; Flynn, E. J. Nanopatterned Protein-Polysaccharide Thin Films by Humidity Regulated Phase Separation. *J. Colloid Interface Sci*. 2018, **532**, 171–181. https://doi.org/10.1016/J.JCIS.2018.07.109.

(41) Banta, R. A.; Collins, T. W.; Curley, R.; O'Connell, J.; Young, P. W.; Holmes, J. D.; Flynn, E. J. Regulated Phase Separation in Nanopatterned Protein-Polysaccharide Thin Films by Spin Coating. *Colloids Surfaces B Biointerfaces* 2020, **190**, Article No. 110967. https://doi.org/10.1016/j.colsurfb.2020.110967.

(42) Huang, C. Phase Separation in Thin Polymer Films: From Self Stratification to Polymer Blend Lithography, *Darmstadt University of Technology*, 2015.

(43) Ghoshal, T.; Maity, T.; Senthamaraikannan, R.; Shaw, M. T.; Carolan, P.; Holmes, J. D.; Roy, S.; Morris, M. A. Size and Space Controlled Hexagonal Arrays of Superparamagnetic Iron Oxide Nanodots: Magnetic Studies and Application. *Sci. Rep*. 2013, **3** (1), Article No. 2772. https://doi.org/10.1038/srep02772.

(44) Guibal, E.; Vincent, T.; Navarro, R. Metal Ion Biosorption on Chitosan for the Synthesis of Advanced Materials. *J. Mater. Sci*. 2014, **49** (16), 5505–5518. https://doi.org/10.1007/s10853-014-8301-5.

(45) Mohanasrinivasan, V.; Mishra, M.; Paliwal, J. S.; Singh, S. K.; Selvarajan, E.; Suganthi, V.; Subathra Devi, C. Studies on Heavy Metal Removal Efficiency and Antibacterial Activity of Chitosan Prepared from Shrimp Shell Waste. *3 Biotech* 2014, **4** (2), 167–175. https://doi.org/10.1007/s13205-013-0140-6.

(46) Pestov, A.; Bratskaya, S. Chitosan and Its Derivatives as Highly Efficient Polymer Ligands. Molecules 2016, 21 (3), Article No. 330. https://doi.org/10.3390/molecules21030330.

(47) Guibal, E.; Touraud, E.; Roussy, J. Chitosan Interactions with Metal Ions and Dyes: Dissolved-State vs. Solid-State Application. World *J. Microbiol. Biotechnol*. 2005, **21** (6–7), 913–920. https://doi.org/10.1007/s11274-004-6559-5.

(48) Varma, A.; Deshpande, S.; Kennedy, J. Metal Complexation by Chitosan and Its Derivatives: A Review. *Carbohydr. Polym*. 2004, **55** (1), 77–93. https://doi.org/10.1016/J.CARBPOL.2003.08.005.

(49) Guibal, E. Interactions of Metal Ions with Chitosan-Based Sorbents: A Review. *Sep. Purif. Technol.* 2004, **38** (1), 43–74. https://doi.org/10.1016/J.SEPPUR.2003.10.004.

(50) Rombouts, I.; Lagrain, B.; Scherf, K. A.; Lambrecht, M. A.; Koehler, P.; Delcour, J. A. Formation and Reshuffling of Disulfide Bonds in Bovine Serum Albumin Demonstrated Using Tandem Mass Spectrometry with Collision-Induced and Electron-Transfer Dissociation. *Sci. Rep.* 2015, **5** (1), Article No. 12210. https://doi.org/10.1038/srep12210.

(51) Saha, B.; Chakraborty, S.; Das, G. A Rational Approach for Controlled Adsorption of Metal Ions on Bovine Serum Albumin−Malachite Bionanocomposite. *J. Phys. Chem. C* 2010, **114** (21), 9817–9825. https://doi.org/10.1021/jp1003243.

(52) de Jong, S.; van de Velde, F. Charge Density of Polysaccharide Controls Microstructure and Large Deformation Properties of Mixed Gels. *Food Hydrocoll*. 2007, **21** (7), 1172–1187. https://doi.org/10.1016/j.foodhyd.2006.09.004.

(53) Taajamaa, L.; Rojas, O. J.; Laine, J.; Kontturi, E. Phase-Specific Pore Growth in Ultrathin Bicomponent Films from Cellulose-Based Polysaccharides. *Soft Matter* 2011, **7** (21), 10386. https://doi.org/10.1039/c1sm06020a.

(54) Mohan, T.; Nagaraj, C.; Nagy, B. M.; Bračič, M.; Maver, U.; Olschewski, A.; Stana Kleinschek, K.; Kargl, R. Nano- and Micropatterned Polycaprolactone Cellulose Composite Surfaces with Tunable Protein Adsorption, Fibrin Clot Formation, and Endothelial Cellular Response. *Biomacromolecules* 2019, **20** (6), 2327–2337. https://doi.org/10.1021/acs.biomac.9b00304.

(55) Huang, E.; Liao, X.; He, Y.; He, B.; Yang, Q.; Li, G. A Novel Route to the Generation of Porous Scaffold Based on the Phase Morphology Control of Co-Continuous Poly(ε-Caprolactone)/Polylactide Blend in Supercritical CO_2. *Polymer (Guildf).* 2017, **118**, 163–172. https://doi.org/10.1016/J.POLYMER.2017.04.065.

(56) Sarazin, P.; Roy, X.; Favis, B. D. Controlled Preparation and Properties of Porous Poly(l-Lactide) Obtained from a Co-Continuous Blend of Two Biodegradable Polymers. Biomaterials 2004, **25** (28), 5965–5978. https://doi.org/10.1016/j.biomaterials.2004.01.065.

(57) Topală, T.; Bodoki, A.; Oprean, L.; Oprean, R. Bovine Serum Albumin Interactions with Metal Complexes. *Clujul Med*. 2014, **87** (4), 215–219. https://doi.org/10.15386/cjmed-357.

(58) Ferranco, A.; Basak, S.; Lough, A.; Kraatz, H.-B. Metal Coordination of Ferrocene–Histidine Conjugates. *Dalt. Trans.* 2017, **46** (14), 4844–4859. https://doi.org/10.1039/C7DT00456G.

(59) Alekseev, V. G.; Semenov, A. N.; Pakhomov, P. M. Complexation of Ag+ Ions with L-Cysteine. Russ. *J. Inorg. Chem*. 2012, **57** (7), 1041–1044. https://doi.org/10.1134/S0036023612070029.

(60) Horzum, N.; Boyacı, E.; Eroğlu, A. E.; Shahwan, T.; Demir, M. M. Sorption Efficiency of Chitosan Nanofibers toward Metal Ions at Low Concentrations. *Biomacromolecules* 2010, **11** (12), 3301–3308. https://doi.org/10.1021/bm100755x.

(61) Oliveira, M.; Simoni, J. A.; Airoldi, C. Chitosan Metal-Crosslinked Beads Applied for n-Alkylmonoamines Removal from Aqueous Solutions – a Thermodynamic Study. *J. Chem. Thermodyn.* 2014, **73**, 197–205. https://doi.org/10.1016/J.JCT.2013.12.030.

(62) Hernández, R. B.; Franco, A. P.; Yola, O. R.; López-Delgado, A.; Felcman, J.; Recio, M. A. L.; Mercê, A. L. R. Coordination Study of Chitosan and Fe^{3+}. *J. Mol. Struct*. 2008, **877** (1–3), 89–99. https://doi.org/10.1016/J.MOLSTRUC.2007.07.024.

(63) He, J. & Kunitake, T. Formation of Silver Nanoparticles and Nanocraters on Silicon Wafers. *Langmuir* 2006, **22** (18), 7881–7884. https://doi.org/10.1021/LA0610349.

(64) Schneider, M.; Maurath, J.; Fischer, S. B.; Weiß, M.; Willenbacher, N.; Koos, E. Suppressing Crack Formation in Particulate Systems by Utilizing Capillary Forces. *ACS Appl.* Mater. Interfaces 2017, 9 (12), 11095–11105. https://doi.org/10.1021/acsami.6b13624.

(65) Beersaerts, G. The Effect of Water Addition on Crack Formation in Inorganic Polymer Cement from Ca-Fe-Al-Silicate Glass, KU Leuven, 2016.

(66) Ghoshal, T.; Holmes, J. D.; Morris, M. A. Development of Ordered, Porous (Sub-25 Nm Dimensions) Surface Membrane Structures Using a Block Copolymer Approach. *Sci. Rep.* 2018, **8** (1), 7252. https://doi.org/10.1038/s41598-018-25446-0.

(67) Medda, L.; Barse, B.; Cugia, F.; Boström, M.; Parsons, D. F.; Ninham, B. W.; Monduzzi, M.; Salis, A. Hofmeister Challenges: Ion Binding and Charge of the BSA Protein as Explicit Examples. *Langmuir* 2012, **28** (47), 16355–16363. https://doi.org/10.1021/la3035984.

(68) Okur, H. I.; Hladílková, J.; Rembert, K. B.; Cho, Y.; Heyda, J.; Dzubiella, J.; Cremer, P. S.; Jungwirth, P. Beyond the Hofmeister Series: Ion-Specific Effects on Proteins and Their Biological Functions. *J. Phys. Chem.* B 2017, **121** (9), 1997–2014. https://doi.org/10.1021/acs.jpcb.6b10797.

(69) Braun, M. K.; Sauter, A.; Matsarskaia, O.; Wolf, M.; Roosen-Runge, F.; Sztucki, M.; Roth, R.; Zhang, F.; Schreiber, F. Reentrant Phase Behavior in Protein Solutions Induced by Multivalent Salts: Strong Effect of Anions Cl^- Versus NO^{3-}. *J. Phys. Chem. B* 2018, **122** (50), 11978–11985. https://doi.org/10.1021/acs.jpcb.8b10268.

(70) Schröder, C. Proteins in Ionic Liquids: Current Status of Experiments and Simulations. *Top. Curr. Chem*. 2017, **375** (2), 1–26. https://doi.org/10.1007/s41061-017-0110-2.

(71) Klähn, M.; Lim, G. S.; Seduraman, A.; Wu, P. On the Different Roles of Anions and Cations in the Solvation of Enzymes in Ionic Liquids. *Phys. Chem. Chem. Phys*. 2011, **13** (4), 1649–1662. https://doi.org/10.1039/C0CP01509A.

(72) Ngwa, W.; Wannemacher, R.; Grill, W.; Serghei, A.; Kremer, F.; Tribikram, K. Voronoi Tessellations in Thin Polymer Blend Films. *Macromolecules* 2004, **37** (5), 1691–1692. https://doi.org/10.1021/MA035987E.

(73) Ghoshal, T.; Shaw, M. T.; Bolger, C. T.; Holmes, J. D.; Morris, M. A. A General Method for Controlled Nanopatterning of Oxide Dots: A Microphase Separated Block Copolymer Platform. *J. Mater. Chem*. 2012, **22** (24), 12083–12089. https://doi.org/10.1039/c2jm30468f.

(74) Zhao, X.; Ma, S.; Hrbek, J.; Rodriguez, J. A. Reaction of Water with Ce–Au (111) and CeO_x/Au (111) Surfaces: Photoemission and STM Studies. *Surf. Sci.* 2007, **601** (12), 2445–2452. https://doi.org/10.1016/J.SUSC.2007.04.106.

(75) Zähr, J.; Oswald, S.; Türpe, M.; Ullrich, H. J.; Füssel, U. Characterisation of Oxide and Hydroxide Layers on Technical Aluminum Materials Using XPS. *Vacuum* 2012, **86** (9), 1216–1219. https://doi.org/10.1016/J.VACUUM.2011.04.004.

(76) George, G.; Anandhan, S. Synthesis and Characterisation of Nickel Oxide Nanofibre Webs with Alcohol Sensing Characteristics. *RSC Adv.* 2014, **4** (107), 62009–62020. https://doi.org/10.1039/C4RA11083H.

(77) Wang, J.; Zhu, L.; Ji, L.; Chen, Z. Preparation of Nanostructured $Cu(OH)_2$ and CuO Electrocatalysts for Water Oxidation by Electrophoresis Deposition. *J. Mater. Res*. 2018, **33** (5), 581–589. https://doi.org/10.1557/jmr.2017.378.

(78) Shukla, D. To Study the Stability of Complexes by Various Parameters Specially with Softness Parameters. *Int. J. Chem. Stud*. 2016, **4** (3), 38–41.

(79) Martin, R. B. Hard & Soft Acids and Bases in *Encyclopedia of Inorganic Chemistry*; Scott, R. A., Ed.; John Wiley & Sons, Ltd: Chichester, UK, 2006; pp 1–5. https://doi.org/10.1002/0470862106.ia269.

(80) Coffey, D. C.; Ginger, D. S. Patterning Phase Separation in Polymer Films with Dip-Pen Nanolithography. *J. Am. Chem. Soc.* 2005, **127** (13), 4564–4565. https://doi.org/10.1021/ja0428917.

(81) Li, Y.; Hu, K.; Han, X.; Yang, Q.; Xiong, Y.; Bai, Y.; Guo, X.; Cui, Y.; Yuan, C.; Ge, H.; Chen, Y. Phase Separation of Silicon-Containing Polymer/Polystyrene Blends in Spin-Coated Films. 2016, **32** (15), https://doi.org/10.1021/acs.langmuir.6b00447.

(82) Łupina, K.; Kowalczyk, D.; Zięba, E.; Kazimierczak, W.; Mężyńska, M.; Basiura-Cembala, M.; Wiącek, A. E. Edible Films Made from Blends of Gelatin and Polysaccharide-Based Emulsifiers - A Comparative Study. *Food Hydrocoll*. 2019, **96**, 555–567. https://doi.org/10.1016/J.FOODHYD.2019.05.053.

(83) Bankoti, K.; Rameshbabu, A. P.; Datta, S.; Maity, P. P.; Goswami, P.; Datta, P.; Ghosh, S. K.; Mitra, A.; Dhara, S. Accelerated Healing of Full Thickness Dermal Wounds by Macroporous Waterborne Polyurethane-Chitosan Hydrogel Scaffolds. *Mater. Sci. Eng. C* 2017, **81**, 133–143. https://doi.org/10.1016/J.MSEC.2017.07.018.

(84) Son, S.-Y.; Park, M.; Lee, D. S.; Lee, S.; Han, J.; Jung, G. Y.; Joh, H.-I. Field Effect in Amorphous Carbon Nanomesh Directly Synthesized from Phase-Separated Polymer Blends. *Carbon*. 2019, **142**, 285–290. https://doi.org/10.1016/J.CARBON.2018.10.042.

(85) Chen, F.; Gällstedt, M.; Olsson, R. T.; Gedde, U. W.; Hedenqvist, M. S. A Novel Chitosan/Wheat Gluten Biofoam Fabricated by Spontaneous Mixing and Vacuum-Drying. *RSC Adv*. 2015, **5** (114), 94191–94200. https://doi.org/10.1039/C5RA18569F.

(86) Nazzi, F. The Hexagonal Shape of the Honeycomb Cells Depends on the Construction Behavior of Bees. *Sci. Rep*. 2016, **6** (March), 1–6. https://doi.org/10.1038/srep28341.

(87) Karihaloo, B. L.; Zhang, K.; Wang, J. Honeybee Combs: How the Circular Cells Transform into Rounded Hexagons. *J. R. Soc. Interface* 2013, **10** (86), 2–5. https://doi.org/10.1098/rsif.2013.0299.

(88) Ball, P. How Honeycombs Can Build Themselves. *Nature* 2013. https://doi.org/10.1038/nature.2013.13398.

(89) Brodoceanu, D.; Elnathan, R.; Prieto-Simón, B.; Delalat, B.; Guinan, T.; Kroner, E.; Voelcker, N. H.; Kraus, T. Dense Arrays of Uniform Submicron Pores in Silicon and Their Applications. *ACS Appl. Mater. Interfaces* 2015, **7** (2), 1160–1169. https://doi.org/10.1021/am506891d.

(90) Zhang, W.; Zhang, D.; Fan, T.; Gu, J.; Ding, J.; Wang, H.; Guo, Q.; Ogawa, H. Novel Photoanode Structure Templated from Butterfly Wing Scales. *Chem. Mater*. 2009, **21** (1), 33–40. https://doi.org/10.1021/cm702458p.

(91) Han, Z.; Niu, S.; Shang, C.; Liu, Z.; Ren, L. Light Trapping Structures in Wing Scales of Butterfly Trogonoptera Brookiana. *Nanoscale* 2012, **4** (9), 2879–2883. https://doi.org/10.1039/c2nr12059c.

(92) Zhao, Q.; Guo, X.; Fan, T.; Ding, J.; Zhang, D.; Guo, Q. Art of Blackness in Butterfly Wings as Natural Solar Collector. *Soft Matter* 2011, **7** (24), 11433–11439. https://doi.org/10.1039/c1sm06167d.

(93) Siddique, R. H.; Donie, Y. J.; Gomard, G.; Yalamanchili, S.; Merdzhanova, T.; Lemmer, U.; Hölscher, H. Bioinspired Phase-Separated Disordered Nanostructures for Thin Photovoltaic Absorbers. *Sci. Adv.* 2017, **3** (10), e1700232. https://doi.org/10.1126/sciadv.1700232.

(94) Davis, A. L.; Nijhout, H. F.; Johnsen, S. Diverse Nanostructures Underlie Thin Ultra-Black Scales in Butterflies. *Nat. Commun*. 2020, **11** (1), 1–7. https://doi.org/10.1038/s41467-020-15033-1.

(95) Raut, H. K.; Dinachali, S. S.; Anash-Antwi, K. K.; Ganesh, V. A.; Ramkrishna, S. Fabrication of Highly Uniform and Porous MgF2 Anti-Reflective Coatings by Polymer-Based Sol–Gel Processing on Large-Area Glass Substrates. *Nanotechnology* 2013, **24** (50). https://doi.org/10.1088/0957-4484/24/50/505201.

(96) Weaire, D.; Hultzler, S. Coarsening in *The Physics Of Foams*; Oxford University Press (OUP), 1999; pp 88–101.

(97) Weaire, D.; Hultzler, S. Quantitative Description of Foam Structures in *The Physics Of Foams*; Oxford University Press (OUP), 1999; pp 28–46.

(98) Corson, F.; Hamant, O.; Bohn, S.; Traas, J.; Boudaoud, A.; Couder, Y. Turning a Plant Tissue into a Living Cell Froth through Isotropic Growth. *Proc. Natl. Acad. Sci. U. S. A.* 2009, **106** (21), 8453–8458. https://doi.org/10.1073/pnas.0812493106.

(99) Gentili, D.; Foschi, G.; Valle, F.; Cavallini, M.; Biscarini, F. Applications of Dewetting in Micro and Nanotechnology. *Chem. Soc. Rev*. 2012, **41** (12), 4430. https://doi.org/10.1039/c2cs35040h.

(100) Dimitrova, L. M.; Boneva, M. P.; Danov, K. D.; Kralchevsky, P. A.; Basheva, E. S.; Marinova, K. G.; Petkov, J. T.; Stoyanov, S. D. Limited Coalescence and Ostwald Ripening in Emulsions Stabilized by Hydrophobin HFBII and Milk Proteins. *Colloids Surfaces A Physicochem. Eng. Asp.* 2016, **509**, 521–538. https://doi.org/10.1016/J.COLSURFA.2016.09.066.

(101) Dai, Y.; Lu, P.; Cao, Z.; Campbell, C. T.; Xia, Y. The Physical Chemistry and Materials Science behind Sinter-Resistant Catalysts. *Chem. Soc. Rev*. 2018, **47** (12), 4314–4331. https://doi.org/10.1039/C7CS00650K.

(102) Behafarid, F.; Roldan Cuenya, B. Coarsening Phenomena of Metal Nanoparticles and the Influence of the Support Pre-Treatment: Pt/TiO_2 (110). *Surf. Sci*. 2012, **606** (11–12), 908–918. https://doi.org/10.1016/J.SUSC.2012.01.022.

(103) Park, C.; Yoon, J.; Thomas, E. L. Enabling Nanotechnology with Self Assembled Block Copolymer Patterns. *Polymer (Guildf).* 2003, **44** (22), 6725–6760. https://doi.org/10.1016/J.POLYMER.2003.08.011.

(104) Wei, M.; Mead, J. Directed Assembly of Polymer Blends Using Nanopatterned Chemical Surfaces. In Functional Polymer Blends; Mittal, V.; *CRC Press: Boca Raton*, 2012; pp 305–325. https://doi.org/10.1201/b11799-11.

(105) Vinod, P. N. The Fire-through Processed Screen-Printed Ag Thick Film Metal Contacts Formed on an Electrochemically Etched Porous Silicon Antireflection Coating of Silicon Solar Cells. *RSC Adv*. 2013, **3** (11), 3618–3622. https://doi.org/10.1039/c2ra20354e.

(106) Bera, A.; Bhattacharya, A.; Tiwari, N.; Jha, S. N.; Bhattacharyya, D. Morphology, Stability, and X-Ray Absorption Spectroscopic Study of Iron Oxide (Hematite) Nanoparticles Prepared by Micelle Nanolithography. *Surf. Sci*. 2018, **669**, 145–153. https://doi.org/10.1016/J.SUSC.2017.11.022.

(107) Shunsheng Ye; Hongyu Wang; Hongyang Su; Lingxia Chang; Shuli Wang; Xuemin Zhang; Junhu Zhang; Bai Yang. Facile Fabrication of Homogeneous and Gradient Plasmonic Arrays with Tunable Optical Properties via Thermally Regulated Surface Charge Density. *J. Mater. Chem. C* 2017, **5** (16), 3962–3972. https://doi.org/10.1039/C7TC00064B.

4.7. APPENDIX

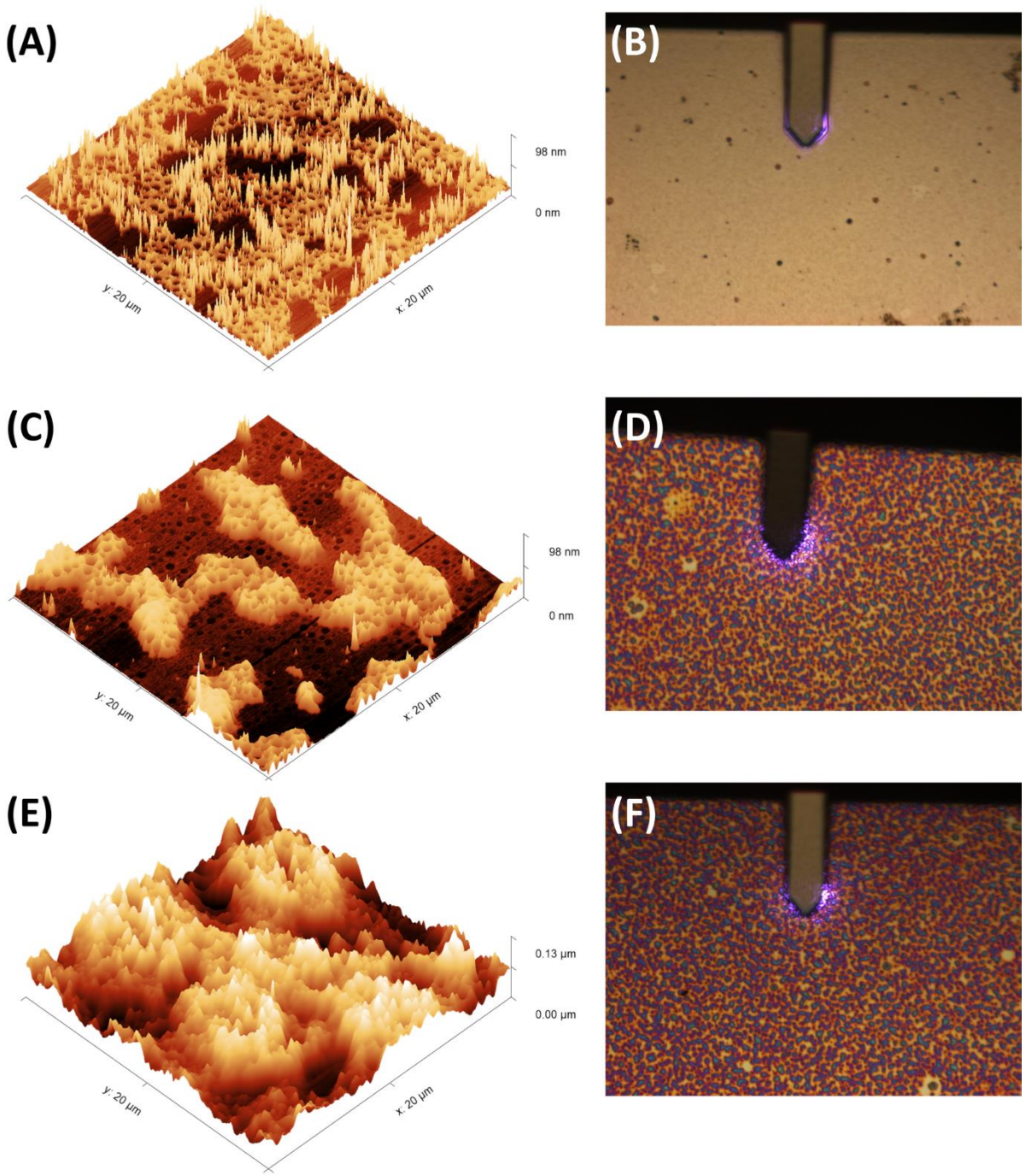


Figure S4.1: *AFM and optical microscopy images of the metal surfaces after metal incorporation and calcination after various different biopolymer template–metal solution contact times.* ***(A)*** *and* ***(B)*** *5 s;* ***(C)*** *and* ***(D)*** *15 s; and* ***(E)*** *and* ***(F)*** *60 s contact times.*

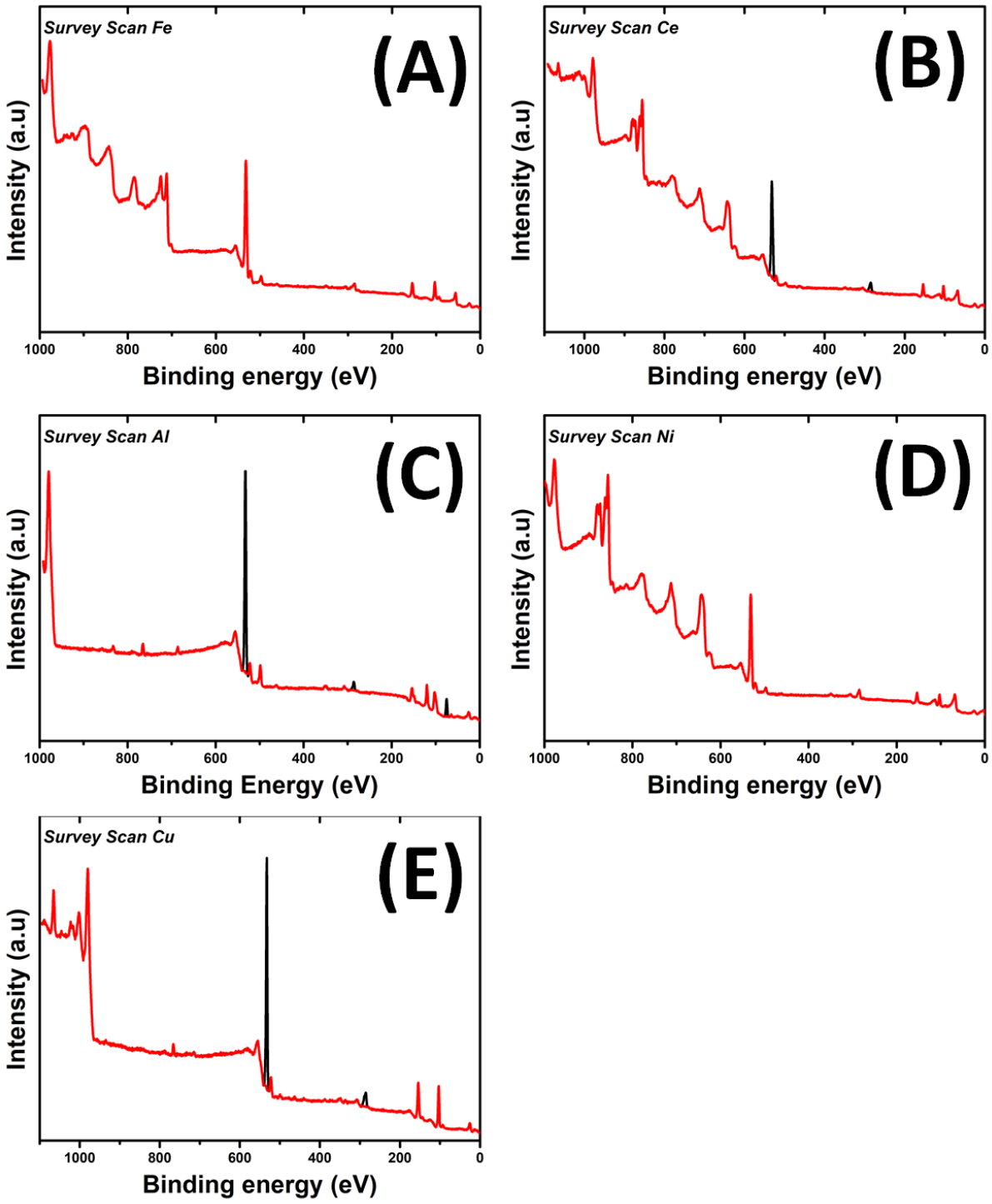


Figure S4.2: *XPS survey spectra of the metal surfaces after metal incorporation and calcination at 700 ºC, at a ramp rate of 20 ºC/min. Survey spectra for* ***(A)*** *Fe;* ***(B)*** *Ce;* ***(C)*** *Al;* ***(D)*** *Ni; and* ***(E)*** *Cu surfaces.*

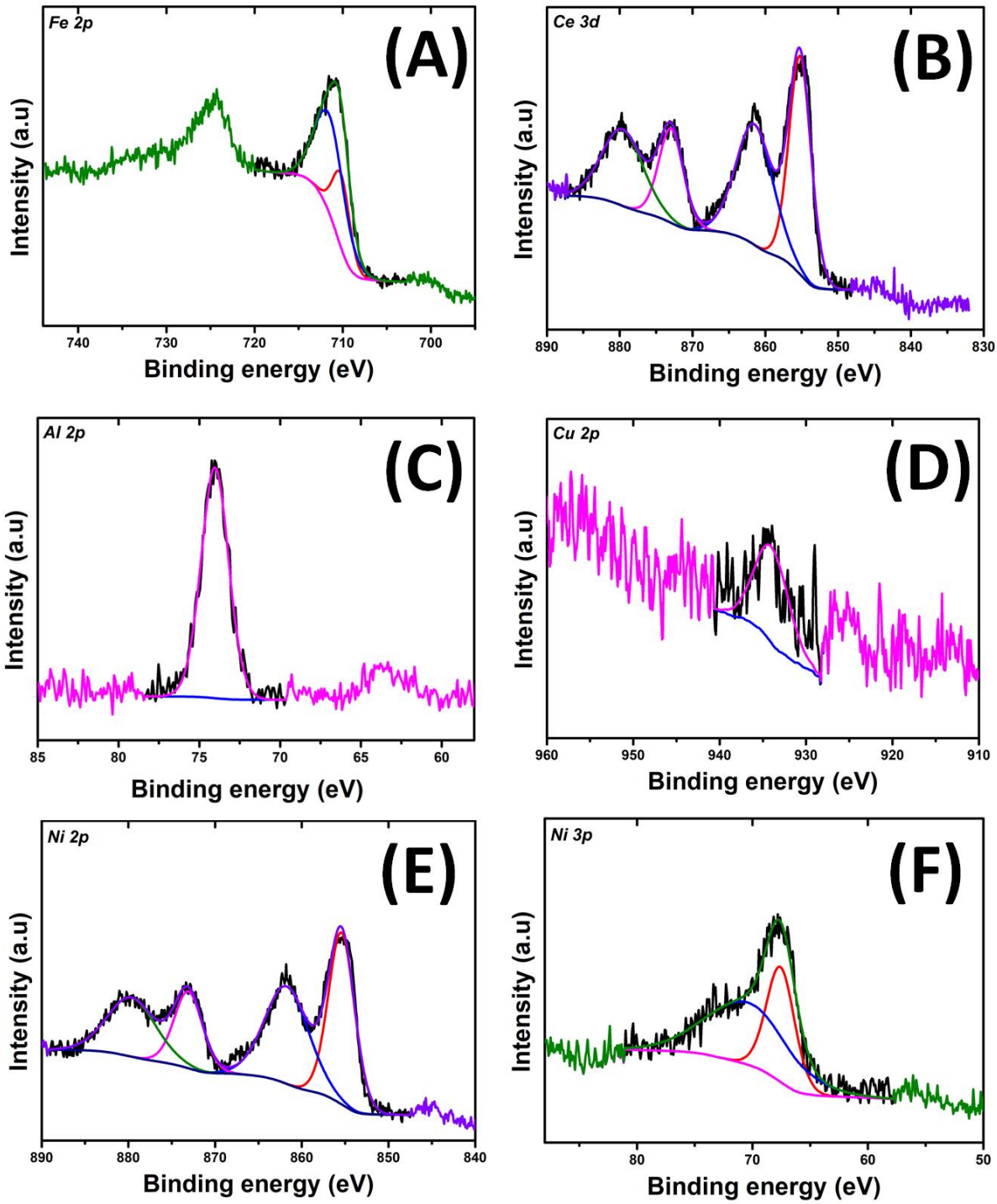


Figure S4.3: *Shows the XPS* ***(A)*** *Fe 2p;* ***(B)*** *Ce 3d;* ***(C)*** *Al 2p;* ***(D)*** *Cu 2p;* ***(E)*** *Ni 2p and* ***(F)*** *Ni 3p spectra of the metal matrix after annealing and calcination treatment.*

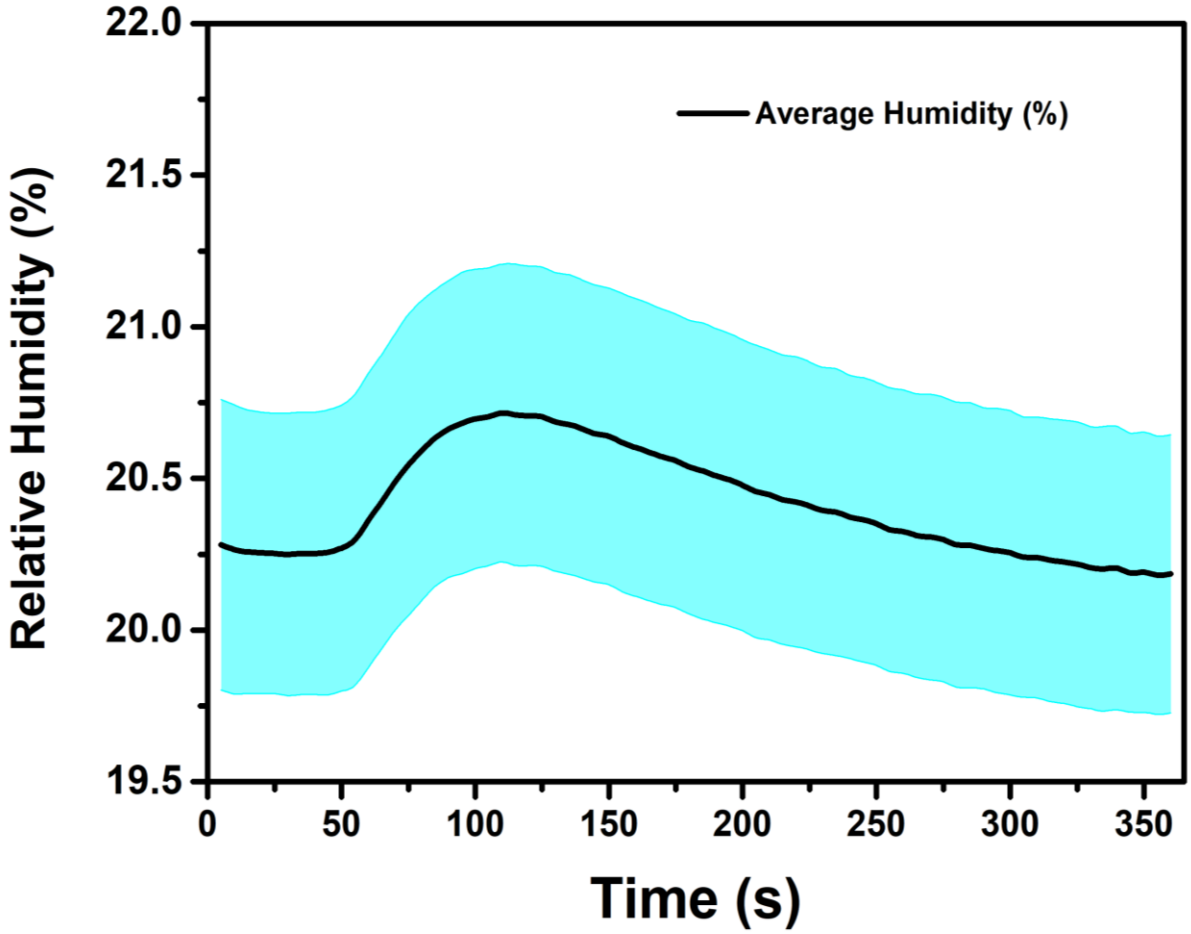


Figure S4.4: *Plot of humidity of the spin-coating chamber as solvent is lost from the sample. The average % RH (black line) plotted as a function of time, with the standard deviation of 4 runs plotted as blue region. Humidity of the chamber never exceeded 22% RH. The majority of solvent loss was achieved after approx. 50 s. Relative Humidity (RH) readings from HOBO MX Temp/RH Logger sensor for 1:1 BSA-Ch blend film cast at 3000 RPM, 20% RH.*

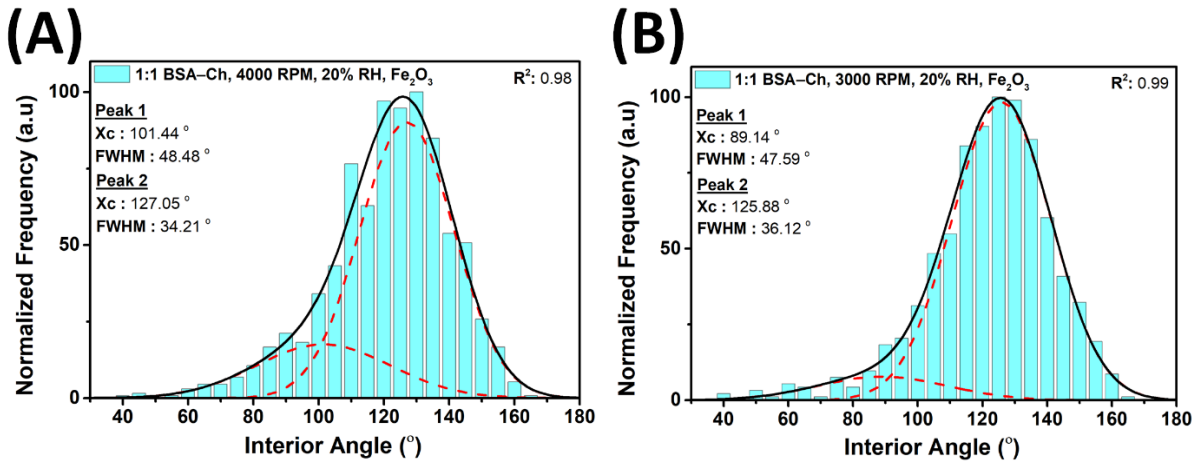


Figure S4.5: *Geometry of Fe2O3 masks. Distribution of angles at the vertices of polygonal pores. Masks generated with biopolymer template 1:1 BSA-Ch blends cast at 20% RH, at* ***(A)*** *4000 rpm and* ***(B)*** *3000 rpm. Higher casting speed corresponds to earlier drying.*

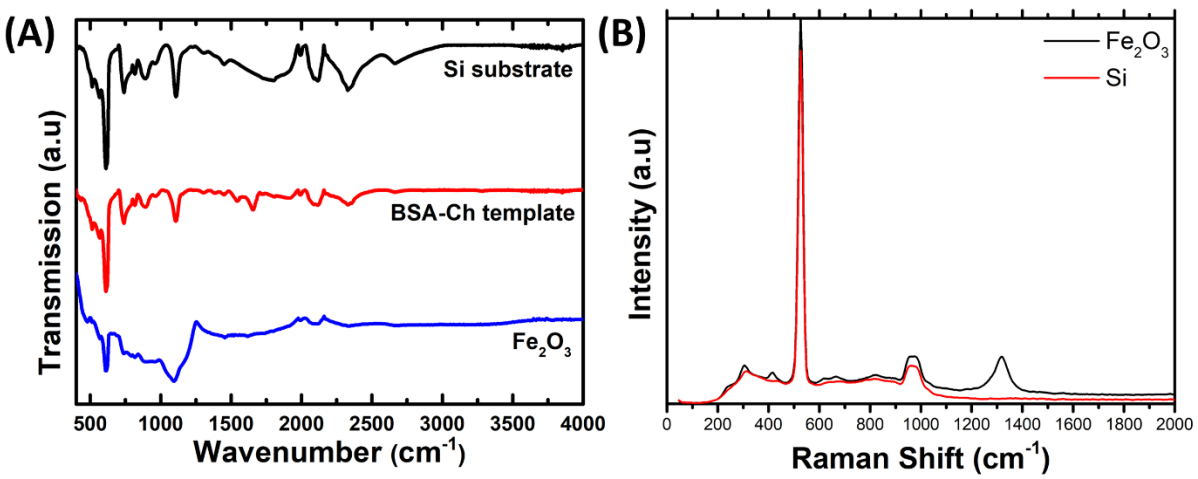


Figure S4.6: (A) *FTIR spectra of Si substrate, biopolymer template and Fe_2O_3 porous matrix after annealing and calcination.* ***(B)*** *Raman spectra of Si substrate and Fe_2O_3 porous matrix after annealing and calcination.*

The FTIR spectra of **Figure S4.6a** show a band at about 480 cm^{-1} corresponding to pseudocubic α-Fe_2O_3.[1] The FTIR data of the biopolymer blend and Si substrate were found to be consistent with what was reported in our previous work.[2] No biopolymer was detected on the substrate after calcination. α-Fe_2O_3 was also confirmed using Raman spectroscopy, **Figure S4.6b**. As with the FTIR spectra, bands mainly arose from the Si substrate due to the small thickness of the film. The broad intense peak band observed at around 1310 cm^{-1} corresponds to the 2LO line occurs due to resonance enhancement.[3] The modes observed 305, 416, 616 cm^{-1} correspond to the E_g modes of α-Fe_2O_3,[3,4] while the modes observed at 662 and 819 cm^{-1} are only observed in highly crystalline hematite, such as commercial α-Fe_2O_3.[3,4]

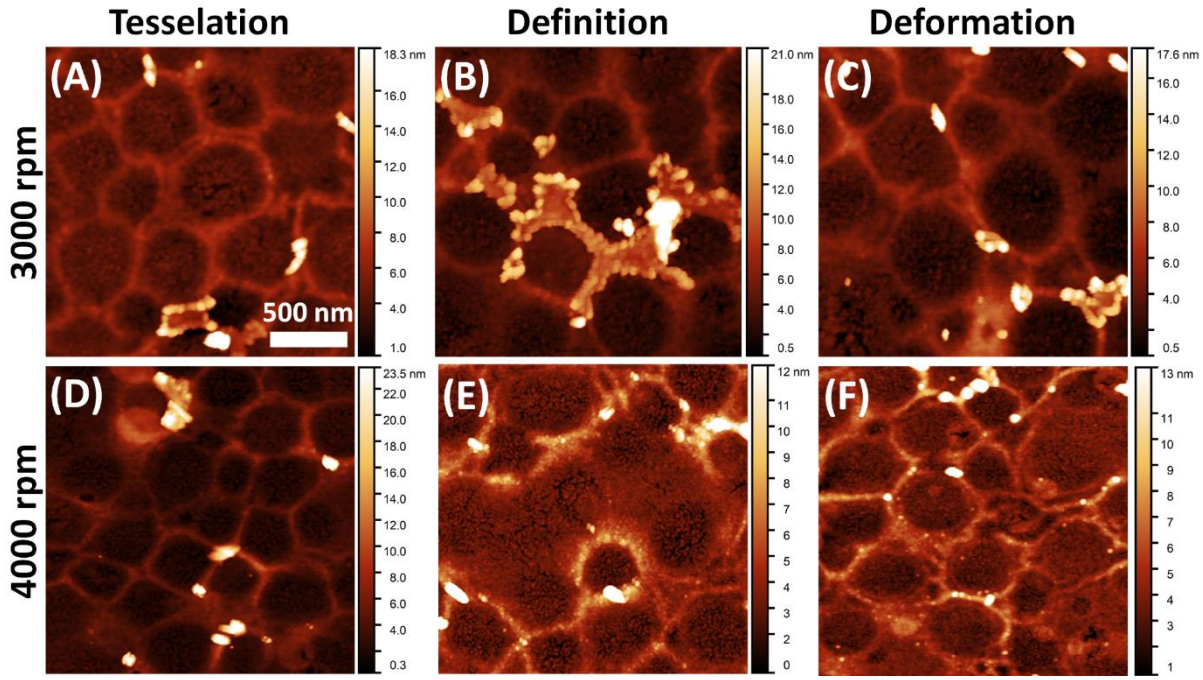


Figure S4.7: *Each image is 2 x 2 µm, scale bar provided in image* ***A****. AFM images of* Fe_2O_3 *metal masks, produced with 1:1 BSA-Ch blend at 20% RH. Metal precursor used was 1 wt%* $Fe(NO)_3.9H_2O$*-EtOH solution. A-C) Shows* Fe_2O_3 *mask created using BSA-Ch blend cast at 3000 RPM. D-F) Shows* Fe_2O_3 *mask created using BSA-Ch blend cast at 4000 RPM.*

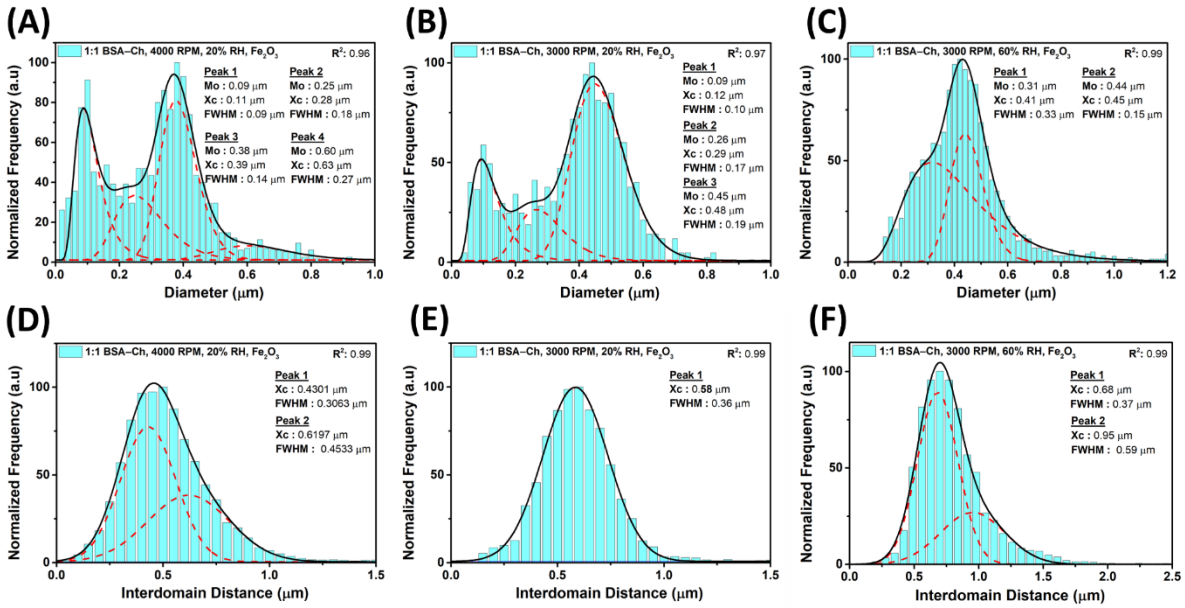


Figure S4.8: *Statistical analysis of Fe_2O_3 masks generated using various biopolymer blends templates. Metal masks were produced as in* ***Figure 4.6****, using 1 wt% $Fe(NO_3)_3.9H_2O$.* ***A****,* ***D)*** *display the normalized PSD and interdomain distance of pores generated with biopolymer blend cast at 4000 rpm and 20% RH.* ***(B, E)*** *corresponds to the PSD and interdomain distance of pores generated with biopolymer blends cast at 3000 rpm, 20% RH.* ***C, F)*** *corresponds to the PSD and interdomain distance pores generated with biopolymer blends cast at 3000 rpm, 60% RH.*

Figure S4.8 shows the PSD and spacing of metal masks generated using various biopolymer templates, which will highlight any issues in incorporation of the metal. The Fe_2O_3 mask generated using BSA–Ch template, 4000 rpm, 20% RH contains 4 modes rather than 2 (**Figure S4.8a**). Small pore formation (0.09 µm) in iron oxide may result from a number of mechanisms; ejection of retained water[5],dehydration/dehydroxylation during conversion of goethite (FeO(OH), an intermediate of iron nitrate nonahydrate decomposition) to hematite[6–8], local stress resulting from rapid local temperature changes or rapid grain growth[9], defects formation during Fe_2O_3 formation.[7] Liu *et al* showed increasing temperature produces larger pore diameter in Fe_2O_3 (though no mechanism was provided), and pores in this mode of the size distribution are of comparable size.[10] It is possible that some pores were overfilled, reducing the diameter, and that the formation of this mode in the PSD is a combination of the above mechanisms.[11] However, we believe the most likely mechanism is strain caused by more acute and obtuse interior angles causing additional pore formation (**Figure S4.5a** & **Figure S4.7f**). In support of this, the production of extra pores is much less evident in **Figure S4.8b**, and non-

existent in **Figure S4.8c**. The large tail in the zone of bigger pores in **Figure S4.8a** (> 0.5 µm) indicates poor resolution between the some of the pores. This may be due to insufficient metal incorporated into the Ch domain, due to the thinner nature of the 4000 rpm biopolymer film. Both modes in the PSD of the biopolymer template are observed in the PSD of the metal mask (0.25 µm and 0.38 µm, **Figure S4.8a**). The addition of smaller and larger pores is reflected in the bimodal spacing between the pores (**Figure S4.8d**) with pores approx. 0.54 ± 0.29 µm apart**.** The number of pores/area (5.72 ± 0.81 pores/µm^2), is slightly increased from the number of BSA spheres/area; the highest number of features/area achieved thus far. We suspect that strain caused by the acute and obtuse interior angles of tessellated pores causes additional pore formation by deformation of the pore wall (i.e. defect pores). In summary, fast solvent evaporation causes tessellation. However, when evaporation is too fast, deformation of the pores occurs due to strain (caused by obtuse and acute interior angles of the pores, e.g. peak 1 in **Figure S4.5a** & **Figure S4.7 d – f**).

Figure S4.8b and **d** shows the size distribution and spacing of pores for the metal oxide produced using 1:1 BSA-Ch template, 3000 rpm at 20% RH. The PSD of the pores (**Figure S4.8b**) matches that of the biopolymer template (**Figure 4.9b**). Again, the peak at 0.09 µm is prominent, indicating a similar mechanism to the 4000 rpm 20% RH biopolymer blend, though to a lesser extent. The absence of a long tail extending past 0.8 µm in **Figure S4.8b** shows better adoption of the biopolymer pattern. This is attributed to the thicker nature of the film (being cast at 3000 rpm), improving the adsorption of the metal precursor due to the presence of more Ch. The number of pores/area matched that of the biopolymer template (4.50 ± 0. 29 pores/µm^2) with a minor decrease in the mean pore diameter (0.37 ± 0.17 µm) due to the mode at 0.09 µm (**Figure S4.8b**). Pore spacing remained unimodal with an average spacing of 0.63 ± 0.35 µm, a slight increase from the biopolymer template it was generated from. The PSD and interpore spacing of the metal mask have a higher similarity to the biopolymer template than the metal mask generated using the 1:1 BSA-Ch template, 4000 rpm at 20% RH. Though the number of features/area is not as high, the retention of the original pattern and higher definition of the pattern make it more suitable as a pattern transfer mask.

Finally, the metal mask generated from BSA-Ch template, 3000 rpm at 60% RH produced a bimodal size distribution. The first peak at 0.31 µm increased in intensity (**Figure S4.8c**) while number of pores/area is slightly lower than the number of BSA spheres in the biopolymer template, with 2.38 ± 0.14 pores/µm^2. The slight reduction in pores/area and reduction in mean pore diameter suggest partial overfilling of the pores and secondary overlayer formation.[11] The

spacing of pores compared to the BSA domains was similar, though, due to the reduction in density, a tail is observed in the pore spacing distribution **(Figure S4.8f)**. Because of the larger pores formed due to coalescing BSA domains, the reduction in features/area compared to the biopolymer template, and the reduction in mean pore diameter, this metal mask is not suitable for pattern transfer.

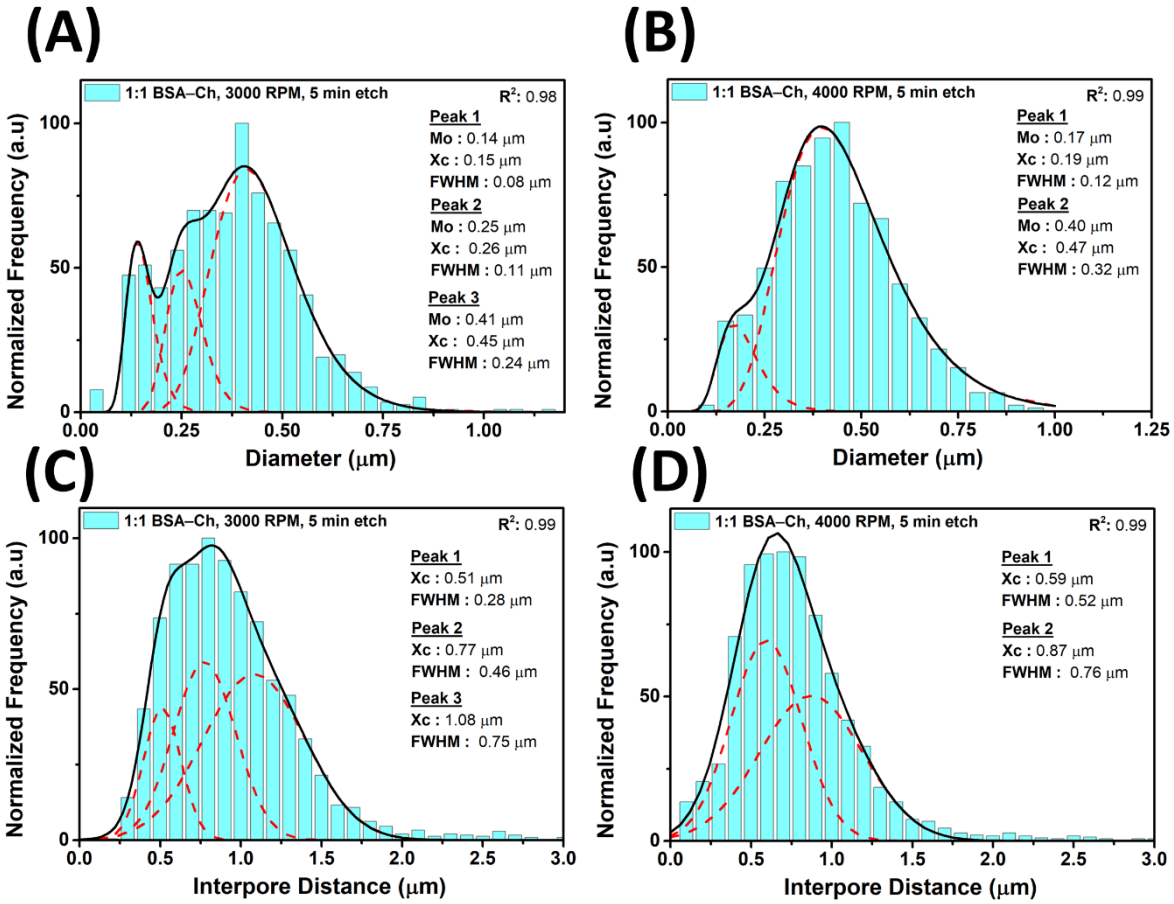


***Figure S4.9**: Statistical analysis substrate after 5 min etch with NH_4F/HNO_3H_2O solution. **A, C)** Correspond to diameter and interpore distance of images in **Figure 4.8g** (3000 rpm, 20% RH). **B, D)** Correspond to diameter and interpore distance of images in **Figure 4.8c** (4000 rpm, 20% RH).*

Figure S4.9 shows the PSD and spacing distribution of pores after a 5 min etch in $NH_4F/HNO_3/H_2O$ solution, with AFM images shown in **Figure 4.8c** and **g**. The 3000 rpm template generated etched pores with a mean diameter of 0.36 ± 0.16 µm, with a max diameter of 1.14 µm, **Figure 4.8c** and **Figure S4.9a**. The number of pores per area decreased to 2.41 ± 0.48 pores/µm^2. This decrease is reflected in the spacing between transferred pores, **Figure S4.9c**, with a broadening of the distribution up to 6.52 µm. For the 3000 rpm template, 53% of

pores were transferred to the surface, showing the BSA did not sufficiently perforate to the substrate. .[12] In contrast, the 4000 rpm template produced pores 0.41 ± 0.16 μm in diameter, with a max diameter of 0.92 μm (**Figure S4.9b**). The number of pores/area decreased to 2.31 ± 0.26 pores/μm^2, with the spacing between pores broadening with a max pore spacing of 6.55 μm (**Figure S4.9d**). This indicates that approx. 41% of pores were transferred by the etching process.

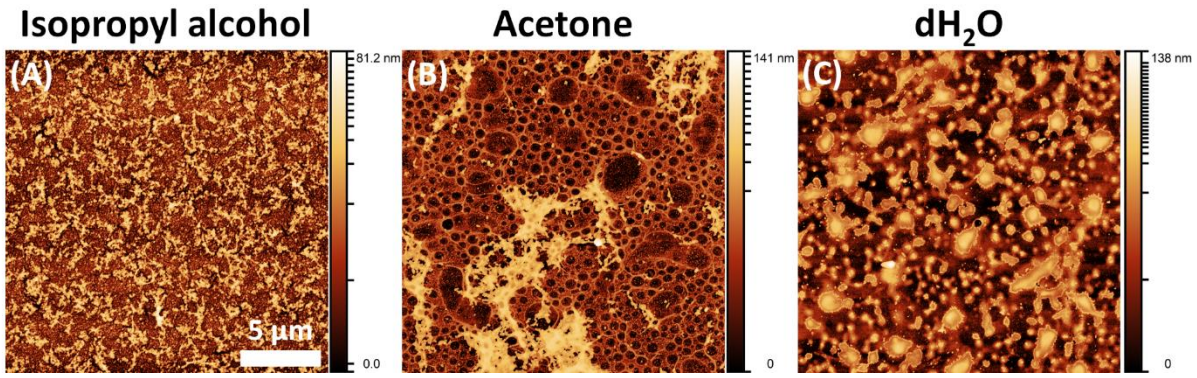


Figure S4.10: *AFM images of the metal surfaces after metal incorporation and calcination biopolymer template–metal solution contact times. Each image is 20 x 20 µm, scale bar provided in image* ***A****. Metal templates were produced with biopolymer template (1:1 BSA-Ch, 3000 RPM, 60% RH) on planar silicon substrates. 1 wt% $Fe(NO_3)_3.9H_2O$-solvent was incorporated for 5 s. Samples were heated to 160 °C for 1 hr, with a ramp rate of 20 °C/min to remove water before calcination. Samples were then placed into a cold furnace, heated to 700 °C and left for 1 hr before removal. Solvents used for incorporation were* ***(A)*** *isopropyl alcohol (IPA);* ***(B)*** *acetone and* ***(C)*** *dH_2O.*

Differing solvent systems are known to elicit differing metal binding selectivity onto polysaccharides in solvents with different dielectric constants.[13] Decreased dielectric constant of the solvent results in a reduction of the amount of metal adsorbed by a biopolymer, though other factors also play a role.[14] Using the dielectric constant of the solvent (solvent polarity) as a predictor of metal binding, metal binding was expected to increase in the order of IPA < $(CH_3)_2CO$ < EtOH <<H_2O using dielectric constants provided by Sherwood *et al* (and references therein).[15] This works well for IPA and H_2O (**Figure S4.10A** and **C**), with dielectric constants in extreme contrast to one another. However, acetone (**Figure S4.10B**) incorporates more metal than EtOH in 5s (shown throughout this work). While dielectric constants may play a partial role in metal incorporation, there are other factors to consider. As water is the least volatile, we would expect slower water evaporation, thereby including more metal in the film. However, as acetone is the most volatile solvent, less metal should be incorporated, though this is not observed. Complexation between ligands and cations depend on the solvents ability to compete for the cation contesting with the ligand. The ability of the solvent to do this is expressed by the solvents donor number.[16] The series of donor numbers for solvents chosen increase accordingly: $(CH_3)_2CO$ < H_2O << EtOH < IPA.[15] Here we see that both acetone and water do not strongly compete to solvate the metal, whereas the alcohols do compete,

"shielding" the ligand from the metal slowing metal uptake.[17] Finally, H_2O was the only solvent to incorporate metal into the BSA domain within 5 s. As the Hofmeister effect also relies on the hydration of the solvent to chaperone metals, the increased availability of water likely plays a role. Additionally, the swelling of the BSA and Ch likely increase the availability of functional groups for chelation within that time.

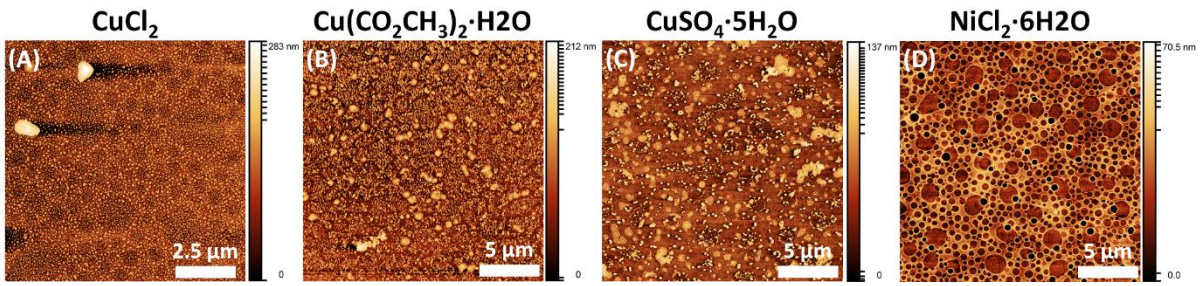


Figure S4.11: *AFM images of metal oxide structures using* ***(A)*** *$CuCl_2$;* ***(B)*** *$Cu(CO_2CH_3).H_2O$;* ***(C)*** *$CuSO_4.H_2O$ and* ***(D)*** *$NiCl_2.6H_2O$ precursors for metal incorporation. Image* ***A*** *is 10 x 10 µm, while image* ***B – D*** *are image 20 x 20 µm in size. Metal templates were produced with biopolymer template (1:1 BSA-Ch, 3000 RPM, 60% RH) on planar silicon substrates. Metal templates were prepared with 1 wt% metal precursor-EtOH. Samples were annealed and calcined as with* ***Figure S4.2****.*

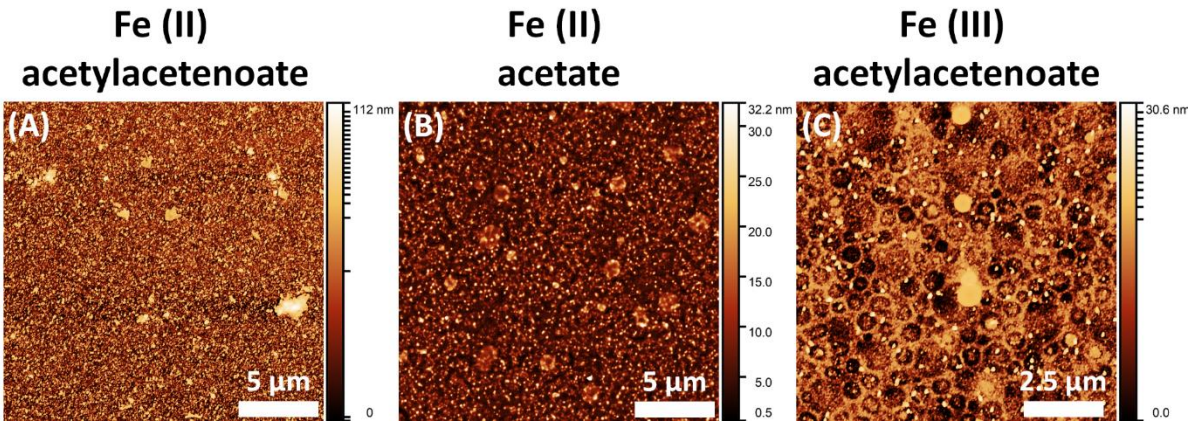
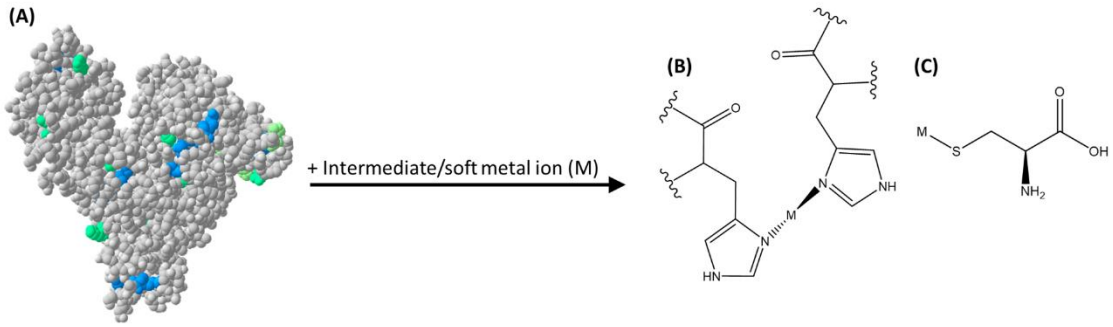
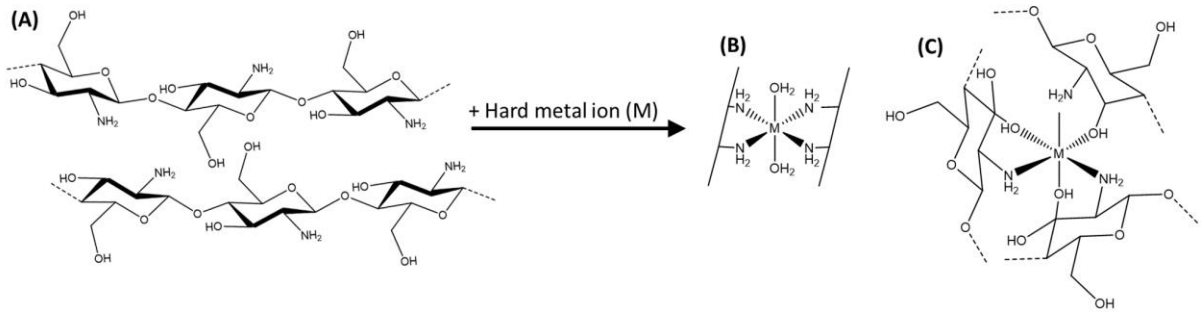


Figure S4.12: *AFM images of iron oxide structures using (A) iron (II) acetylacetonate; (B) iron (II) acetate; and (C) iron (III) acetylacetonate. Metal templates produces with biopolymer template (1:1 BSA-Ch, 3000 RPM, 60% RH) on planar silicon substrates. Image A and B are 20 x 20 µm, while image C is 10 x 10 µm in size. Metal templates were prepared with 1 wt% metal precursor-EtOH. Samples were heated to 160 °C for 1 hr, with a ramp rate of 20 °C/min to remove water before calcination. Samples were then placed into a cold furnace, heated to 700 °C and left for 1 hr before removal.*

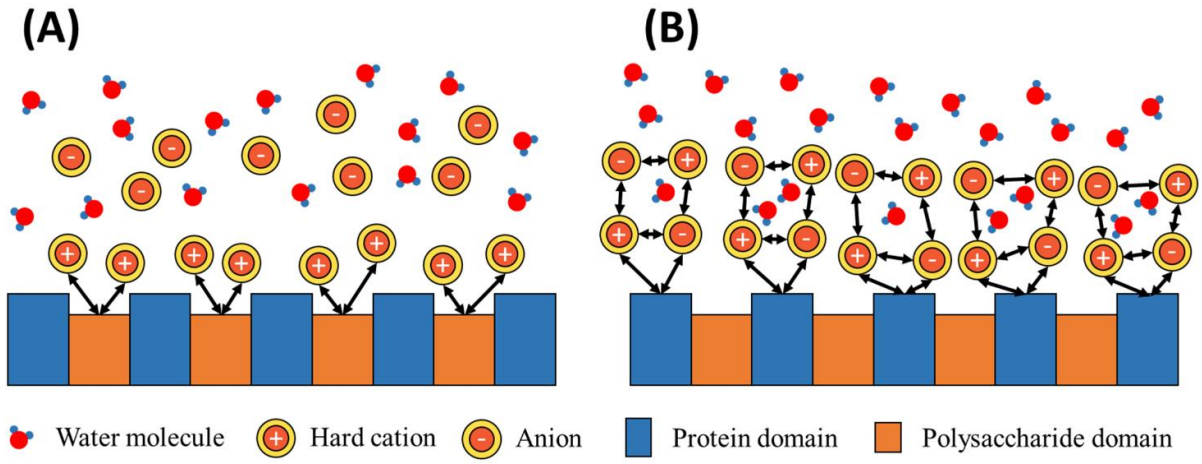
The Fe^{2+} precursor with the acetylacetonate anion (**Figure S4.12A**) incorporated little metal, as expected due to the softer nature of the cation. Using a more strongly hydrated anion, acetate allowed for partial incorporation of Fe into the BSA domain (**Figure S4.12B**). Less metal was incorporated than in **Figure S4.12B**, as Cu^{2+} is a softer cation than Fe^{2+}, with both likely bonding to Cys and His residues.[18] Increasing the hardness of the Fe cation (**Figure S4.12C**), while using the same concentration and anion as **Figure S9A,** incorporated far more metal into the Ch domain, as with all Fe^{3+} samples in the bulk of this work. However, the sample is poorly resolved and not suitable for potential applications, highlighting the importance of the cation charge, and nature of the anion.[19]



Scheme S4.1: (A) *3D structure of BSA (Protein Data Bank ID: 3v03, www.rcsb.org) using Swiss-Pdb Viewer V.4.1 software, where the metal binding sites are indicated by colour. Cysteine (Cys, 35 residues, sulfhydryl groups, blue) and histidine (His, 16 residues, imidazole groups, green).* ***(B)*** *Proposed structure for His-M complex.* ***(C)*** *Proposed structure for Cys-M complex. Metal-AA structures drawn using Chemdraw Professional V16.0.1.4.*[19-23]



Scheme S4.2: ***(A)*** *Structure of chitosan polysaccharide created using Chemdraw Professional V16.0.1.4(77).* ***(B,C)*** *Proposed structure for Ch-M complex.*



Scheme S4.3: *Arrows depict strong Coulomb interactions between ion species and film surface.* ***A)*** *Depicts hard cations binding to polysaccharide via amine groups. Anion (i.e.* Cl^-*) does not direct cation to protein domain.* ***B)*** *Depicts late stage cation binding to protein domain. Ions approach surface in a pairwise fashion. Anions (i.e.* NO_3^-*) chaperone cation to protein domain. Any repulsion of the cation to the protein domain is offset by the anion. Cation binding to polysaccharide domain is omitted for clarity in* ***(B).***

4.7.1. APPENDIX REFERENCES

(1) Krehula, S.; Musić, S. The Effect of Iridium (III) Ions on the Formation of Iron Oxides in a Highly Alkaline Medium. *J. Alloys Compd*. 2012, **516**, 207–216. https://doi.org/10.1016/J.JALLCOM.2011.12.052.

(2) Banta, R. A.; Collins, T. W.; Curley, R.; O'Connell, J.; Young, P. W.; Holmes, J. D.; Flynn, E. J. Regulated Phase Separation in Nanopatterned Protein-Polysaccharide Thin Films by Spin Coating. *Colloids Surfaces B Biointerfaces* 2020, **190**, Article No. 110967. https://doi.org/10.1016/j.colsurfb.2020.110967.

(3) Chen, L.; Yang, X.; Chen, J.; Liu, J.; Wu, H.; Zhan, H.; Liang, C.; Wu, M. Continuous Shape- and Spectroscopy-Tuning of Hematite Nanocrystals. *Inorg. Chem.* 2010, **49** (18), 8411–8420. https://doi.org/10.1021/ic100919a.

(4) Ahmmad, B.; Leonard, K.; Shariful Islam, M.; Kurawaki, J.; Muruganandham, M.; Ohkubo, T.; Kuroda, Y. Green Synthesis of Mesoporous Hematite (α-Fe_2O3) Nanoparticles and Their Photocatalytic Activity. Adv. Powder Technol. 2013, **24** (1), 160–167. https://doi.org/10.1016/J.APT.2012.04.005.

(5) Zboril, R.; Mashlan, M.; Petridis, D. Iron (III) Oxides from Thermal Processes - Synthesis, Structural and Magnetic Properties, Mössbauer Spectroscopy Characterization, and Applications. *Chem. Mater*. 2002, **14** (3), 969–982. https://doi.org/10.1021/CM0111074.

(6) Kashiwaya, Y.; Akiyama, T. Nanocrack Formation in Hematite through the Dehydration of Goethite and the Carbon Infiltration from Biotar. J. Nanomater. 2010, Article ID 235609. https://doi.org/10.1155/2010/235609.

(7) Jia, F.; Ramirez-Muñiz, K.; Song, S. Mechanism of the Formation of Micropores in the Thermal Decomposition of Goethite to Hematite. *Surf. Interface Anal*. 2015, **47** (4), 535–539. https://doi.org/10.1002/sia.5744.

(8) Wieczorek-Ciurowa, K.; Kozak, A. J. The Thermal Decomposition of $Fe(NO_3)_3 \cdot 9H_2O$. *J. Therm. Anal. Calorim.* 1999, **58** (3), 647–651. https://doi.org/10.1023/A:1010112814013.

(9) Cho, W. C.; Kim, C. G.; Jeong, S. U.; Park, C. S.; Kang, K. S.; Lee, D. Y.; Kim, S. D. Activation and Reactivity of Iron Oxides as Oxygen Carriers for Hydrogen Production by Chemical Looping. *Ind. Eng. Chem. Res.* 2015, **54** (12), 3091–3100. https://doi.org/10.1021/ie504468a.

(10) Liu, H.; Zhang, Z.; Li, Q.; Chen, T.; Zhang, C.; Chen, D.; Zhu, C.; Jiang, Y. Novel Method for Preparing Controllable Nanoporous α-Fe_2O_3 and Its Reactivity to SCR De-NO_x. *Aerosol Air Qual. Res*. 2017, **17** (7), 1898–1908. https://doi.org/10.4209/aaqr.2017.05.0188.

(11) Ghoshal, T.; Holmes, J. D.; Morris, M. A. Development of Ordered, Porous (Sub-25 Nm Dimensions) Surface Membrane Structures Using a Block Copolymer Approach. *Sci. Rep.* 2018, **8** (1), 7252. https://doi.org/10.1038/s41598-018-25446-0.

(12) Guo, X.; Liu, L.; Zhuang, Z.; Chen, X.; Ni, M.; Li, Y.; Cui, Y.; Zhan, P.; Yuan, C.; Ge, H.; Wang, Z.; Chen, Y. A New Strategy of Lithography Based on Phase Separation of Polymer Blends. *Sci. Rep*. 2015, **5** (Article 15947). https://doi.org/10.1038/srep15947.

(13) Al-Qunaibit, M.; Khalil, M.; Al-Wassil, A. The Effect of Solvents on Metal Ion Adsorption by the Alga Chlorella Vulgaris. *Chemosphere* 2005, **60** (3), 412–418. https://doi.org/10.1016/J.CHEMOSPHERE.2004.12.040.

(14) Al-Qunaibit, M. H. Divalent Cu, Cd, and Pb Biosorption in Mixed Solvents. *Bioinorg. Chem. Appl.*, 2009, Article ID 561091. https://doi.org/10.1155/2009/561091.

(15) Sherwood, J.; Clark, J. H.; Fairlamb, I. J. S.; Slattery, J. M. Solvent Effects in Palladium Catalysed Cross-Coupling Reactions. *Green Chem*. 2019, **21** (9), 2164–2213. https://doi.org/10.1039/C9GC00617F.

(16) Ansari Fard, M.; Rounaghi, G. H.; Chamsaz, M.; Taheri, K. Study of Complex Formation between 18-Crown-6 and Diaza-18-Crown-6 with Uranyl Cation (UO_2^{2+}) in Some Binary Mixed Aqueous and Non-Aqueous Solvents. *J. Incl. Phenom. Macrocycl. Chem*. 2009, **64** (1–2), 49–56. https://doi.org/10.1007/s10847-009-9535-8.

(17) Chu, Y.; Yang, Z.; Rodgers, M. Solvation of Copper Ions by Acetone. Structures and Sequential Binding Energies of $Cu^+(acetone)_x$, x = 1–4 from Collision-Induced Dissociation and Theoretical Studies. *J. Am. Soc. Mass Spectrom*. 2002, **13** (5), 453–468. https://doi.org/10.1016/S1044-0305(02)00355-0.

(18) Maglio, O.; Nastri, F.; Lombardi, A. Structural and Functional Aspects of Metal Binding Sites in Natural and Designed Metalloproteins in *Ionic Interactions in Natural and Synthetic Macromolecules*; Ciferri, A., Perico, A., Eds 1st.; John Wiley & Sons, Inc.: Hoboken, NJ, USA, 2012; pp 361–450. https://doi.org/10.1002/9781118165850.ch11.

(19) Okur, H. I.; Hladílková, J.; Rembert, K. B.; Cho, Y.; Heyda, J.; Dzubiella, J.; Cremer, P. S.; Jungwirth, P. Beyond the Hofmeister Series: Ion-Specific Effects on Proteins and Their Biological Functions. *J. Phys. Chem. B* 2017, **121** (9), 1997–2014. https://doi.org/10.1021/acs.jpcb.6b10797.

(20) Topală, T.; Bodoki, A.; Oprean, L.; Oprean, R. Bovine Serum Albumin Interactions with Metal Complexes. *CLUJUL Med*. 2014, **87** (4), 215–219. https://doi.org/10.15386/cjmed-357.

(21) Saha, B.; Chakraborty, S.; Das, G. A Rational Approach for Controlled Adsorption of Metal Ions on Bovine Serum Albumin−Malachite Bionanocomposite. *J. Phys. Chem. C* 2010, **114** (21), 9817–9825. https://doi.org/10.1021/jp1003243.

(22) Ferranco, A.; Basak, S.; Lough, A.; Kraatz, H.-B. Metal Coordination of Ferrocene–Histidine Conjugates. *Dalt. Trans.* 2017, **46** (14), 4844–4859. https://doi.org/10.1039/C7DT00456G.

(23) Alekseev, V. G.; Semenov, A. N.; Pakhomov, P. M. Complexation of Ag^+ Ions with L-Cysteine. *Russ. J. Inorg. Chem*. 2012, **57** (7), 1041–1044. https://doi.org/10.1134/S0036023612070029.

Chapter 5

Conclusion and Future Work

5.1 CONCLUSION

Biopolymer blends have a wide array of applications in bottom-up manufacturing of structures due to the facile nature of production, tuneable feature size, tuneable morphology, potential to reuse agricultural waste and applicability in industrial scale techniques. Of interest to myself is their application in future optoelectronic devices. Current interest in polymer blends stems from a desire to achieve a greater range of feature sizes, outside the capable range of BCP, in a rapid and cheap fashion. These polymers are still derived from petroleum oil, and require environmentally damaging extraction of the finite raw chemicals, synthetic manufacturing of the polymer and refinement of the polymer once produced. To achieve polymers with varying chemistry, new synthesis routes must be discovered. Production of patterns also require the use of organic solvents, often environmentally unfriendly. Biopolymers by their very nature are renewable, sustainable, environmentally friendly, require little refinement, are easily accessible and use environmentally benign solvents throughout their processing. A plethora of biopolymers exist, providing an inexhaustible reservoir of chemical diversity. While work must still be done to overcome the challenges of using a biopolymer blend system, our work shows that these blends are viable candidates for next-generation smart materials. As the need for sustainable manufacturing increases, I foresee growing interest in this bottom-up approach to design surfaces.

In summary, I have reported in this thesis the morphological control of biopolymer blended films, by regulating atmospheric humidity to modulate solvent evaporation. In **Chapter 2**, I reported the effect of humidity on film formation. Casting was done using a Meyer bar. Use of FA (formic acid) ensured segregated phase separation and fast solvent evaporation. Morphology was dependant on atmospheric conditions, biopolymers used, *r*, and solution viscosity. AFM indicated that PG/Ch blends were subject to gelation, making them unsuitable for future work. With reduced humidity, vitrification of the phase separation process took place earlier. This was attributed to fast solvent evaporation arresting feature growth. Similarly, by increasing the viscosity of the discontinuous phase (Ch), protein phase growth was impeded. BSA/Ch blends provided films with clear phase boundaries, necessary for the fabrication of templates. Blends achieved a smaller feature size than any previous biopolymer blends and were comparable or exceeded current synthetic polymer blends.

Chapter 3 described the use of BSA/Ch blends deposited on a substrate using spin coating as the casting technique. The formation of BSA continuous phases and salami structures occurred at high wt% concentrations of BSA, low spin speeds or a combination of the two factors. Through selective buffered etching of the biopolymer films, and selective metal incorporation and water contact angle characterisation, BSA was identified as the discontinuous phase and Ch as the continuous phase. Both the selected phase removal, and selective iron incorporation, were a first for films of this nature. An iron oxide copy of the Ch domain was achieved by selectively incorporating a hard metal cation into the Ch domain before annealing. Ch rim formation around the BSA domain occurred, resulting from pinning of the triple-phase protein-polysaccharide-air boundary. Identification of the growth mechanism for high protein or high polysaccharide content blends was also determined to be either Ostwald ripening or coalescence, depending on the casting conditions.

Chapter 4 combined the environmental control demonstrated in **Chapter 2** with the spin casting and metal incorporation technique explained in **Chapter 3**, to develop a metal mask suitable for pattern transfer. Selective incorporation of the metal depended on two primary factors; the metal salt cation and the metal salt anion. Due to the lone pair on the primary amine of Ch, hard metals were chelated and incorporated into the Ch domain, when using an anion with weak protein affinity, *e.g.* Cl^-, producing a porous matrix. Cracking of the porous matrix upon annealing was prevented by pre-heating the sample at 160 °C to remove water. Using an anion with a stronger protein affinity (NO_3^-), result in hard metals being shuttled to the protein backbone. Using strongly hydrated anions, *e.g.* SO_4^{2-}, resulted in metals being shuttled to protein functional groups. Anions such as NO_3^- and SO_4^{2-} result in particulate formation in the BSA domain. Solvents with weak solute interactions and low dielectric constant resulted in improved metal incorporation into the biopolymer blend. Tessellation of the biopolymer blend occurred when the environmental control detailed in **Chapter 2** and deposition technique outlined in **Chapter 3** were combined, highly uncommon for polymer blends. A maximum of 53% of pores were successfully transferred to the substrate.

5.2 FUTURE WORK

The films produced in this thesis are ideal candidates for AR (antireflective) applications, where polydisperse sub-micron features are required. Voronoi tessellation provides a bottom-up method of realising pores identical to those of butterfly wings. The

morphology, size, and disordered nature of butterfly wings is what provides them with their amazing AR properties. For butterfly wings, "randomness is the origin of the remarkable broadband and omnidirectional anti-reflective property".[1] The disordered nature of 2D pores in a butterfly wing is an improvement on synthetic films which are produced using a periodic array of features (pores or pillars).[2] While other polymer blend film research has focused on achieving disordered patterned thin films, > 100 nm pores to emulate butterfly wings[3], they cannot achieve: (1) the tessellated nature of butterfly wing pores, thus achieving the high number of pores/area shown in this work and (2) pores with the correct SD (approx. 300 – 800 nm in diameter).[4–7] To fully capitalise on this work in future studies, total transference of pores to the substrate must be achieved. There are a few approaches that could be used to achieve this.

Approach #1; discussed in **Chapter 4**, environmental controls could achieve full perforation of BSA to the substrate.[8,9] With sufficient control, after metal incorporation and annealing, fully perforated pores could be transferred to the substrate via etching. This method would be ideal, as it would require the least amount of post-processing. However, as both biopolymers are just varying degrees of hydrophilic, achieving this will be difficult. The WCA (water contact angle) in **Chapter 4** show there is some difference in hydrophilicity between BSA and Ch, so this should be achievable. As BSA is more hydrophobic, increasing humidity would improve BSA perforation[8,9], as evidenced in **Figure 4.8**. However, this will lead to longer phase growth times, producing larger structures. The tessellation results from the blend being in a frozen state, while being highly packed. To maintain tessellation and pore sizes, higher spin speeds may be required at higher humidities. This may introduce shear effects, as discussed in **Chapter 3**.

Approach #2: to avoid the complexities of modifying the internal structure of the BSA/Ch film, a simple reactive ion etch could be used to remove Ch at the bottom of film pores, after BSA removal.[10] This would fully expose the Si substrate. However, requires more post processing than just achieving BSA perforation, and runs the risk of expanding the diameter of already perforated pores, making this technique less attractive than **Approach #1**. Alternatively, enzymes could be used to develop the template. Though much more environmentally friendly, this is a timely process, and would hinder the possibility of industrial adoption.[11]

Approach #3: similar to etching residual Ch at the bottom of pores to expose the substrate, residual iron could be removed through a similar etch. However, the same issues (expanding the diameter of pores) exist here. The removal of residual Ch would have to be

compared to the removal of residual iron, to determine which method better retains the morphology of the biopolymer template.

Approach #4: after using buffer to selectively remove the BSA phase, and residual Ch is removed using a reactive ion etch, a CHF_3 etch could then be used to transfer the biopolymer template pattern to the substrate, without the need for metal.[11,12] However, finding the right etch recipe can be difficult, if one wishes to retain the fidelity of the biopolymer template.

Approach #5: Polymer brushes are used when preparing patterned BCP films, to prevent preferential adsorption of one block to the substrate.[13] Already, brushes exist which repel BSA adsorption onto a surface, such as poly(oligo(ethylene glycol) monomethacrylate) [14], or prevent adsorption, such as poly(2-(dimethylamino)ethyl methacrylate).[15] Using a polymer brush could allow for full perforation of the BSA domain. However, brush layers are avoided if possible, as developing them can be complex, and adds additional processing steps to prepare the surface.[13]

Finally, using the information gained in **Chapters 3** and **4**, metal binding to the biopolymer PTF could be optimized in 3 ways.

Approach #1: An alternative protein could be chosen with no metal binding sites, *i.e.* no histidine or cysteine residues. This would achieve only binding to the polysaccharide phase, reducing the number of variable when including metal into the PTF. Alternatively, by using a viscous polysaccharide and a protein with a high affinity for specific metals, *i.e.* haemoglobin, a dot matrix could be formed without incorporation into the polysaccharide phase.

Approach #2: This approach looks to the future of materials chemistry and is one of the more ambitious ideas. Rather than looking to nature to produce the biopolymers needed for PTFs, we could utilise nature to produce proteins to our specifications. Synthetic biology is a sub-section of genetics and biochemistry. Using modular parts, cells (typically *E. coli*) can be programmed to perform various tasks, such as producing specific proteins. Most proteins produced in this manner have a polyhistidine-tag (His-tag, 6 histidine amino acids in succession). This His-tag allows for purification of the protein from all other proteins within the cell after lysis. His-tags chelate chromatography resins which contain divalent metals, such as Ni^{2+}, Cu^{2+}, or Co^{2+}. Cu^{2+} resins provide the poorest specificity. Ni^{2+} resins are the most common, though non-specifically bind to proteins with groups of histidine. Co^{2+} resins produce the highest purity filtrates, with minimal non-specific interactions with proteins. Using this knowledge, a protein could be designed, in a similar manner to BCPs, with blocks

of Hi-tags. This would ensure both high purity of the protein after chromatography, and high metal binding capacity when producing a metal film.

Approach #3: Lastly, a variant on **Approach #2**, would to be to create a recombinant protein divided into blocks, similar to BCPs. Rather than blending with a polysaccharide, this recombinant protein could be used as a replacement for BCPs, as the AAs are covalently bonded. Block 1 would need to contain a polar amino acid for metal binding, such as histidine or cysteine, while the second block would need to contain a hydrophobic amino acid to promote phase separation. With enough dissimilarity between the block, phase separation of the blocks would occur upon casting. This approach would analogous to Ps-*b*-PEO.[16] While this would create a sustainable source of biologically produced BCPs, **Approach #2** and **#3** would be difficult as yields for recombinant proteins are notoriously low.

5.3 REFERENCES

(1) Siddique, R. H.; Gomard, G.; Hölscher, H. The Role of Random Nanostructures for the Omnidirectional Anti-Reflection Properties of the Glasswing Butterfly. *Nat. Commun*. 2015, **6** (1), 1–8. https://doi.org/10.1038/ncomms7909.

(2) Wang, W.; Zhang, W.; Fang, X.; Huang, Y.; Liu, Q.; Bai, M.; Zhang, D. Omnidirectional Light Absorption of Disordered Nano-Hole Structure Inspired from Papilio Ulysses. *Opt. Lett.* 2014, **39** (14), 4208. https://doi.org/10.1364/ol.39.004208.

(3) Siddique, R. H.; Donie, Y. J.; Gomard, G.; Yalamanchili, S.; Merdzhanova, T.; Lemmer, U.; Hölscher, H. Bioinspired Phase-Separated Disordered Nanostructures for Thin Photovoltaic Absorbers. *Sci. Adv*. 2017, **3** (10), e1700232. https://doi.org/10.1126/sciadv.1700232.

(4) Zhang, W.; Zhang, D.; Fan, T.; Gu, J.; Ding, J.; Wang, H.; Guo, Q.; Ogawa, H. Novel Photoanode Structure Templated from Butterfly Wing Scales. Chem. Mater. 2009, 21 (1), 33–40. https://doi.org/10.1021/cm702458p.

(5) Zhang, Z.; Yu, K.; Lou, L.; Yin, H.; Li, B.; Zhu, Z. Morphology-Controlled Synthesis of ZnO Replicas with Photonic Structures from Butterfly (Papilio Paris) Wing Scales for Tunable Optical Properties. *Nanoscale* 2012, **4** (8), 2606. https://doi.org/10.1039/c2nr30284e.

(6) Siddique, R. H.; Donie, Y. J.; Gomard, G.; Yalamanchili, S.; Merdzhanova, T.; Lemmer, U.; Hölscher, H. Bioinspired Phase-Separated Disordered Nanostructures for Thin Photovoltaic Absorbers. *Sci. Adv*. 2017, **3** (10), e1700232. https://doi.org/10.1126/sciadv.1700232.

(7) Liu, H.; QibinZhao; Zhou, H.; Ding, J.; Zhang, D.; Zhu, H.; Fan, T. Hydrogen Evolution via Sunlight Water Splitting on an Artificial Butterfly Wing Architecture. *Phys. Chem. Chem. Phys.* 2011, **13** (23), 10872. https://doi.org/10.1039/c1cp20787c.

(8) Huang, C.; Moosmann, M.; Jin, J.; Heiler, T.; Walheim, S.; Schimmel, T. Polymer Blend Lithography: A Versatile Method to Fabricate Nanopatterned Self-Assembled Monolayers. *Beilstein J. Nanotechnol*. 2012, **3**, 620–628. https://doi.org/10.3762/bjnano.3.71.

(9) Huang, C.; Förste, A.; Walheim, S.; Schimmel, T. Polymer Blend Lithography for Metal Films: Large-Area Patterning with over 1 Billion Holes/Inch^2. *Beilstein J. Nanotechnol*. 2015, **6**, 1205–1211. https://doi.org/10.3762/bjnano.6.123.

(10) Guo, X.; Liu, L.; Zhuang, Z.; Chen, X.; Ni, M.; Li, Y.; Cui, Y.; Zhan, P.; Yuan, C.; Ge, H.; Wang, Z.; Chen, Y. A New Strategy of Lithography Based on Phase Separation of Polymer Blends. *Sci. Rep*. 2015, **5** (Article 15947). https://doi.org/10.1038/srep15947.

(11) Jiang, B.; Yang, J.; Li, C.; Zhang, L.; Zhang, X.; Yang, P. Water-Based Photo- and Electron-Beam Lithography Using Egg White as a Resist. *Adv. Mater. Interfaces* 2017, **4** (7), Article No. 1601223. https://doi.org/10.1002/admi.201601223.

(12) Caillau, M.; Crémillieu, P.; Laurenceau, E.; Chevolot, Y.; Leclercq, J.-L.; Alekseev, S.; Chevalier, C.; Delair, T. Fifty Nanometer Lines Patterned into Silica Using Water Developable Chitosan Bioresist and Electron Beam Lithography. *J. Vac. Sci. Technol. B Nanotechnol. Microelectron. Mater. Process. Meas. Phenom.* 2017, **35** (60GE01). https://doi.org/10.1116/1.4996870.

(13) Mokarian-Tabari, P.; Collins, T. W.; Holmes, J. D.; Morris, M. A. Brushless and Controlled Microphase Separation of Lamellar Polystyrene-b-Polyethylene Oxide Thin Films for Block Copolymer Nanolithography. *J. Polym. Sci. Part B Polym. Phys*. 2012, **50** (13), 904–909. https://doi.org/10.1002/polb.23082.

(14) Inoue, Y.; Nakanishi, T.; Ishihara, K. Adhesion Force of Proteins against Hydrophilic Polymer Brush Surfaces. *React. Funct. Polym.* 2011, **71** (3), 350–355. https://doi.org/10.1016/j.reactfunctpolym.2010.11.017.

(15) Wang, X.; Berger, R.; Ramos, J. I.; Wang, T.; Koynov, K.; Liu, G.; Butt, H. J.; Wu, S. Nanopatterns of Polymer Brushes for Understanding Protein Adsorption on the Nanoscale. *RSC Adv*. 2014, **4** (85), 45059–45064. https://doi.org/10.1039/c4ra07623k.

(16) Ghoshal, T.; Shaw, M. T.; Bolger, C. T.; Holmes, J. D.; Morris, M. A. A General Method for Controlled Nanopatterning of Oxide Dots: A Microphase Separated Block Copolymer Platform. *J. Mater. Chem.* 2012, **22** (24), 12083–12089. https://doi.org/10.1039/c2jm30468f.